Durham E-Theses

Numerical analysis of deformation in the upper part of subduction zones

Park, M.J.M.

NUMERICAL ANALYSIS OF DEFORMATION

IN THE UPPER PART OF

SUBDUCTION ZONES

BY

M.J.M. PARK

A thesis submitted for the degree of

Doctor of Philosophy in the

University of Durham

Graduate Society   January 1981

To my parents

ABSTRACT

The stresses and deformation in an accretionary prism, and the crystalline basement behind and beneath it, have been modelled using finite element analysis, assuming a visco-elastic Maxwell rheology for the rocks involved.

A new method for finding the effect of lateral variations in density and body forces on the deformation in such models has been developed, so that the balance between weight and basal shear in the accretionary prism, and the associated displacement and stress distributions, could be modelled.

Analysis shows that there is an equilibrium basal stress that supports the weight of the accreted sediments. Above this stress the accretionary prism is built higher, and below it subsides and spreads up the basal slope. The average value for this stress was found to be 12 MPa for the Middle America subduction zone and 5 MPa for the central Aleutians.

Models of these two subduction zones show important differences in surface displacement and stress distribution, due to the slope and extent of the overriding basement rocks. In the island arc model, it was concluded that the igneous crust extended beneath the Aleutian terrace to the edge of the inner trench slope, while in the case of the Middle America subduction zone the continental basement is cut back at depth and parts of it are underlain by accreted sediments.

Displacement boundary conditions were applied to the basal thrust to investigate the effects of coupling and decoupling on it, and in this way the repeat time for earthquakes, at a depth of c. 15 km in the Middle America subduction zone, was predicted to be c. 250 yr, or less.

Finally, the results for a simple accretionary wedge, applied to the mechanics of a thrust sheet, show that the basal gradient is an important controlling factor, and that gravitational forces alone cannot cause thrust motion up a basal slope, unless the thrust wedge is supported (at the end lower down the basal slope) by stresses which are lithostatic or greater.

ACKNOWLEDGEMENTS

CONTENTS

CHAPTER 3 THE FINITE ELEMENT METHOD

BIBLIOGRAPHY

But thou shalt flourish in immortal youth,

Unhurt amidst the wars of elements,

The wrecks of matter, and the crush of worlds.

Joseph Addison, *Cato*, V, i, 28.

CHAPTER 1

FEATURES OF SUBDUCTION ZONES AND THEIR PHYSICAL SIGNIFICANCE

1.1 Evidence for Subduction

One of the most important implications of the now widely accepted
theory of plate tectonics, is that oceanic lithosphere is subducted
into the mantle along deep sea trenches. Over the past decade, a considerable
number of observations have been made which support this hypothesis, the
evidence falling into four main categories; earthquake seismology, seismic
reflection and refraction profiles, and direct sampling of the material
in, and near trenches.

1.1.1 Earthquake seismology

Perhaps the most convincing argument supporting subduction is the
asymmetry of the earthquake zones associated with island arcs and
continental margins.

A large proportion of intermediate and deep earthquakes (i.e. all
those below about 50 km depth) are associated with deep sea trenches, and
have hypocentres which define regions, known as Benioff zones, dipping
at angles between 30° and 60° approximately, beneath volcanic chains,
which may be on continental crust (e.g. the Andes), or which may form
island arcs (e.g. the Aleutian Islands) if the crust above the Benioff
zone is oceanic. Isacks and Molnar (1971) analysed 204 sets of hypocentre
and focal mechanism data, and presented profiles of all the major Benioff
zones. From this analysis, they showed that in nearly all cases one of
the principal stresses associated with the earthquake was aligned parallel
to the dip of the Benioff zone, and since the stress down-dip may be
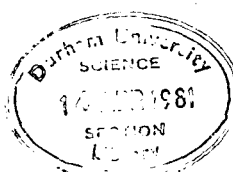
either tensional or compressional, they deduced that the earthquakes usually take place within a sinking slab of lithosphere, rather than on a single thrust plane at its upper surface. More recently, however, detailed analyses have been made of the seismic zone beneath Northeastern Honshu, Japan (Hasegawa et al., 1978; Yoshii, 1979; Hasegawa et al., 1979), which show that in this case, the seismicity lies on two parallel planes, associated with the upper surface and the interior of the subducted plate, respectively.

Seismic zones have also been shown (Oliver and Isacks, 1967; Barazangi et al., 1972; Hasegawa et al., 1979) to coincide with regions of high Q (quality factor) which act as waveguides for high frequency shear waves, and which are continuous with the oceanic lithosphere that is seaward of the trench.

These observations imply that the oceanic lithosphere sinks, or is pushed, through a bend of up to about 60°, into the mantle where it is assimilated.

1.1.2 Seismic reflection profiles

Although seismic reflection profiles are often made obscure by the acoustically opaque region resulting from intense deformation in the inner (landward) wall of the trench, they show that this deformation is due to thrusting. In addition, in many profiles (Hilde et al., 1969; von Huene, 1972; Beck and Lehner, 1974; Seely et al., 1974) the oceanic basement, layer 2, can be traced, dipping at 5° or 10°, beneath the trench sediments, which lie horizontally and are undeformed except close to the inner trench wall. Occasionally the subducted crust can be traced beneath the deformed region for as much as 30 to 40 km from the trench, and an example of this is shown, from the Lesser Antilles complex, in Fig. 1.1
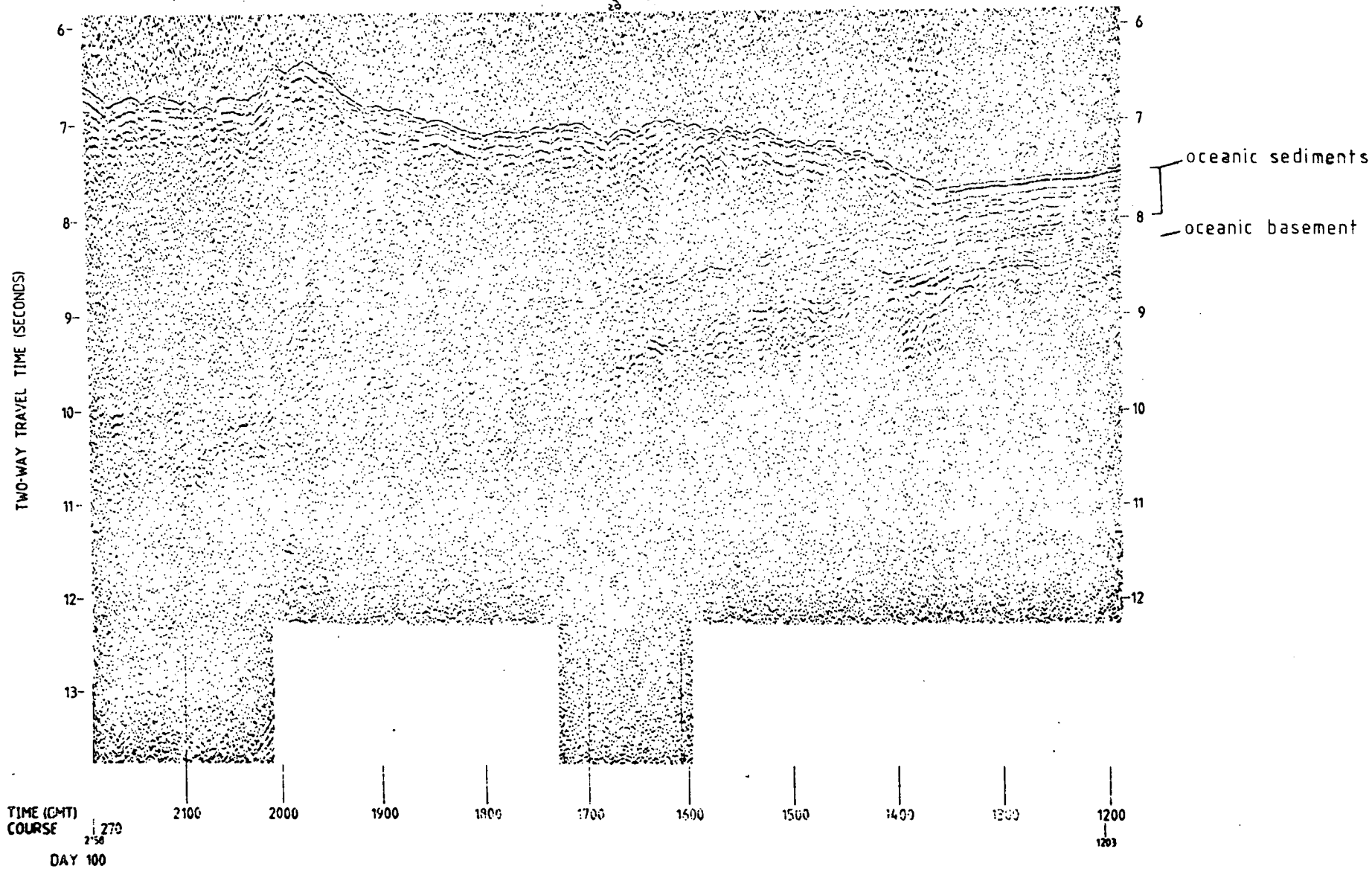
Fig. 1.1: Monitor record of an E-W seismic reflection profile across the toe of the Caribbean accretionary complex due East of Guadeloupe, ship speed 9 km hr^{-1} (recorded by Durham University on R.R.S. Discovery, Cruise 109, April, 1980).

(unpublished data collected by Durham University Department of Geological Sciences on Cruise 109 of the RRS Discovery, 10 March - 19 April, 1980; see also Beck and Lehner, 1974). Note that in this profile, subducted oceanic sediments can also be seen overlying the (layer 2) basement.

When results from reflection work and gravity profiles are combined (e.g. Grow, 1973a), the resulting models are consistent with subduction.

1.1.3 Seismic refraction profiles

Seismic refraction profiles across trenches (e.g. Hussong et al., 1976; Meyer et al., 1976; Curray et al., 1977; Boynton et al., 1979) show that the Mohorovičić discontinuity, at the base of the oceanic crust, dips down under the trench, while the Moho on the landward side can be followed at roughly the same level (though depressed a certain amount by crustal thickening) right up to the edge of the trench.

The oceanic crustal rocks (layers 2 and 3) are brought into contact with the mantle, at a depth of c. 20 km in the Sunda arc (Curray et al., 1977), and at a depth of c. 50 km under the East of the Bolivar Basin, Western Colombia (Meyer et al., 1976). The latter depth is the larger because the overriding plate in this case carries continental crust, rather than oceanic as in the Sunda arc.

1.1.4 Rock sampling

Cores taken as part of the Deep Sea Drilling Project (hereinafter referred to as D.S.D.P.), in particular on Leg 66 across the accretionary complex landward of the Middle America trench (Moore et al., 1979a, 1979b; Moore and Watkins, 1979), together with the associated reflection profiles, show that sediments are carried by the oceanic plate into the trench, where

some are sheared off, together with sediments deposited in the trench, against the inner trench wall. The igneous oceanic basement (layers 2 and 3) and any remaining sedimentary cover continue beneath the accreted sediment wedge and finally into the mantle.

1.2 General Description of a Subduction Zone

The term "subduction zone" is taken broadly, to include all the features resulting from subduction of oceanic lithosphere, from the volcanic arc to the outer rise in front of the trench.

Although at first sight the features seen in subduction zones seem to vary considerably, by comparing bathymetric profiles across a great number of trenches and seismic profiles where available, Karig and Sharman (1975; Karig, 1974; see also Dickinson and Seely, 1979) have developed a general subduction zone cross-section, which is the basis for the terminology used here (Fig. 1.2).

The oceanic lithosphere is bowed upward as an elastic response to the bend imposed by subduction (see, e.g., Watts and Talwani, 1974; Caldwell et al., 1976) forming an "outer rise" of about 0.3 to 0.5 km in height, at about 50 km in front of the trench. The trench itself is typically 5 or 6 km deep and contains a wedge of sediments, usually turbidites derived from the island arc or continent, which varies in thickness from nearly zero in the Tonga-Kermadec trench to over 1 km in the Middle America trench.

Behind the trench is a region called the "accretionary prism", composed of tectonized sediments that have been scraped onto the overriding plate, and of an overlying, relatively undeformed sedimentary cover. The igneous crust of the island arc, or continental plate, abuts onto the accretionary prism, perhaps underlying part or all of it, and the
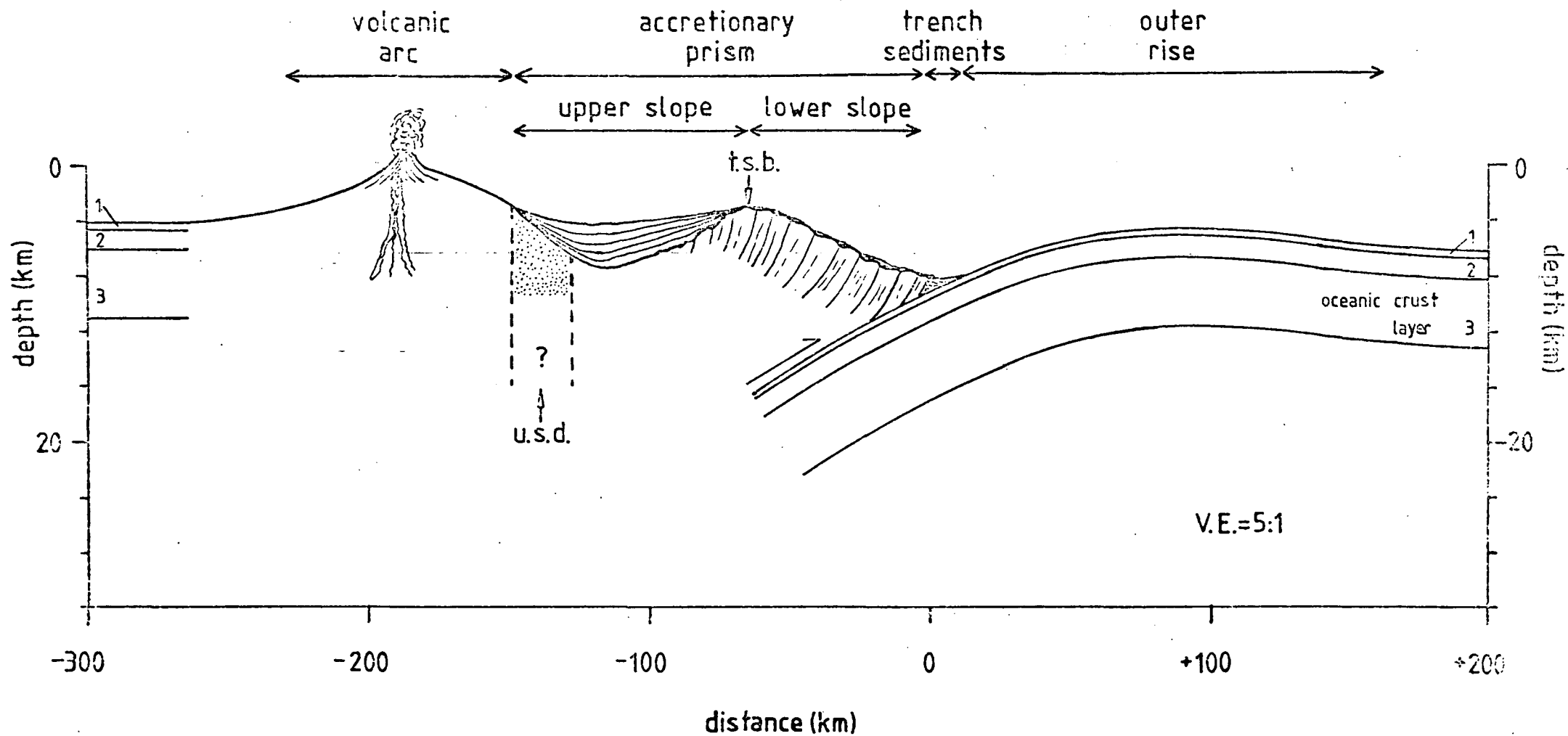
Fig. 1.2: A generalized cross-section of a subduction zone. See
text for discussion and explanation of terms (after
Karig, 1974).

join between igneous and sedimentary crust, near the surface, is called the "upper slope discontinuity" (or "u.s.d." in Fig. 1.2), but its nature is not clearly understood (see Section 1.4.2).

The accretionary prism is divided into two parts, the upper and lower inner trench slopes, by a change in gradient (which can take several forms; see Section 1.3) known as the "trench slope break" (or "t.s.b." of Fig. 1.2; Dickinson, 1973). The lower slope consists of deformed sediments which have been lifted up by sometimes as much as 5 km, and often has ridges along it parallel to the trench which may be the surface expression of imbricate thrusts (Dickinson and Seely, 1979). The upper slope on the other hand is not rising as quickly as the trench slope break, and is partially, or completely, filled with scarcely-deformed sediments derived from the island arc, and from the trench slope break where the latter is above sea level.

All the above features can be traced for great distances, typically several hundred kilometres, along the strike of the arc-trench system, which is ample justification for considering two-dimensional models of subduction zones.

1.3 The Lower Slope and Trench Slope Break

Seismic reflection profiles over the lower slope (Beck and Lehner, 1974; Seely et al., 1974) show sets of landward dipping reflectors within the generally opaque acoustic basement, some of which are particularly strong and are interpreted as listric thrust faults. Seismic refraction (Curray et al., 1977) and gravity data (Grow, 1973a) indicate that the lower slope is underlain by material with a low seismic velocity compared to oceanic layer 2, and a density of 2200 to 2400 kg m^{-3}, which lies on the oceanic crust being subducted.

The interpretation of this data as a prism of deformed sediments accreted by being scraped off the underlying oceanic crust, is supported by the results from some of the Deep Sea Drilling Project holes (Kulm et al., 1973; Creager et al., 1973; Ingle et al., 1975; Hussong et al., 1978; Moore et al., 1979; von Heune, Auboin et al., 1980). Of these, one of the more recent legs, number 66 (co-chiefs Moore and Watkins) is particularly useful, as seven holes were drilled between a site just forward of the trench and one near the edge of the continental crust, as shown in Fig. 1.3 (combined with structures shown on seismic lines MX-16 and OM-7N made by the University of Texas Marine Science Institute (UTMSI)).

The sediments in the trench are flat-lying and undeformed until close to the toe of the trench slope where the reflection profile shows folding and the start of the landward dipping reflectors (see also Hilde et al., 1969; von Heune, 1972). The degree of deformation increases rapidly to a maximum at the toe of the slope where thrust slices (Ingle et al., 1975; Moore, J.C., and Karig, 1976) are formed and sheared off the sinking plate. A good example of this is shown in Fig. 1.4, at the toe of the Middle America accretionary complex (Shipley et al., 1980).

Further up the slope the uppermost rocks, below the apron of muds, are less deformed, while the angle of the landward dipping reflectors increases. The cores from D.S.D.P. sites 488, 491 and 492 show an important characteristic, in that significant deformation begins in older sediments (but at shallower depths below the present sea bed) from one site to the next up-slope. Interbedded sand- and mudstone sequences were encountered in all three holes, which Moore et al. (1979) interpret as being trench turbidites.

Using the above information and the fossils found in each core it is possible to find the rate of uplift at each site and to assign a rate
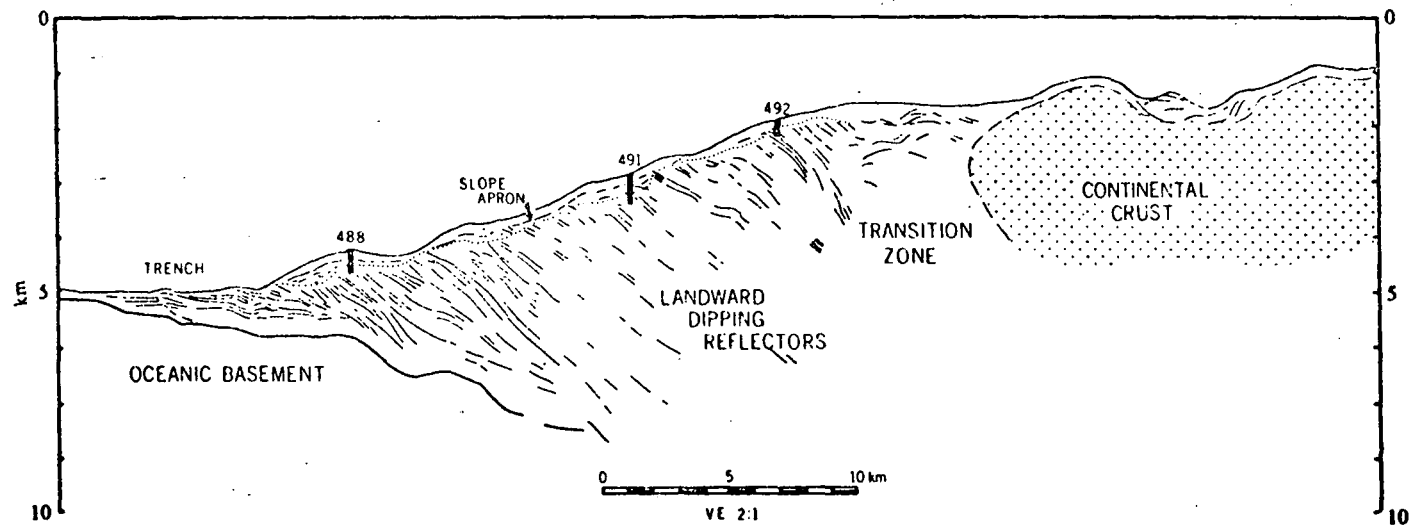
Fig. 1.3:   A seismic reflection profile across the Middle America trench,
South-East of Acapulco, showing the sites of some of the
D.S.D.P. Leg 66 boreholes (Moore et al., 1979b).
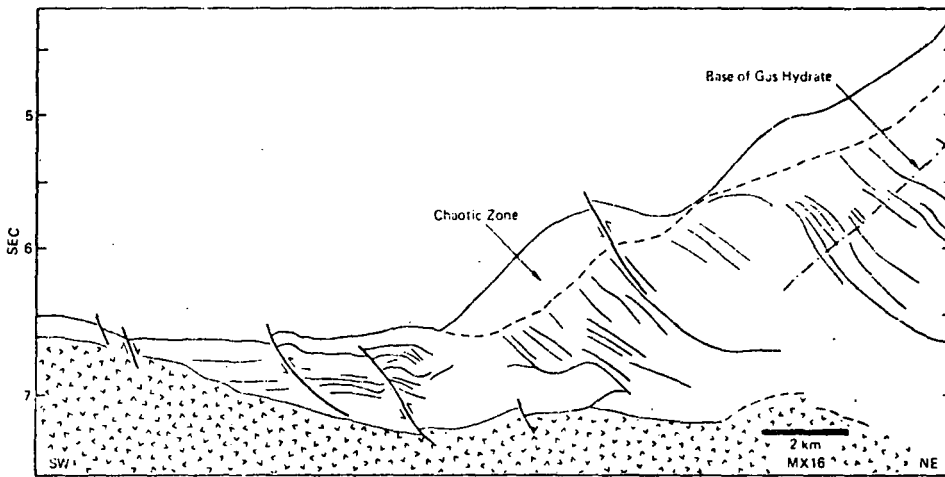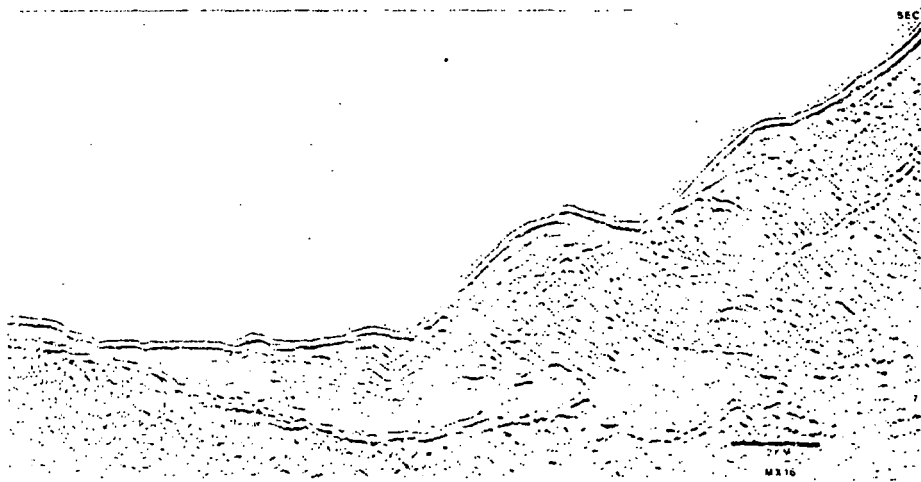
Fig. 1.4:   A migrated time section across the toe of the accretionary
            complex shown in Fig. 1.3 (U.T.M.S.I. Line MX16, Shipley
            et al., 1980, fig. 8).

of deformation to each. At the toe of the accretionary prism uplift occurs at about 500 m Myr^{-1}, and is reduced to about 100 m Myr^{-1} by the time the sediments have been raised 2 km above the trench floor. The rate of deformation at site 492 is about 0.1, and at 491 about 0.2, of the rate at the toe, site 488 (Moore et al 1979b).

The overall result of D.S.D.P. Leg 66 was to show that trench sediments and pelagic sediments from the incoming oceanic plate are scraped off at the toe of the inner trench slope and accreted to the base of the prism, involving slope sediments in the deformation as they are forced upward by further accretion beneath them. There are no major stratigraphic inversions observed in any one hole (even though site 488 was positioned over a suspected thrust plane) and the landward-dipping reflectors may well be the bedding surfaces between sand- and mudstone units, so that a significant part of the shear motion must be taken up on small shear surfaces throughout the accretionary prism rather than on major thrust faults.

However, Moore, G.F. and Karig (1976) present convincing evidence, on the basis of the deformation of basins on the inner slope, that there are major thrusts in a large number of cases. The slope basins are ponded behind ridges of acoustically opaque material (the deformed sedimentary basement), and their deformation suggests that the slope sediments are included in the accretionary prism by shearing along thrust planes.

It is not necessarily the case that all the sediments being carried into the subduction zone are accreted at the toe of the prism. Fig. 1.1, from the Lesser Antilles, shows oceanic sediments subducted about 30 km under the accretionary wedge. Watkins et al. (in press), on the basis of the D.S.D.P. Leg 66 results, postulate that, of the

total influx into the Middle America trench (90% from the trench sediments, 10% carried in on the oceanic plate), only 25% of the sediments are accreted on the inner trench slope. They conclude that 50% are subducted into the mantle, and that the remaining 25% are sheared off the subducted plate at greater depth and "underplated" beneath the accretionary prism.

If there is very little sediment to be scraped off the oceanic plate, then some basaltic oceanic crust may be accreted. Fig. 1.5 is a cross-section of the Mariana Trough, showing the sites where holes were drilled on D.S.D.P. Leg 60 (Hussong et al., 1978). The results of drilling at sites 460 and 461 were consistent with the accretion of oceanic crust, in that igneous and metamorphic rocks of the kind commonly found in ophiolites were recovered, but it is possible that these were fragments of the oceanic basement beneath the island arc. However, basaltic and ultramafic rocks are recovered by dredging on such slopes (Petelin, 1964; Fischer and Engel, 1969) which support the accretion mechanism.

The trench slope break is taken to be the point at which the sediments have been pushed up to their maximum height by the accretionary process and at which the deformation, due to that uplift, ceases. As such, the trench slope break takes four distinct forms (Fig. 1.6; Karig and Sharman, 1975; Karig, 1974).

(a) The first type of trench inner slope, taken to be the youngest, shows no significant distinction between the upper and lower slope. In these trenches (e.g. New Hebrides, Solomons and New Britain) igneous oceanic crust may be accreted on the very steep inner slope (Petelin, 1964), and subduction has not been active long enough to develop an accretionary prism.

(b) The second type displays a distinct break of slope on the trench inner wall and a very small, if any, upper slope basin (e.g. Mariana,
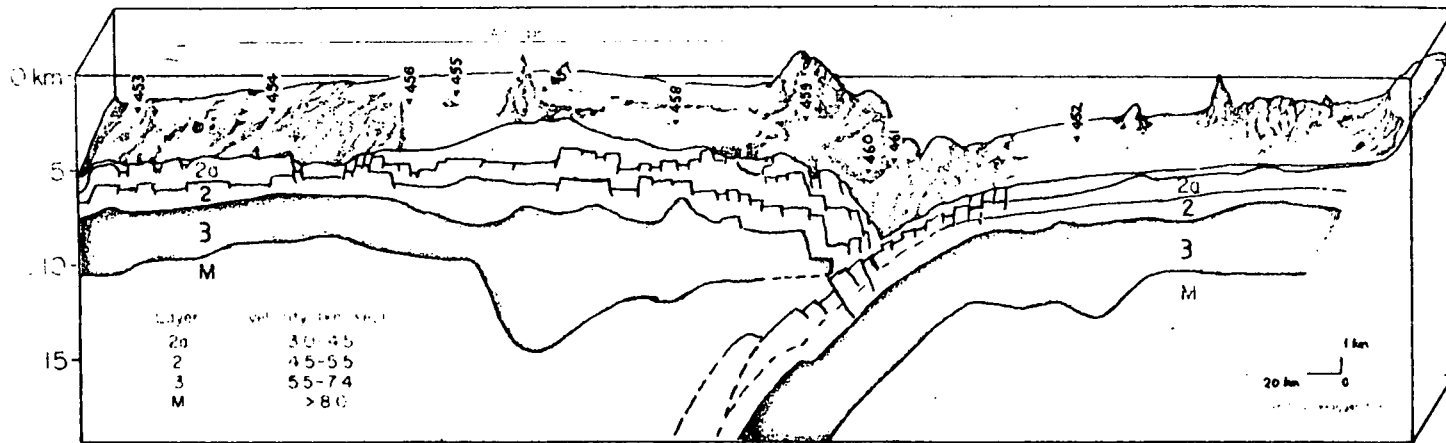
Fig. 1.5: A generalized cross-section of the Mariana Islands subduction
zone at Lat. 18°N, showing drill-sites from D.S.D.P. Leg 60
(Hussong, Uyeda et al., 1978).
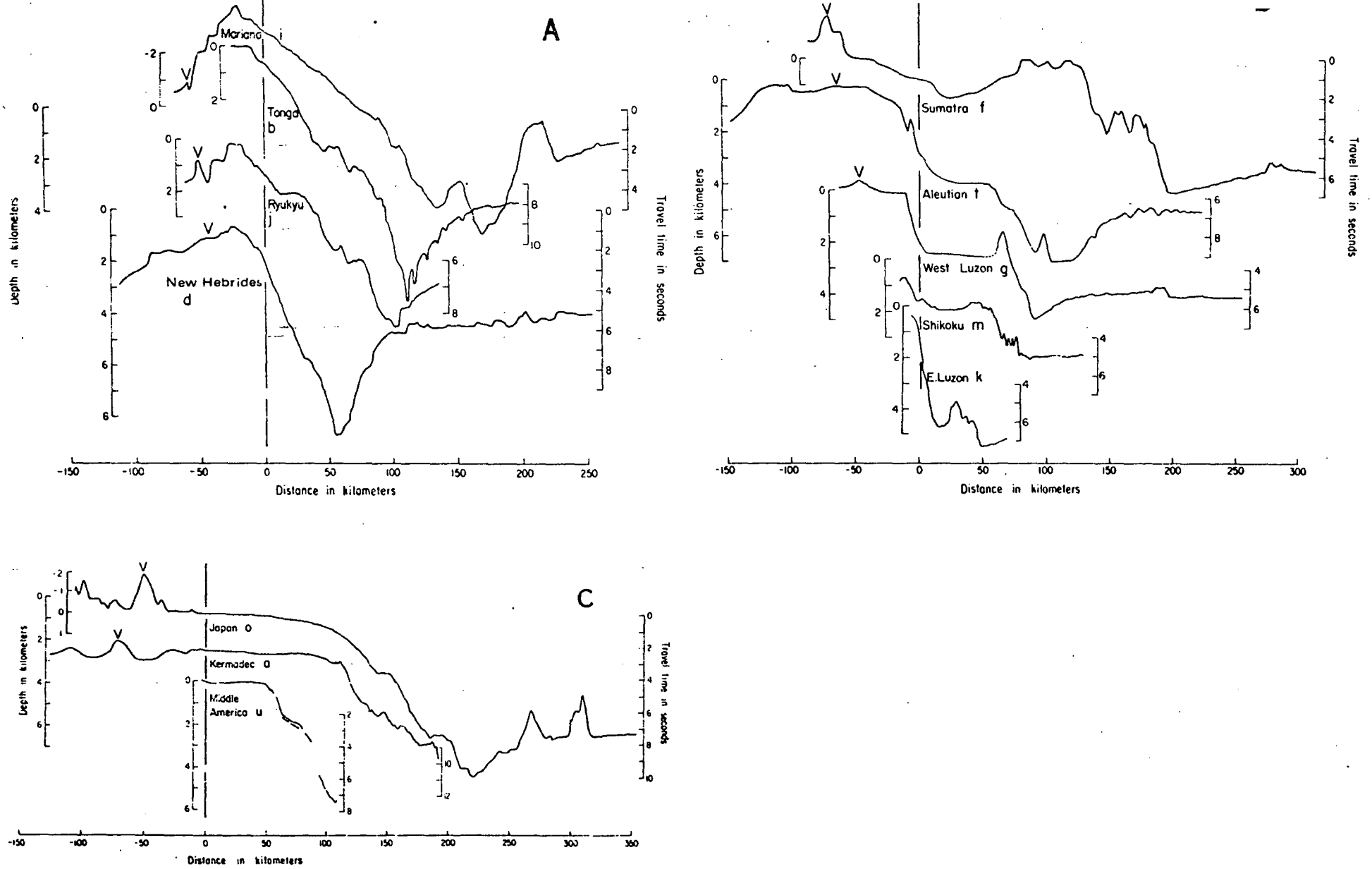
Fig. 1.6: Bathymetric profiles across various inner trench slopes showing different structures dependent on age and sediment influx (Karig and Sharman, 1975).

Tonga, Ryuku). At this type of trench, there is only a small thickness of pelagic sediments on the incoming plate and little or no terrigenous supply to the trench, and again dredging (Fischer and Engel, 1969) recovers basaltic rocks.

(c) In the third type there is a thick layer of sediment on the plate and in the trench. However this is not derived from the frontal or volcanic arc, but from a more distant source, the trench wedge being brought in by turbidity currents. Trenches of this type (Luzon, Shikoku, Central Aleutians, Sumatra) show the trench slope break as a well developed ridge, since it is raised up by the thickness of the accretionary prism, but there are no terrigenous sediment sources to fill the depression in the upper slope behind it.

(d) The final type corresponds to those trenches where the terrigenous sediment influx is large so that the upper slope is completely filled with sediments and forms a bench or terrace. If enough of these sediments are deposited in the trench, then the lower slope in front of the terrace is formed of accreted sediments regardless of the thickness of the pelagic sediment feed, (e.g. Eastern Aleutians), but if this is not the case, and if the pelagic sediments are thin, then although the terrace sediments are well developed, oceanic crust may still be accreted at the toe of the inner slope (e.g. Japan).

1.4 The Upper Slope

The upper slope, where it is developed, forms a basin of flat-lying and undeformed sediments which lap onto the ridge in front of it (generally the trench slope break) and onto the continent or island arc behind it. It is a feature which shows up well on reflection profiles (e.g. von Heune et al., 1971; Seely et al., 1974; Karig, 1977; Karig et al.,

1980) and in refraction work, where a common estimate of the depth of the sediments is 2 or 3 km (Curray et al., 1977). The widths of upper slope basins vary considerably, from less than 10 km in the East Luzon trench (Karig and Sharman, 1975) to about 100 km in the Tobago trough (Westbrook, 1975).

Although the whole upper slope region is thought to undergo absolute subsidence, at least after it has reached a certain size (Karig, 1977), it is convenient to consider the motion relative to the leading edge, and relative to the trailing edge, separately.

1.4.1 The leading edge

The ridge in front of the upper slope basin is a rising unit of tectonized sediments. The relative movement is demonstrated by the folding of the sediments over basement arches and drape structures on the rearward flank of the ridge. Reflection profiles for D.S.D.P. sites 186 and 187 (Grow, 1973b) show this draping, but the best evidence is where the ridge is above water level, for example the Mentawai Islands in the Sunda Arc, and Barbados in the Caribbean.

Karig (1977) gives a cross-section to the landward side of Nias Island, based on proprietary reflection profiles and an exploration well. He shows that the upper slope sediments are draped over a region of flexures on the East side of the island, and interprets these structures as the result of thrust slices that have been rotated just past the trench slope break and which are now subsiding with perhaps normal movement on old thrust faults. The sediments are barely deformed, maintaining continuity of bedding planes, and there is no evidence for any thrust faulting along this edge of the basin.

Westbrook (1975) shows, using reflection profiles across the Tobago

Trough, that the basin sediments are folded over basement arches just behind the Barbados ridge. These are interpreted as the surface expression of seaward-dipping thrust faults, formed during the uplift of the Barbados ridge as a secondary feature directly above the point of subduction of oceanic crust beneath crystalline basement, and over 100 km from the present trench slope break. Similar basement arches are seen in the Aleutians (Grow, 1973b), and may be the result of the seaward dipping thrust faults discussed by Seely (1977). This interpretation is in conflict with that of Karig and Sharman (1975) who regard both Nias and Barbados as regions of the trench slope break (see section 1.5.2, below).

1.4.2 The trailing edge and basement

The fact that the upper slope basin is subsiding relative to the volcanic arc, or continental crust (Karig et al., 1980), together with the angle of contact between them which is often steep, at least near the surface (von Heune et al., 1971; Hussong et al., 1976; Curray et al., 1977; Moore et al., 1979), suggests that there must be some decoupling between the accreted sediments and the igneous crust. This corresponds to the upper slope discontinuity defined in Section 1.2 (following Karig, 1974), but its behaviour at depth is poorly determined (see below, in this section).

As the width of the upper slope basin increases, so the deepest sedimentary layers within it tilt further (Grow, 1973b), but in such a manner that the axis of the basin remains near to the volcanic arc (von Heune et al., 1971; Seely et al., 1974; Karig, 1974), indicating that the subsidence is greatest close to the discontinuity. This implies that a large part of the relative motion between volcanic arc and basin is localized near the upper slope discontinuity rather than being evenly

distributed over the whole upper slope.

It is most likely, then, that faulting occurs at the leading edge of the continental or arc crust. This is certainly the case in the Eastern Aleutians, where there is a distinct system of steeply-dipping faults (von Heune et al., 1971), however the nature of these faults, whether normal or high-angle reverse is unclear. Karig (1977) interprets the work of Murdock (1969a and b) on earthquake focal mechanisms in this region as being evidence that the upper slope discontinuity is a reverse fault dipping at about 50° landward, but the fault shown by Murdock does not seem to be certain above a depth of 15 km, and the high angle thrust earthquakes may be part of the Benioff zone, if the latter has a shallow dip to start with and then bends steeply below the upper slope (Model B of Grow, 1973a; see Fig. 1.8).

Hussong et al. (1976) have interpreted reflection and refraction profiles across the Peru-Chile trench (at about latitude 10°S) as showing normal faulting in an analogous position at the edge of the upper slope, although in this case there is a very poorly-developed basin. From the velocity structure they suggest that continental material is being sheared off at its contact with the subducting plate, as do Curray et al. (1977) in the case of the Sunda and Banda arcs, and that these thrust planes dip progressively more steeply landward at shallower depths until they turn over and become normal faults close to the surface.

If this occurs then the two types of fault may simply represent different degrees of rotation of the basal thrust and could both be due to the same possible mechanism (see Fig. 1.7).

The disruption of the crystalline basement beneath the upper slope makes it difficult to find how far it extends towards the trench. Magnetic profiles (e.g. Grow, 1973a; Karig et al., 1978) can trace it as far as

a)
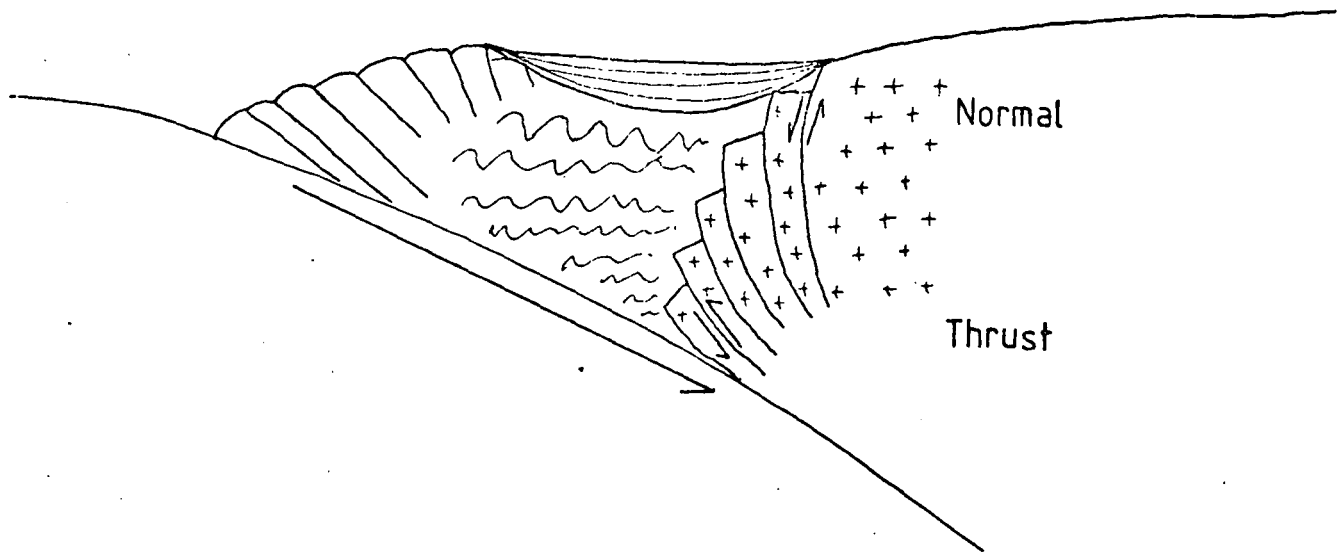
b)
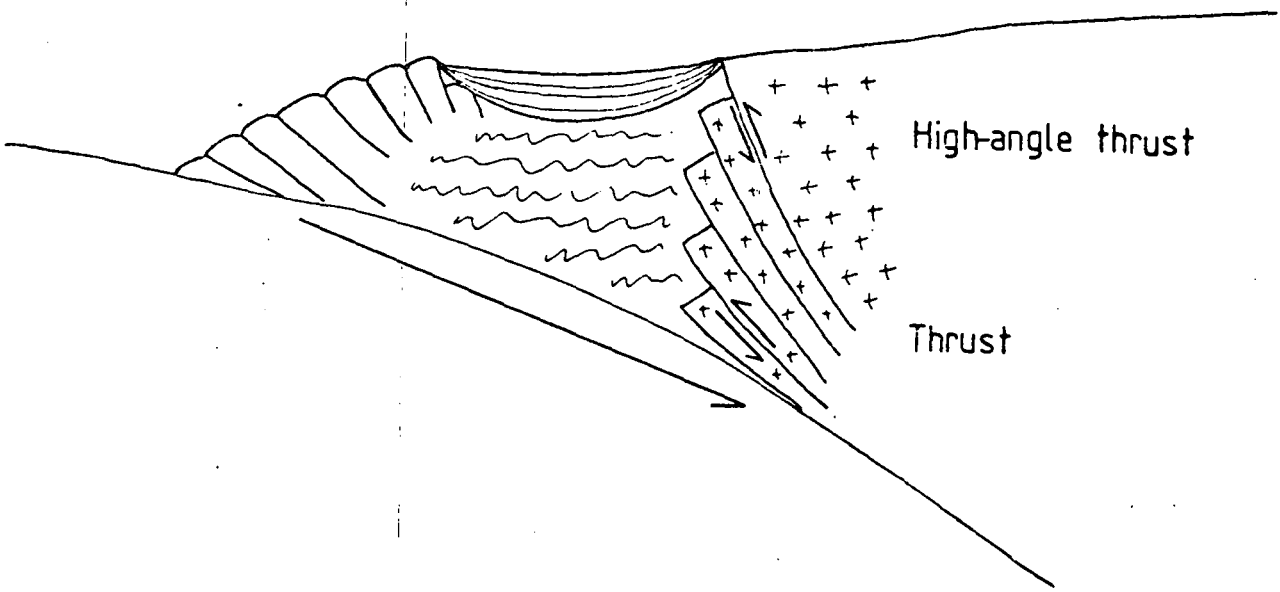
Fig. 1.7: A mechanism which leads to either
           a) normal faulting (after Hussong et al., 1976), or
           b) high-angle thrust faulting (after Curray et al., 1977),
           at the upper slope discontinuity.

the edge of the upper slope basin, which was confirmed by D.S.D.P. Leg 66 (Moore et al., 1979a), and a little beyond, but further than that the anomalies cannot be identified until the oceanic magnetic anomalies due to the sinking plate are seen.

Refraction profiles show oceanic-like crust beneath the upper slope basin in the Eastern Aleutian, Java and Lesser Antilles subduction zones (Shor and von Heune, 1972; Curray et al., 1977; Boynton et al., 1979), and a similar result is indicated in the Central Aleutians (Grow, 1973a). However there is a certain amount of ambiguity because the velocities in the supposed oceanic crust are reduced near the trench, and Karig (1977) suggests that the observed structure may be due to increasing the seismic velocity of accreted sediments by compaction and dewatering, rather than to underlying igneous crust. This ambiguity is illustrated in Fig. 1.8, showing two possible interpretations, made by Grow (1973a), of the geophysical data across the Central Aleutians. If the basement is indeed oceanic crust, then it is faulted and thickened by thrusting, and reaches a maximum thickness near the point of subduction, where it comes into contact with subducted oceanic basement.

An additional mechanism, which would help the development of upper slope basins is due to the sediments within them. Once the basin has been formed, the extra thickness and degree of compaction of the sediments in the deeper part of the basin will create a greater load there, so that the weight of sediments will cause a differential load on the upper slope, accentuating its original slope and increasing the rate of subsidence further, while keeping the axis of the basin nearly fixed.
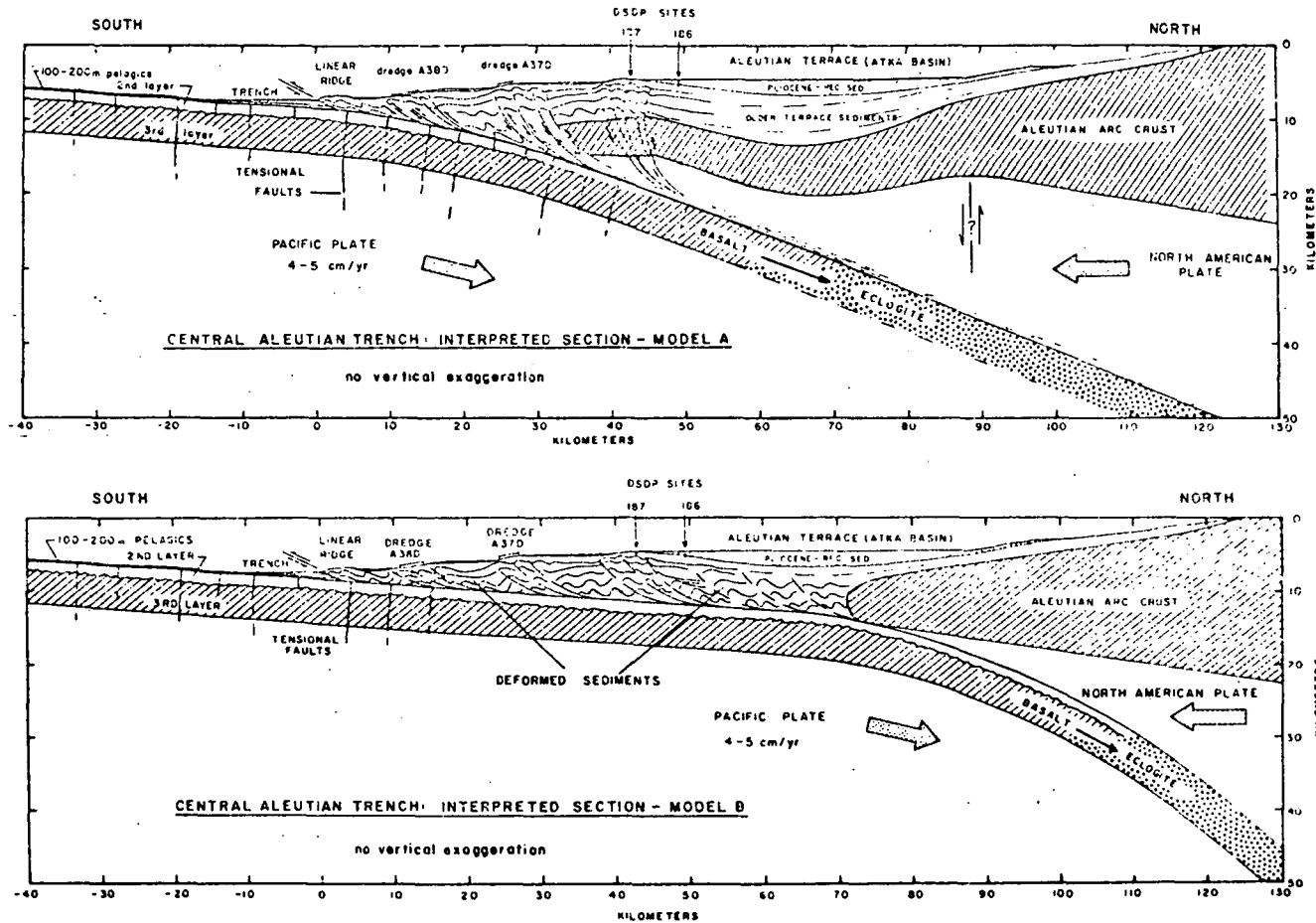
Fig. 1.8: Two cross-sections of the Central Aleutian Islands accretionary complex, both consistent with geophysical observations (Grow, 1973a).

1.5 Evolution of Subduction Zones

1.5.1 A frame of reference

In order to discuss the development of a subduction zone, and in particular the arc-trench gap, it is necessary to choose a fixed frame of reference. Ideally this frame of reference should be in the original continental (or oceanic) crust of the overriding plate and should remain relatively undisturbed during the whole period of subduction. This ideal, however, due to volcanic activity and other forms of tectonic deformation as well as the sediment covering, is impossible to attain or identify.

The upper slope discontinuity seems a likely candidate for the fixed point, especially since it initially represents the edge of the upper continental slope in many cases (e.g. Middle America trench). However, the nature and even the position of the upper slope discontinuity is still not at all clear, as described earlier (Section 1.4.2), and if tectonic erosion of the leading edge of the continental (or island arc) crust occurs (as shown in Fig. 1.7) then it will migrate away from the trench. In addition to this, there is evidence in the Eastern Aleutians and Japan (Karig and Sharman, 1975; Matsuda and Uyeda, 1971) to suggest that the upper slope may be sheared onto the overriding plate as a complete unit, so that the upper slope discontinuity jumps forward to a position near the old trench slope break, and a new accretionary complex is built onto the front of perhaps a series of older ones.

The volcanic arc, although not such a fundamentally important region to the structure of a subduction zone, is a lot easier to define and is subject to less movement over longer time periods than the upper slope discontinuity (Karig and Sharman, 1975). Although there is evidence that in some cases the volcanic arc can migrate either way, the rate at which

it does so is small compared with the size of the accretionary prism (Dickinson (1973) quotes a value of 2 km Myr^{-1}), and Karig et al. (1976) show that to a first approximation the horizontal distance from the volcanic arc to the bend, or position of maximum curvature, in the Benioff zone is constant for nearly all arcs, irrespective of the trench-arc gap.

The volcanic arc is therefore taken as the fixed point of reference when considering the development of the accretionary complex, but it should be remembered that the whole subduction zone may move relative to the mantle, due for example to back-arc spreading, or to the pull that may be exerted (forwards) by the sinking slab.

1.5.2 Development of an accretionary prism

The basic assumption made in describing the development of the accretionary prism is that the main differences in trench profiles, other than those due to the available volume of sediment, are due to the length of time each trench has been subducting continuously. Other effects will be discussed in the next section.

When subduction begins, the inner slope does not have a break (e.g. New Hebrides) and the oceanic plate bends sharply down beneath the island arc, which is very close (less than 100 km) to the trench. Sediments and perhaps oceanic crust are accreted to the toe of the inner slope, and the trench slope break is developed.

The trench slope break then moves forwards as further material is accreted, the rate depending on the rate of subduction and the supply of sediments, and a basin is developed behind it on the upper slope, containing a sediment thickness which varies from one arc to another (see Section 1.3). This development is represented (in Fig. 1.6) by the sequence E. Luzon, Shikoku, Aleutians, and also in some studies of ancient

subduction zones, for example the lower Paleozoic accretionary prism
to the South-East of the Southern Uplands fault (Leggett et al., 1979).

Estimates of the rate of sedimentation and the rate of accretion
in the Shikoku subduction zone (Moore, J.C. and Karig, 1976) are consistent
and an accretion rate of about 15 km^2 Myr^{-1} per length of arc is derived.
Using this and data from D.S.D.P. site 298 (Ingle et al., 1975) a strain
rate of 3 to 5×10^{-13} s^{-1} is estimated for the fold cored at the toe of
the inner slope, assuming a steady subduction rate of 12 to 20 mm yr^{-1}.
While the lower of these two estimates could be taken up by folding
alone, the higher would be likely to cause significant thrusting. It
is almost certain that both processes take place.

As the accretionary prism becomes wider the initial angle of the
oceanic plate becomes shallower, but the steep section of the Benioff
zone remains fixed. Karig et al. (1976) show this to be the elastic
response of the plate to the increasing sedimentary load. The increase
in dip of the subducted slab occurs where it comes into contact with the
basement of the overriding plate.

In accretionary prisms where the toe of the prism has migrated
more than about 50 km from the point of subduction, it is sometimes possible
to see two ridges, one at the top of the steepest part of the inner trench
slope, about 30 km from the trench and another, higher one over the point
of subduction. Examples are Hawley Ridge in the Central Aleutians (Grow,
1973a), the Mentawai and Nicobar Islands in the Sumatra arc (Karig, 1977)
and the Barbados ridge in the Caribbean (Westbrook, 1975). Westbrook
suggests that the trench slope break represents the height to which the
accreted sediments may be thrust against their weight, and that another
higher ridge is formed by further compression over the point of subduction,
corresponding to the Bouguer gravity minimum. Unless the accretionary

prism has developed to a width of 50 km from toe to upper slope basin, the second sedimentary ridge cannot be distinguished from the trench slope break, so this is a feature of well-developed subduction zones where there is a good supply of sediments to the trench.

1.5.3 Complicating factors

The comparatively simple model discussed so far only takes into account straightforward subduction, in that it only describes continuous convergence perpendicular to the trench. However, in many cases the convergence has not always been either of these things.

The rate of subduction may change, or subduction may stop completely and then start up again. When a further subduction pulse begins, the trench, upper slope discontinuity and volcanic arc may all move their positions either together or separately (e.g. Matsuda and Uyeda, 1971), and if a marginal basin has been formed behind the volcanic arc, then the "polarity" of subduction may reverse (Karig, 1974) and the back arc basin may be subducted beneath the island arc, along a seaward dipping Benioff zone.

The region is again complicated further if the direction of subduction is not perpendicular to the trench. The transverse component of subduction is taken up either by shearing in a back arc basin, where one exists, or on the upper slope (Karig, 1974) and the margin may be truncated by displacing parts of the accretionary prism at rates of 15 to 20 km Myr^{-1}. This may have happened in California and along the Middle America trench (Karig et al., 1978).

1.6 Summary

An outline has been given of the observations made on subduction zones and the mechanisms proposed to explain them. The aim of this thesis is to form numerical models, based on current observational data, to investigate the deformation of, and stresses within accretionary prisms, and to find the dependence of this behaviour on their lithology and on boundary conditions, particularly the basal shear stresses exerted by the subducted oceanic crust.

CHAPTER 2

PHYSICAL PROPERTIES OF ROCKS USED IN LITHOSPHERIC MODELS

2.1 Elastic Properties

The elastic properties of rocks may be found from one of three broad categories of measurement.

Firstly, values for seismic wave velocities may be found from experiments on the crust and mantle, from which it is possible to derive the elastic parameters necessary for modelling assuming some density distribution. These lithospheric measurements include both large scale (e.g. earthquake seismology) experiments which give average parameter values for the crust and upper mantle, and more detailed (e.g. seismic refraction) experiments in particular areas.

The second category is that of laboratory experiments. These include direct measurement of the elastic properties of samples of rock types thought to be similar to those in the region of interest, and of samples actually taken from that region, for example in Deep Sea Drilling Project cores.

The final category includes the values derived from analytical modelling of the lithosphere. The models are, for the most part, models of the flexure of the oceanic plate being subducted at a trench, based on bathymetric profiles across the trench and outer rise, and on the angle of dip of the Benioff zone beneath the island arc.

2.1.1 Experiments on the upper mantle

The broad velocity structure of the lithosphere may be found from earthquake seismology. Bott (1971a) shows the radial P wave velocity distribution for the whole earth found by Jeffreys (1939) and Gutenberg (1959) which are similar, except in the upper mantle where Gutenberg shows a low velocity zone at a depth of about 100 km. More recent studies (e.g. Toksöz et al., 1967; Julian and Anderson, 1968) have increased the resolution of the P velocity distribution in the upper mantle, and have confirmed the existence of a low velocity zone at depths of about 100 - 200 km.

All these studies give values for the P wave velocity, α_m, in the topmost mantle of

$$\alpha_m = 7.9 - 8.1 \text{ km s}^{-1}$$

and in the low velocity zone of

$$\alpha_m \simeq 7.8 \text{ km s}^{-1}.$$

An alternative method for finding α_m, in the mantle immediately below the Moho, is the measurement of Moho headwave velocities in seismic refraction experiments. Bott (1971a, p.114) summarises these results for several different tectonic regions, and shows that typical values are

$$\alpha_m = 8.0 - 8.2 \text{ km s}^{-1}.$$

However in an area of volcanic activity, such as an island arc, the velocity may be as low as

$$\alpha_m = 7.5 \text{ km s}^{-1},$$

as, in the case of Japan, shown by Yoshii and Asano (1972) and Yoshii (1979).

Shear wave velocities for the mantle cannot be found by seismic refraction, but in addition to travel time studies of earthquake body

waves, the dispersion of surface (Love or Rayleigh) waves may be used to find S wave velocities, β_m. These experiments give results of

$$\beta_m = 4.4 - 4.7 \text{ km s}^{-1}$$

for the uppermost mantle, and

$$\beta_m = 4.1 - 4.4 \text{ km s}^{-1}$$

for the low velocity zone (see, for example, Bott, 1971a; Yu and Mitchell, 1979).

The lower values for the uppermost mantle (~ 4.4 km s^{-1}) are associated with tectonically active areas, or young oceanic lithosphere. As the oceanic lithosphere becomes older (further from a spreading ridge), β_m increases from 4.4 km s^{-1} to 4.6 km s^{-1} (approximately) over about 50 or 100 M yr (Yu and Mitchell, 1979).

One further parameter is needed before the Young's modulus, E_m, and Poisson's ratio, ν_m, of the upper mantle can be calculated, namely the density, ρ_m. This may be found, either by assuming a mantle composition and extrapolating the density from that measured to that at the required depth, or by using the Nafe-Drake curve relating the density of a rock to its P wave velocity (Bott, 1971a, p.66). In either case the density of the upper mantle may be taken to be

$$\rho_m = 3300 \text{ kg m}^{-3}.$$

In order to obtain the elastic parameters from these values of α_m, β_m, ρ_m the following relations must be used:

$$\alpha = \left(\frac{\lambda + 2\mu}{\rho} \right)^{\frac{1}{2}} \qquad \qquad 2.1a$$

$$\beta = \left(\frac{\mu}{\rho} \right)^{\frac{1}{2}} \qquad \qquad 2.1b$$

(Malvern, 1969, p.550; Jaeger and Cook, 1976, p.351) where λ and μ are Lamé's elastic constants, from which E_m and ν_m may be derived, using

$$\nu_m = \frac{\lambda}{2(\lambda + \mu)} \qquad \text{2.2a}$$

$$E_m = \frac{\mu(3\lambda + 2\mu)}{(\lambda + \mu)} \qquad \text{2.2b}$$

(Malvern, 1969, p.280; Jaeger and Cook, 1976, p.351).

Hence, for a fairly active region, with

$$\alpha_m = 7.9 \text{ km s}^{-1} \quad \text{and} \quad \beta_m = 4.5 \text{ km s}^{-1}$$

Equations 2.1 and 2.2 give the following values of Poisson's ratio and Young's modulus for the upper mantle

$$\nu_m = 0.26$$

$$E_m = 170 \text{ GPa}.$$

2.1.2 Experiments on the crust

Earthquake seismology methods give the broad velocity structure for the crust, as for the mantle, again using surface wave dispersion for S waves and earthquake arrival times for both P and S. However, seismic refraction methods are more effective in the crust, particularly for localized structures. All these methods are discussed by Bott (1971a), and typically give values of

$$\alpha_{uc} = 6.0 - 6.2 \text{ km s}^{-1}$$

$$\alpha_{lc} = 6.5 - 7.0 \text{ km s}^{-1}$$

as the compressional velocities of the upper and lower crust respectively, and

$$\beta_c = 3.4 - 3.7 \text{ km s}^{-1}$$

as the average crustal shear velocity.

Velocities in sediments vary considerably according to the degree of compaction, giving compressional velocities of

$$\alpha_{sed} = 1.6 - 3.5 \text{ km s}^{-1}.$$

However, there have been many refraction profiles made across trenches (see Chapter 1, Section 1.1), and these all give similar distributions of α within the sediments comprising the accretionary prism, examples of which are shown in Fig. 2.1 (Hussong et al., 1976; Kieckhefer et al., 1980), so that compressional velocities may be assigned more accurately to sediments in the region of interest.

Although it is more difficult to find shear velocities in seismic refraction experiments, since the S arrivals are always later than P, it is sometimes possible to find the ratio (α/β) and hence, through Equations 2.1 and 2.2, Poisson's ratio

$$\nu = \frac{(\alpha/\beta)^2 - 2}{2((\alpha/\beta)^2 - 1)} \,. \qquad\qquad 2.3$$

Boynton et al. (1979) have used this fact, and apparent S and P wave velocities to estimate Poisson's ratios of

$$\nu = 0.260 \pm 0.008$$

and $\nu = 0.267 \pm 0.007$

for the igneous crust beneath the Lesser Antilles (average $\alpha = 6.2 \text{ km s}^{-1}$), and the same layer together with underlying sediments, respectively.

Nagumo et al. (1980) used an ocean bottom seismometer on the inner wall of the Japan trench to record local earthquakes. P to S and S to P conversions were detected at the boundary between the accreted sediments and the subducted oceanic crust, a very strongly reflecting boundary whose position was determined using reflection methods. The ratio (α/β) was
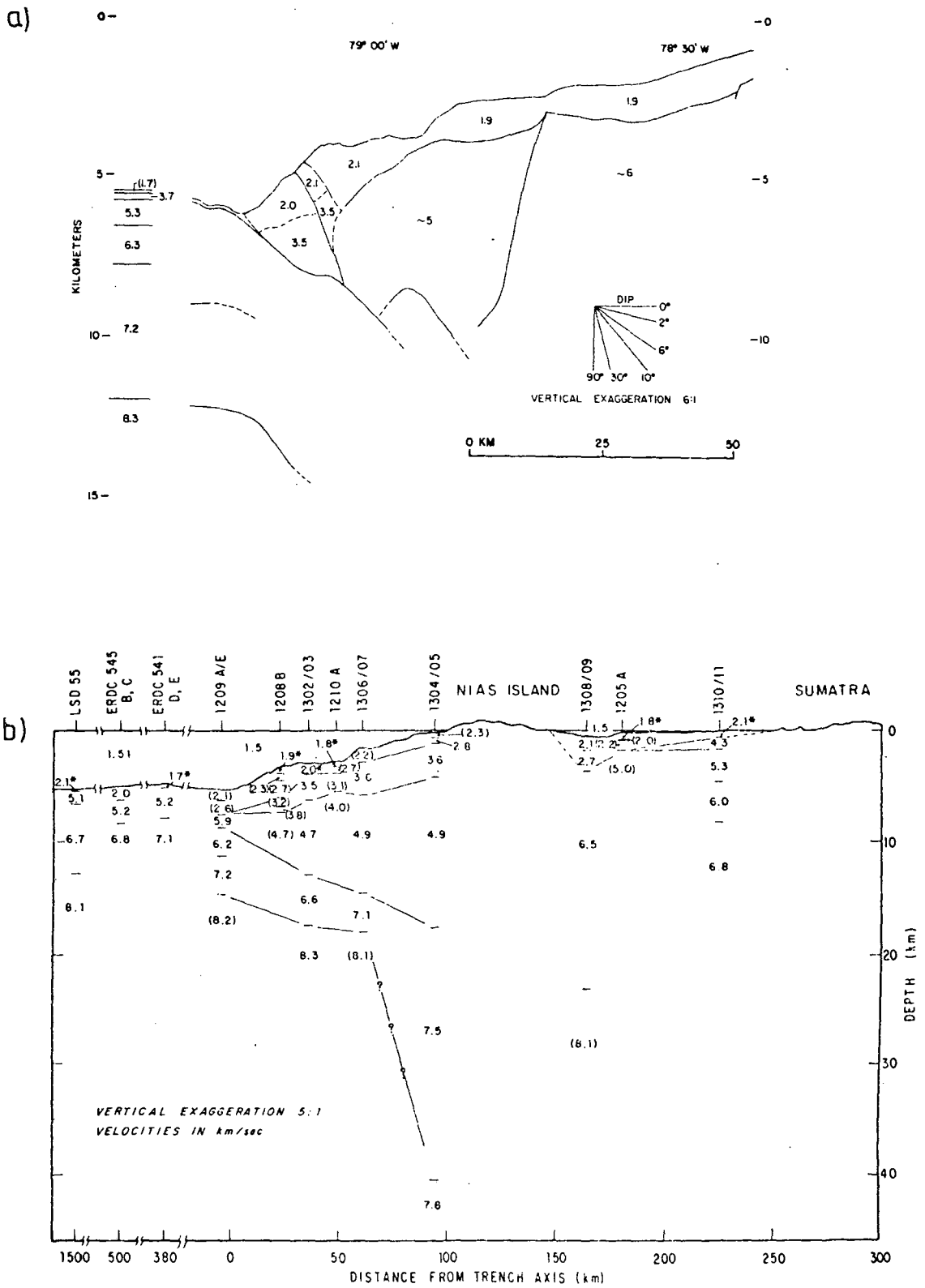
Fig. 2.1: Two distributions of P wave velocities within subduction zones
obtained from seismic refraction profiles,
a) from the Peru-Chile trench at Lat. c. 12°S (Hussong et al., 197
b) from the Sunda trench at Lat. c. 1°N (Kiecklefer et al., 1980)

calculated from the delay times between P and PS and between SP and S, and gave (using Equation 2.3)

$$\nu = 0.41.$$

This represents the average Poisson's ratio in the toe of the accretionary prism, which had an average velocity

$$\alpha = 2.3 \text{ km s}^{-1}$$

according to the reflection data.

The average density of the crust is in the range

$$\rho_C = 2800 - 2900 \text{ kg m}^{-3}$$

(Bott, 1971a) according to gravity measurements and extrapolation from the measured densities of basement outcrops.

Local density variations, especially for shallower rocks, may be estimated to about 100 kg m^{-3} from the Nafe-Drake curve of α against ρ (see Section 2.1.3, below). For example, in the case of the toe of the Japan trench inner wall (with $\alpha = 2.3$ km s^{-1}), the density is

$$\rho = 2100 \text{ kg m}^{-3}.$$

Hence, taking as average velocities

$$\alpha_C = 6.2 \text{ km s}^{-1} \quad \text{and} \quad \beta_C = 3.5 \text{ km s}^{-1}$$

and using Equations 2.1 and 2.2, the average elastic parameters for the crust are

$$\nu_C = 0.27$$

$$E_C = 87 - 90 \text{ GPa.}$$

Similarly, the average parameters for the toe of the accretionary prism, in the instance of the Japan trench cited earlier, are

$$\nu = 0.41$$

$$E = 4.9 \text{ GPa.}$$

2.1.3 <u>Direct measurement</u>

Birch (1966) and Gerrard (1977) give summaries of experiments to measure the elastic parameters of rocks directly. These experiments are mostly performed by applying stresses to the samples and measuring the strains, though in some harder rocks (e.g. basalt or dunite) the elastic parameters are calculated from longitudinal and transverse wave velocities in the sample. Some average values taken from these two papers are shown in Table 2.1.

Source	Rock-type	E/GPa	ν
Birch (1966)	Andesite	40	0.16
		54	0.18
Gerrard (1977)	Andesite	32	0.15
Birch	Phyllite	10-30	
Gerrard	Phyllite	70	0.26-0.5
	Clay	~ 1	0.27-0.45

Table 2.1: Elastic parameters for various rock-types.

Due to the effects of confining pressure, these figures will be more reliable for shallower, than for deeper, rocks and sediments. Note that the parameters found for the inner wall of the Japan trench, in Section 2.1.2, fall between those given for phyllites and clays, which might be expected as they represent average values for the low temperature metamorphic rocks of the accretionary prism and the overlying apron of mud.

A third compilation of experiments of this kind is represented

by the Nafe-Drake curve. Ludwig et al. (1970) show two curves, for
P and S wave velocities each as a function of density, and a third,
derived from the first two, of Poisson's ratio against density (see
Fig. 2.2). Although this set of data is most reliable for P velocities,
the parameters due to Boynton et al. (1979) and Nagumo et al. (1980)
cited in Section 2.1.2, and the average values for the crust are all
consistent with both the P and S velocity curves.

Analyses of various physical properties of cores from the Deep
Sea Drilling Project have been made, but the only one of these that
can be effectively used to determine elastic parameters for accretionary
wedges is density. For example, holes 186 and 187 of Leg 19, drilled
into the sedimentary complex on the inner wall of the Aleutian trench,
gave densities (Lee, 1973) of

$\rho = 1700 - 1900$ kg m^{-3},

increasing with depth. Taking the higher density (1900 kg m^{-3}), and
assuming that the empirical results represented by the Nafe-Drake curves
(Fig. 2.2) are representative of rocks under the conditions in the
accretionary prism, S and P wave velocities may be read from the graph,
from which the elastic parameters are calculated to be

$\nu = 0.46$

$E = 1.6$ GPa.

2.1.4 Parameters derived from analytical models

There have been several analyses of the flexure of the lithosphere
assuming it to be an elastic (or elastic-plastic) plate overlying a
viscous fluid (e.g. Walcott, 1970; Watts and Cochran, 1974; Karig et al.,
1976; Turcotte et al., 1978). In these calculations the important
parameter is the flexural rigidity,
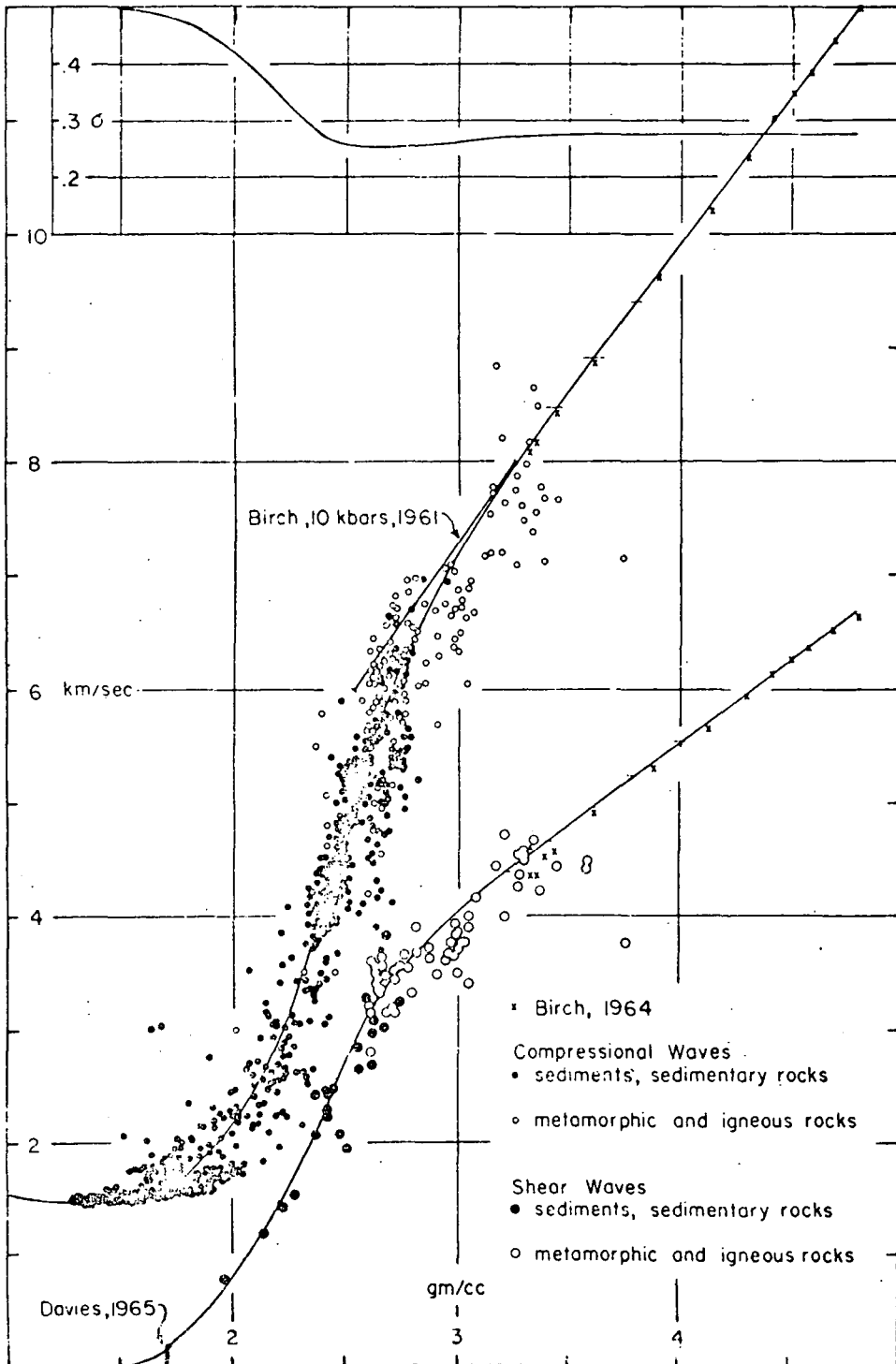
Fig. 2.2: A graph of experimental P (centre curve) and S wave velocities (lower curve) plotted against rock density, together with the Poisson's ratio (upper curve) derived from the first two (Ludwig et al., 1970).

$$D = \frac{E\,h^3}{12(1 - \nu^2)} \qquad\qquad 2.4$$

where h is the thickness of the elastic lithosphere. Walcott (1970) gives several values for D ranging from 5×10^{22} Nm for the Basin and Range Province, Western U.S.A., to 10^{25} Nm for parts of the Canadian shield.

Obviously D can only be used to find E or ν (using Equation 2.4) if one is already known together with the lithospheric thickness, but it is an independent check on the elastic properties found otherwise. For oceanic lithosphere Walcott gives

$D = 2 \times 10^{23}$ Nm

which together with a lithospheric thickness and Poisson's ratio

h = 30 km

$\nu = 0.27$

give a Young's modulus

E = 80 GPa,

consistent with Section 2.1.2.

2.1.5 Discussion

The chief difficulties in deriving elastic parameters for the lithosphere are that it is impossible to re-create conditions in the laboratory to accurately match those in the crust and mantle themselves, and that it is difficult to study the properties of rocks buried beneath several kilometres of other rocks.

Parameters obtained from seismic wave velocities may be subject to inaccuracy, because they represent the response to an oscillating stress system, with frequency up to about 30 Hz, which additionally has an amplitude negligible compared with the stresses in the lithosphere.

On the other hand, although comparable stresses may be applied to rock samples in the laboratory or in outcrops, it is hard to achieve the conditions of temperature and confining pressure necessary to simulate great depths.

A further inevitable problem in finding lithospheric properties is the time-scale involved, but this is discussed further in Section 2.2.

Despite all these difficulties, the results shown in Section 2.1 are consistent and give, at the least, guidelines as to the elastic properties that should be used in lithospheric models.

2.2 Effective Viscosities

2.2.1 Lithospheric viscosity

Many experiments have been performed to find creep equations, especially on olivine and ultrabasic rocks to simulate the upper mantle, and these are reviewed comprehensively by Weertman (1975) and Tullis (1979). The steady-state strain rate is found to obey a power law

$$\dot{\varepsilon} = A \exp(-Q/RT)(\sigma/\mu)^n \qquad\qquad 2.5$$

where μ is the shear modulus (equal to Lamé's constant in Ch. 3, Equation 3.14), n is a number between 1 and 10 (theoretically n = 3 for glide-controlled dislocation creep (Weertman and Weertman, 1975)), Q is the activation energy and A a constant both dependent on the material, R is the universal gas constant and T is the absolute temperature.

However there are considerable differences between the parameter values given by various authors (see, for example, Weertman and Weertman, 1975, table 2), and in addition there may be inaccuracies due to extrapolation. The reasons for this are that, not only is it difficult

to produce temperatures and pressures in the laboratory comparable
with those in the mantle, but it is impossible to conduct experiments
over lengths of time which are comparable with the ages of geological
structures. Therefore the steady-state creep observed in the laboratory
is assumed to persist over very much longer times, and the constants
in Equation 2.5 are assumed to apply to much smaller rates of strain
than can be measured accurately.

Although Equation 2.5 describes the behaviour of samples better
than the equations of a Maxwell substance (Ch. 3, Equation 3.36) with
a constant Newtonian viscosity, it is found that in models of lithospheric
flexure the difference between these two types of modelling is not
significant to first order (Bischke, 1974; Melosh and Raefsky, 1980),
and Cathles (1975) concludes that the viscosity of the upper mantle is
constant at 10^{21} N s m^{-2} throughout.

The most important consequence of non-linear creep is that the
effective viscosity ($n_{eff} = \sigma/\dot{\varepsilon}$) is lower for high stresses and higher
for low stresses, so that large deviatoric stresses relax faster than
in the linear equivalent to start with, but once they have relaxed to
a certain extent the deformation becomes slower. The time when the
strain rates for linear and non-linear creep become equal depends on
the constants in Equation 2.5 and on the value chosen for the effective
Newtonian viscosity.

In the light of these uncertainties, it was considered to be a
good approximation for the purposes of this thesis (where the emphasis
will be on crustal deformation) to consider only constant Newtonian
viscosities.

Models of lithospheric flexure often take the lithosphere to be
elastic (see references in Section 2.1.4, above), but this is not

considered to be realistic because of the extremely large resultant deviatoric stresses, approaching 1 GPa (Melosh, 1978). Various possibilities for lithospheric viscosity, n_ℓ, have been suggested in the range $10^{22} - 10^{26}$ N s m^{-2}. Some examples are:

$$n_\ell \geqslant 10^{25} \text{ N s m}^{-2}$$

(Melosh, 1978; Melosh and Raefsky, 1980),

$$n_\ell > 10^{24} \text{ N s m}^{-2}$$

for stable continental lithosphere (Artyushkov, 1973), and

$$n_\ell \simeq 10^{23} \text{ N s m}^{-2}$$

(Walcott, 1970; Bischke, 1974; de Bremaecker, 1977), which agrees with Artyushkov's value for tectonically active lithosphere.

On the basis of these figures, average values for lithospheric viscosities are taken to be

$$n_c = 10^{25} \text{ N s m}^{-2}$$

$$n_m = 10^{23} \text{ N s m}^{-2}$$

for the crust and uppermost mantle respectively.

2.2.2 Crustal viscosities

Very little work has been done on power-law creep for crustal materials. One example is given by Parrish et al. (1976) who give equations of the form of 2.5 for wet and dry quartzite, but again the results must be extrapolated from laboratory strain-rates, greater than 10^{-7} s^{-1}, to typical geological rates of 10^{-14}s^{-1}.

Bearing in mind the lack of such data for sediments and other crustal rocks, and other approximations inherent in the modelling, it would not be justifiable to use non-linear deformation in this study.

Parrish et al. consider that quartzite in the Earth's crust deforms with a viscosity of about

$$\eta_{qzt} = 4 \times 10^{20} \text{ N s m}^{-2},$$

based on their power law creep equation, and they quote Heard and Raleigh's result (1972) for the viscosity of marble under the same conditions (a temperature of 500 °C and a strain-rate of 10^{-14} s^{-1}) as

$$\eta_{marb} = 3 \times 10^{20} \text{ N s m}^{-2}.$$

Handin (1966) gives a table of effective viscosities for some limestones and evaporites. The majority of these lie between 10^{12} and 10^{17} N s m^{-2}, with a strong correlation between strain-rate and viscosity (the higher the strain-rate, the lower the viscosity). There are only two effective viscosities quoted for rates of strain less than 10^{-10}s^{-1}, which are

$$\eta_{gyp} > 2 \times 10^{18} \text{ N s m}^{-2}$$

for gypsum, and

$$\eta_{lst} > 2 \times 10^{21} \text{ N s m}^{-2}$$

for limestone, at strain-rates of 10^{-12} and 10^{-14} s^{-1} respectively.

Stein and Wickham (1980), in their finite element model of fault zones associated with folding, list values of viscosity for sandstones, limestones and shales varying between 10^{19} and 10^{21} N s m^{-2}. The average value they use, for homogeneous models, is

$$\eta = 3.2 \times 10^{20} \text{ N s m}^{-2}.$$

Finally, Cowan and Silling (1978), in choosing parameters on which to base scale models of an accretionary prism, took a value of

$$\eta_{sed} = 10^{14} \text{ N s m}^{-2}$$

for the viscosity of the whole sedimentary complex. However they do not explain their choice, which is at least 4 orders of magnitude lower than the values quoted above.

The viscosities for crustal material given in this section can be used to give guidelines to the values which could be used in a visco-

elastic model, but one of the aims of this thesis is to find the importance of the viscosity, and variations in it, in an accretionary prism, and closer bounds on its value (see Chapter 5).

2.3 Conditions for Failure of Rocks

Whether a rock will fracture along a given plane or not depends on the shear stress τ in that plane and on the stress σ normal to it.

Stress is a tensor quantity, and so σ and τ relating to a plane at an angle θ to the minimum principal stress σ_3 (the greatest compression), and perpendicular to the plane containing σ_1 and σ_3, are

$$\sigma = \sigma_1 \cos^2\theta + \sigma_3 \sin^2\theta \qquad\qquad 2.6a$$

$$\tau = -\sigma_1 \cos\theta \sin\theta + \sigma_3 \cos\theta \sin\theta \qquad\qquad 2.6b$$

(Price, 1966; Jaeger and Cook, 1976). Rearranging Equations 2.6

$$\sigma = \frac{(\sigma_1 + \sigma_3)}{2} - \frac{(\sigma_1 - \sigma_3)}{2} \cos2\theta$$

$$= \sigma_m - \tau_m \cos2\theta \qquad\qquad 2.7a$$

$$\tau = \frac{(\sigma_3 - \sigma_1)}{2} \sin2\theta$$

$$= -\tau_m \sin2\theta \qquad\qquad 2.7b$$

where σ_1 and σ_3 are the maximum and minimum principal stress (usually both being in the plane of a finite element model, with the intermediate principal stress, σ_2, perpendicular to the cross-section), and σ_m and τ_m are the mean stress and maximum shear stress respectively,

$$\sigma_m = \frac{(\sigma_1 + \sigma_3)}{2} \qquad\qquad 2.8a$$

$$\tau_m = \frac{(\sigma_1 - \sigma_3)}{2} . \qquad\qquad 2.8b$$

From Equations 2.7 it can be seen that τ and σ satisfy

$$f \equiv (\sigma - \sigma_m)^2 + \tau^2 - \tau_m^2 = 0 \qquad\qquad 2.9$$

which on a graph of τ against σ, represents a circle, centre $(\sigma_m, 0)$, radius τ_m. This circle is known as a Mohr circle and a graph of this kind (Fig. 2.3), usually drawn for positive τ only, is called a Mohr diagram.

The locus of all points (σ, τ) on a Mohr diagram where failure occurs in a particular material defines the fracture envelope for that material (e.g. Fig. 2.5). If the Mohr circle for a stress distribution lies entirely below the fracture envelope then no failure is predicted, while if it touches then the sample is expected to fracture at an angle θ to the minimum principal stress given by

$$\tan 2\theta = \frac{\tau}{(\sigma - \sigma_m)} \qquad\qquad 2.10$$

where (σ, τ) is the point at which the fracture envelope is tangent to the circle (see Fig. 2.4, where the σ-axis has been plotted conventionally with compression to the right).

To determine how near to failure an element in a finite element model is (Ch. 3), or by how much it has failed, it is necessary to determine a degree of failure for the stress system within it. Consider the stress system σ_1, σ_3 shown in Fig. 2.4 for which combination of σ_m and τ_m failure is not predicted. To cause failure, the stress system must be altered in one of two ways (or a combination of the two); either σ_m must be reduced to σ_m' keeping τ_m constant, or τ_m must be increased until the Mohr circle touches the fracture envelope. Thus the value of τ_m necessary for failure, and indeed the type of failure (Sections 2.3.1 to 2.3.3), depends on σ_m, while the size of τ_m determines whether the material will actually fail, for a given σ_m.
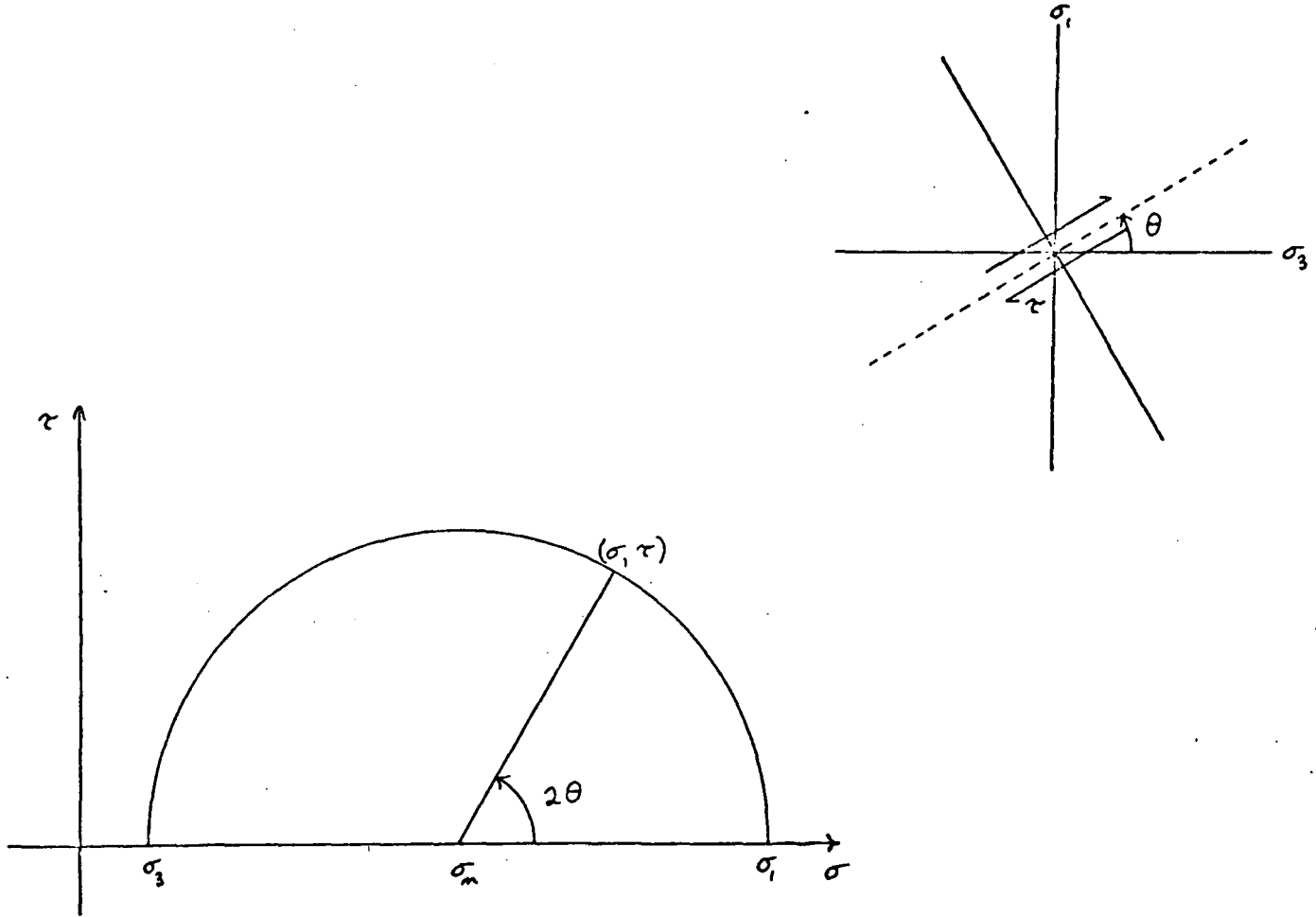
Fig. 2.3: A Mohr circle and its associated stress system (see text for explanation).
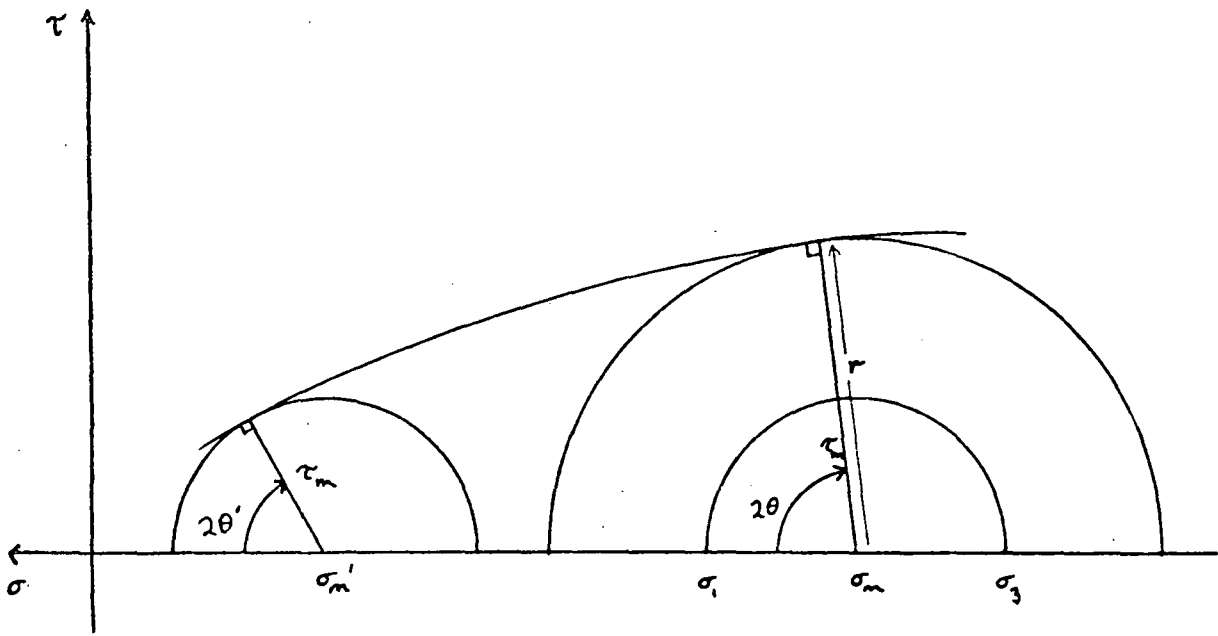
Fig. 2.4: The Mohr representation of a fracture envelope, with compression plotted to the right (cf. Fig. 2.3, where compression is to the left; see text for definition of symbols).

Let the value of τ_m needed be r, the shortest distance from $(\sigma_m,0)$ perpendicular to the envelope, then the degree of failure, C, is defined as

$$C = 1 - \frac{\tau_m}{r} . \qquad 2.11$$

This definition is a convenient dimensionless number, since it allows a direct comparison of degrees of failure between stress systems liable to different types of failure. C is positive if failure is not predicted, zero at failure, and becomes more negative the more the material is stressed beyond its fracture limit. In other words, if failure is predicted in several parts of a model, the region with the largest negative value of C is the most likely to fail.

2.3.1 Open-crack failure

To calculate the conditions for fracturing when open cracks are present, the (2-dimensional) simple Griffith theory is followed (as in Jaeger and Cook, 1976). The basic assumption of this theory is that failure occurs perpendicular to the surface of a crack when the tensile stress in that surface exceeds a value characteristic of the material, and that in this way cracks propagate, leading to failure of the whole rock.

By maximizing the crack surface tension, it is found that failure will occur at an angle θ to the greatest principal compression given by

$$\cos 2\theta = -\frac{\tau_m}{2\sigma_m} \qquad 2.12a$$

or $\quad \theta = 0.$ \hfill 2.12b

Condition 2.12a can only apply if $|2\sigma_m| > |\tau_m|$, so that the open crack region is divided into two types.

a) $|2\sigma_m| \leqslant |\tau_m|$

Under this condition, 2.12b applies, i.e. failure occurs along the direction of the minimum principal stress in response to the maximum principal stress, σ_1. The condition for failure is then

$$\sigma = \sigma_1 = T \qquad\qquad 2.13$$

where T is the uniaxial tensile strength of the rock.

The fracture envelope for this region is reduced to the point A at (T,0), (Fig. 2.5) and for any stress system with

$$T > \sigma_m \geqslant -T \qquad\qquad 2.14a$$

failure occurs at A. In this case

$$r = T - \sigma_m$$

$$\therefore \quad C = \left(\frac{T - \sigma_1}{T - \sigma_m}\right) \qquad\qquad 2.14b$$

is the degree of failure according to Equation 2.11.

A further possibility must be mentioned here, namely

$$\sigma_m \geqslant T. \qquad\qquad 2.15a$$

For these stress systems tensional failure, with $\theta = 0$, occurs for all values of τ_m, so in this case the degree of failure must be redefined and the expression

$$C = \left(\frac{T - \sigma_m}{T}\right) \qquad\qquad 2.15b$$

is used.

b) $|2\sigma_m| > |\tau_m|$

Again following Jaeger and Cook (1976), failure occurs at

$$\tau_m^2 = r^2 = -4T\sigma_m \qquad\qquad 2.16$$

This value of τ_m is substituted into the Mohr circle Equation 2.9 whence the fracture envelope is found by setting
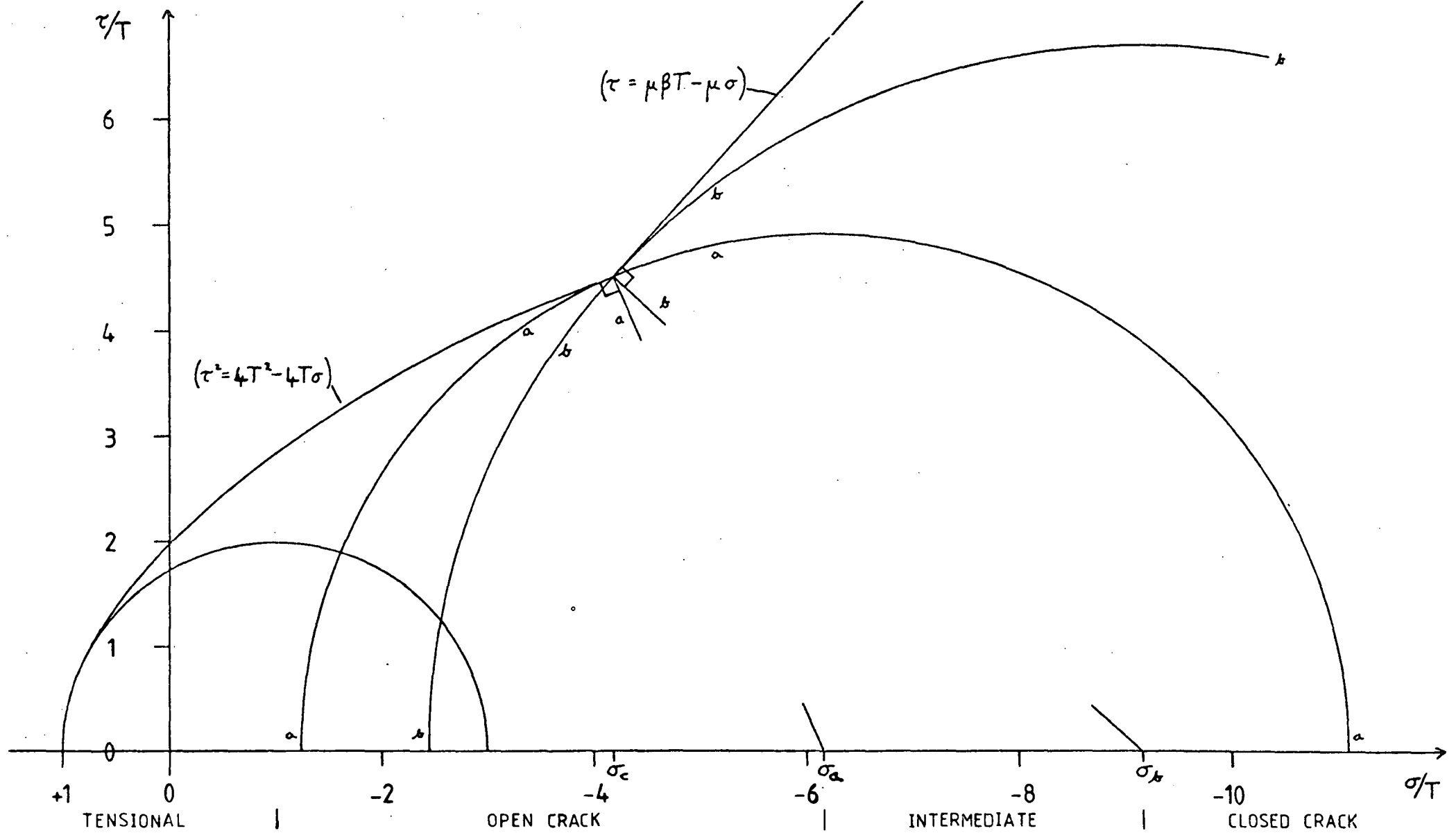
Fig. 2.5: The failure envelope used for determining the type and degree of failure in finite element models.

$$\frac{df}{d\sigma_m} = 0$$

and eliminating σ_m. The result is

$$\tau^2 = 4T^2 - 4T\sigma \qquad\qquad 2.17$$

a parabola which cuts the σ-axis at $(T,0)$ and the τ-axis at $(0,2T)$
(AB of Fig. 2.5).

However this analysis only holds while all the cracks are open.
Assuming that it holds until σ_m is more compressional than a stress σ_a
(see Fig. 2.5 and Section 2.3.3 below), then the characteristics of
open crack compressional failure are

$$-T > \sigma_m > \sigma_a \qquad\qquad 2.18a$$

and, using Equations 2.11 and 2.16,

$$C = 1 - \frac{\tau_m}{(-4T\sigma_m)^{\frac{1}{2}}} \qquad\qquad 2.18b$$

2.3.2 Closed-crack failure

If the normal compression across a crack is greater than a
certain value σ_c, then the crack will close and the simple Griffith
theory of section 2.3.1 will not hold. There is now a frictional shear
stress τ_f on the crack

$$\tau_f = \mu(\sigma_c - \sigma)$$

where μ is the coefficient of friction between the sides of the crack.

If this effect is included in a similar derivation to that used
to obtain the open-crack failure criteria (McClintock and Walsh, 1962;
Jaeger and Cook, 1976), the result is

$$\alpha\tau_m + \sigma_m = \beta T \qquad\qquad 2.19$$

at failure. α and β are dimensionless constants given by

$$\alpha = \frac{(\mu^2 + 1)^{\frac{1}{2}}}{\mu} \qquad\qquad 2.20a$$

$$\beta = \frac{2(1 - \sigma_c/T)^{\frac{1}{2}}}{\mu} + \frac{\sigma_c}{T} \qquad\qquad 2.20b$$

Again, a similar calculation to that in Section 2.3.1 gives the fracture envelope

$$\tau = \mu\beta T - \mu\sigma \qquad\qquad 2.21$$

representing the region BC in Fig. 2.5.

If $\quad |\sigma_c| \ll T$

$$\tau = 2T - \mu\sigma \qquad\qquad 2.22$$

which is the Mohr-Coulomb fracture envelope (Price, 1966; Jaeger and Cook, 1976) with a cohesive strength of 2T and the coefficient of internal friction replaced by μ, the sliding friction in the crack.

The size of σ_c has been quoted as: -2T (Brace, 1964), -3T (McClintock and Walsh, 1962), -4.19T (Murrell, 1965) and -10T (Digby and Murrell, 1976). Murrell's value of

$$\sigma_c = -4.19T$$

is used in all the finite element models, together with his friction coefficient

$$\mu = 1.09$$

unless stated otherwise. These give

$$\alpha = 1.36$$

$$\beta = -0.0198.$$

The derivation of Equation 2.19 requires that all the cracks should be closed. Let this be the case where σ_m is less (more compressive) than σ_b (Fig. 2.5 and Section 2.3.3 below).

This type of failure is thus described by

$$\sigma_m < \sigma_b \qquad \qquad 2.23a$$

and, from Equation 2.19

$$r = (\beta T - \sigma_m)/\alpha$$

$$\therefore \quad C = 1 - \frac{\alpha \, \tau_m}{(\beta T - \sigma_m)} \quad . \qquad \qquad 2.23b$$

The angle of fracture, θ, in the closed crack region is given by the normal from $(\sigma_m, 0)$ to the fracture envelope, that is by

$$\tan 2\theta = 1/\mu \qquad \qquad 2.24$$

and is independent of σ_m because the envelope is a straight line for σ_m in this region (cf. Equation 2.10 for open-crack failure and Equation 2.28 for the intermediate region).

2.3.3 The intermediate region

The modified Griffith theory of fracture (McClintock and Walsh, 1962) combines the open and closed crack theories described in the previous two sections. The transition from one part of the fracture envelope to the other occurs smoothly in reality, as the stress normal to the cracks approaches σ_c, but here the transition is approximated by a change from the parabolic to the straight line portions at a single point (σ_c, τ_c) (B in Fig. 2.5).

Two Mohr circles are defined in Fig. 2.5; one which is tangent to the parabola AB at B (circle a), and one which is tangent to the line BC at B (circle b). According to this approximation, failure occurs at B, namely $\sigma = \sigma_c$, $\tau = \tau_c$, for all values of σ_m between σ_a and σ_b (the centres of a and b respectively).

To find the value of σ_a, first substitute the value of τ_m at

open-crack failure (Equation 2.16) into the Mohr circle Equation 2.19, giving

$$f \equiv (\sigma - \sigma_m)^2 + \tau^2 + 4T\sigma_m = 0.$$

On the envelope

$$\frac{df}{d\sigma_m} = -2(\sigma - \sigma_m) + 4T = 0$$

so, setting $\sigma = \sigma_c$, $\sigma_m = \sigma_a$,

$$\sigma_a = \sigma_c - 2T \qquad\qquad 2.25$$

$$\therefore \; \sigma_a = -6.19T$$

using the value of σ_c from Section 2.3.2.

Similarly for σ_b, substituting Equation 2.19 into 2.9

$$f \equiv (\sigma - \sigma_m)^2 + \tau^2 - \left(\frac{\beta T - \sigma_m}{\alpha}\right)^2 = 0$$

$$\frac{df}{d\sigma_m} = -2(\sigma - \sigma_m) + \frac{2(\beta T - \sigma_m)}{\alpha^2} = 0$$

$$\therefore \; \sigma_b = (\mu^2 + 1)\,\sigma_c - \mu^2 \beta T \qquad\qquad 2.26$$

$$\therefore \; \sigma_b = -9.14T$$

using the definition of α (Equation 2.20a) and the values of μ, β and σ_c from Section 2.3.2.

The failure parameters for the intermediate region are thus

$$\sigma_a \geqslant \sigma_m \geqslant \sigma_b \qquad\qquad 2.27a$$

with

$$r^2 = (\sigma_c - \sigma_m)^2 + \tau_c^2$$

$$\therefore \; C = 1 - \frac{\tau_m}{((\sigma_c - \sigma_m)^2 + \tau_c^2)^{\frac{1}{2}}} \qquad\qquad 2.27b$$

τ_c, the shear stress corresponding to a normal stress σ_c, at failure,

is given by either Equation 2.17 or 2.21 as

$$\tau_c = 4.55T.$$

The angle of failure, θ, in the intermediate region is given by the line from $(\sigma_m, 0)$ to (σ_c, τ_c), that is by

$$\tan 2\theta = \frac{\tau_c}{(\sigma_c - \sigma_m)} \qquad\qquad 2.28$$

2.3.4 Tensile strength

In Sections 2.3.2 and 2.3.3 the failure criteria have all been calculated in terms of the uniaxial tensile strength, T, and it provides the scale for the graph of τ against σ (Fig. 2.5).

The value used here for T in large-scale finite element models is

T = 50 MPa

which is the average value for igneous rocks given by Service and Douglas (1973, based on work by Brace, 1961), and is a good average value for the whole crust.

However the tensile strength in the upper crust is somewhat lower. Goldsmith et al. (1976) give various tensile strengths for Barre granite, the average of which is

T = 12.6 MPa

while values common for metamorphic and sedimentary rocks (in the upper crust) are even lower. Some of these are shown in Table 2.2 below.

Note that the strengths quoted from Handin (1966) were derived from measurements of the cohesive strengths for the samples (Equation 2.22 shows that the cohesive strength, defined for a Mohr-Coulomb failure criterion, is equal to 2T), and are averages of the data presented there.

Reference	Material	T/MPa
Handin (1966)	Sandstone (dry)	18
	Limestones	10
	Shales	8.0
	Sandstone (wet)	7.3
Jaeger and Cook (1976)	Marble	6.9
Brace (1964)	Marble	5.4
Handin (1966)	Greywackes	5.3
Jaeger and Cook (1976)	Sandstone	3.6
Handin (1966)	Schists	2.9
	Phyllites	1.0

Table 2.2: Tensile strengths of various upper crustal rocks

2.3.5 Applicability of failure criteria

The modified Griffith theory of failure describes the conditions for brittle failure of rocks only. For this reason the theory is applicable to rocks in the upper crust, but becomes an increasingly poor approximation with depth, as rocks become more ductile. This ductility is taken into account by the viscous part of the rheology used in the models (see Chapter 3, Section 3.4), but failure may still occur at these depths and as a first approximation the same form of failure criterion is used throughout.

No problem arises in the mantle where brittle failure would be inapplicable, because the mean stress σ_m is always too large for failure to occur under realistic stress distributions.

CHAPTER 3

THE FINITE ELEMENT METHOD

3.1 Introduction

Analytical solutions to geodynamic problems may only be found by making many simplifying assumptions about the section of the lithosphere under investigation, particularly with respect to boundary conditions between regions with different properties. Therefore solutions are often found numerically and one of the most versatile methods of this type is finite element analysis, a numerical technique for finding the stress distribution in an elastic continuum, which can also be extended to visco-elastic media (see Section 3.4).

The first step in the method, is to divide the body (for the purposes of this thesis, a cross-section taken through the lithosphere) into elements, the boundaries of which intersect to form nodes.

Assumptions are made about the behaviour of the materials comprising the body, which allow an equation to be derived relating the stresses within the elements to the displacements of the nodes (Equation 3.22), which, together with equilibrium conditions, leads to the stiffness equation (3.30)

$$K \tilde{\delta} = \tilde{F}.$$

A solution of this equation, by matrix inversion, gives the displacements $\tilde{\delta}$ of the nodes for a given set of loads $\tilde{F}$ ($\tilde{\delta}$ and $\tilde{F}$ both being column vectors), applied to a body with stiffness matrix K.

In this way, the displacements and hence, through the stress equation (3.22), the stresses in the body may be found for any set of external boundary conditions.

3.2 The Relationship between Stresses and Displacements

3.2.1 The shape function

The element shape function $N(x,y)$ is a matrix which relates the displacements u_x, u_y at a point (x,y) within an element to the displacements δ_{i_x} δ_{i_y} of each node i on the element's boundary, through the equation

$$\tilde{u} = N \tilde{\delta} \qquad\qquad 3.1$$

In general $\tilde{u}$ is a column vector of dimension ℓ, the number of degrees of freedom of each node, and $\tilde{\delta}$ has dimension ℓm, where m is the number of nodes on the element, so that N is $[\ell \times \ell m]$.

However, this study is restricted to 2 dimensions (x,y) and each element is a simple 3-noded triangle with one node at each corner so

$$\ell = 2$$

$$m = 3$$

and N is a $[2 \times 6]$ matrix.

Reducing the number of degrees of freedom of the element to 6 means that the shape function is linear, and following Zienkiewicz (1971), the displacement function within the element may be shown to be

$$\tilde{u} = \sum_i [n_i \ I] \ \tilde{\delta}_i \qquad\qquad 3.2$$

where $\tilde{\delta}_i$ is the displacement vector for node i, I is the $[2 \times 2]$ identity matrix, the sum is over the three nodes numbered i, j, m and

$$n_i = \frac{1}{2\Delta} (n_i + b_i x + c_i y) \qquad\qquad 3.3$$

where Δ is the area of the element,

$$2\Delta \quad = \quad \begin{vmatrix} 1 & x_i & y_i \\ 1 & x_j & y_j \\ 1 & x_m & y_m \end{vmatrix} \quad , \qquad\qquad 3.4$$

$$a_i = x_j y_m - x_m y_j \qquad\qquad 3.5a$$

$$b_i = y_j - y_m \qquad\qquad 3.5b$$

$$c_i = x_m - x_j \qquad\qquad 3.5c$$

and a_j, a_m etc. are found by cyclic permutation of i, j, m.

The displacement column vector for the element is defined as a list of the displacement vectors for each node

$$\tilde{\delta} = \begin{pmatrix} \tilde{\delta}_i \\ \tilde{\delta}_j \\ \tilde{\delta}_m \end{pmatrix} \qquad\qquad 3.6$$

so that from Equations 3.1 and 3.2, the element shape function,

$$N = [n_i I, \; n_j I, \; n_m I] \quad . \qquad\qquad 3.7$$

3.2.2 The strain matrix

It is convenient, when dealing with 2-dimensional models, not to use all 9 components of the strain tensor, defined generally by

$$\varepsilon_{pq} = \frac{1}{2}\left(\frac{\partial u_p}{\partial x_q} + \frac{\partial u_q}{\partial x_p} \right) \qquad\qquad 3.8$$

where p,q run over 1, 2, 3 corresponding to the x, y, z directions (see, for example, Jaeger and Cook, 1976; Malvern, 1969).

Instead a 3-component column vector is defined,

$$\tilde{\varepsilon} = \begin{pmatrix} \varepsilon_x \\ \varepsilon_y \\ \gamma_{xy} \end{pmatrix} \equiv \begin{pmatrix} \varepsilon_{xx} \\ \varepsilon_{yy} \\ 2\varepsilon_{xy} \end{pmatrix}. \qquad 3.9$$

$\tilde{\varepsilon}$ is a function of position and, within a particular element, the strain matrix, B, is defined such that

$$\tilde{\varepsilon} = B\,\tilde{\delta}. \qquad 3.10$$

From Equations 3.2, 3.8 and 3.9 it can be seen that

$$B = [B_i,\ B_j,\ B_m] \qquad 3.11$$

where

$$B_i = \begin{pmatrix} \dfrac{\partial n_i}{\partial x} & 0 \\ 0 & \dfrac{\partial n_i}{\partial y} \\ \dfrac{\partial n_i}{\partial y} & \dfrac{\partial n_i}{\partial x} \end{pmatrix}. \qquad 3.12$$

Using Equations 3.3 and 3.5, Equation 3.12 gives B explicitly as

$$B = \frac{1}{2\Delta} \begin{pmatrix} b_i & 0 & b_j & 0 & b_m & 0 \\ 0 & c_i & 0 & c_j & 0 & c_m \\ c_i & b_i & c_j & b_j & c_m & b_m \end{pmatrix} \qquad 3.13$$

and so, for a given set of nodal displacements $\tilde{\delta}$, the strain $\tilde{\varepsilon}$ (and the stress through Equation 3.19) is constant over each element.

3.2.3 The elasticity matrix

When treating the stresses in a model, it is similarly convenient to reduce the stress tensor, given generally for an isotropic elastic material by

$$\sigma_{pq} = \lambda\,\theta\,\delta_{pq}^{K} + 2\,\mu\,\varepsilon_{pq} \qquad 3.14$$

(see e.g. Malvern, 1969; Jaeger and Cook, 1976) where λ, μ are Lamé's elastic constants (μ is equal to the shear modulus), δ_{pq}^{K} is the Kroenecker delta function defined by

$$\delta_{pq}^{K} = 1 \quad \text{if } p = q$$

$$\delta_{pq}^{K} = 0 \quad \text{otherwise,}$$

and where

$$\theta = \sum_{r=1}^{3} \varepsilon_{rr},$$

to the column vector

$$\tilde{\sigma} = \begin{pmatrix} \sigma_x \\ \sigma_y \\ \tau_{xy} \end{pmatrix} \equiv \begin{pmatrix} \sigma_{xx} \\ \sigma_{yy} \\ \sigma_{xy} \end{pmatrix} . \tag{3.15}$$

To find the relationship between $\tilde{\sigma}$ and $\tilde{\varepsilon}$, rewrite Equations 3.14 in terms of the Poisson's ratio ν and Young's modulus E of the material, using the relations (see Malvern, 1969; Jaeger and Cook, 1976)

$$\nu = \frac{\lambda}{2(\lambda + \mu)} \quad \text{and} \quad E = \frac{\mu(3\lambda + 2\mu)}{(\lambda + \mu)} , \tag{3.16}$$

and including any initial strains (ε_{x0}, ε_{y0}, ε_{z0}, γ_{xy0}) in the model prior to the application of any loads which give (see Zienkiewicz, 1971)

$$\varepsilon_x = \frac{\sigma_x}{E} - \frac{\nu}{E}\sigma_y - \frac{\nu}{E}\sigma_z + \varepsilon_{x0} \tag{3.17a}$$

$$\varepsilon_y = -\frac{\nu}{E}\sigma_x + \frac{\sigma_y}{E} - \frac{\nu}{E}\sigma_z + \varepsilon_{y0} \tag{3.17b}$$

$$\gamma_{xy} = \frac{2(1 + \nu)}{E}\tau_{xy} + \gamma_{xy0} . \tag{3.17c}$$

The lithospheric structures to be studied are very much larger parallel to, than perpendicular to strike (in particular subduction zones continue for distances along strike very much larger than the arc-trench gap), so that it is valid to restrict the displacements of the model to

the plane of cross-section (x,y). To impose these conditions of plane strain, the total strain in the z-direction must be set to zero

$$0 = \varepsilon_z = -\frac{\nu}{E}\sigma_x - \frac{\nu}{E}\sigma_y + \frac{\sigma_z}{E} + \varepsilon_{z0}$$

or $\qquad \sigma_z = \nu(\sigma_x + \sigma_y) - E\,\varepsilon_{z0}$. $\hfill$ 3.18

Substituting this expression for σ_z, and inverting Equations 3.17,

$$\tilde{\sigma} = D(\tilde{\varepsilon} - \tilde{\varepsilon}_0) \hfill 3.19$$

which defines the elasticity matrix, D, given in the case of plane strain by

$$D = \frac{E(1 - \nu)}{(1 + \nu)(1 - 2\nu)} \begin{pmatrix} 1 & \nu/(1-\nu) & 0 \\ \nu/(1-\nu) & 1 & 0 \\ 0 & 0 & \frac{(1-2\nu)}{2(1-\nu)} \end{pmatrix} . \hfill 3.20$$

The initial strain vector in Equation 3.19 is defined differently from the total strain vector (Equation 3.9), because of the restriction to plane strain. The calculations that give Equations 3.19 and 3.20 also yield

$$\tilde{\varepsilon}_0 = \begin{pmatrix} \varepsilon_{x0} + \nu\,\varepsilon_{z0} \\ \varepsilon_{y0} + \nu\,\varepsilon_{z0} \\ \gamma_{xy0} \end{pmatrix} . \hfill 3.21$$

If there are initial stresses $\tilde{\sigma}_0$ (defined in the same way as in Equation 3.15) in the body, then Equation 3.19 becomes the stress equation

$$\tilde{\sigma} = D(\tilde{\varepsilon} - \tilde{\varepsilon}_0) + \tilde{\sigma}_0. \hfill 3.22$$

Note that the stress required to restrict the model to plane strain is σ_z, given separately by Equation 3.18, and this will always be the principal stress parallel to strike.

3.3 The Stiffness Equation

To derive the stiffness equation for the body, relating the nodal displacements to the applied forces, it is necessary to consider the energy of the system comprising the body and all external forces, at equilibrium.

The internal forces on the body are those due to its elastic properties, work done against which increases the body's total strain energy.

Three types of external force are considered: firstly distributed loads $\tilde{p}$ per unit volume, in particular those due to gravity; secondly, loads $\tilde{q}$ per unit area applied to the surface of the body, for example forces due to lithostatic pressure at its ends; and thirdly, any other forces $\tilde{R}$ which may be applied to the nodes directly.

All forces may, in general, be functions of position within the model.

If the system is at equilibrium, and an arbitrary, small displacement $(\Delta\tilde{\delta})$ is imposed on the nodes of the model, then the change in energy of the whole system must be zero, since the equilibrium position must necessarily be an energy minimum. That is to say

$$\Delta U - \Delta W = 0 \qquad\qquad 3.23$$

where ΔU is the increase in strain energy of the body and ΔW is the work done on it by the external forces.

The increase in strain energy of the model is

$$\Delta U = \int_V (\Delta\tilde{\varepsilon})^T \tilde{\sigma} \ d^3V \qquad\qquad 3.24$$

where the integral is over the whole volume V of the body, and a superscript ^{T} denotes a matrix (or column vector) transpose.

The work done by the external forces is

$$\Delta W = (\Delta\tilde{\delta})^T \tilde{R} + \int_V (\Delta\tilde{u})^T \tilde{p} \, d^3V + \int_S (\Delta\tilde{u})^T \tilde{q} \, d^2S \qquad 3.25$$

where S is the surface of the model.

From Equations 3.1 and 3.10

$$\tilde{u} = N \tilde{\delta} \qquad\qquad \text{and} \qquad\qquad \tilde{\varepsilon} = B \tilde{\delta}$$

$$\therefore \quad (\Delta\tilde{u})^T = (\Delta\tilde{\delta})^T N^T \qquad \text{and} \qquad (\Delta\tilde{\varepsilon})^T = (\Delta\tilde{\delta})^T B^T, \qquad 3.26a,b$$

and rewriting the stress equation, 3.22

$$\tilde{\sigma} = D B \tilde{\delta} - D \tilde{\varepsilon}_0 + \tilde{\sigma}_0 \quad , \qquad\qquad 3.27$$

so Equations 3.23, 3.24 and 3.25 may be expanded to give

$$0 = \int_V (\Delta\tilde{\delta})^T B^T D B \tilde{\delta} \, d^3V - \int_V (\Delta\tilde{\delta})^T B^T D \tilde{\varepsilon}_0 \, d^3V + \int_V (\Delta\tilde{\delta})^T B^T \tilde{\sigma}_0 \, d^3V$$

$$- (\Delta\tilde{\delta})^T R - \int_V (\Delta\tilde{\delta})^T N^T \tilde{p} \, d^3V - \int_S (\Delta\tilde{\delta})^T N^T \tilde{q} \, d^2S. \qquad 3.28$$

In this equation, the matrices N, B, D and the column vectors $\tilde{\delta}$ and $(\Delta\tilde{\delta})$ have been extended to cover the whole model. If there are M nodes then $\tilde{\delta}$, $(\Delta\tilde{\delta})$ and $\tilde{R}$ are [2M x 1], B is [3 x 2M] and N is [2 x 2M]. D is still [3 x 3], and $\tilde{\varepsilon}_0$ and $\tilde{\sigma}_0$ are still [3 x 1], but all three are discontinuous functions of position (x,y) (as are B and N), having the values pertaining to the element containing the point (x,y) (see Zienkiewicz, 1971).

Since it is an arbitrary displacement, Equation 3,28 holds for all values of $(\Delta\tilde{\delta})$, and so $(\Delta\tilde{\delta})^T$ may be cancelled out.

Rearranging Equation 3.28 accordingly

$$\left(\int_V B^T D B \, d^3V \right) \tilde{\delta} = \tilde{R} + \int_V N^T \tilde{p} \, d^3V + \int_S N^T \tilde{q} \, d^2S + \int_V B^T D \tilde{\varepsilon}_0 \, d^3V$$

$$- \int_V B^T \tilde{\sigma}_0 \, d^3V \quad . \qquad\qquad 3.29$$

All these quantities have the dimensions of force, and 3.29 may thus be rewritten as the stiffness equation

$$K \tilde{\delta} = \tilde{F}.$$ 3.30

where, by definition, the stiffness matrix,

$$K = \left(\int_V B^T D B \, d^3V \right)$$ 3.31

and the total force vector,

$$\tilde{F} = \tilde{R} + \tilde{F}_p + \tilde{F}_q + \tilde{F}_{\varepsilon_0} + \tilde{F}_{\sigma_0}$$ 3.32

with

$$\tilde{F}_p = \int_V N^T \tilde{p} \, d^3V \qquad , \qquad \tilde{F}_q = \int_S N^T \tilde{q} \, d^2S,$$ 3.33a, b

$$\tilde{F}_{\varepsilon_0} = \int_V B^T D \tilde{\varepsilon}_0 \, d^3V \quad , \qquad \tilde{F}_{\sigma_0} = - \int_V B^T \tilde{\sigma}_0 \, d^3V,$$ 3.33c,d

the force vectors due to the volume loads, surface loads, initial strains and initial stresses, respectively.

Note that different approaches to the derivation of Equation 3.30 can lead to differences in sign used in the defining equations, 3.33 (cf. Zienkiewicz, 1971; Dean, 1973; Kusznir, 1976; Woodward, 1976; Hinton and Owen, 1977).

When plane strain, 3-noded triangular elements are used, the integrals in Equations 3.31 and 3.33 need not often be solved explicitly. For instance, Equation 3.31 applied to a single element e becomes

$$K^e = z \Delta B^T D B$$ 3.34

since B and D are constant over e, where z is the thickness of the model perpendicular to the x,y plane (usually set to unity and neglected, since it appears as a factor in all the Equations 3.33 and 3.31, and therefore is cancelled out in Equation 3.30), and Δ is the area of the triangle as defined in Section 3.2.1.

The global stiffness matrix, K, of Equation 3.31, is then formed by summing the terms from all the element stiffness matrices, K^e, according to the nodes which they relate (Zienkiewicz, 1971).

3.4 Visco-elastic analysis

The rheological model used for the lithosphere is that of a Maxwell substance (Jaeger and Cook, 1976), which deforms elastically according to its Young's modulus E and Poisson's ratio ν, as described by Equations 3.17, and then relaxes at a rate depending on its (dynamic) viscosity η until there are no remaining deviatoric stresses. The deviatoric stresses approach zero exponentially with a time constant t_m, called the Maxwell time, where

$$t_m = 2\eta/E .$$

3.35

The strain rate for a Maxwell substance is

$$\dot{\varepsilon}_{pq} = \frac{(1 + \nu)}{E} \dot{\sigma}'_{pq} + \frac{1}{2\eta} \sigma'_{pq}$$

3.36

(Housner and Vreeland, 1966; Malvern, 1969; Zienkiewicz et al., 1968), where σ'_{pq} is the deviatoric stress tensor

$$\sigma'_{pq} = \sigma_{pq} - \delta^K_{pq} \sigma_h$$

3.37a

with $\sigma_h = \frac{1}{3} \sum_r \sigma_{rr}$,

3.37b

the hydrostatic stress.

The last term in Equation 3.36 is the viscous creep rate, which may be expressed in column vector form (see Equations 3.9 and 3.15) as

$$\dot{\varepsilon}_c = \frac{1}{2\eta} \begin{pmatrix} \sigma'_x \\ \sigma'_y \\ 2\tau_{xy} \end{pmatrix}$$

3.38a

with $\dot{\varepsilon}_{zc} = \frac{1}{2\eta} \sigma'_z .$

3.38b

$\dot{\varepsilon}_{zc}$ is not necessarily zero, despite the restriction to plane strain, as long as the total strain in the z-direction is zero, i.e. using Equation 3.36, if

$$\frac{\sigma'_z}{2\eta} = -\frac{(1 + \nu)}{E} \dot{\sigma}'_z \quad . \tag{3.39}$$

These creep rates are integrated up to a given time T, and incorporated as an initial strain vector (Equation 3.21),

$$\tilde{\varepsilon}_{0c} = \begin{pmatrix} \varepsilon_{xc} & + & \nu\ \varepsilon_{zc} \\ \varepsilon_{yc} & + & \nu\ \varepsilon_{zc} \\ & \gamma_{xyc} & \end{pmatrix} \tag{3.40}$$

into the stiffness Equation 3.30, through a term $\tilde{F}_{\varepsilon_{0c}}$, defined as in Equation 3.33c.

Solving the stiffness equation then gives $\tilde{\delta}(T)$, the total displacement at time T, including both elastic and creep components.

The integration of Equations 3.38 to Equations 3.40 is performed by dividing the total time T into time increments, length t, and iterating to find the creep for each increment, as follows:

a) At the beginning t_1 of each time increment, the stiffness equation is solved to find the displacement, and hence the stress $\sigma(t_1)$. This stress is used to calculate a creep rate, using Equations 3.38.

b) Assuming the creep rate is constant throughout the increment, it is integrated to find the creep for the increment, i.e.

$$\tilde{\varepsilon}_c(t_1 + t) - \tilde{\varepsilon}_c(t_1) = \dot{\tilde{\varepsilon}}_c(t_1 + t/2) \times t \tag{3.41}$$

and this is added into the initial strain vector, according to Equation 3.40.

c) The stiffness equation is solved again, to find the stress at the end of the increment, $\sigma(t_1 + t)$.

d) Using the average value of deviatoric stress for the time increment

$$\sigma'_{av} = \frac{1}{2} (\sigma'(t_1 + t) + \sigma'(t_1)),$$ 3.42

the creep rate for the increment, $\dot{\varepsilon}_c(t_1 + t/2)$, is re-evaluated and steps (b) to (d) are repeated, until the values for $\sigma(t_1 + t)$ on successive iterations converge to within a specified tolerance.

e) The whole process is repeated from $t_1 = 0$ until $t_1 = T - t$, to give the displacements and stress system at time T, as required.

The iterations for a particular time increment will only converge if the creep is not too large compared to the elastic displacement. Thus the incremental time must be of the same order of magnitude as the Maxwell time, t_m, or smaller. So, using Equation 3.35,

$$t \lesssim \frac{2\eta}{E}$$ 3.43

for every element of the model.

The number of iterations necessary depends on t and on the complexity of the model, but for any model, as the elastic stresses are relaxed, fewer iterations are needed, so that if a model is to be run for a long time on the computer, the processing time for each increment becomes less, making it feasible to study models over reasonably long geological times.

3.5 Boundary Conditions and Loads

The internal boundary conditions between regions with different physical properties in a finite element model are the same as those between any two adjacent elements, which depend on the shape function for the type of element used. The linear shape function chosen means that the displacements $\bar{u}$ in the elements are continuous across the boundary, which ensures displacement continuity throughout the model.

However the boundary enclosing the whole model is initially free, and boundary conditions may be imposed on it, either by fixing the displacement of boundary nodes or by externally applied forces. The latter may act, not only on the boundaries but also throughout the model, as a result of distributed loads, for example due to the body's density under the force of gravity.

3.5.1 Applied forces

Loads, both on the surface and distributed throughout the body, are applied by adding terms of the form given in Equations 3.33a and 3.33b to the total force vector in the stiffness equation (3.30).

The most commonly used distributed load or body force, is that due to gravity, in which case, using the previous notation, for a particular element e

$$\tilde{p} = \begin{pmatrix} 0 \\ \\ \rho g \end{pmatrix} \tag{3.44}$$

where g is the gravitational field strength and ρ is the material density for the element.

Using Equation 3.33a

$$\tilde{F}_p = \int_e N^T \tilde{p} \, z \, dx \, dy$$

$$\begin{pmatrix} F_{pix} \\ F_{piy} \end{pmatrix} = \frac{1}{2\Delta} \int_e \begin{pmatrix} a_i + b_i x + c_i y & 0 \\ 0 & a_i + b_i x + c_i y \end{pmatrix} \begin{pmatrix} 0 \\ \rho g \end{pmatrix} dx \, dy \tag{3.45}$$

where F_{pix}, F_{piy} are the x and y components of the part of $\tilde{F}_p$ relating to node i, and where the thickness of the element z, has been set to unity.

If coordinates are used with origin at the centroid of e, then

$$\int_e x \, dx \, dy = \int_e y \, dx \, dy = 0 \; ; \quad \int dx \, dy = \Delta \qquad \text{3.46a,b}$$

and

$$a_i = \frac{2\Delta}{3} \qquad \text{3.46c}$$

(see Zienkiewicz, 1971, p. 50), so that Equation 3.45 becomes

$$F_{pix} = 0$$

$$F_{piy} = \frac{1}{3} \Delta \rho g \qquad \text{3.47}$$

and the same expressions are found for $\tilde{F}_{pj}$ and $\tilde{F}_{pm}$. In other words, one third of the weight of the element is applied at each of its nodes, and this result holds for all 3-noded triangular elements irrespective of the coordinate origin used.

Similarly, if a uniform surface load, q per unit area, is applied to the boundary of an element between nodes i and j, half of the total force on the boundary is applied at each node, i.e.

$$F_{qix} = \frac{1}{2} q \, (y_j - y_i) \; ; \quad F_{qiy} = \frac{1}{2} q \, (x_j - x_i) \qquad \text{3.48}$$

and these equations are valid for all angles of the surface to the axes.

Both these pairs of equations (3.47 and 3.48) could have been reached without integration, but the application of a varying load, for example lithostatic pressure on the end of a model, is more complicated.

Consider the element shown overleaf, with

$$q = \rho g y \qquad \text{3.49}$$

applied along the surface $x = 0$ (as a simplification) between y_i and y_j. Equation 3.33b with the restriction to $x = 0$, and with $z = 1$ gives the force on node i as

$$\tilde{F}_{q_i} = \frac{1}{2\Delta} \int_{y_i}^{y_j} \begin{pmatrix} a_i + c_i y & 0 \\ 0 & a_i + c_i y \end{pmatrix} \begin{pmatrix} \rho g y \\ 0 \end{pmatrix} dy \qquad \text{3.50}$$
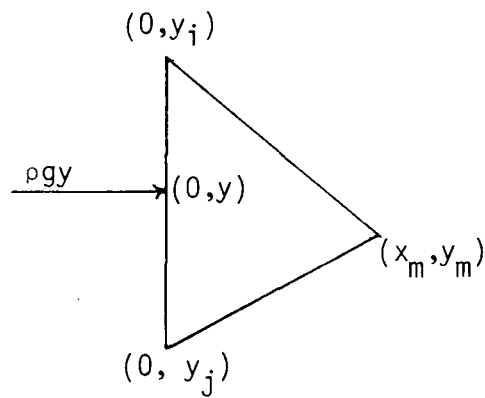
$$\therefore \quad \tilde{F}_{q_i x} = \frac{\rho g}{2\Delta} \left(\frac{a_i}{2} (y_j^2 - y_i^2) + \frac{c_i}{3}(y_j^3 - y_i^3) \right) .$$

3.51

For the simple triangle shown, Equations 3.4 and 3.5 give

$$a_i = -x_m y_j \quad ; \qquad c_i = x_m$$

3.52a,b

and $2\Delta = x_m(y_i - y_j)$.

3.52c

If Equations 3.52 are substituted into equation 3.51, factorisation and cancellation yield the result

$$F_{q_i x} = \rho g \left(\frac{y_j - y_i}{2} \right) \cdot \left(\frac{y_j + 2y_i}{3} \right)$$

3.53a

and an identical calculation gives

$$F_{q_j x} = \rho g \left(\frac{y_j - y_i}{2} \right) \cdot \left(\frac{y_i + 2y_j}{3} \right)$$

3.53b

all other components of $\tilde{F}_q$ for this element being zero.

The force applied at node i is thus equal to the lithostatic pressure at a depth 1/3 of the way between i and j (and at node j, 2/3 of the way), times half the area of the boundary.

Note that the sum

$$F_{q_i x} + F_{q_j x} = \frac{1}{2} \rho g (y_j^2 - y_i^2)$$

3.54

which is the total force on the boundary predicted by integrating $\rho g y$ along it.

If a similar calculation is performed for an element with a sloping face (i.e. $x_i \neq x_j$) the same equation (3.53a) for $F_{q_i x}$ results, but there

is also a force in the y-direction given by

$$F_{q_{iy}} = -\rho g \left(\frac{x_j - x_i}{2} \right) \cdot \left(\frac{y_j + 2y_i}{3} \right)$$ 3.55

and similarly for $F_{q_{jy}}$, since the force q acts perpendicularly to the boundary.

3.5.2 Fixed displacements

A finite element model must be restrained in order to obtain a unique solution to the stiffness equation (3.30)

$$K\tilde{\delta} = \tilde{F}$$ 3.30

The effect of having an unrestrained model, mathematically, is to make the stiffness matrix, K, singular and, in order to prevent this, the model must be held in some way that involves altering K. At least one node must be fixed in the x-direction and at least one in y to prevent translations of the whole body, and in addition these two nodes must not be the same or else the model would be able to rotate freely.

To fix one displacement component of one node, say δ_s, the equation relating to it in the set of equations represented by 3.30, namely

$$\sum_{r=1}^{2M} K_{sr} \delta_r = F_s \quad ,$$ 3.56

where M is the number of nodes in the model, must be replaced by one of the form

$$\delta_s = \delta_s^{\ *}$$ 3.57

where $\delta_s^{\ *}$ is the value at which δ_s is to be fixed.

All the components of K in the row relating to δ_s are set to zero except for the diagonal term K_{ss}, which is set at a constant value of the same order of magnitude as the other terms in K (to maintain its

stability for the inversion subroutine), and the relevant component of

the force vector is replaced by this constant multiplied by $\delta_s{}^*$:

$$K_{sr} = 0 \qquad r = 1, 2M \quad, r \neq s \qquad\qquad 3.58a$$

$$K_{ss} = 10^{12} \qquad\qquad 3.58b$$

and $\quad F_s = 10^{12} \times \delta_s{}^*$. $\qquad\qquad 3.58c$

Thus Equation 3.56 has been replaced by

$$K_{ss} \, \delta_s = F_s \quad, \qquad\qquad 3.59$$

or $\quad 10^{12} \times \delta_s = 10^{12} \, \delta_s{}^*$

as required by Equation 3.57.

As a simple illustration, consider a [3 x 3] matrix K in an equation

similar to 3.30 (although this could not refer to a model where each node

has 2 degrees of freedom, $\ell = 2$, in Section 3.2.1) where the component δ_2

is to be set at $\delta_2{}^*$. Then is Equation 3.30 is initially

$$\begin{pmatrix} K_{11} & K_{12} & K_{13} \\ K_{21} & K_{22} & K_{23} \\ K_{31} & K_{32} & K_{33} \end{pmatrix} \begin{pmatrix} \delta_1 \\ \delta_2 \\ \delta_3 \end{pmatrix} = \begin{pmatrix} F_1 \\ F_2 \\ F_3 \end{pmatrix} \qquad\qquad 3.60$$

after fixing δ_2 it becomes

$$\begin{pmatrix} K_{11} & K_{12} & K_{13} \\ 0 & 10^{12} & 0 \\ K_{31} & K_{32} & K_{33} \end{pmatrix} \begin{pmatrix} \delta_1 \\ \delta_2 \\ \delta_3 \end{pmatrix} = \begin{pmatrix} F_1 \\ 10^{12}\delta_2{}^* \\ F_3 \end{pmatrix}. \qquad\qquad 3.61$$

3.6 Testing the Method

To test the finite element program and to investigate some of the

effects of visco-elastic modelling, a comparison was made with an

analytical solution by Lee et al. (1959; see also Zienkiewicz et al., 1968).

In their paper they derive an expression for the stresses in an infinite

hollow cylinder of visco-elastic material (obeying the linear strain-rate

Equation 3.36) encased in a thin elastic shell, due to an applied pressure

at the centre.

The parameters used for the visco-elastic cylinder are:

inner radius $r_i = 2"$

outer radius $r_o = 4"$

Poisson's ratio $\nu = 1/3$

Young's modulus $E = 10^5$ psi

viscosity $\eta = 3/8 \times 10^5$ psi (time units)

and for the elastic shell, taken to be steel:

thickness $h = 4/33"$

Poisson's ratio $\nu_s = 1/\sqrt{11}$

Young's modulus $E_s = 3 \times 10^7$ psi

These units were originally chosen to simplify the calculations of Lee et al., but the solution, obtained using the Laplace transform method, is independent of units so that all length and stress units may be scaled without altering the result.

The maximum and minimum principal stresses are in the plane of a cross-section through the cylinder and are oriented radially and tangentially. The radial stress within the visco-elastic material is a function of time, t, and distance from the centre, r,

$$\sigma_r(r,t) = -p \left(f(t) + \frac{r_o^2}{r^2} g(t) \right) \qquad 3.62a$$

and the tangential stress is

$$\sigma_\theta(r,t) = -p \left(f(t) - \frac{r_o^2}{r^2} g(t) \right) \qquad 3.62b$$

where p is the pressure applied inside the cylinder from time t = 0, and f and g are functions dependent on the material properties, and given in this case by

$$f(t) = 1 - 0.005363 \exp(-0.9849\,t) - 0.6331 \exp(-0.3528\,t) \qquad 3.63a$$

$$g(t) = 0.001341 \exp(-0.9849\,t) - 0.1583 \exp(-0.3528\,t) \qquad 3.63b$$

to 4 significant figures.

Equations 3.62 and 3.63 show that the tangential stress is always greater (more tensional) than the radial, but that they approach each other with distance from the centre. In addition, the stresses approach a hydrostatic state with $\sigma_r = \sigma_\theta = -p$, as t becomes large.

The finite element grid used is shown in Fig. 3.1. Only a quadrant of the cylinder is modelled, since by constraining the ends only to move radially they become planes of symmetry, a fact which was confirmed by the lack of edge effects near the ends of the model. In all cases, the stresses at a particular radius varied by at most 1% over the whole model.

The radial and tangential stresses from the finite element program for various different times are shown in Fig. 3.2 together with those calculated from Equations 3.62 and 3.63, all as fractions of the applied pressure, p.

The finite element stresses are obtained by averaging the stresses in adjacent elements (e.g. 30 and 31, or 28 and 29 of Fig. 3.1) and taking these as the stresses at the centre of the pair. It is necessary to take the mean stresses because the method assumes the stress within each element to be constant, which introduces errors particularly in regions where there is a high stress gradient.

The model stresses (Fig. 3.2) match the analytical stresses well, the largest errors being about 0.02 in (σ_θ/p) and 0.005 in (σ_r/p). The greatest errors occur in the solutions for short times, and close to the centre (small r). Two reasons for this are; that the stress gradient is higher for smaller r, so that the discretization of the stresses is more important, and secondly that boundary effects, due to the pressure being applied at the inner nodes, are greater. These effects are both reduced as the model relaxes.
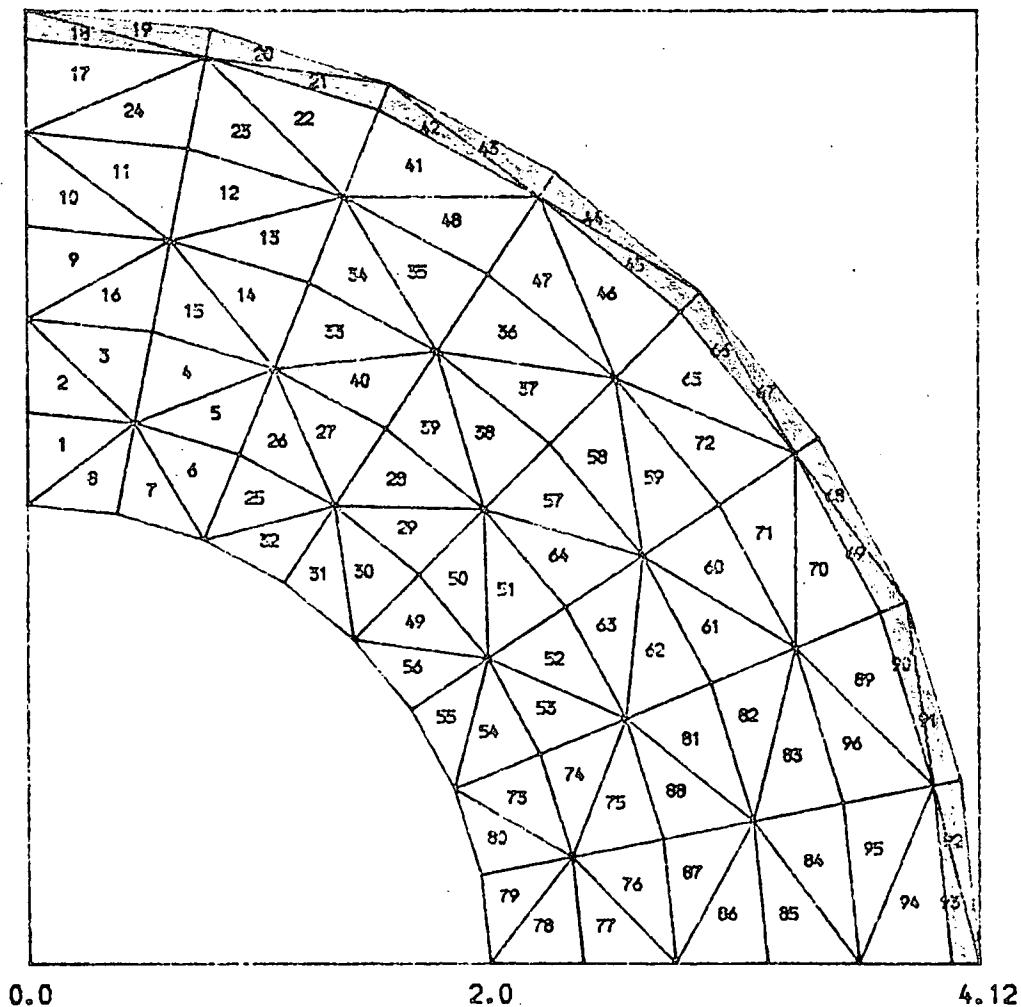
Fig. 3.1: Finite element grid for a visco-elastic cylinder enclosed in a steel case (shaded), used to test the computer program.
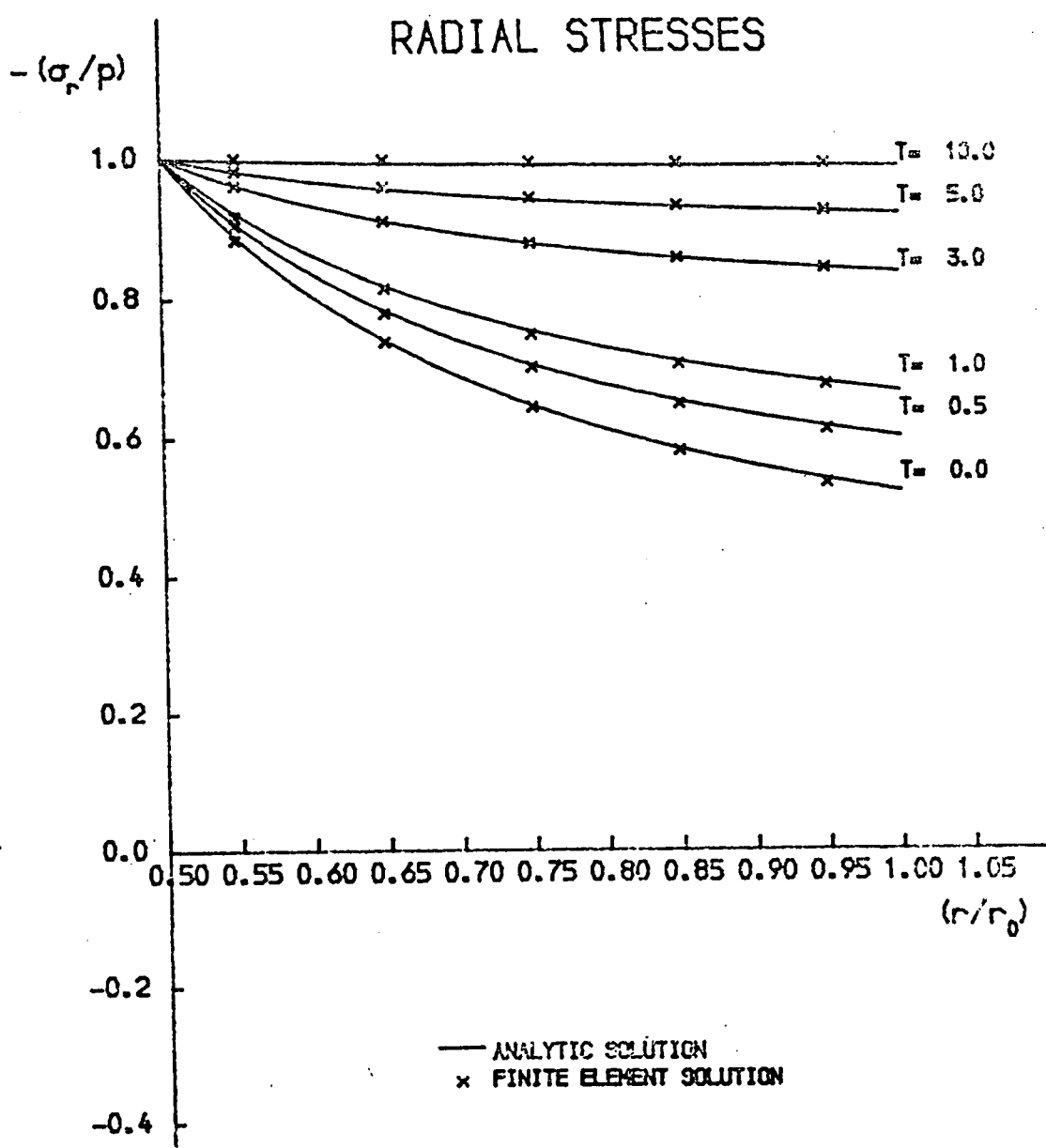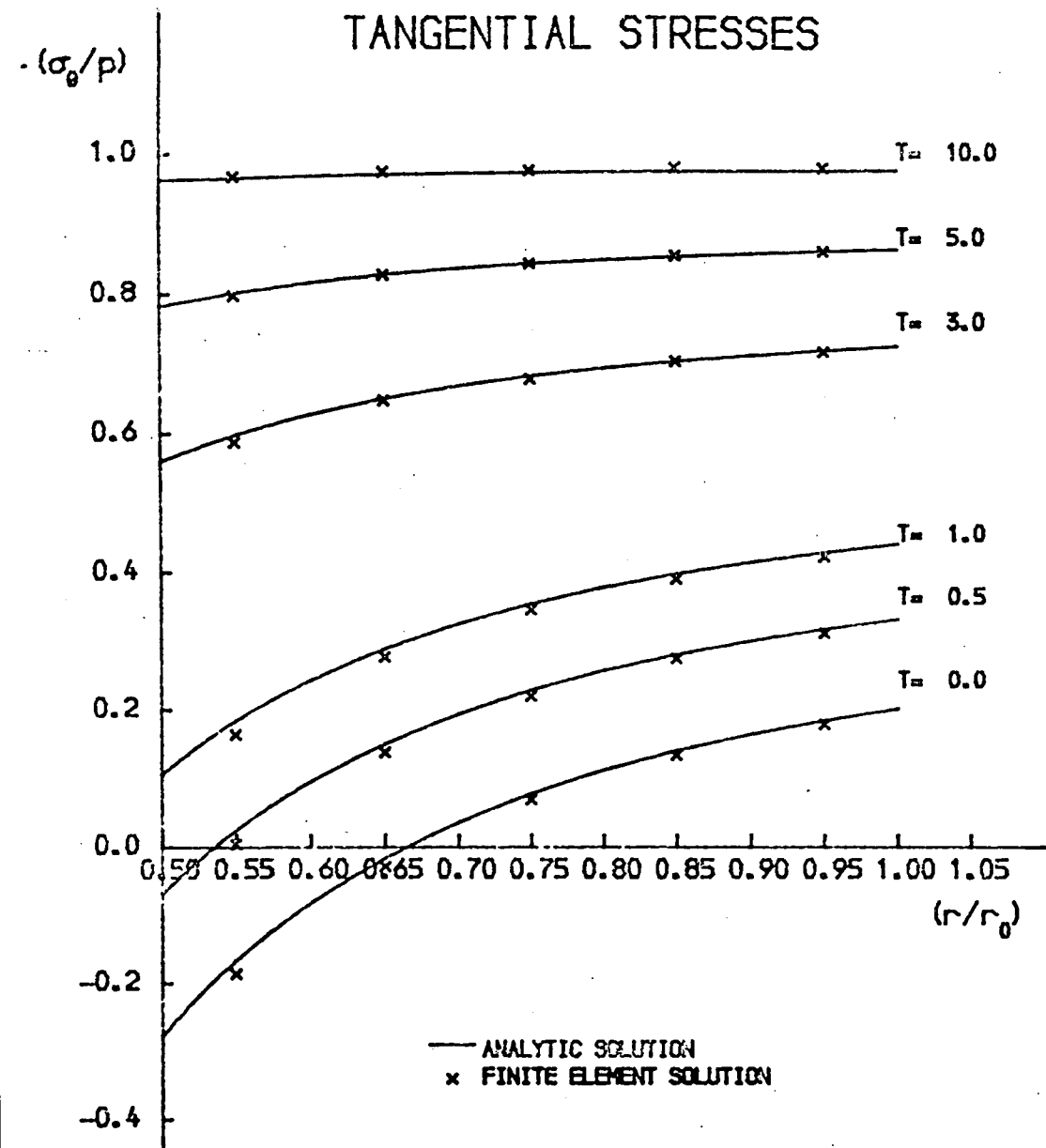
Fig. 3.2: Radial and tangential stresses in the cylinder model (Fig. 3.1) as a function of distance from the centre, for various times, t, comparing analytical with finite element results.

The orientation of the principal stresses provides a further check on the model. The angles of the stresses in all the elements are correct to within 1°, on the elastic model, an error which is reduced to less than 0.5° by averaging as described earlier.

As the stresses become closer to a hydrostatic state the errors in the angles increase, so that for t = 10 time units, the angles are only radial to within 5°, reduced to 2° by averaging. This is easily understood, since if all the deviatoric stresses were relaxed, the stress would be uniform in all directions, and so there would be no particular orientation for the principal stresses. In such a case the program sets the angle, arbitrarily, at 45°.

CHAPTER 4

BODY FORCES IN FINITE ELEMENT MODELS

4.1 Introduction

An important problem encountered when using the finite element method to model the Earth's crust or lithosphere, is how to take into account realistically the effect of weight on the stress distribution.

If a section of lithosphere had had no stress acting on it other than that due to gravity, over a period significantly longer than the Maxwell time,

$$t_m = \frac{2\eta}{E} \quad , \qquad \qquad \text{(Equation 3.35)}$$

then there would be no deviatoric stresses remaining within it. Taking the definition of Jaeger and Cook (1976), such a stress system, where the principal stresses, σ_1 and σ_3 (assumed to be in the plane of the model), are equal throughout, is called a "hydrostatic" distribution. In addition, if the model is composed of uniform horizontal layers of thickness h_ℓ and density ρ_ℓ, the principal stresses at a point P are

$$\sigma_1 = \sigma_3 = - \sum_\ell h_\ell \rho_\ell g \qquad \qquad 4.1$$

where g is the gravitational field strength and the summation is over all the layers above P. This type of stress system (again following Jaeger and Cook's definition) is called a "lithostatic" distribution, and is the same as that described by Anderson (1942) as the "standard state", on which any stresses due to externally applied forces are superimposed.

Two difficulties arise. Firstly, a lithostatic stress distribution cannot be attained in an elastic model (as discussed in Sections 4.2.1 and 4.2.2, below), and secondly, if there are lateral variations in

density, the differences in the distributed loads (due to the weight of the rocks) may cause significant deviatoric stresses, which must be included in any model (see Sections 4.3 and 4.5).

In this chapter a method of modelling the stresses due to those body forces is put forward (Section 4.4), and applied to the particular example of a passive continental margin (Section 4.5).

4.2 A Laterally Uniform, Layered Model

4.2.1 The effect of fixing the sides of the model

In general the elastic stress distribution due to body forces in a model is not lithostatic, even in the case of a model with uniform horizontal layers such as that in Fig. 4.1.

Two reasons for this difference are the restrictions imposed on the model by holding the ends fixed, and by confining it to plane strain.

To find the effect of these restrictions, consider the model of Fig. 4.1. The elasticity equation (Equation 3.19) is

$$\tilde{\sigma} = D(\tilde{\varepsilon} - \tilde{\varepsilon}_0) \qquad\qquad 4.2$$

Assuming that there are no initial strains,

$$\tilde{\varepsilon}_0 = 0,$$

and invoking the symmetry of the model to show that

$$\gamma_{xy} = 0, \tau_{xy} = 0,$$

in other words that σ_x, σ_y are the principal stresses

$$\left.\begin{array}{l} \sigma_1 = \sigma_x \\ \sigma_3 = \sigma_y \end{array}\right\} \qquad\qquad 4.3$$

the elasticity equation (4.2), becomes

LAYER MODEL (1)

X / KILOMETRES

ρ_1

ρ_2

ρ_3
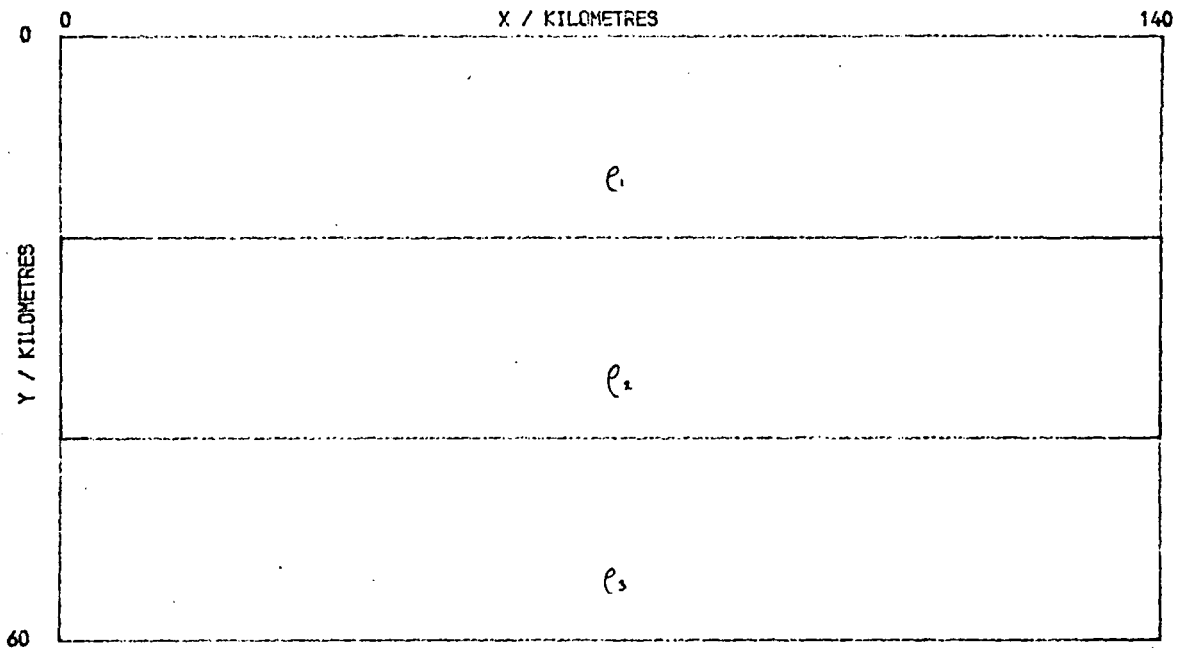
Fig. 4.1: A simple, uniform layer model of the lithosphere.

LAYER MODEL (2)

X / KILOMETRES

$\rho_1 \rightarrow \rho_1 - \bar{\rho}$

MOHO

$\rho_3 \rightarrow \rho_3 - \bar{\rho}$
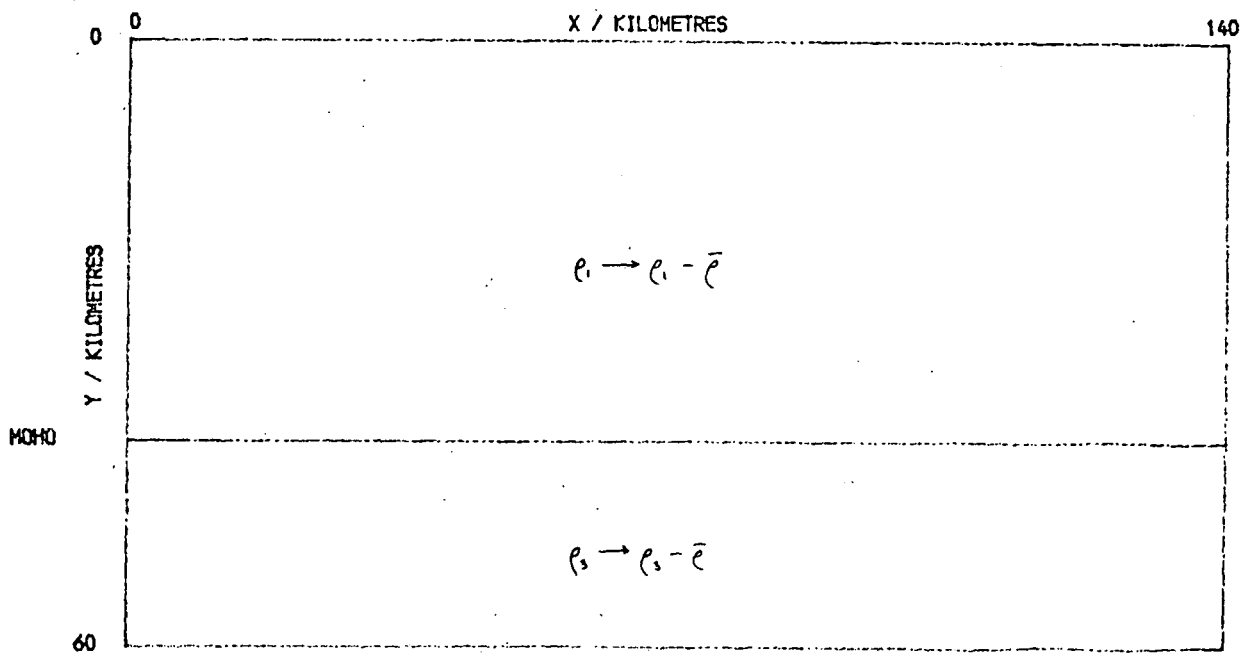
Fig. 4.2: Illustration of the subtraction of a uniform density $\bar{\rho}$ (see text).

$$\begin{pmatrix} \sigma_1 \\ \sigma_3 \end{pmatrix} = \left(\frac{E(1 - \nu)}{(1 + \nu)(1 - 2\nu)} \right) \begin{pmatrix} 1 & \frac{\nu}{1-\nu} \\ \frac{\nu}{1-\nu} & 1 \end{pmatrix} \begin{pmatrix} \varepsilon_x \\ \varepsilon_y \end{pmatrix} \qquad 4.4$$

Now, since the sides of the model in Fig. 4.1 are held and all the layers have uniform density in x, all the x-displacements are negligible

i.e. $\varepsilon_x \ll \varepsilon_y$ everywhere.

Thus, from Equation 4.4,

$$\frac{\sigma_1}{\sigma_3} = \frac{\nu}{(1 - \nu)} \qquad 4.5$$

and the only degrees of freedom remaining are ε_y for each element, or equivalently δ_y for each node.

If, therefore, the model in Fig. 4.1 is analysed by an elastic finite element method, the resultant stresses are, for each element

$$\sigma_3 = - \sum_{\ell} h_\ell \rho_\ell g \qquad \text{(Equation 4.1)}$$

$$\text{and} \quad \sigma_1 = - \frac{\nu}{(1 - \nu)} \sum_{\ell} h_\ell \rho_\ell g \qquad \text{(Equation 4.5)}$$

If the element is in a layer with a Poisson's ratio of 0.25, (corresponding in terms of the Lamé constants, to $\lambda = \mu$; see Ch. 3, Equation 3.16), Equation 4.5 gives

$$\sigma_1 = \sigma_3/3 \qquad 4.6$$

and the principal stresses are both compressions, equal to the lithostatic pressure, vertically, and 1/3 as large, horizontally.

The principal deviatoric stresses arising from this distribution are defined by

$$\sigma_1' = \sigma_1 - \frac{(\sigma_1 + \sigma_2 + \sigma_3)}{3}$$

$$\text{and} \quad \sigma_3' = \sigma_3 - \frac{(\sigma_1 + \sigma_2 + \sigma_3)}{3}$$

which, in a 2-dimensional analysis, are commonly reduced to the definitions

$$\sigma_1' = \frac{(\sigma_1 - \sigma_3)}{2}$$ 4.7

and $\sigma_3' = \frac{(\sigma_3 - \sigma_1)}{2}$.

Using Equations 4.6 and 4.7

$$\sigma_1' = -\sigma_3/3$$

$$\sigma_3' = \sigma_3/3$$ 4.8

These equations (4.8) represent deviatoric stresses of a compression equal to 1/3 of the total lithostatic pressure vertically, with a tension of equal magnitude horizontally.

Given that the lithostatic pressure at the base of a 40 km thick crust of average density 2800 kg m^{-3} is about 1 GPa (or 10 kbar), this effect would swamp any deviatoric stresses due to applied loads on a lithospheric model of this type.

It is important to note that this is not an edge effect, in the sense that increasing the length of the model (in x) does not alter the stress distribution.

4.2.2 Stress boundary conditions

Service and Douglas (1973) suggest that the ends of a model should be held in place by applying suitable horizontal forces at the nodes on the sides. These forces would represent the forces exerted by the lithosphere on either side of the model, but would not necessarily be equivalent to the forces exerted, lithostatically, by an equal thickness of rock.

Finding the right values for these forces is very difficult. The

number of nodes in a model makes them impractical to calculate, and trial and error methods show the model to be very sensitive to the forces used. For example, if an attempt is made to hold the base with forces, rather than fixed displacements (see Ch. 3, Section 3.5), on a more complicated model (such as one of those in Ch. 6), even after several trials the displacements of the basal nodes are still up to $\sim$ 100 m, and vary considerably from node to node.

If the sides of the model are held motionless in the x-direction by forces, the same argument as in Section 4.2.1 applies, and although the sides of the model can move if loads are then applied to it, the stresses due to these loads are still obscured by the elastic deviatoric stresses due to the model's weight.

A second type of stress boundary condition might be one which created a lithostatic stress system in the model on which a further stress distribution would be superimposed. However, as Anderson (1942) states (on p. 141), the standard state cannot be produced in a model restricted to plane strain. If lithostatic stresses are applied to the sides of a uniform model (or to one side, with the other fixed as an axis of symmetry), the elastic stress system depends strongly on the value of Poisson's ratio assigned to it, and will only be lithostatic for the case $\nu = 0.5$, compared to the usual values for rocks of about 0.3. Note that, although materials with $\nu = 0.5$ cannot be modelled by the finite element formulation of Chapter 3 (see Equation 3.20), models with $(0.5 - \nu) = 10^{-8}$ show stress systems with negligible deviatoric stresses.

The deviatoric stresses are increased if there are any property contrasts within the body (even in the form of uniform horizontal layers), and are typically of the order of 0.1 GPa (1 kbar), a figure which cannot

be neglected in most cases.

4.2.3 Subtraction of a uniform density

It has been suggested (Kusznir, 1976) that in order to see the deviatoric stresses due to applied loads more clearly, a uniform density should be subtracted from all the densities in a layered model. Thus, for instance, the densities in Fig. 4.2 might be replaced by $(\rho_1 - \bar{\rho})$ and $(\rho_3 - \bar{\rho})$ respectively, where $\bar{\rho} = (\rho_1 + \rho_3)/2$. The justification for this is that the stiffness equation (see Equation 3.30),

$$K\tilde{\delta} = \tilde{F} \qquad\qquad 4.9$$

is linear, so that any stress systems may be superimposed. It is then assumed that the resultant deviatoric stresses represent those that exist in the lithosphere, since a uniform density distribution, implicitly assumed to give a lithostatic stress distribution, has been subtracted. Now the density above the Moho is negative and that below is positive so, on an elastic solution of the constitutive equation (4.9), large vertical deviatoric tensions appear near the Moho.

These tensions arise because the stress distribution subtracted was not lithostatic, but the elastic stress distribution due to the application of body forces, as described in Section 4.2.1. There are large vertical deviatoric tensions at the base of the crust and small vertical compressions at the top of the mantle, because a much (c. 3 times) larger compression has been subtracted from the vertical than from the horizontal stresses. If no loads, other than those due to gravity, were applied, then the ratio of the two principal stresses throughout the body would remain at $\nu:(1 - \nu)$ (or about 1:3), which would still mask the deviatoric stresses due to any loads then applied.

The resulting stress system is entirely dependent on the value of

$\bar{\rho}$ arbitrarily subtracted from the model densities and is thus purely an artefact of the method used.

4.2.4 Density stripping

Instead of subtracting a uniform density from the whole model to reveal the deviatoric stresses, densities may be subtracted in uniform horizontal layers (Bott and Dean, 1972; Dean, 1973; Kusznir, 1976). This is more satisfactory for a model such as those in Figs. 4.1 and 4.2, since it would reduce either model to a zero density throughout, and would therefore not introduce any misleading stress systems. Loads could be applied to the model without the superposition of any body forces, and if the total (rather than deviatoric) stress system were required, a lithostatic distribution, based on the densities subtracted, could be added to that calculated.

The latter result could not be derived directly from a solution of Equation 4.9, for the reasons described in Sections 4.2.1 and 4.2.2 but would give a realistic distribution, if the lithosphere has had time to relax to a lithostatic stress system, before the loads were applied. If this is to be the case, the lithosphere would have to be significantly older than the Maxwell time, $2\eta/E$, as described in Section 4.1.

4.3 Models with Lateral Density Variations

4.3.1 Density stripping

The density stripping method, described in Section 4.2.4 above, is not so successful if there are lateral density changes within any of the layers. As an illustration of this point, the model shown in Fig. 4.3

STRIP MODEL
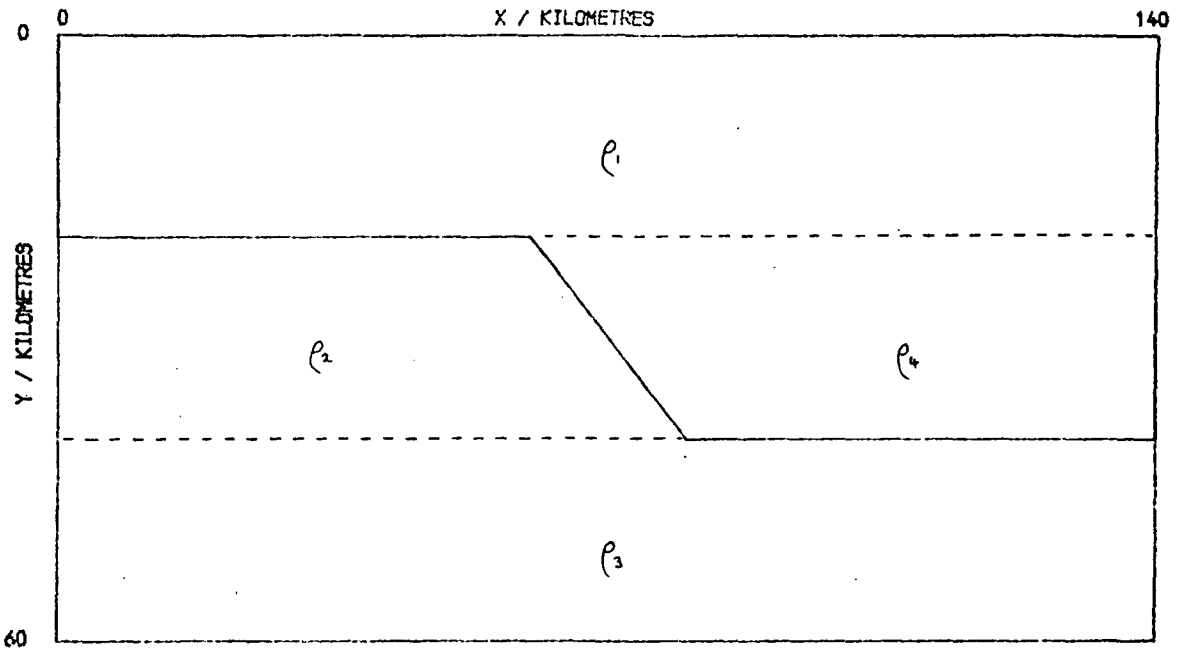
Fig. 4.3:   A model to illustrate the effects of lateral density variations.

STRIP

ELEMENT MESH
(WITH ELEMENT NUMBERS)
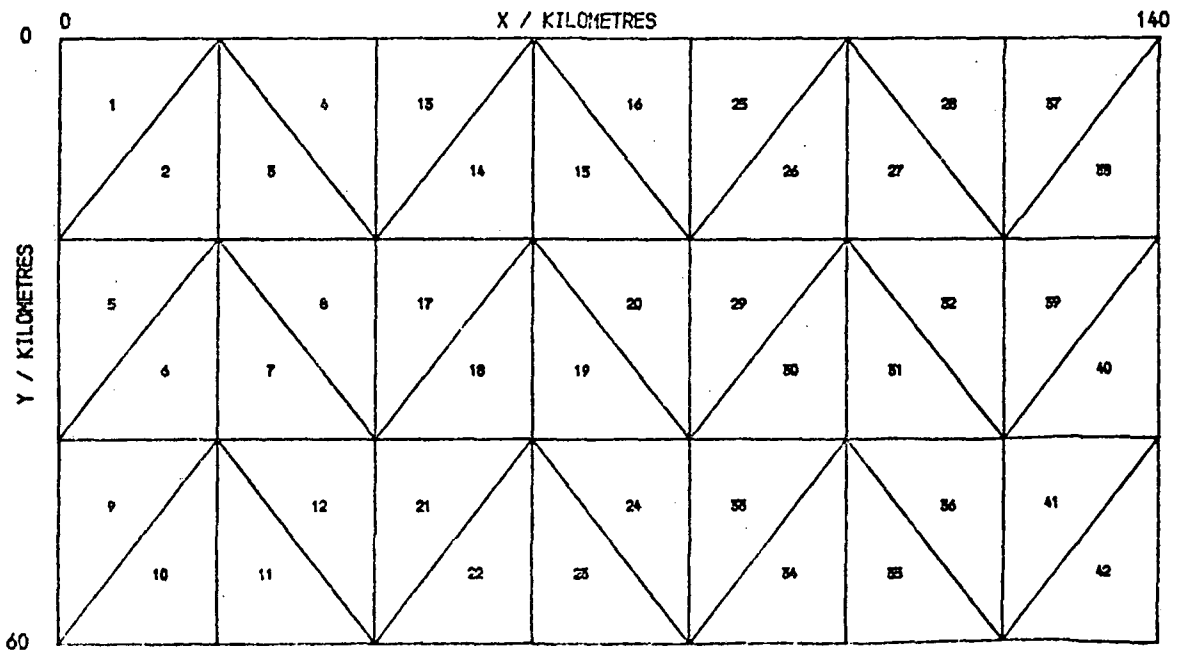
Fig. 4.4:   The finite element grid used for the model of Fig. 4.3.

was analysed both elastically and visco-elastically, with material properties as shown in Table 4.1 (see Ch. 2) and using a grid as shown in Fig. 4.4.

Material number	1	2	3	4
Density/kg m^{-3}	2800	3300	3300	2800
Young's Modulus/GPa	90	170	170	90
Poisson's ratio	0.266	0.260	0.260	0.266
Viscosity/N s m^{-2}	10^{25}	10^{23}	10^{23}	10^{25}

Table 4.1: Visco-elastic parameters used in the models of Section 4.3 (see Fig. 4.3).

If this model is analysed elastically with the full densities as above, the resulting principal stresses are as shown in Fig. 4.5. Although some of the stress vectors have rotated due to the effect of the density change in the middle layer, the overall stress distribution is of the type described in Section 4.2.1, with the vertical stress being approximately equal to the lithostatic pressure and the horizontal being a factor of $(\nu/(1 - \nu))$ smaller.

Figures 4.6 and 4.7 show the result of density stripping. In Fig. 4.6, a density of 2800 kg m^{-3} has been subtracted from the top and middle layers, and 3300 kg m^{-3} from the bottom layer, the only non-zero density remaining being $\rho_2 = 500$ kg m^{-3}, while in Fig. 4.7 3300 kg m^{-3} has been subtracted from the middle, so that the only non-zero density is $\rho_4 = -500$ kg m^{-3}.

The differences between these two models are immediately obvious.
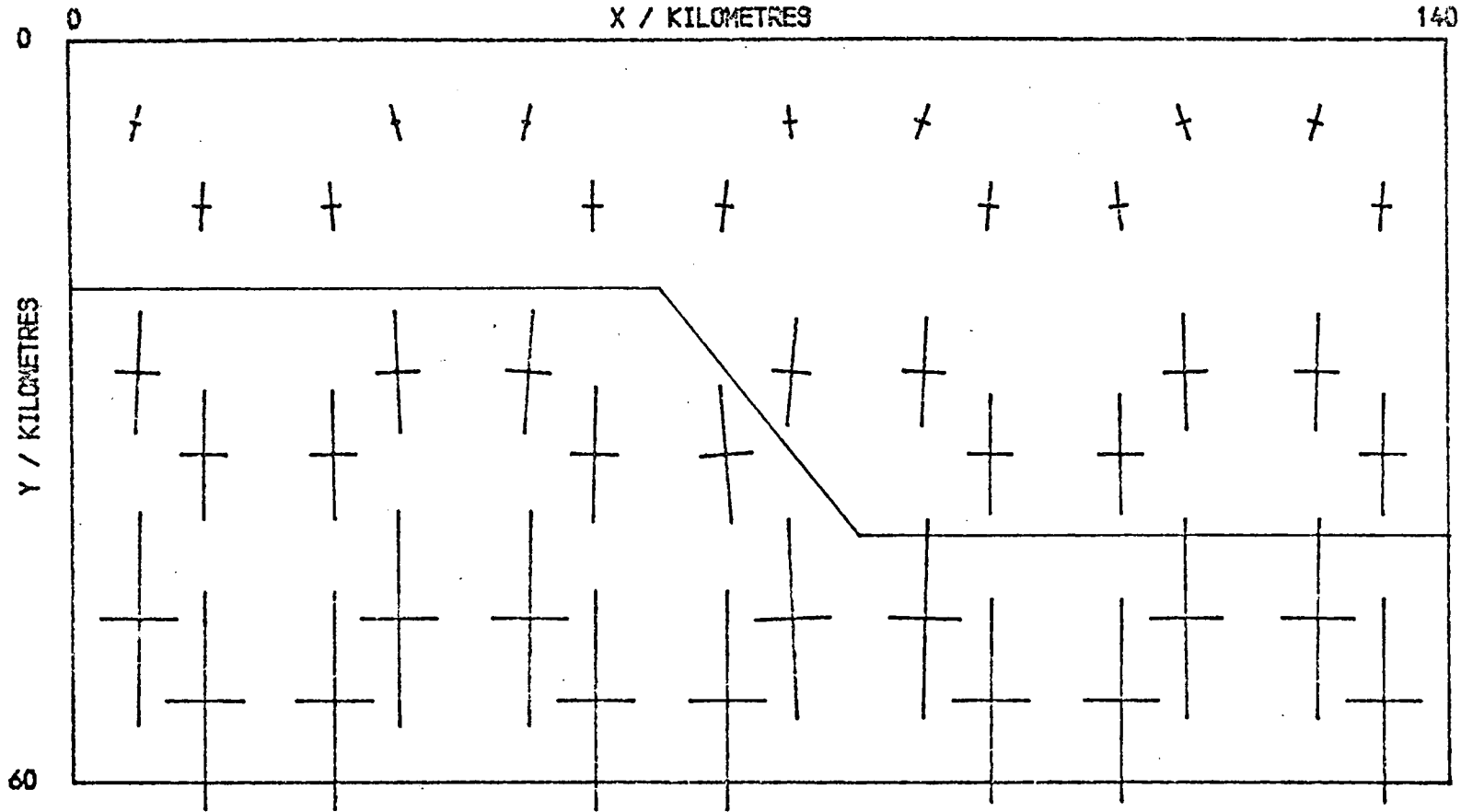
Fig. 4.5: Elastic principal stresses in the model of Figs. 4.3 and 4.4.
The two principal stresses in the plane of the model are
plotted at the centroid of each element, the length of the
vector giving the magnitude of the stress (the vector is dashed
for a tensional stress) and the angle giving the principal
stress orientation. Note that, owing to vertical exaggeration,
these angles cannot be compared directly with angles on the model.
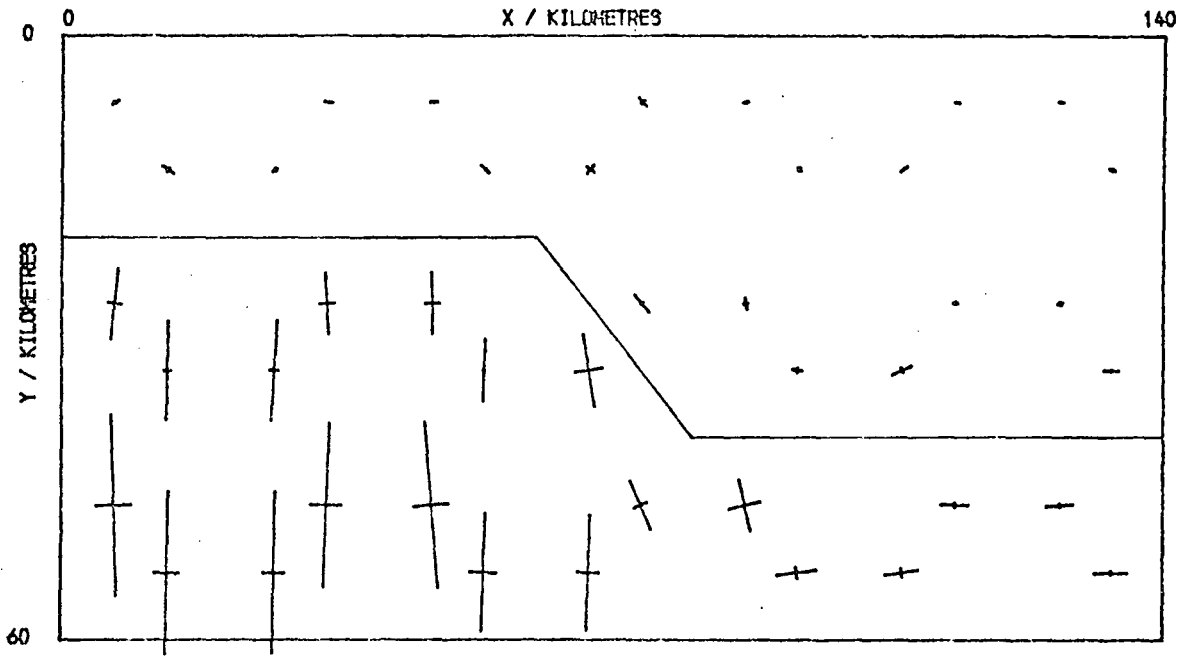
Fig. 4.6: The elastic principal stresses in the model (Fig. 4.3) after density stripping (a density of 2800 kg m^{-3} has been subtracted down to 40 km, 3300 kg m^{-3} below)
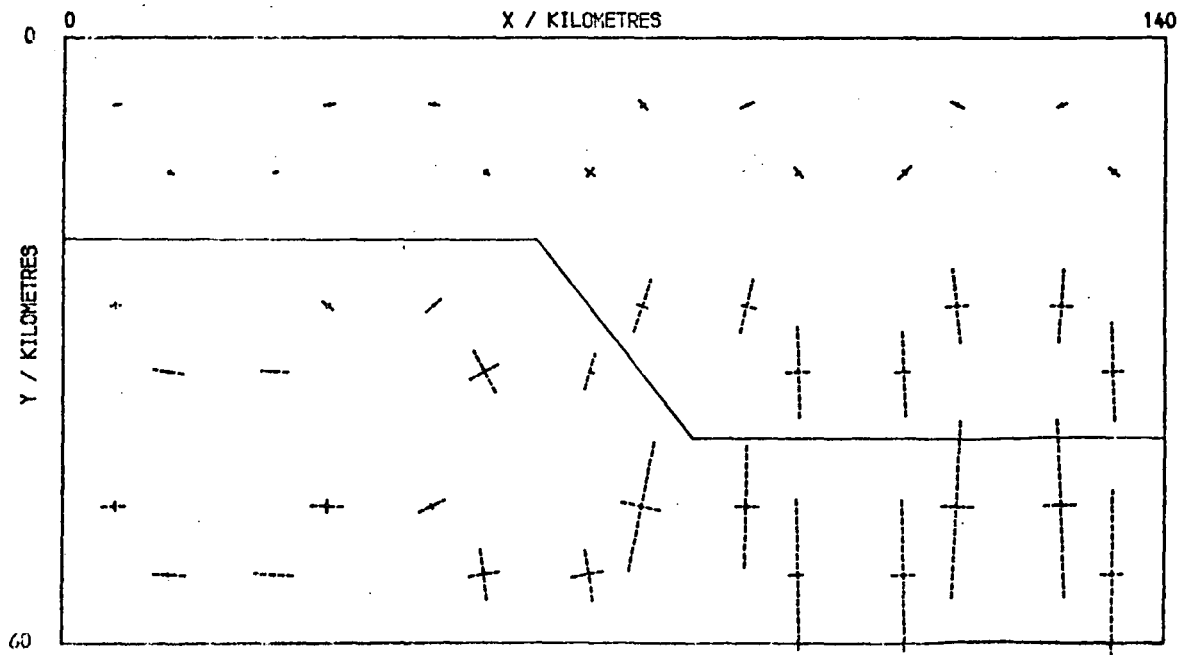
Fig. 4.7: Elastic principal stresses after subtraction of a density of 2800 kg m^{-3} down to 20 km, 3300 kg m^{-3} below.

In Fig. 4.6, the only significant stresses are in the left half of the model and are compressive, while in Fig. 4.7 the largest stresses are to the right and are tensile.

If the lithostatic stress distributions, due to the density layers subtracted from each model, are added to their respective stripped stress systems (Figs. 4.6 and 4.7), the resulting stresses (see Figs. 4.8 and 4.9) are the same to within, at most, 5%. In this respect the two different models may be said to be different ways of representing the same relative stress distribution. However, this is only a qualitative comparison, and quantitatively there are important differences.

Firstly, although the magnitudes (and signs) of the stresses in Figs. 4.8 and 4.9 are so similar, this is only because the deviatoric stresses in each model are so much smaller (< 5%) than their hydrostatic values, but the angles of the resultant stresses (which depend on the deviatoric stresses only) differ significantly.

Secondly, the strains calculated depend on the stresses without the addition of any lithostatic distribution, and if these two models (Figs. 4.6 and 4.7) are taken to represent the same relative stress distribution, then a choice must be made between the strains shown in Figs. 4.10 and 4.11 to decide which represents the actual strains in the lithosphere.

In a model representing a real cross-section of the lithosphere, this choice would be made according to which model seemed geologically the more feasible, but this model was chosen to show that the choice would necessarily be subjective, whatever the model.
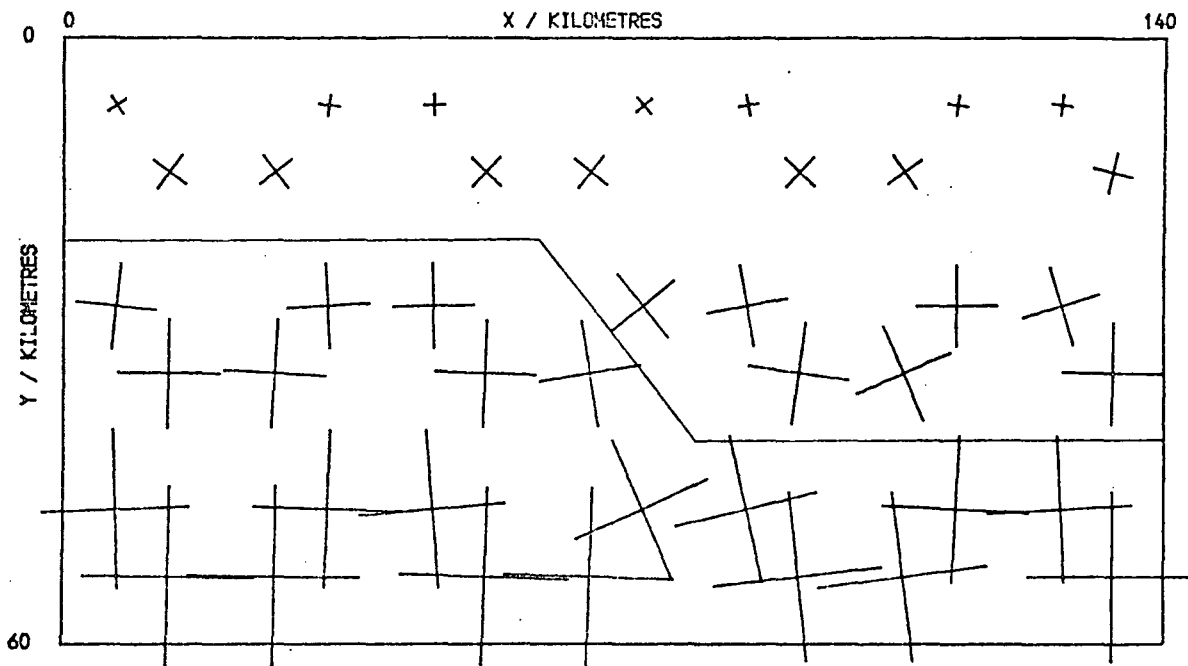
Fig. 4.8: The elastic stress distribution of Fig. 4.6 after the addition of
a lithostatic system due to the subtracted density distribution.
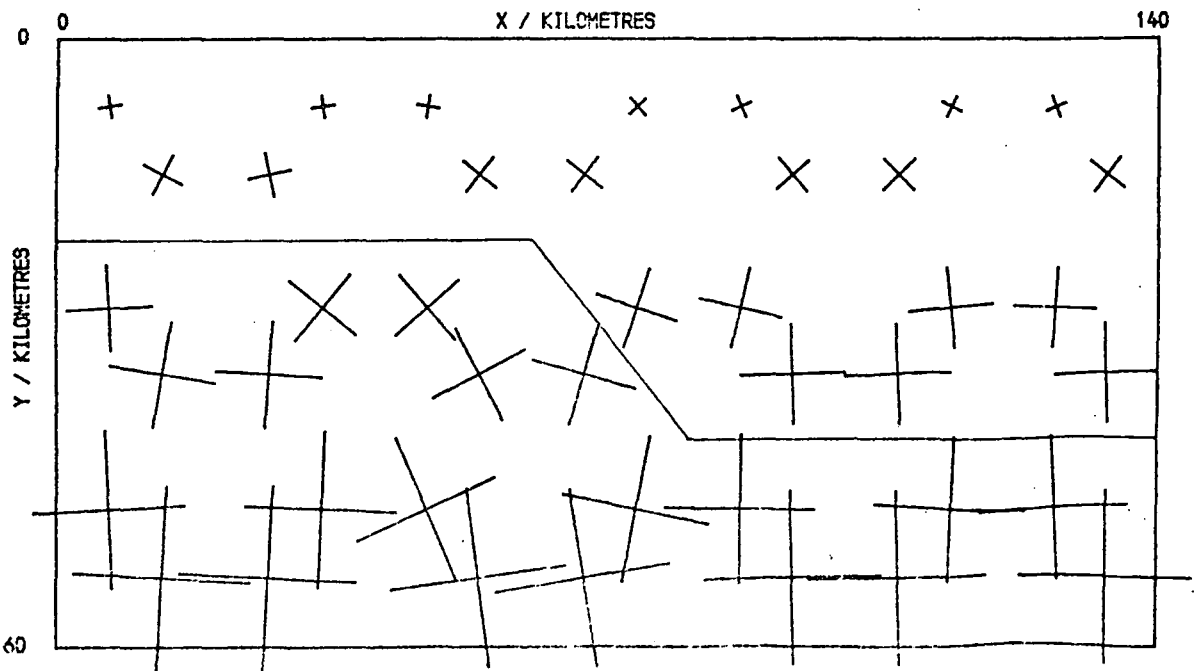
Fig. 4.9: The elastic stress distribution of Fig. 4.7 after the addition of
lithostatic stresses due to the subtracted densities.
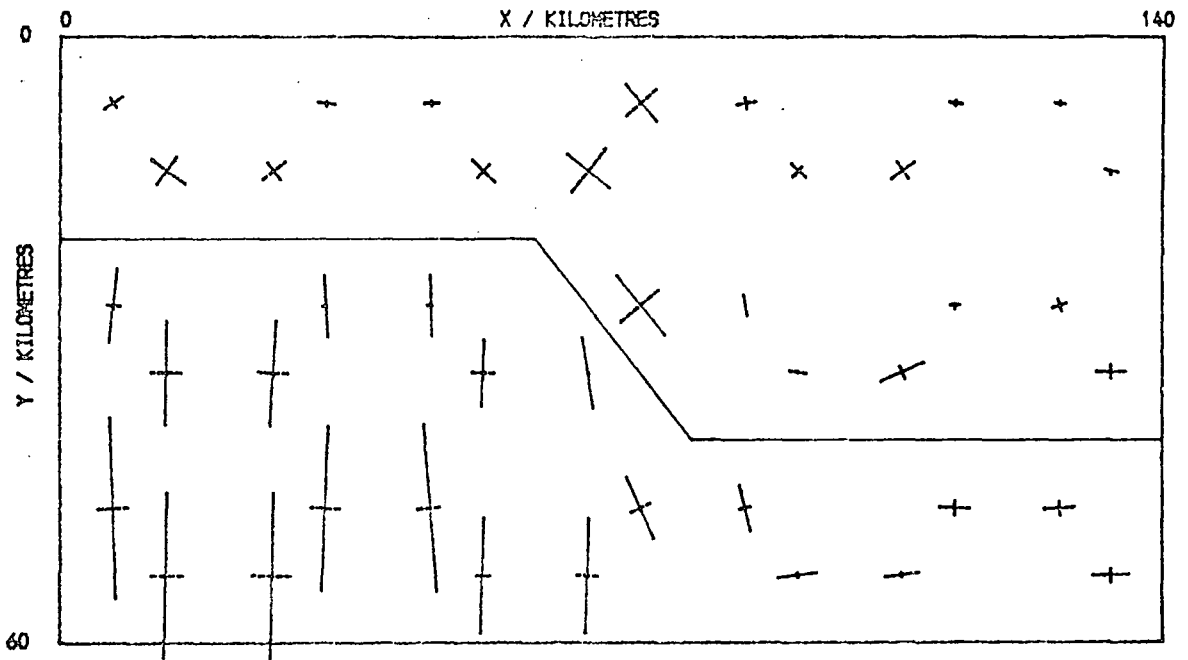
Fig. 4.10:   The elastic principal strains in the model of Fig. 4.6.
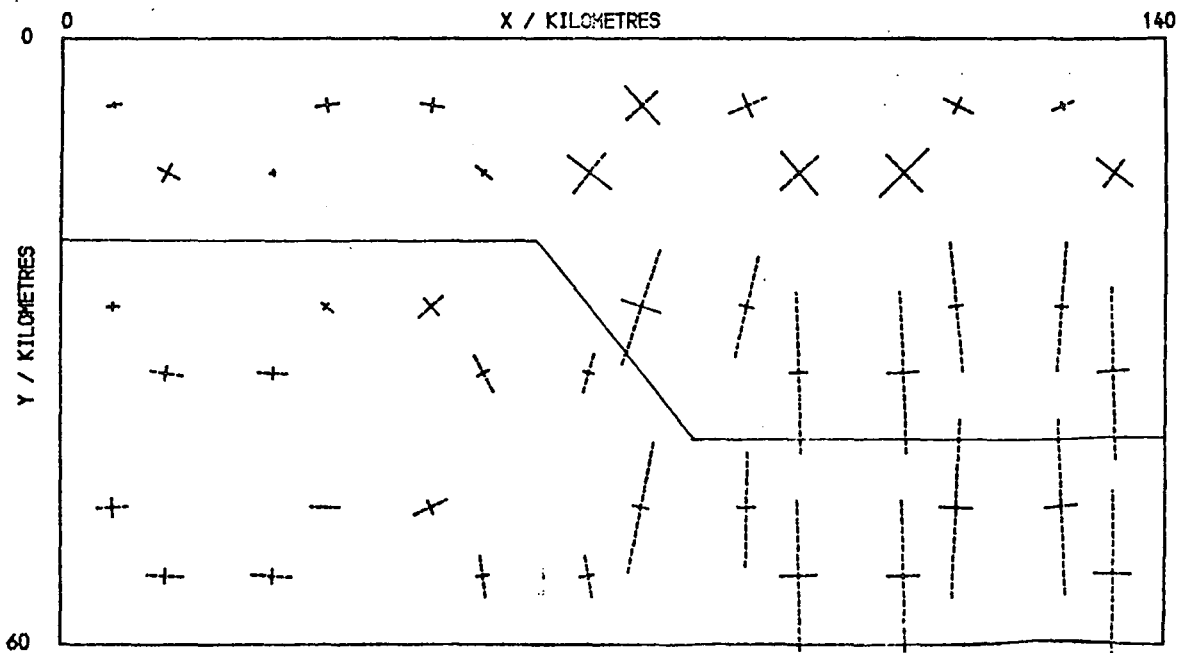
Fig. 4.11:   The elastic principal strains in the model of Fig. 4.7.

4.3.2 Further considerations

The principal reason for the difficulties discussed so far in
this chapter, has been that the effects of the body forces have been
examined using elastic models. This method of analysis causes two
further problems, one in trying to attain some sort of lithostatic
starting model, and the other in the size of the displacements and
strains that it gives.

The finite viscosity of the crust means that a simple layered
model, such as in Fig. 4.1, gives a stress system which will relax
visco-elastically to a lithostatic distribution, if it is left for a
time significantly greater than the Maxwell relaxation time (see Equation
3.35)

$$t_m = 2\eta/E$$

which, setting

$$\eta \simeq 10^{25} \text{ N s m}^{-2}$$

and $E \simeq 10^{11}$ Pa

gives

$$t_m \simeq 6 \text{ Myr.}$$

Hence t_m is smaller than the age of many geological structures,
and this is the justification for using density stripping in cases
where loads are applied to a simple layered model, as suggested in
Section 4.2.4. However, in cases where there are lateral changes in
density, there remain deviatoric stresses due to density changes which
make an important contribution to the final stress system. These stresses
must therefore be calculated, and included in the final analysis when
other loads are applied, rather than simply adding in lithostatic stresses.

The second problem is related to the displacements given by an
elastic solution. If full densities are used, these displacements can

be quite large (typically 300 m) compared to the size of the elements used, an effect which is enhanced when the materials involved have low values for E, their Young's modulus. Together with the resulting stress pattern, they represent the effect of compaction that would occur if gravity were instantaneously applied to a model of the shape and composition given.

An objection to this is that the geological structure being modelled has the dimensions of the initial model, and not those of the displaced result, so that the shape of the resultant surface is not that observed. This can be very important, because topography is one of the most easily obtained sets of data for a geological feature, particularly in the regions relevant to this study (see Ch. 1, Section 1.2). Rates of change of depth can also be found (for example, from the D.S.D.P. data, described in Ch.1, Section 1.3), so that a direct comparison between the calculated and observed displacements of the section's surface would be a useful check on the analysis.

Any alternative method of modelling geological structures must take this into account, and provide means to allow realistically for the stresses supporting the model's weight.

4.4 A Method for Initializing Models

4.4.1 The object of the method

To avoid the difficulties discussed in Sections 4.1 to 4.3 of this Chapter, a new method has been developed for dealing with body forces in a finite element model.

The basis of the method is the derivation of a hypothetical starting model, which, when allowed to relax visco-elastically for a given time,

will deform to the required initial model of the lithosphere, based on observation.

The starting model achieved is a mathematical convenience, and its shape may bear little or no resemblance to the real lithosphere, because the method applies gravity to a complete lithospheric model, while in reality the crust is formed gradually, with gravity acting throughout the process, and material properties vary during the period of formation.

However, if the crust were elastic, then the elastic displacements between the starting model and the required model would represent the compaction of the rocks under the force of gravity, assuming them to be formed instantaneously and in the absence of any other applied loads or tectonic stresses.

Similarly, when the starting model relaxes visco-elastically to the required model in a time equal to the age of the latter, then the displacements represent a broad averaging of all effects, e.g. compaction, sedimentation and erosion, over its lifetime.

The stresses formed in the initialized model are those stresses that are necessary to support the model's density distribution at its particular age, assuming that it behaves visco-elastically.

4.4.2 The method

The method used involves repeated solutions of the elastic or visco-elastic displacements, using the finite element methods described in Chapter 3. On each successive solution the model is modified according to the displacements of the previous solution, until the displaced model shape is the required initial model.

Let one co-ordinate of one node within the model, at the beginning

of the nth solution, be x_n, and the displacement, after the nth solution, in that degree of freedom be δ_n. x_0 is set as the required co-ordinate for the observed model.

The process begins with the zeroth solution that displaces x_0 to $(x_0 + \delta_0)$ and continues as illustrated in Fig. 4.12, below:

Figure 4.12: Illustration of the model initialization process.
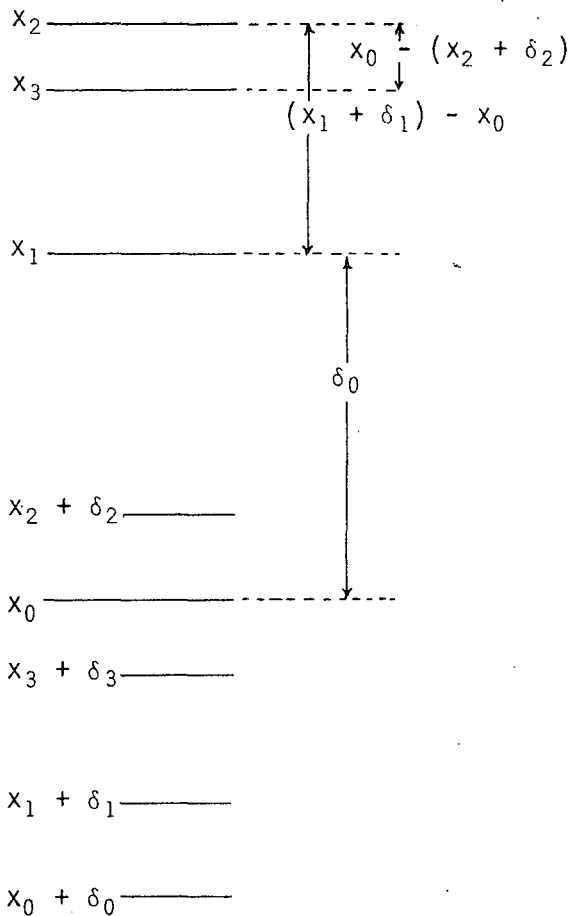
x_0 in solution 0 gives δ_0

set $x_1 = x_0 - \delta_0$

x_1 in solution 1 gives δ_1

set $x_2 = x_1 - ((x_1 + \delta_1) - x_0)$

$\qquad = x_0 - \delta_1$

x_2 in solution 2 gives δ_2

set $x_3 = x_2 + (x_0 - (x_2 + \delta_2))$

$\qquad = x_0 - \delta_2$

and so on, until solution (n-1) gives δ_{n-1}, then

$x_n = x_0 - \delta_{n-1}$

and if the solutions converge $|(x_n + \delta_n) - x_0| \to 0$, as n, the number of the solution, increases.

When convergence has been achieved to within the required tolerance, the co-ordinates x_n are used for the initial model and the stresses $\tilde{\sigma}_n$ are used as the starting stresses for finding the visco-elastic response to any further applied loads. Note that the combination,

achieved by this method, of the initial stress system and that due to the additional forces is non-linear for visco-elastic models.

4.4.3 Examples

The results of applying the initialization process to the layer model (Fig. 4.1 with ρ_1 = 2800 kg m^{-3}, ρ_2 = ρ_3 = 3300 kg m^{-3}) and to the model, with lateral density variation, of Section 4.3.1 (Fig. 4.3), both using the grid of Fig. 4.4, are shown in Figs. 4.13 and 4.14 respectively. These two diagrams show the stress patterns due to weight in the models, after they have been allowed to relax for 10 Myr, which would be superimposed on any stresses caused by other forces applied to lithosphere of that age.

In the layer model (Fig. 4.13) the deviatoric stresses in the mantle have been relaxed entirely, while in the crust there is a laterally uniform remanent deviatoric stress system. The magnitudes of the stresses in the mantle differ positively and negatively from those expected lithostatically by about 10%, due to the coarse grid used, but if the stresses in pairs of elements (e.g. 5 and 6, or 11 and 12 in Fig. 4.4) are averaged, they give the correct lithostatic value at the centre of the pair to within 0.5% (an effect which is discussed in Chapter 3, Section 3.6).

The Maxwell times (see Section 3.4) are, for the mantle

$$t_m^m = \frac{2\eta_m}{E_m} \simeq 4 \times 10^4 \text{ yr}$$

and for the crust

$$t_m^c = \frac{2\eta_c}{E_c} \simeq 7 \times 10^6 \text{ yr}$$

so that 10 Myr is significantly greater than t_m^m but of the same order as t_m^c. Thus the stresses in Fig. 4.13 are as expected, the only remaining
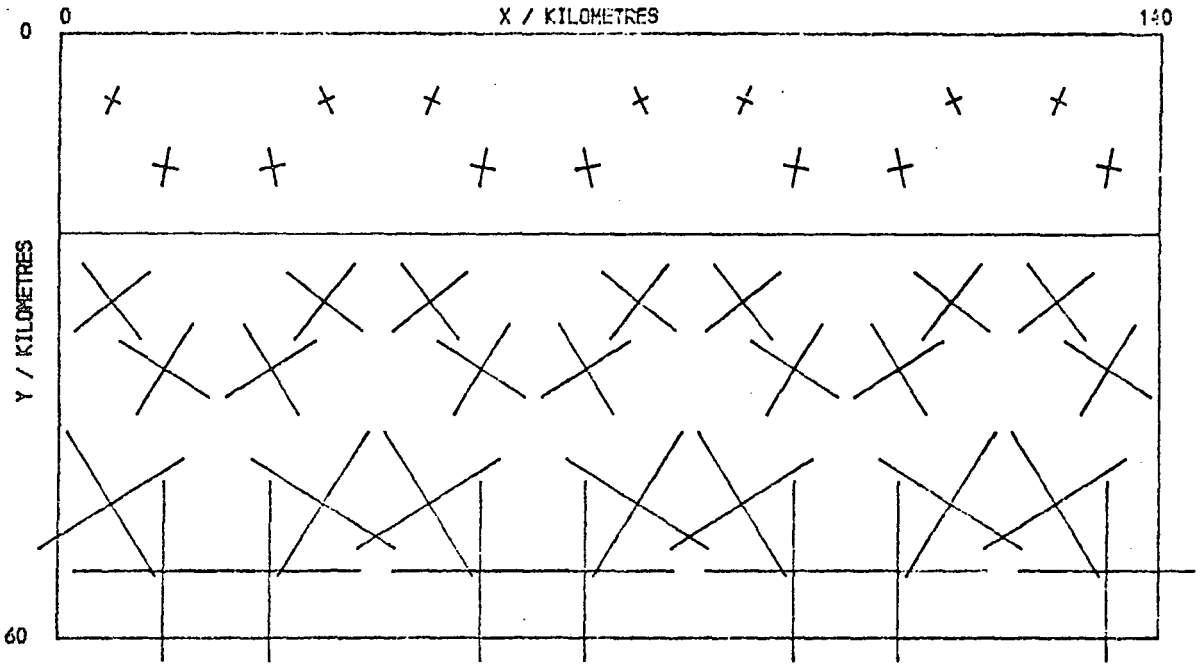
Fig. 4.13: The model of Fig. 4.1 (uniform layers), initialized visco-elastically for 10 Myr, as described in the text.
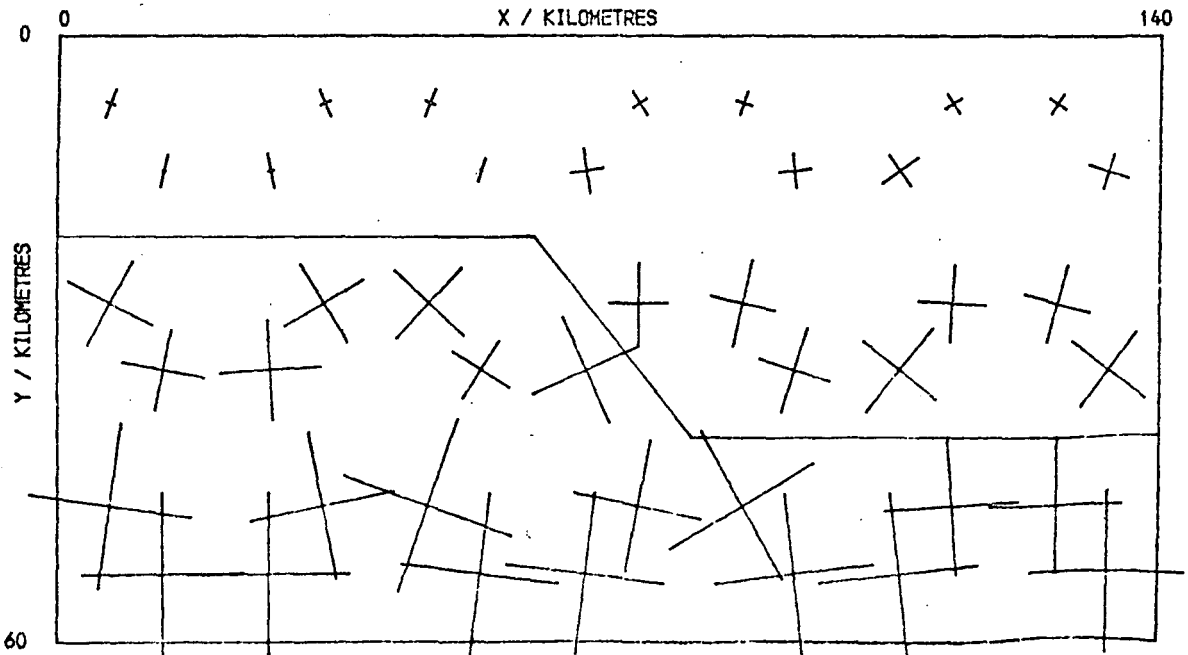
Fig. 4.14: The model of Fig. 4.3, initialized visco-elastically for 10 Myr.

deviatoric stresses being in the crust.

A comparison of Fig. 4.13 with 4.14 shows clearly the effect of a
lateral density contrast in one layer. The viscous spreading of the
portion of mantle above 40 km depth, under its weight, has pushed the
stiffer, lighter crust to the right, increasing the horizontal compression
in the crust to the right of the step in the Moho, and therefore reducing
the near-horizontal deviatoric tensions (seen in Fig. 4.13) in the
thicker crustal section. At the same time, the deviatoric tensions in
the thinner crust to the left of the step are increased. There are no
deviatoric stresses remaining in the mantle, as before, but the lateral
change in viscosity and density has caused some variation from the
lithostatic distribution.

The stress pattern shown in Fig. 4.14 is very different from those
given by elastic analysis using density stripping (see Figs. 4.6 to 4.9)
and is taken to be more realistic (if such a model existed) since a
visco-elastic model is closer to the rheologies postulated for the
lithosphere than an elastic one.

4.5 Body Forces at Passive Margins

4.5.1 Elastic Models

Several of the points discussed in this chapter are illustrated
by analysis of an Atlantic-type, or passive, continental margin. Bott
and Dean (1972; Dean, 1973) have made a study of this type of margin
using an elastic finite element model, with an oceanic density distribution
subtracted (density stripping as described in Sections 4.2.4 and 4.3.1),
and a simplified copy of their model is shown in Figs. 4.15 and 4.16.
The elastic properties used here are as before (Section 4.3.1, Table 4.1)

X / KILOMETRES
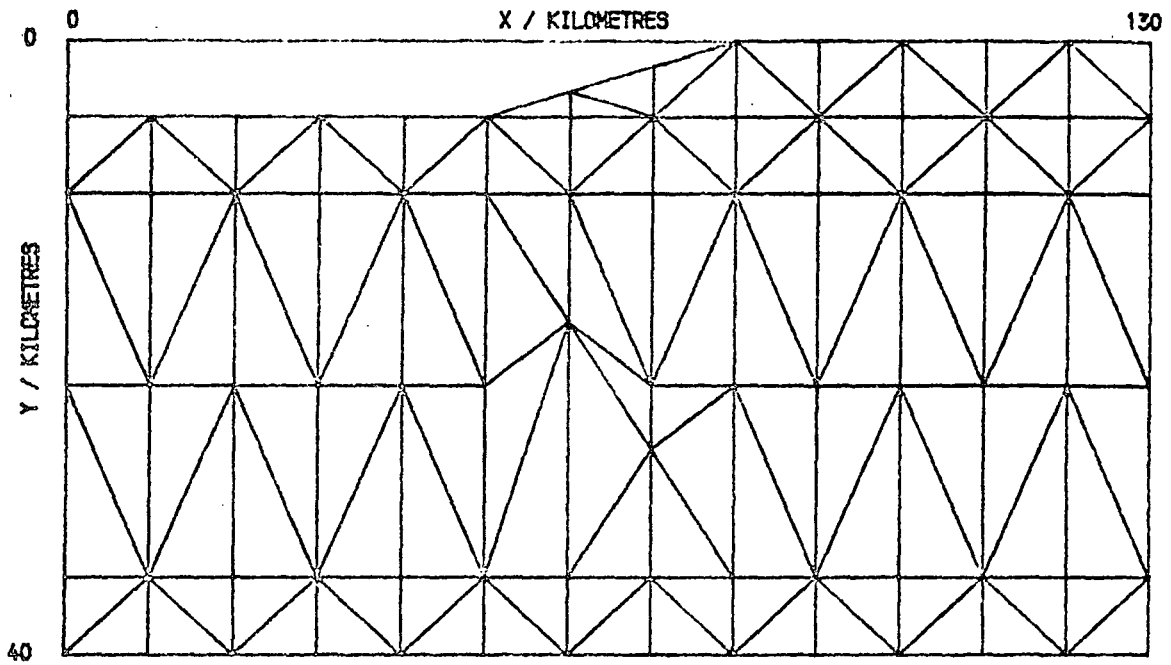
Fig. 4.15:   Finite element grid for a passive margin model.

PASSIVE MARGIN MODEL

X / KILOMETRES
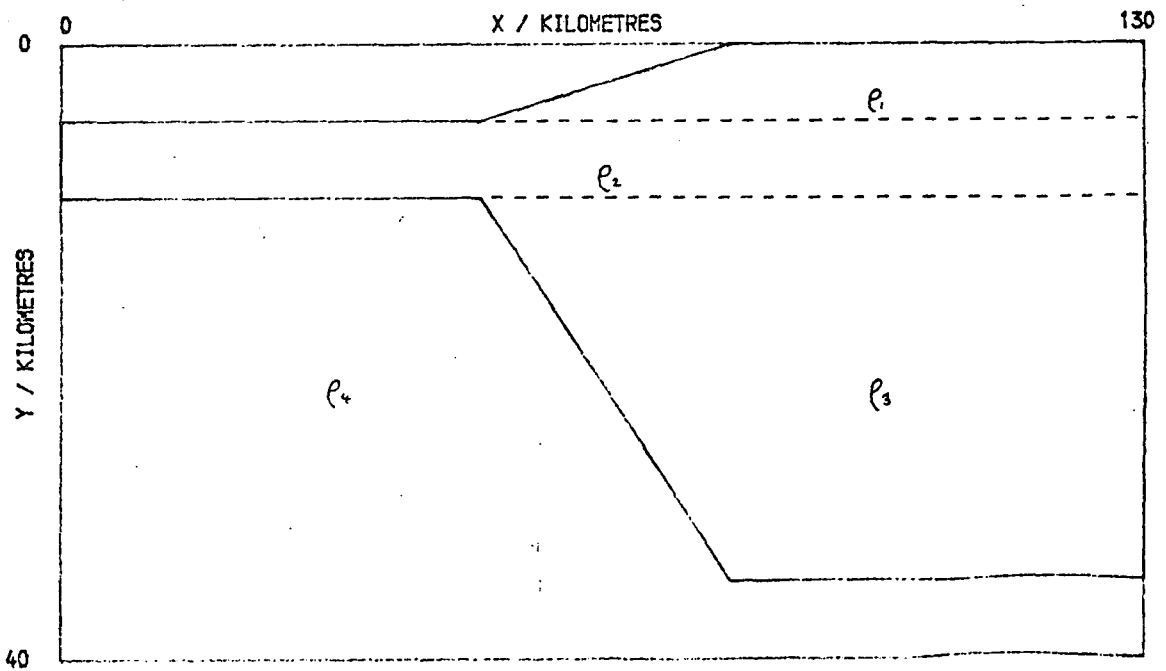
Fig. 4.16:   Density distribution in the model of Fig. 4.15.

$$\nu_c = 0.266$$

$$\nu_m = 0.260$$

$$E_c = 9.0 \times 10^{10} \text{ Pa}$$

$$E_m = 1.7 \times 10^{11} \text{ Pa}$$

where the subscripts c and m refer to crust and mantle respectively. The densities are chosen so that, for the model dimensions shown, the margin is in isostatic equilibrium, i.e. the lithostatic pressure at 35 km depth, the base of the continental crust, would be the same on either side of the margin. This gives

$$\rho_c = 2922 \text{ kg m}^{-3}$$

if $\quad \rho_m = 3300 \text{ kg m}^{-3}$.

Fig. 4.17 shows the result of an elastic analysis of the model with stripped densities (see Fig. 4.16) of

$$\rho_1 = 1892 \text{ kg m}^{-3}$$

$$\rho_3 = -378 \text{ kg m}^{-3}$$

$$\rho_2 = \rho_4 = 0 \quad ,$$

(the density of sea water, $\rho_w = 1030 \text{ kg m}^{-3}$, having been subtracted from ρ_1), and with both ends fixed in the x-direction. This model corresponds to that used by Bott and Dean (1972) and gives similar results both qualitatively and quantitatively, any difference being due to the different crustal densities used. The resulting stress distribution is the elastic response to the variation in density load across the continental margin.

An alternative elastic solution is shown in Fig. 4.18, with only the right (continental) end of the model held, which gives a better approximation to the boundary conditions on the oceanic side of the margin, transmitted through the lithosphere from a spreading centre. This boundary condition releases the restriction on the horizontal
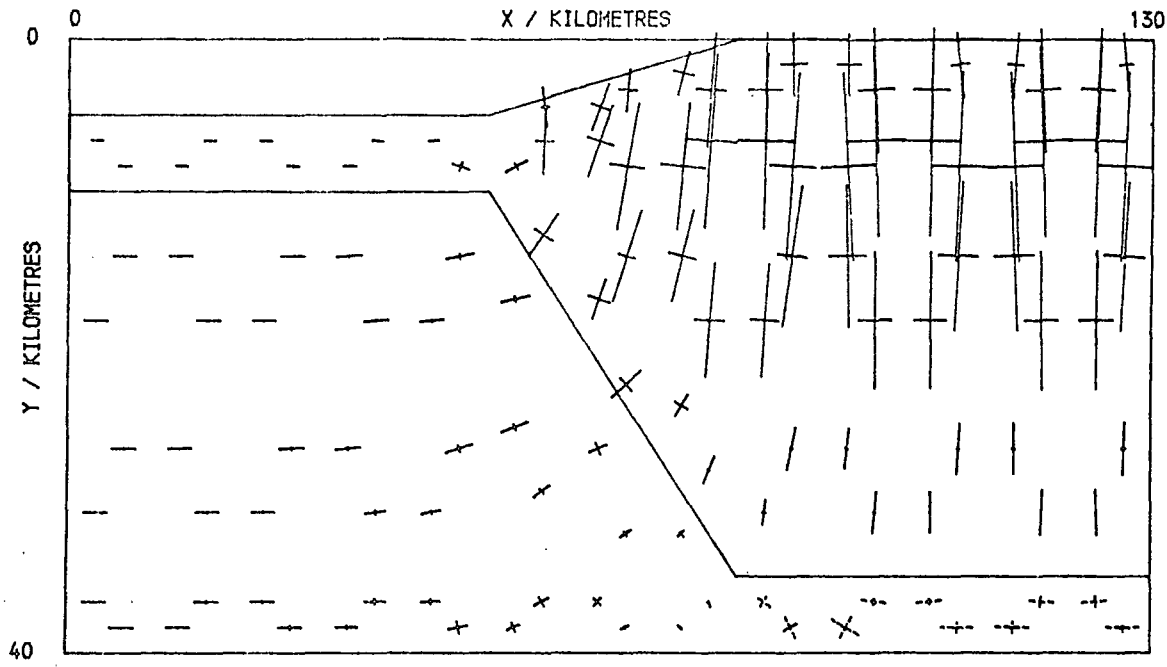
Fig. 4.17: The elastic principal stresses in the passive margin model
(Fig. 4.15), with stripped densities and both ends held horizon-
tally.
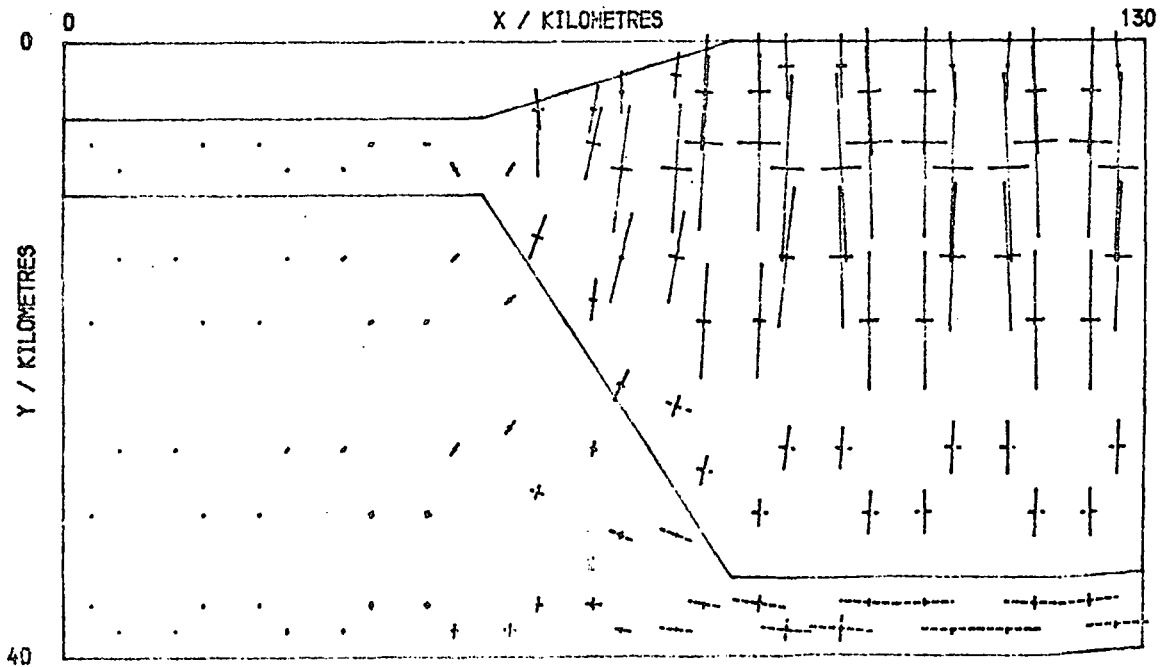
Fig. 4.18: As above, but with the left-hand (oceanic) boundary free to move.

stresses which forced them to be approximately $\nu/(1 - \nu)$ times the vertical stresses, according to Section 4.2.1 (although there were some horizontal displacements in Fig. 4.17 so that the rule was not obeyed exactly, particularly beneath the oceanic crust). Thus in Fig. 4.18 all the horizontal stresses are more tensional, but the stress pattern is not significantly altered otherwise.

The greatest values of the maximum shear stress, shown plotted against depth in Fig. 4.19,

$$\tau_m = \frac{(\sigma_1 - \sigma_3)}{2} \qquad\qquad 4.10$$

(see Chapter 2, Section 2.3), which occur at a depth of about 10 km in each case, are

τ_m = 34 MPa in Fig. 4.17 (both ends fixed)

τ_m = 38 MPa in Fig. 4.18 (oceanic end free)

and τ_m = 37 MPa in fig. 2 of Bott and Dean's paper.

In all these models it was assumed that the stress patterns are to be superimposed on a lithostatic stress distribution, which, although not a solution to the elastic stress equations as discussed earlier (Section 4.2.2), may be assumed to be the standard state in the oceanic lithosphere.

However, these models make several approximations. They do not account for any change in the stresses due to contrasts in elastic properties (other than density) between oceanic mantle and lower continental crust, and secondly, they make the implicit assumption that the load due to the density differences between oceanic and continental lithosphere is applied instantaneously to the standard state. Neither of these approximations can be avoided in an elastic model because alterations to the standard state due to variations in material properties
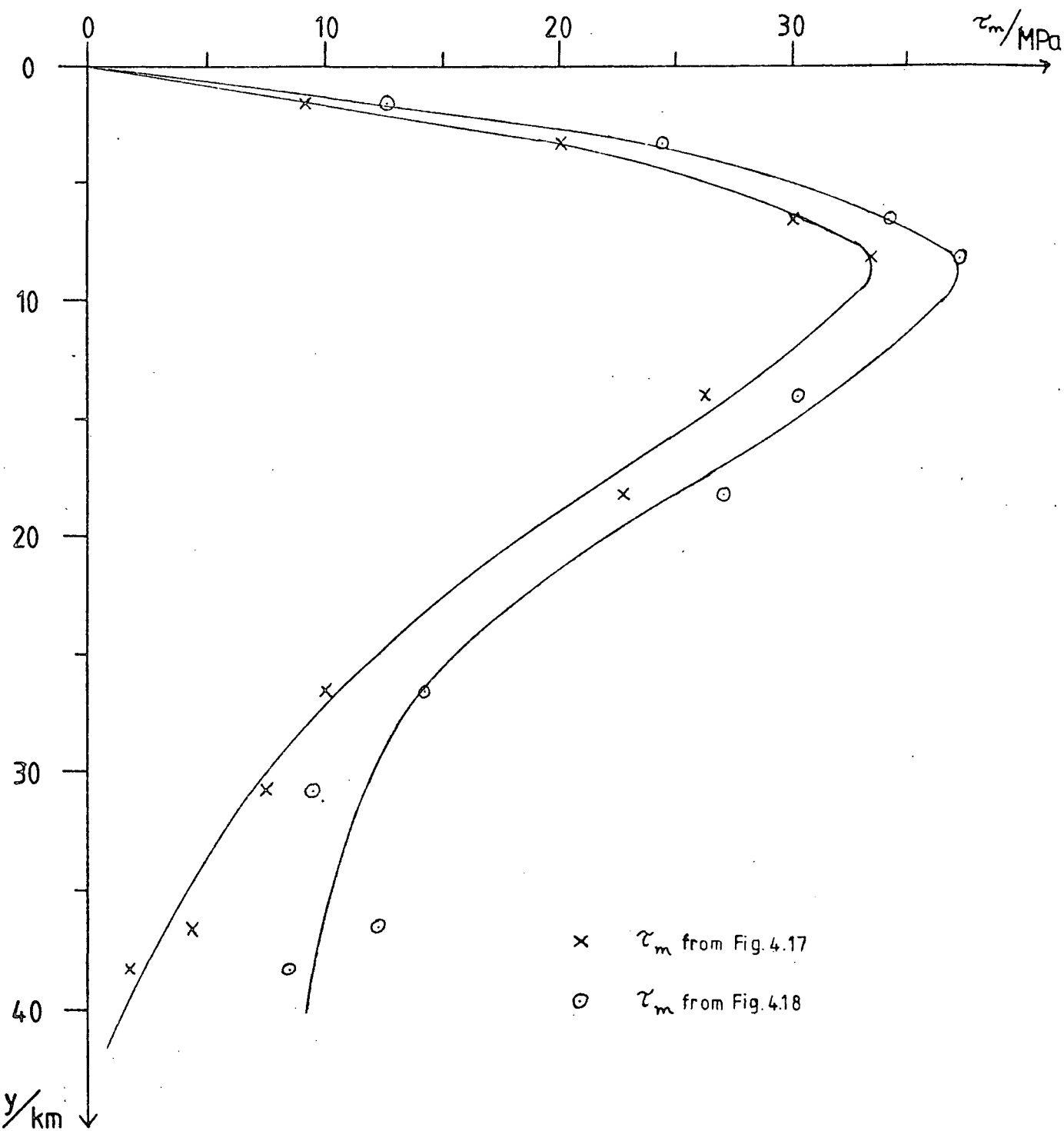
Fig. 4.19: Graphs of maximum shear stress, τ_m, vs. depth, y, for the stress distributions of Figs. 4.17 and 4.18.

and persistence of load cannot be calculated elastically.

A third approximation made in the models of Figs. 4.17 and 4.18 is the treatment of the water as a load to be removed by subtracting ρ_w from the density of the upper part of the continental crust. However, if water can penetrate into the pore spaces in the crust, it does not act as a load, but merely reduces the effective stresses within the rock (Hubbert and Rubey, 1959). The maximum shear stress, τ_m, is unchanged by this since both σ_1 and σ_3 are reduced by the pore pressure, p, in Equation 4.10, but the mean stress

$$\sigma_m = \left(\frac{\sigma_1 + \sigma_3}{2}\right) \qquad 4.11$$

is replaced by $(\sigma_m + p)$, so that brittle failure is more likely (see Chapter 2, Section 2.3). Rubey and Hubbert (1959) report significant pore pressures down to several kilometres depth in continental crust, often exceeding that due to the head of water, while Drury (1979) estimates that porosity drops to 1% or less at 2 km depth in a 7 km - thick oceanic crust. On the basis of these figures, and making broad simplifications because of the model used (Fig. 4.15), the pressure due to the column of water at the centroid is subtracted from the stresses in each element of the upper continental crust only (the region marked ρ_1 in Fig. 4.16).

4.5.2 Visco-elastic models

Taking all the factors discussed in Section 4.5.1 into consideration, the visco-elastic method described in Section 4.4 was applied to the model, and Fig. 4.20 shows the stresses after 10 Myr of visco-elastic relaxation, the whole crust having a viscosity of

$$\eta_c = 10^{25} \text{ N s m}^{-2}$$
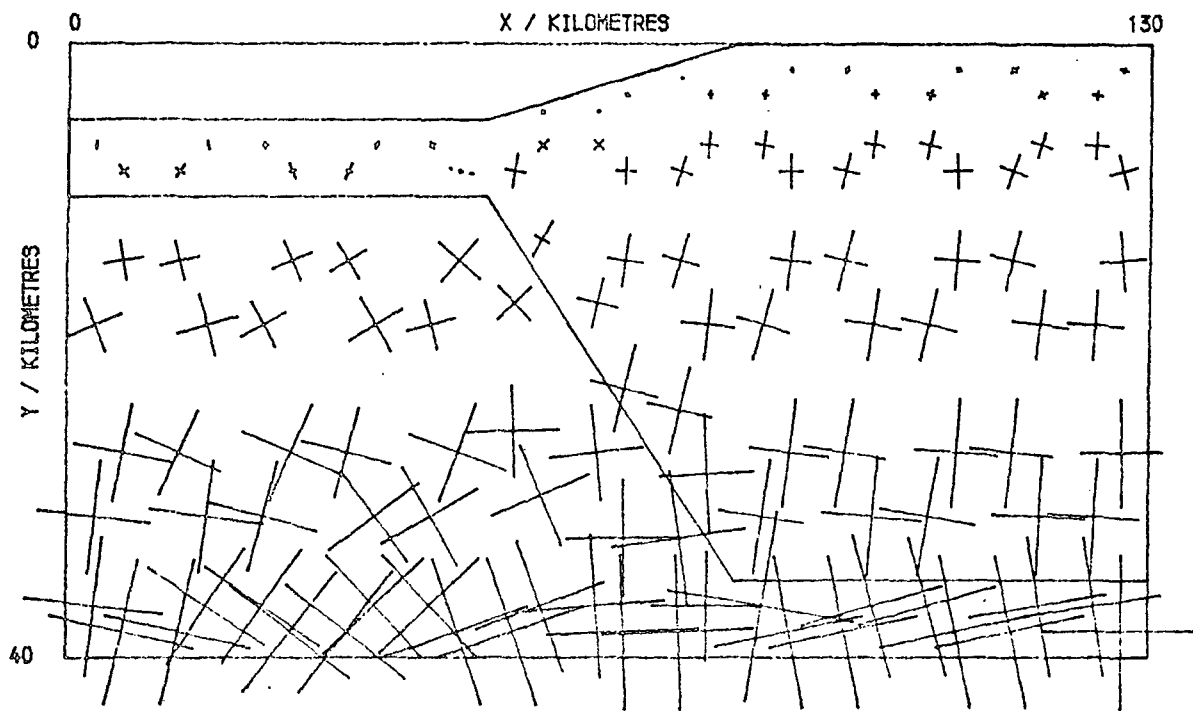
Fig. 4.20: The principal stresses in the passive margin model after 10 Myr
of visco-elastic relaxation, with both ends fixed horizontally.
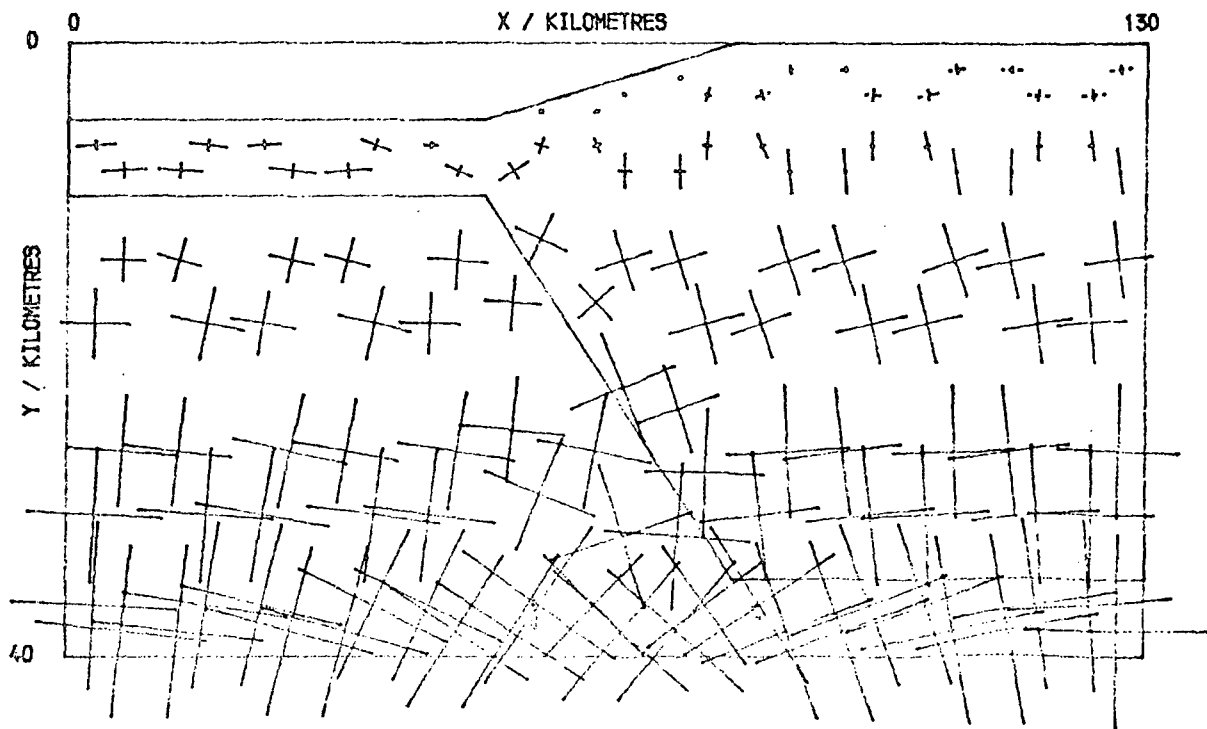
Fig. 4.21: The principal stresses in the passive margin model after 10 Myr
with a reduced viscosity in the lower crust ($\eta_{lc} = 10^{24}$ N s m^{-2})
and both ends fixed horizontally.

and the mantle of

$$\eta_m = 10^{23} \text{ N s m}^{-2}$$

(see Ch. 2, Section 2.2), with both ends of the model fixed in the x-direction.

As in Section 4.4.3, all the stresses in the mantle have relaxed to a hydrostatic state, leaving residual deviatoric stresses in the crust. These stresses are, as before, in the form of horizontal deviatoric tensions, but instead of rising to a maximum at about 10 km and then approaching zero with depth, the maximum shear increases from about 10 MPa near the surface to 100 MPa (1 kbar) at the base of the continental crust. In addition there is a concentration of stress reaching $\tau_m \simeq 100$ MPa in the oceanic crust at the base of the continental slope where tensional failure is predicted by the finite element program, according to the criteria of Ch. 2, Section 2.3.

This stress system is at variance with the features usually observed at passive margins, and one important reason for this is the uniform crustal viscosity chosen. Bott (1971b) proposed that creep should occur in the lower crust, resulting in strain rates of the order of 10^{-16} s^{-1} in response to stresses of about 50 MPa, which implies an effective viscosity for the lower crust of

$$\eta_{lc} = 10^{24} \text{ N s m}^{-2}.$$

Using this value for the viscosity of the crust below 10 km depth (i.e. the region marked ρ_3 in Fig. 4.16), and leaving the viscosity of the upper crust at

$$\eta_{uc} = 10^{25} \text{ N s m}^{-2},$$

the stress system shown in Fig. 4.21 was obtained, again after 10 Myr relaxation with both ends fixed in the x-direction. The result of the viscosity contrast has been to concentrate the deviatoric stresses in

the upper, higher viscosity crust, an effect described by Kusznir and Bott (1977). The maximum shear in the continent rises, more rapidly than in Fig. 4.20, to 130 MPa at the base of the upper crust and then drops abruptly to about 50 MPa in the lower crust. High angle tensile failure is predicted in the upper continental crust in agreement with Bott (1971b).

However, this model does not yet correspond with observation in that there are large horizontal deviatoric compressions in the oceanic crust, giving a maximum shear of up to 100 MPa. These compressions are reduced, by a factor of 10, by altering the boundary conditions on the oceanic lithosphere, and Fig. 4.22 shows the stress distribution obtained by applying lithostatic stresses, rather than fixed displacements, to the left end of the model.

The final model gives a qualitatively similar deviatoric stress distribution to the elastic models (Bott and Dean, 1972; and Figs. 4.17 and 4.18), in that the only significant deviatoric stresses are in the continental crust, and are horizontal tensions. In addition they increase with depth in the upper crust, down to about 10 km, and then decrease with depth to the base. The depth distribution of maximum shear has, however, a different shape (compare Figs. 4.19 and 4.23) and the greatest value in the visco-elastic model is about 170 MPa, about 5 times as large as in the elastic models.

Artyushkov (1973) has calculated the effect of changes in thickness of a viscous layer supported by an inviscid substratum. In this case he shows that, if the layer remains in isostatic equilibrium, then the change in the average horizontal stress due to an increase in height ζ of the top layer, density ρ, is

$$\Delta\sigma = \rho\,g\,\zeta \tag{4.12}$$

PASSIVE (6HL) @ 10 MYR.

MAXIMUM STRESS = 11.717 KBAR.

STRESS VECTORS

(BROKEN LINES TENSIONAL)

0   X / KILOMETRES   130
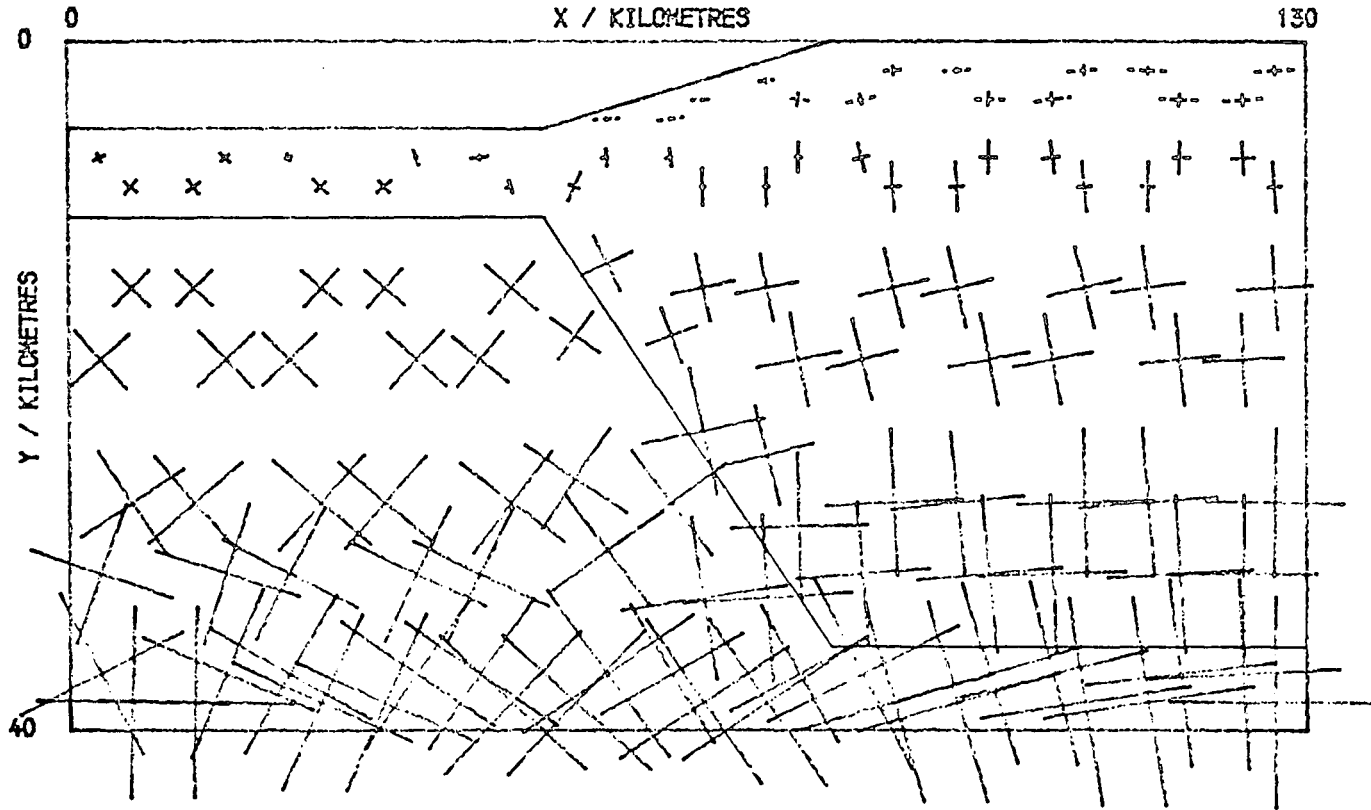
Fig. 4.22: The principal stresses in the passive margin model with
$n_{lc} < n_{uc}$, after 10 Myr (Fig. 4.21), but with lithostatic
stresses applied to the left-hand side.
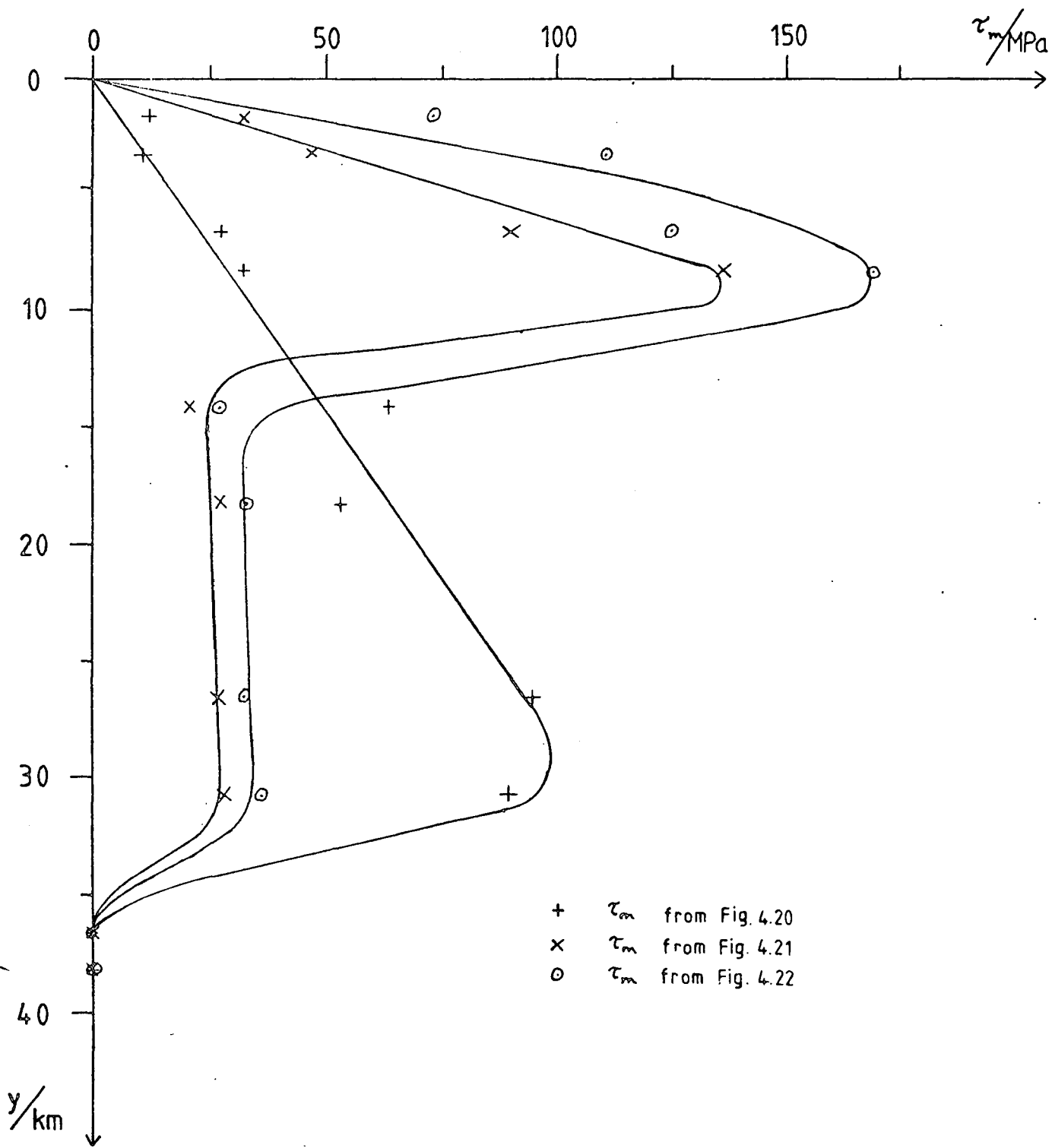
Fig. 4.23: Graphs of maximum shear stress, τ_m, vs. depth, y, for the stress distributions of Figs. 4.20, 4.21, and 4.22.

Substituting in the values for the passive margin model (Fig. 4.16) an average maximum shear stress is obtained,

$$\bar{\tau}_m = \tfrac{1}{2} \Delta\sigma = 72 \text{ MPa}.$$

The mean value calculated from the graph of τ_m against depth for the final model (Fig. 4.23) is

$$\bar{\tau}_m \simeq 60 \text{ MPa}.$$

The visco-elastic finite element model therefore produces a similar result to Artyushkov's analytical solution.

It must be noted, however, that two of the assumptions on which Equation 4.12 is based, do not hold for this model. Firstly the change in thickness of the crust across the margin is comparable with its average thickness, and secondly the upper mantle has a finite viscosity. The former of these tends to reduce $\Delta\sigma$, by a factor of about 60% (if the model crustal thicknesses are used in Artyushkov's equations), while the latter, by introducing significant coupling between the crust and mantle (even though $n_{1c} = 10 \ n_m$), increases it. Nevertheless the agreement between the values of $\bar{\tau}_m$, even if only to within a factor of 2, is significant because the two methods are completely independent.

One further interesting feature of the stress distribution in Fig. 4.22 is the persistence of the horizontal deviatoric tension into the continental crust, an effect also discussed by Bott and Dean (1972). A version of the final visco-elastic model extending a further 110 km into the continent showed that the tensions only decreased by a few percent (less than 5%) 160 km from the margin, again in agreement with Artyushkov (1973).

The stress system of Fig. 4.22 will be considerably modified in reality by faulting, which will relax some of the deviatoric tensions, especially near the margin; by any stresses applied to the whole

lithospheric plate, for instance due to density contrasts at mid-ocean ridges; and by any other tectonic influences, particularly from outside the plane of the model.

CHAPTER 5

THE BALANCE BETWEEN WEIGHT AND BASAL SHEAR IN AN ACCRETIONARY PRISM

5.1 Introduction

If a wedge of sediments with a sloping top, such as an accretionary prism, were to exist without any shear along its base, then it would spread under its own weight, assuming that its rheology had some viscous or other time-dependent component, until its surface was horizontal. The only conditions that could allow such a structure to be stable are, either that it should have a perfectly elastic rheology, with a great enough strength to support the deviatoric stresses set up by the asymmetric density distribution in the wedge, or that it should be supported by stresses applied to its boundaries.[1]

In this chapter it will be assumed that the accretionary prism in a subduction zone is supported by a shearing stress imparted to its base by the oceanic plate being subducted.

Two mechanisms are considered for the transmission of this basal stress; firstly through a weak shear zone between the overlying sediment pile and the underlying oceanic crust, and secondly by a direct frictional contact between them. The chief difference between these two types of contact, apart from their structural implications, is that in the first the shear stress is uniform along the whole base, while in the second it increases with depth, due to the dependence of the shear on the normal stress across the shear plane.

The geological consequences of these two mechanisms will be discussed and the stress needed to support the wedge found in both cases, and additionally the effect on the deformation of varying some

[1] If the material had a plastic rheology, a surface gradient could be supported, if the necessary deviatoric stresses were below the yield stress.

of the other model parameters will be examined, in particular the gradients of the upper and lower surfaces of the wedge.

5.2 Description of the Model

5.2.1 Shape and properties

The model used for the investigations in this chapter is based on the seismic reflection line across the Middle American Trench shown in Fig. 1.3 (Moore et al., 1979b), and consists of the material beneath the inner trench slope, for 20 km from the trench axis, approximating both the top surface and the base by straight lines. The resulting model, divided into elements, is shown in Fig. 5.1.

Tha parameters used for the model, using the guidelines given in Chapter 2, are listed in Table 5.1.

Property	Symbol	Value
Young's Modulus	E	10 GPa
Poisson's Ratio	ν	0.27
Density	ρ	2500 kg m^{-3}
Viscosity	η	10^{22} N s m^{-2}

Table 5.1: Material properties used in the wedge model.

These values are taken to be constant throughout the wedge, in order to separate the observed effects from those due to contrasts in material properties, which will be considered in Chapter 6.

A further implicit assumption is that the parameters are isotropic.
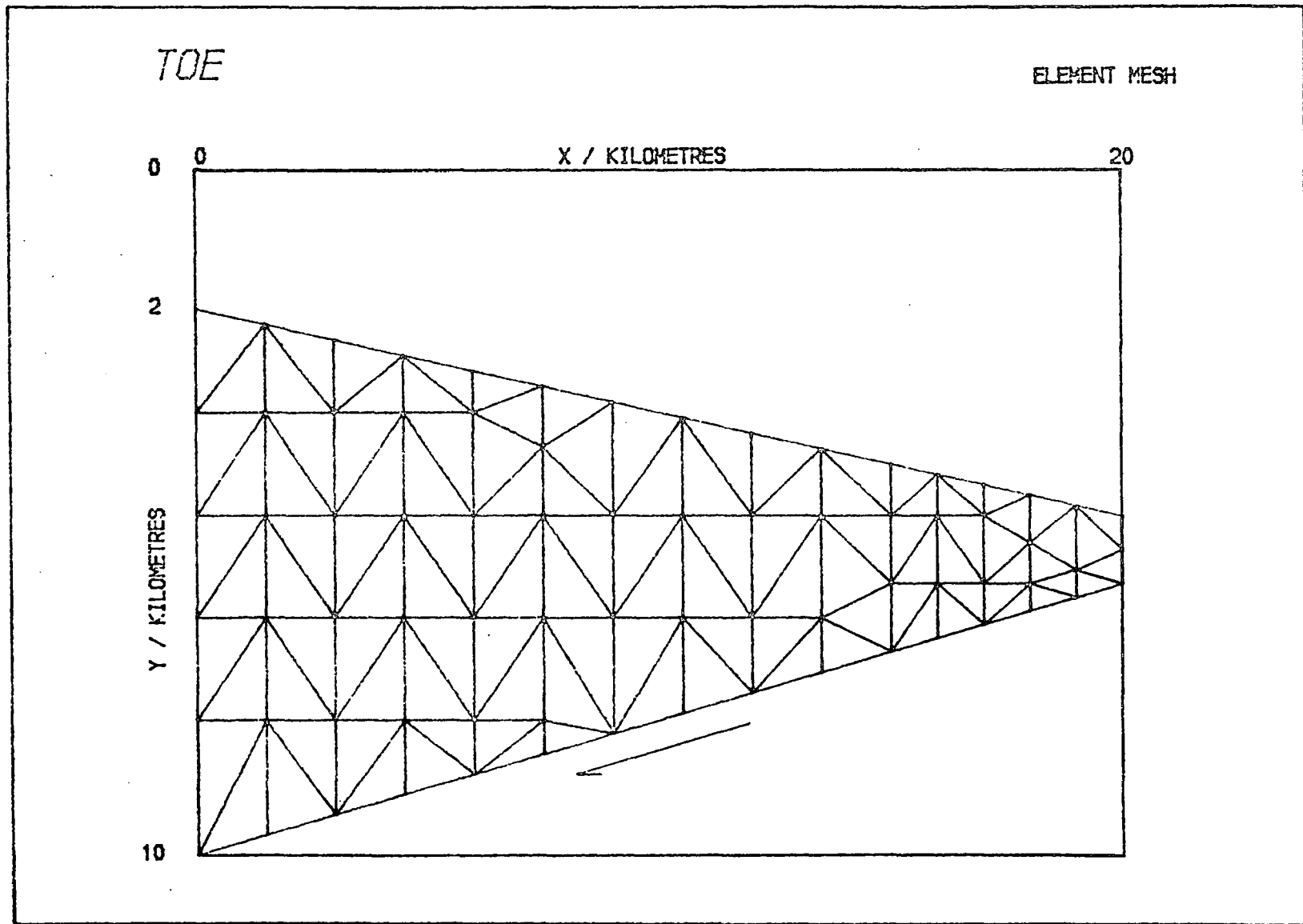
Fig. 5.1: Finite element grid for the first model of an accretionary wedge.

If there is a series of imbricate thrust faults in the accretionary
prism, as discussed in Chapter 1, then there will definitely be some
anisotropy, particularly in Young's modulus and viscosity. Once thrust
faults have been formed it is easier to deform the material parallel,
rather than perpendicular, to the faults, both through creep along the
faults and elastically. A more sophisticated model might attempt to
evaluate the effect of a set of such thrusts, but, although finite
elements have been used to model faults (Goodman et al., 1968; Bischke,
1974; Goodman, 1976), little is known of the properties and distribution
of such faults in an accretionary prism, and it is considered that
such investigations are beyond the scope of this thesis.

5.2.2 Boundary conditions

The boundary conditions on the four faces of the model (Fig. 5.1)
are as follows:

a) the left-hand (landward) end of the wedge is held fixed in the
    x-direction, but allowed to move in y (see Ch. 3, Section 3.5.2);

b) the base is fixed similarly, but in a rotated co-ordinate
    system, so that it cannot move perpendicular to the boundary,
    but is allowed to move parallel to its slope, so that a basal
    shear (described further in the following sections of this
    chapter) may be applied;

c) the right-hand end is bounded by trench sediments, and litho-
    static stresses due to these, taking a density of 1700 kg m^{-3}
    (see Ch. 2, Section 2.1.3) is applied using the method of
    Ch. 3, Section 3.5.1, the underlying assumption here being that
    the trench sediments are unconsolidated and may be regarded as
    fluid in this respect;

d) the upper surface is left free, since the water does not exert a force on the surface (as discussed in Ch. 4, Section 4.4.1), if it is assumed that there are sufficient pores in the wedge to allow the water to permeate through it.

5.3 Uniform Basal Shear

5.3.1 Description of the boundary conditions

It has been suggested (e.g. Seely, 1977) that an accretionary wedge may be underlain by a basal shear zone of pelagic and hemi-pelagic sediments that have been carried down by the oceanic plate. These sediments have a high water content, and if the pore pressure were increased, on subduction, to a value close to the mean stress, they would become so weak as to behave like a low-viscosity fluid (this situation corresponds to an effective mean stress $(\sigma_m)_{eff} \approx 0$, in Fig. 2.5 of Ch. 2, combined with a small value of T, the tensile strength).

If this is the case, then stresses are transmitted from the plate being subducted to the overriding accretionary prism through flow in a viscous boundary layer. If the thickness and viscosity of the shear zone are d and $n_{s.z.}$, respectively, and the velocity down-dip of the subducted oceanic crust is v, with respect to the accreted sediments, then the shear stress, τ, on the base of the wedge is given by:

$$\tau = \frac{v}{d} \cdot n_{s.z.} \qquad\qquad 5.1$$

Equation 5.1 is independent of depth, so that the shear stress applied to the accretionary prism is constant along its base.

To fulfil this boundary condition, forces (calculated according

to Ch. 3, Section 3.5.1) are applied at the basal nodes, parallel to
the dip of the base, while all other boundary conditions are as
described above in Section 5.2.2.

5.3.2 Elastic models

The instantaneous deformation of the model under a combination of
its weight and basal shear stress is illustrated by Figs. 5.2 and 5.3,
where the surface deformation is shown both with and without exaggeration.

If the basal stress is small, then the weight of the model causes
the thick end of the wedge to subside more than the thin end. This
subsidence, being transmitted horizontally due to the Poisson's ratio
of the material, tends to push up the front of the wedge, but the effect
is offset by the pressure of the trench sediments and gravitational
sliding down the basal slope.

In all elastic models with basal stresses between 0 and 100 MPa
the surface remains approximately a straight line, but it is rotated
according to the stress applied between the angles shown in Fig. 5.2
(with no shear giving a rotation of c. 0.1° anti-clockwise) and
Fig. 5.3 (with 100 MPa shear, giving a rotation of c. 0.4° clockwise),
the whole variation only being c. 0.5°.

The deformed surface is parallel to the original for a basal
shear between 10 MPa (Fig. 5.4) and 20 MPa (Fig. 5.5), and so the
stress to support the wedge is in this interval, but it can be
narrowed down further using a visco-elastic method (see next section).

The effect of a basal shear of 10 MPa on the principal stresses
is illustrated in Figs. 5.6 and 5.7. When no basal shear is applied
(Fig. 5.6), the stresses in the deeper parts of the model are aligned
so that the minimum principal stress (i.e. the greatest compression) is
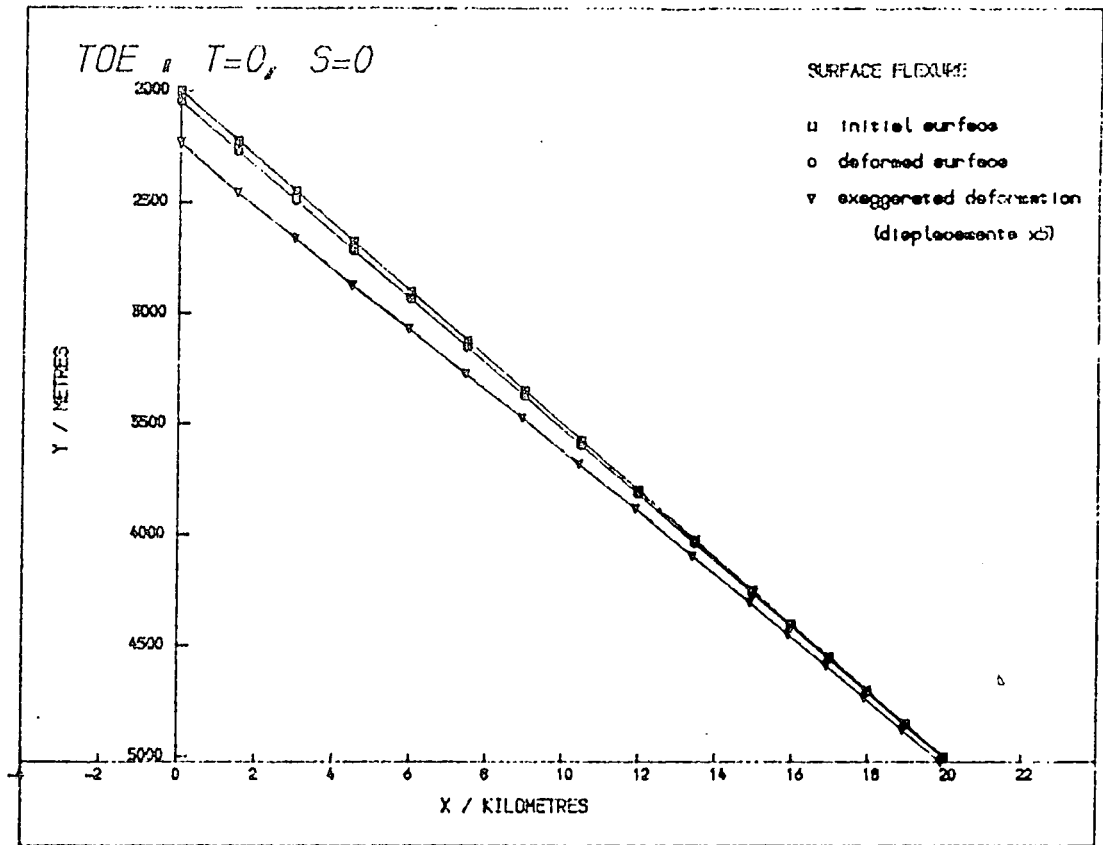
Fig. 5.2: Deformation of the wedge surface as an elastic response to weight
alone. Squares show nodal points on the original surface, circles
their deformed positions, and triangles the same exaggerated by
multiplying all displacements by a factor of 5.
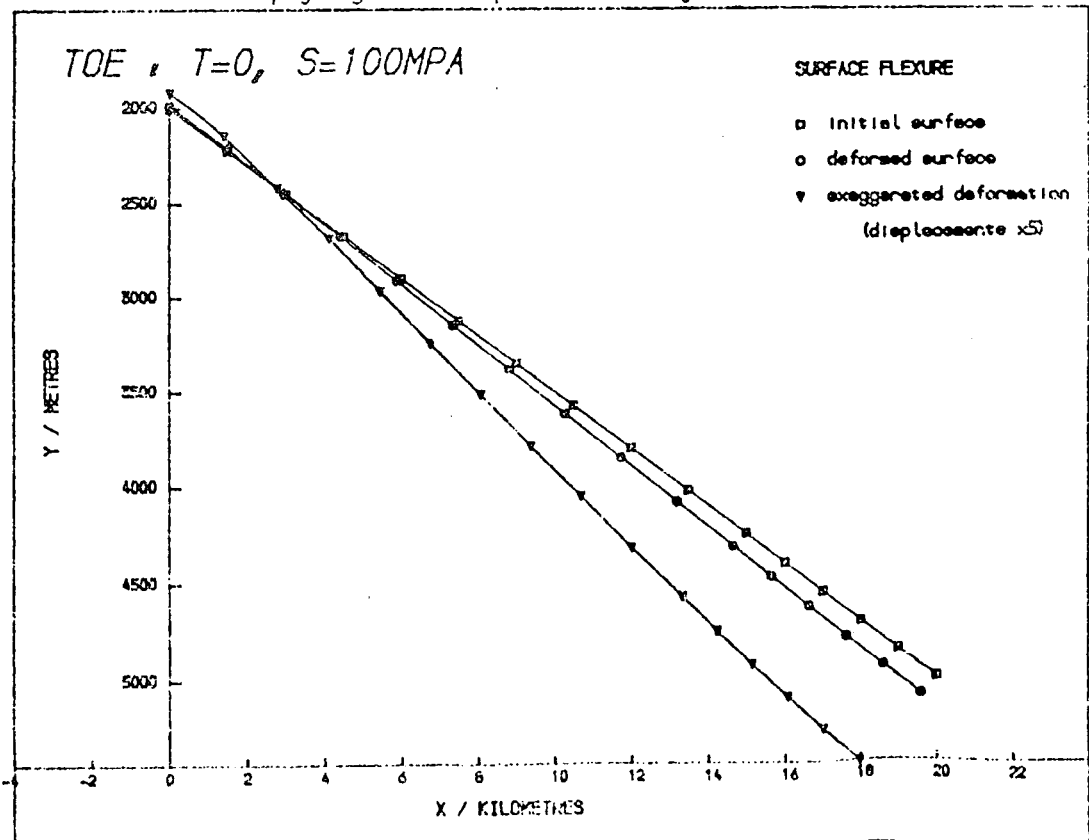
Fig. 5.3: Elastic deformation of the wedge surface in response to weight
and a basal shear of 100 MPa.
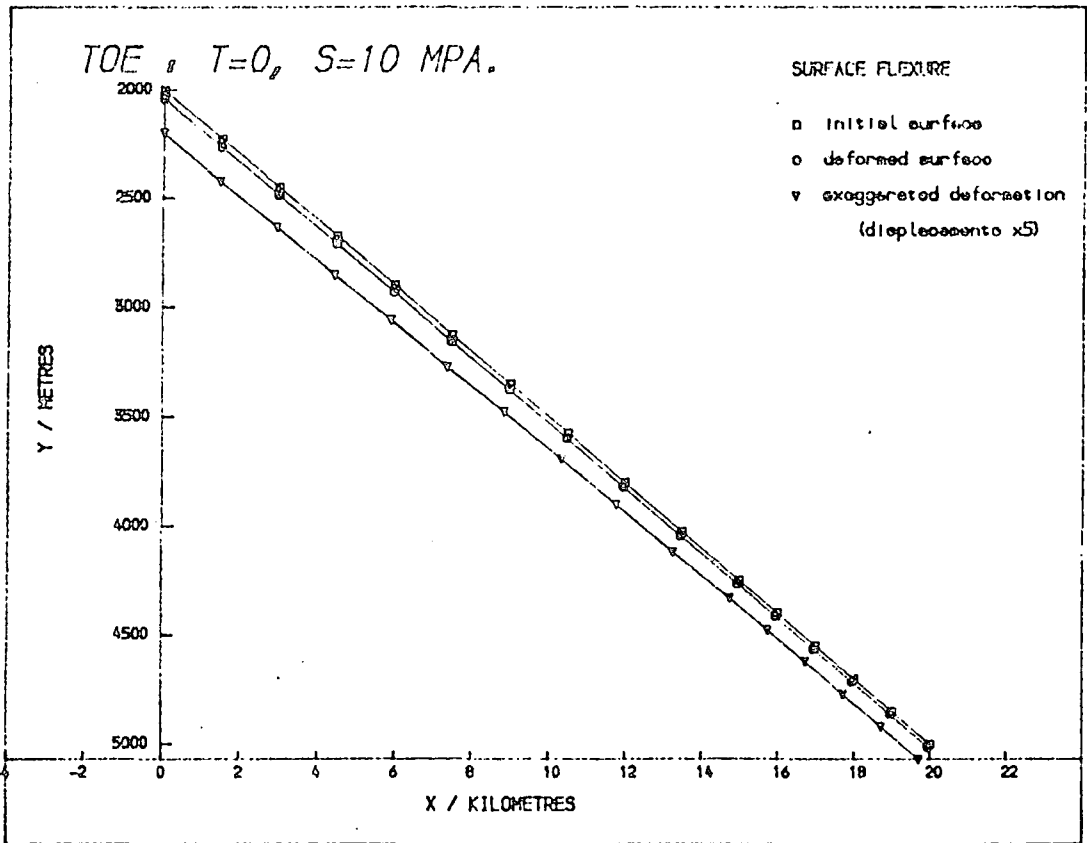
Fig. 5.4: Elastic deformation of the wedge surface in response to a basal shear of 10 MPa.
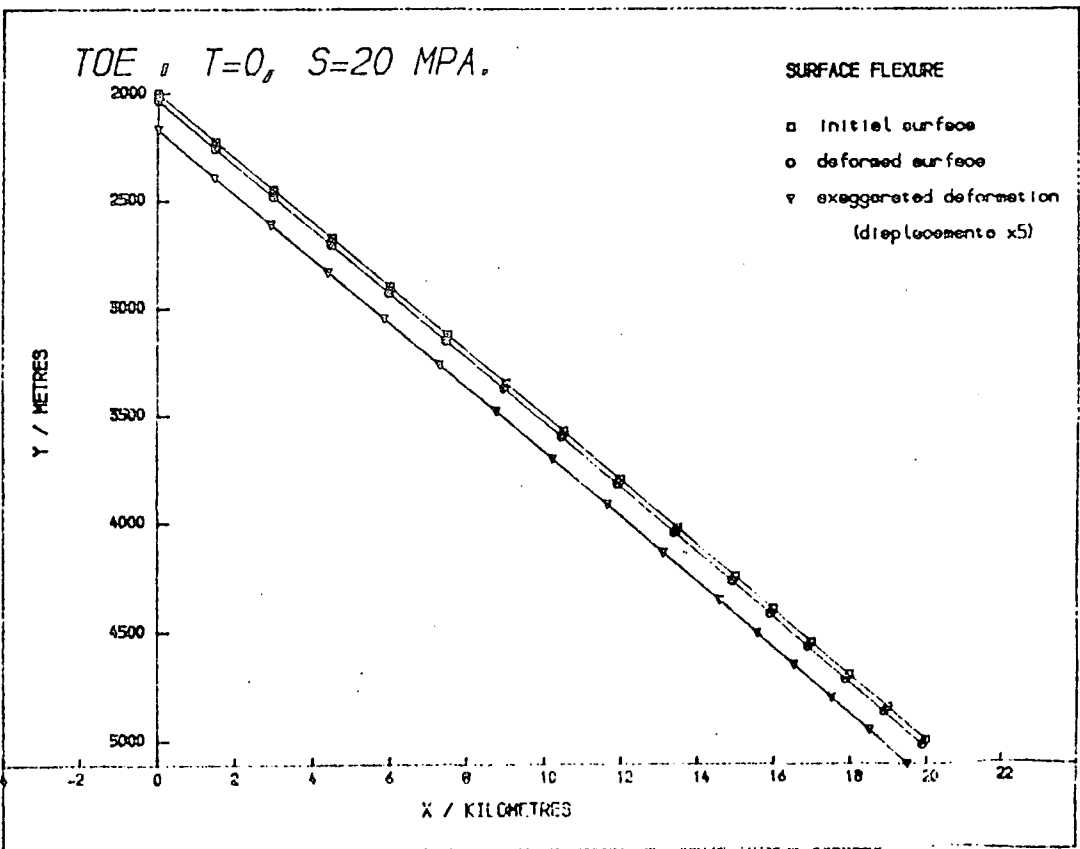
Fig. 5.5: As above, for a basal shear of 20 MPa.

TOE : T=0, S=0

MAXIMUM STRESS = 150.7 MPA.

STRESS VECTORS
(BROKEN LINES TENSIONAL)

X / KILOMETRES

100 MPA
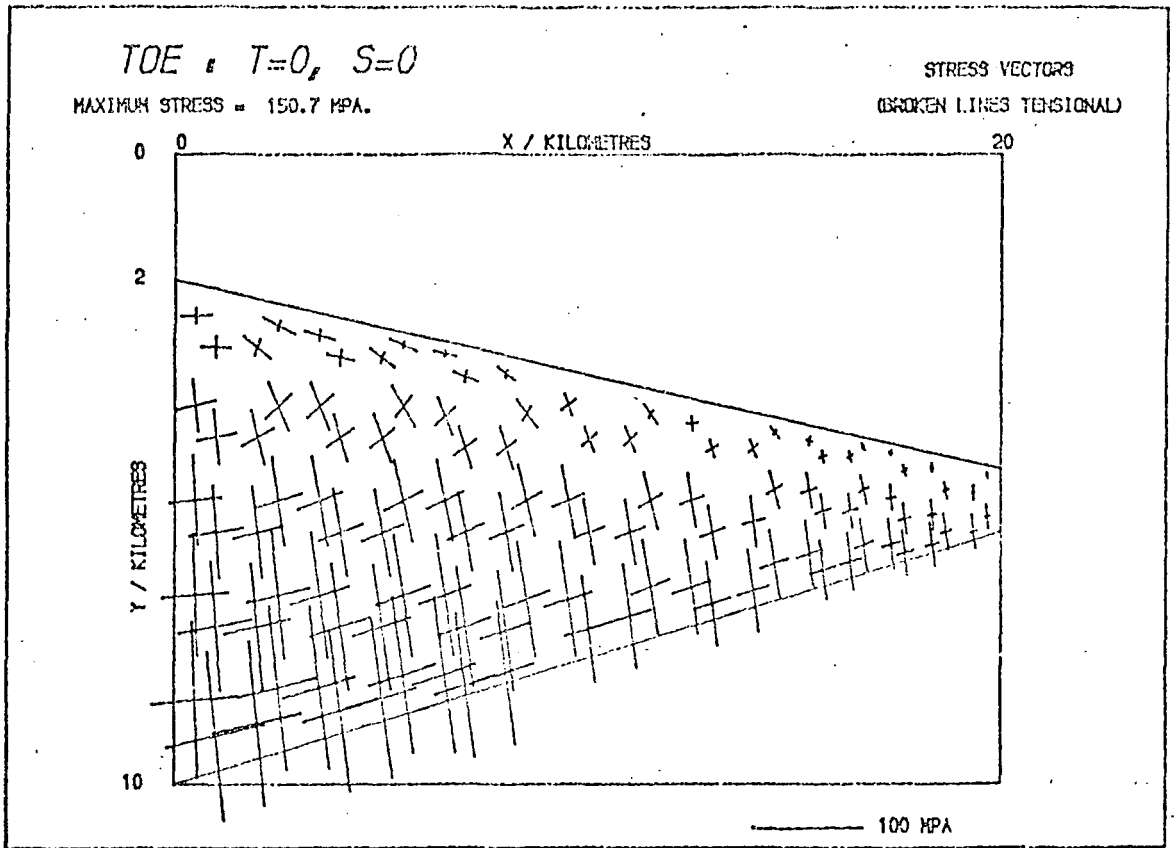
Fig. 5.6: Elastic principal stresses in the wedge in response to weight alone. The stresses do not appear to be at right-angles due to vertical exaggeration, but their magnitudes are scaled equally in all directions (see text).

TOE : T=0, S=10MPA

MAXIMUM STRESS = 153.6 MPA.

STRESS VECTORS
(BROKEN LINES TENSIONAL)

X / KILOMETRES

100 MPA
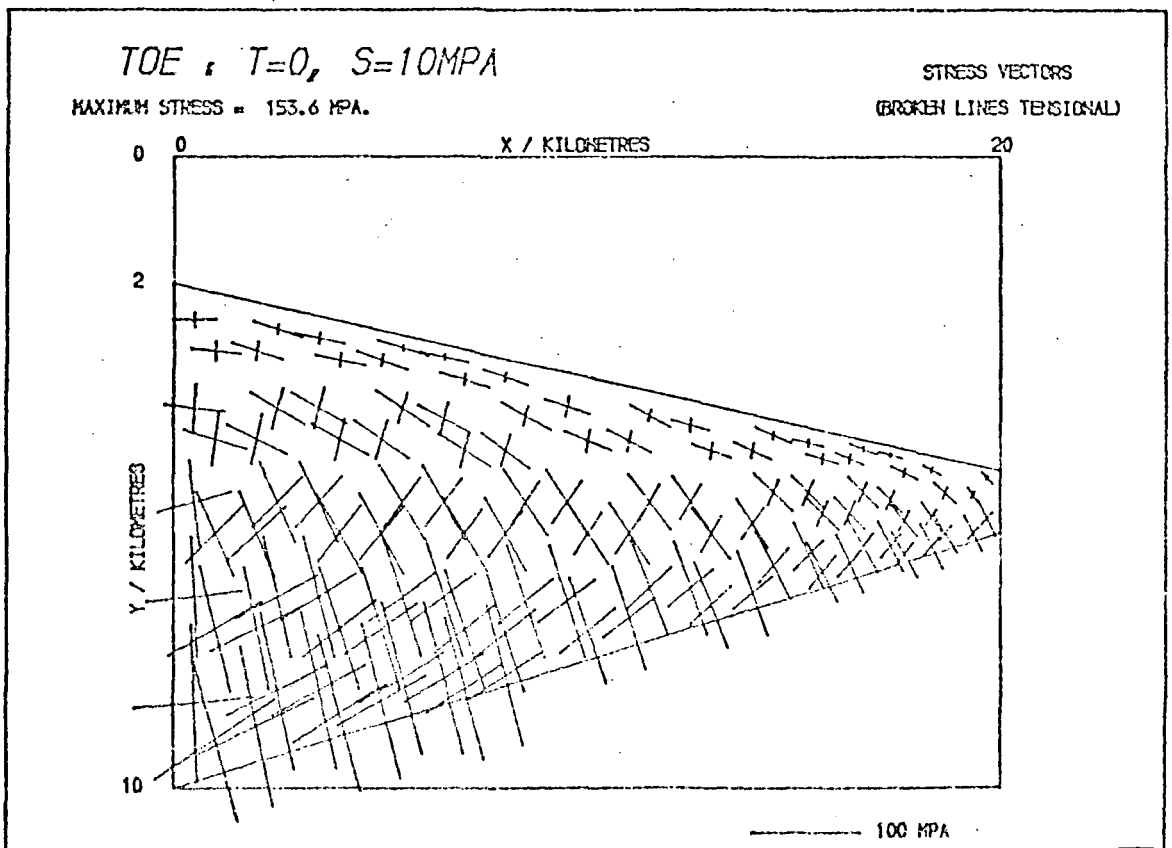
Fig. 5.7: Elastic principal stresses in the wedge in response to weight and a basal shear of 10 MPa.

perpendicular to the base and the maximum stress is parallel to it. Although the upper surface has moved down and to the left overall, there are deviatoric compressions in the upper part, roughly parallel to the slope, corresponding to a tendency to slump down-slope.

In Fig. 5.7, where there is a basal shear of 10 MPa, these compressions in the shallower parts are intensified, and the deeper stresses are rotated in response to the component of horizontal compression introduced by the boundary stress.

Note that in Figs. 5.6 and 5.7, as in all other stress vector diagrams from this chapter onwards, the stress vectors are plotted so that their angles may be compared directly with the (vertically exaggerated) model, which means that the principal stresses do not appear to be at right-angles. The magnitudes of the stresses are, however, scaled equally in all directions so that comparison between them is straightforward.

5.3.3 Visco-elastic models

The visco-elastic models in this chapter were all run starting from a model initialized elastically as described in Ch.4, Section 4.3.

. If the wedge is allowed to subside visco-elastically without any restraining stresses it behaves as might be expected, in that it flows in such a way as to flatten out the surface, subsiding at the landward end (by c. 200 m) and pushing forwards and up the slope at the oceanward end (by c. 400 m; see Fig. 5.8).

Conversely, if a shear stress of 20 MPa is applied to the base, then the landward end is pushed up (by c. 80 m) and the oceanward end is bent down (by c. 400 m; see Fig. 5.9).

This effect increases with the basal shear, and if a stress of
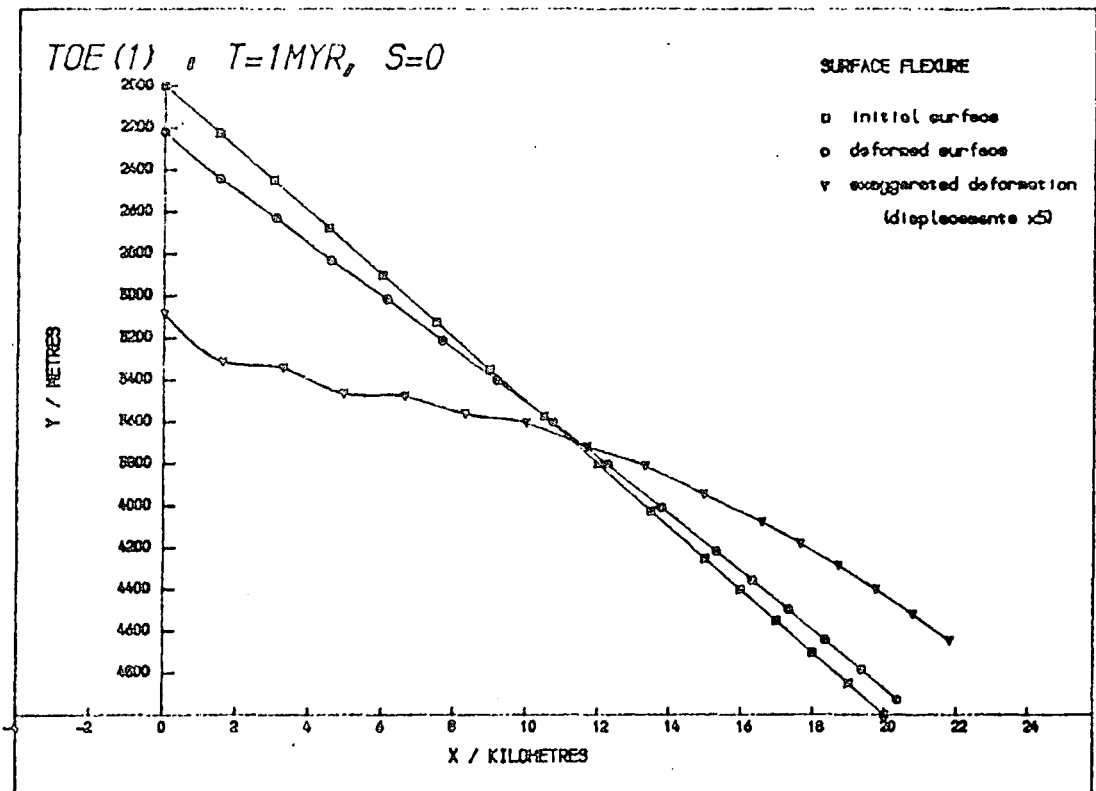
Fig. 5.8:   Surface displacements of the wedge after 1 Myr of visco-elastic
            deformation, with no basal shear stress applied.
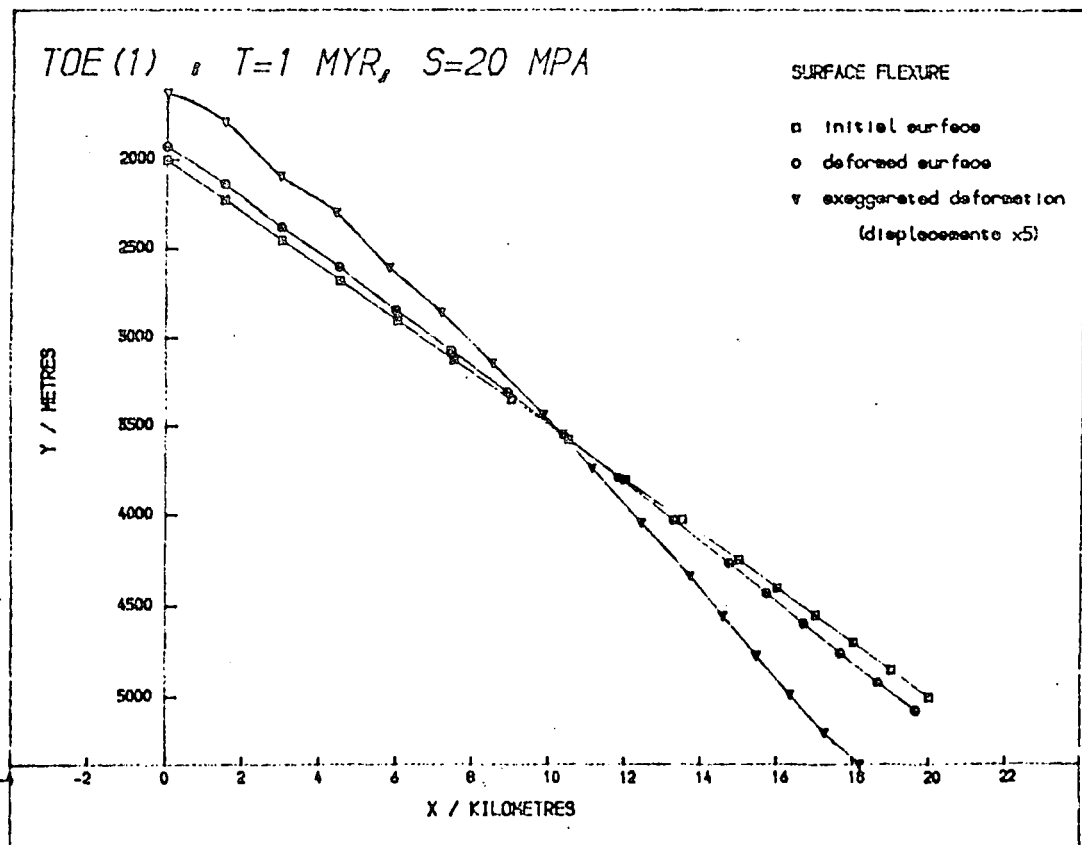
Fig. 5.9:   As above, but with a basal shear of 20 MPa.

100 MPa is applied, the uplift of the left-hand end is about 1 km, while the depression at the right-hand end is about 4 km.

Starting with the bounds found in the previous section (10 - 20 MPa), several visco-elastic models were run to find the shear stress needed to support the model's weight, two of which (for basal shears of 10 MPa and 15 MPa respectively) are shown in Figs. 5.10 and 5.11 to illustrate the sensitivity of the surface deformation to the applied shear. Clearly the value needed to keep the surface still is between these two, and using Figs. 5.12 and 5.13 it appears that 12 MPa is the best approximation (to 2 significant figures), although there are still displacements of about 50 m.

This balance is reflected in the principal stress system (see Figs. 5.14 and 5.15). After 1 Myr, if there is no basal stress, there are significant remaining deviatoric stresses throughout the model, varying approximately from 10 MPa to 25 MPa (Fig. 5.14), and in particular, there are deviatoric tensions of 10-15 MPa near, and approximately parallel, to the surface of the model due to the forward movement of the wedge.

In the model with a basal shear of 12 MPa (Fig. 5.15) these deviatoric stresses are almost entirely nullified in the left-hand part of the wedge and near the upper surface, and the stress system is very nearly hydrostatic. The deviatoric stress levels are between about 3 MPa and 8 MPa for the whole of the landward part (i.e. for $x < 15$ km) and are less than 5 MPa along the entire upper surface. However, along the base where the sole thrust becomes shallower ($x > 15$ km), the deviatoric stresses are increased relative to the model without basal shear, because the effect of weight in this region is smaller than that due to the applied shear, and here the maximum
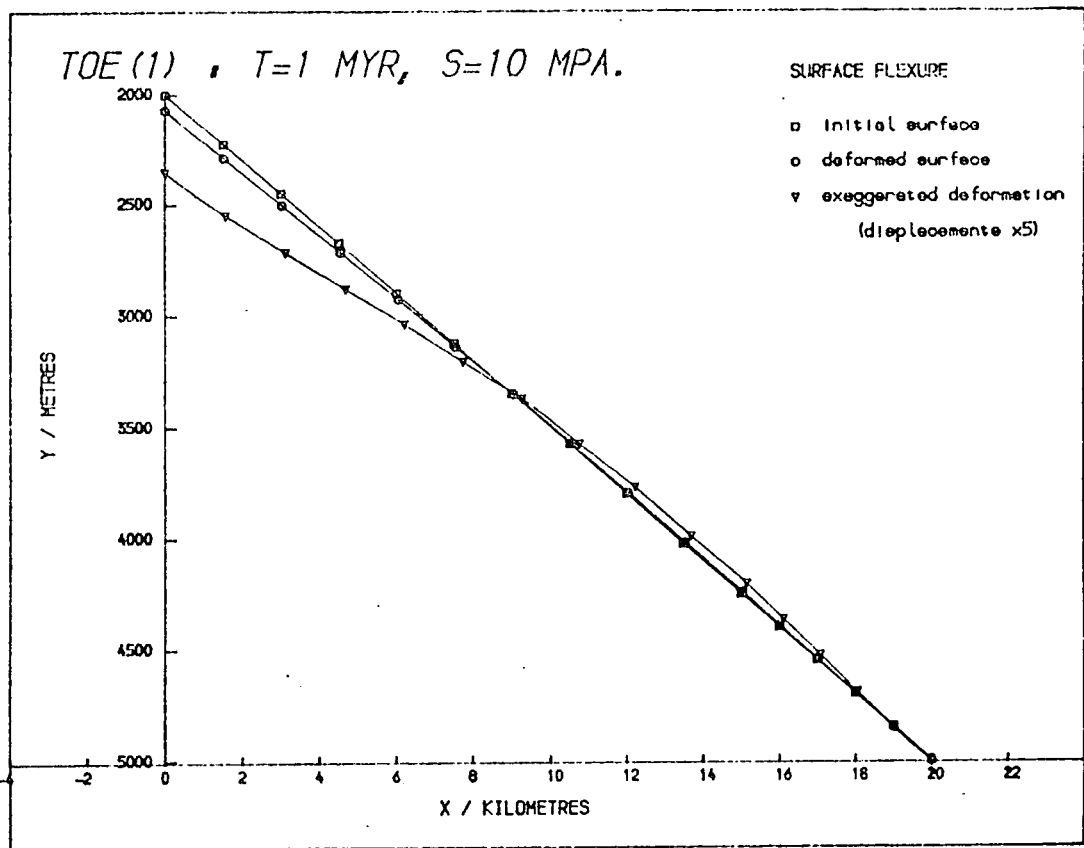
Fig. 5.10: Surface displacements of the wedge after 1 Myr, with a basal stress of 10 Mpa.
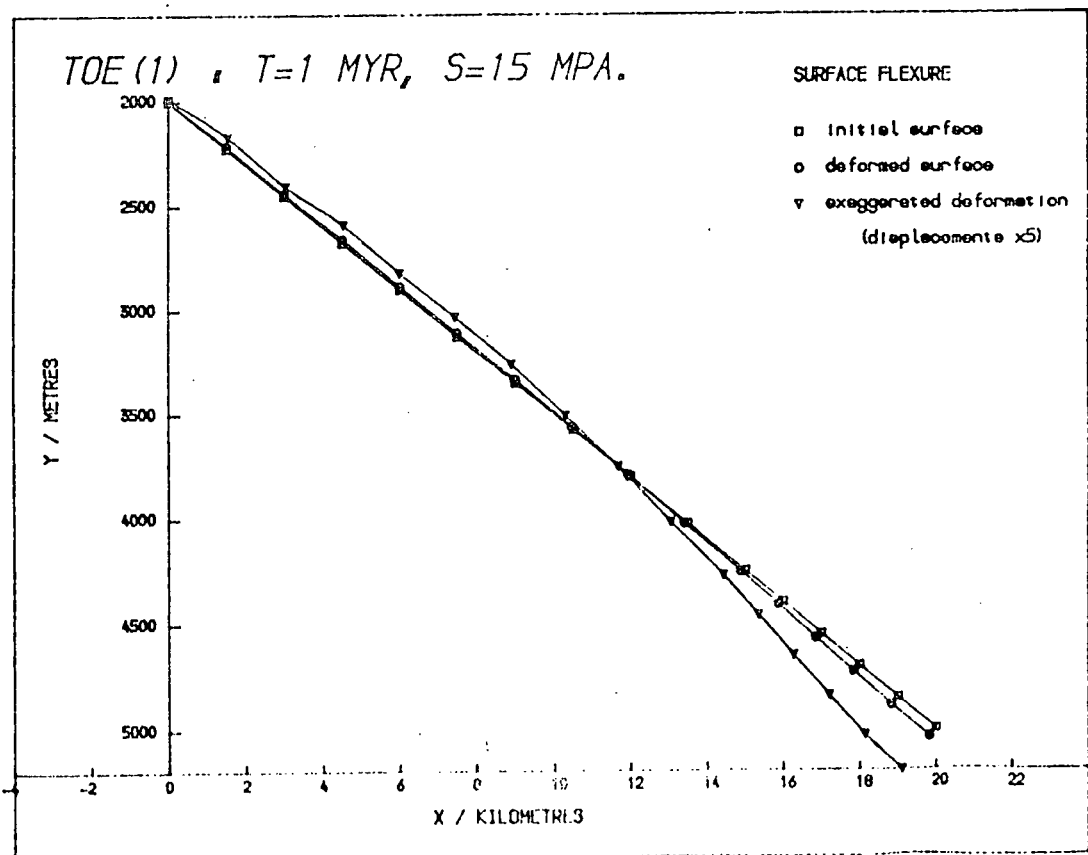
Fig. 5.11: As above, but with a basal shear stress of 15 MPa.
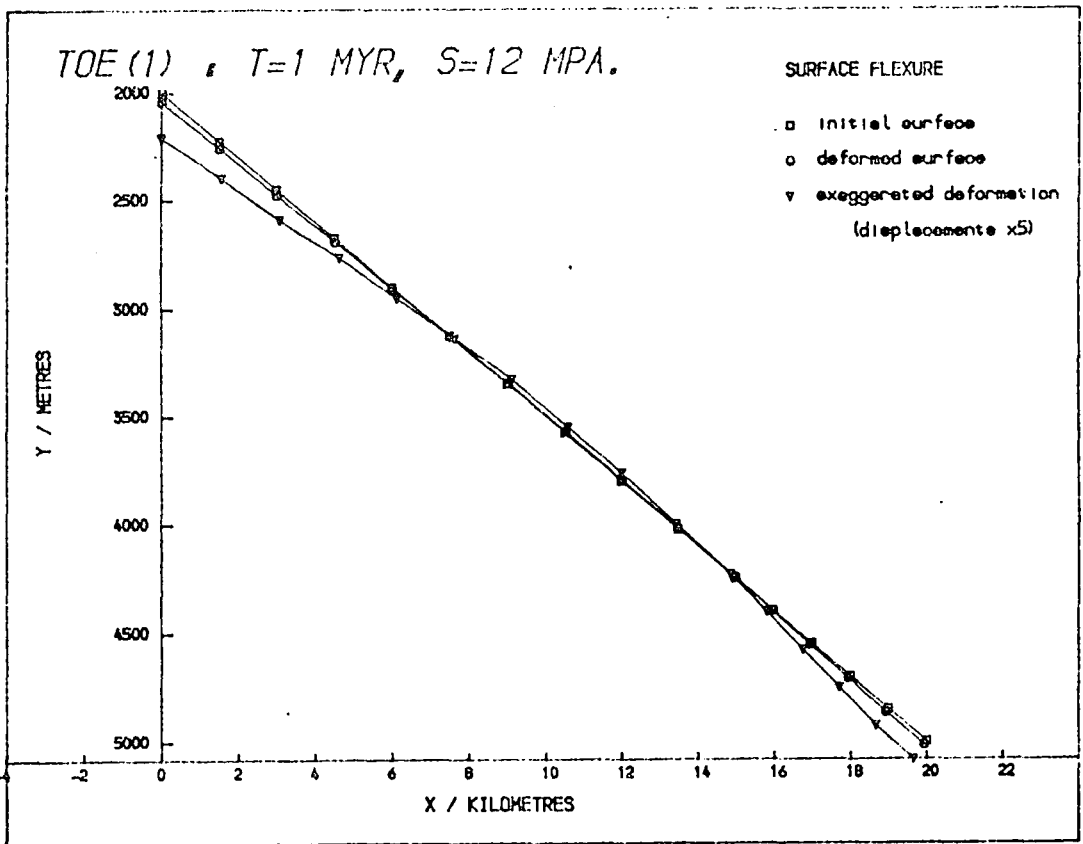
Fig. 5.12: Surface displacements of the wedge after 1 Myr, with a basal shear stress of 12 MPa.
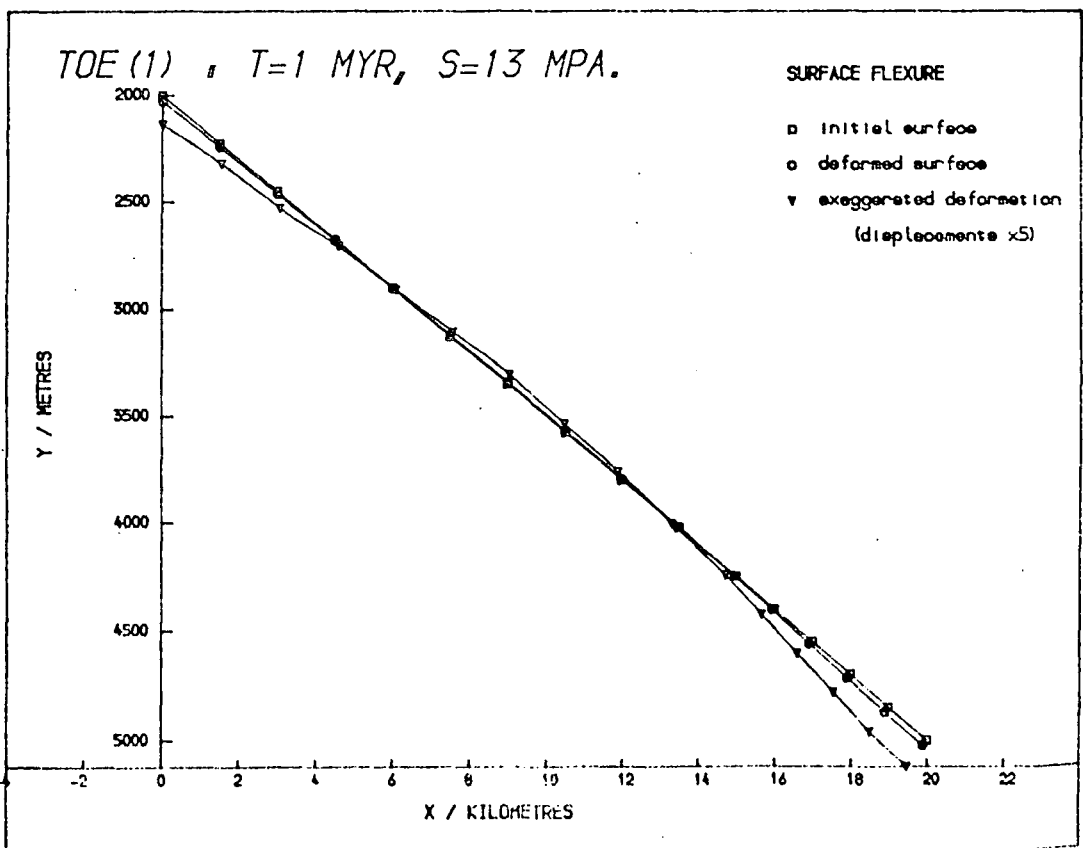
Fig. 5.13: As above, but with a basal stress of 13 MPa.
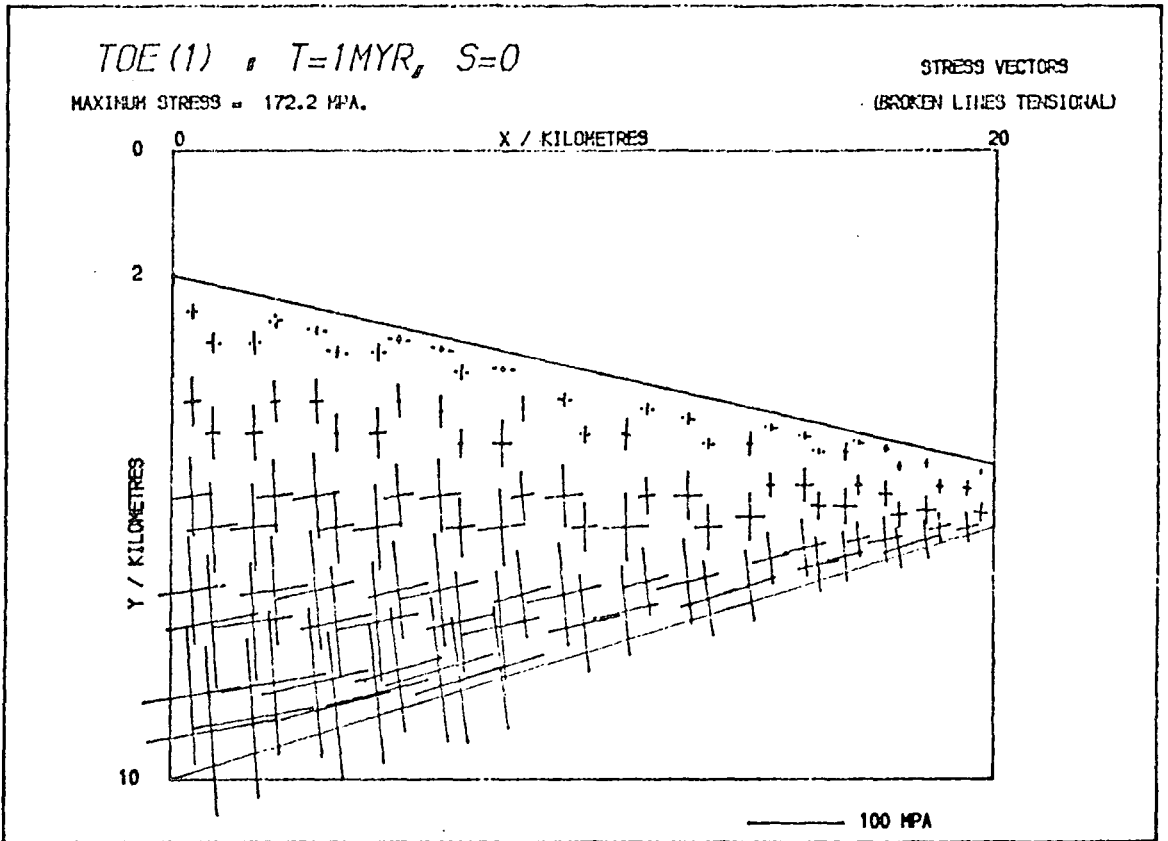
Fig. 5.14:   Principal stresses in the wedge after 1 Myr with no basal shear.
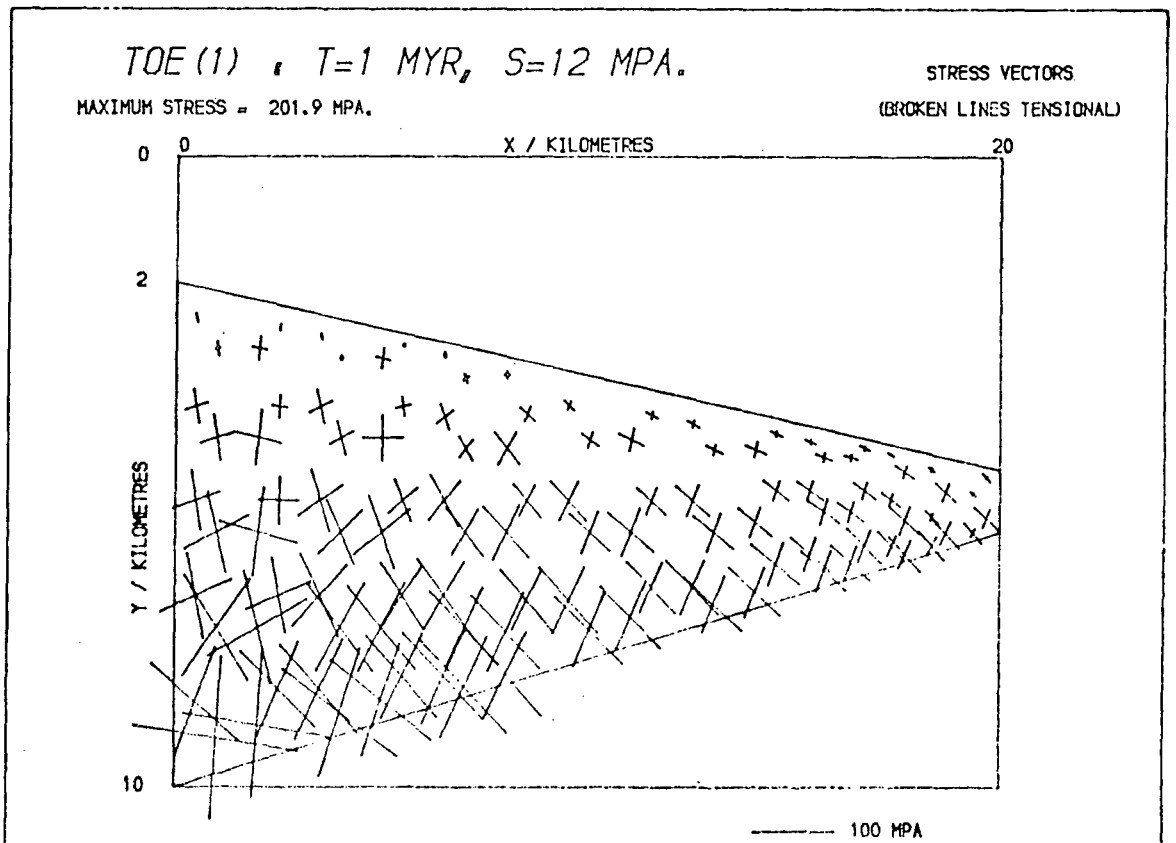
Fig. 5.15:   As above, with a basal shear stress of 12 MPa.

shear stress is c. 10 MPa, parallel to the base.

5.3.4 Implications of the value of the basal shear stress

As discussed in the previous section, it is found that a shear stress of

$$\tau = 12 \text{ MPa}$$

is needed to support the wedge of accreted sediments represented by Fig. 5.1, which agrees with the estimate (to an order of magnitude) made by McKenzie (1977; Richter and McKenzie, 1978) based on the stress drops calculated from measurements of earthquakes at subduction zones.

Given the magnitude of the basal stress it is possible to make some deductions about the nature of the shear zone referred to in Section 5.3.1. The convergence rate at this section of the Middle American trench is given by Karig et al. (1978) as

$$v = 70 \text{ mm yr}^{-1},$$

so using this and the shear stress obtained, the ratio of viscosity to thickness of the shear zone is found through Equation 5.1 to be

$$\frac{n_{s.z.}}{d} = \frac{\tau}{v} \simeq 5 \times 10^{15} \text{ N s m}^{-3}.$$

The thickness of hemipelagic muds and clays just seaward of the trench is 100 to 200 m according to the results of D.S.D.P. Leg 66 (Moore et al., 1979a; Shipley et al., 1980), so assuming this represents the thickness, d, of the shear zone, its viscosity is

$$n_{s.z.} = 10^{18} \text{ N s m}^{-2}.$$

Clearly, if the shear zone is narrower the estimated viscosity will be lower, but a lower limit may still be found to the possible

viscosity of the wedge, since it must be appreciably larger than the
shear zone viscosity in order to define the shear zone as such. So

$$\eta \gg \eta_{s.z.} \qquad\qquad 5.2$$

or $\eta \gg 10^{18}$ N s m^{-2}

if the shear zone is about 100 m thick. This is consistent with most
of the viscosities given in Ch. 2 (Section 2.2), but is much larger
than that of Cowan and Silling (1978; namely, $\eta = 10^{14}$ N s m^{-2}). The
effective viscosity of the wedge is taken to be 10^{22} N s m^{-2} in this
chapter (see Sections 5.2 and 5.6.1).

5.4 Basal Friction

5.4.1 Description of the boundary conditions

The second mechanism for the transmission of shear stress to the
base of the accretionary prism is a frictional one. If the sediment
wedge and the underlying oceanic crust can be considered as two distinct
tectonic units sliding past each other, then the stress on each is

$$\tau = -\mu\sigma_n \qquad\qquad 5.3$$

where σ_n is the normal stress across the boundary between them and
μ is the coefficient of sliding friction between the two surfaces.

In reality, sediments from the trench are carried down by the
oceanic plate being subducted and are probably accreted in thrust slices
onto the accretionary prism, which means that there are several units
in the system, variously interrelated, and in addition to this the
oceanic crust carries sedimentary layers over the main basaltic section.
This method therefore assumes that all the accreted sediments above
the basal thrust act as a single unit, resting on top of another single

unit, the oceanic crust.

A second assumption is that the coefficient of friction is constant under the whole accretionary wedge. This assumption is quite a good one, since Byerlee (1978) concludes that for the normal stresses encountered at depth in the crust, rock types and confining pressures have little or no effect on friction coefficients. However he states that the effect of a fault gouge on μ may be dependent on its composition, so that in the finite element models of this section μ must be regarded as an average for the whole thrust plane.

Finally an assumption must be made to estimate the normal stress across the base. As stated in Section 5.2.2, the base is fixed so that it cannot move in a direction normal to itself, so to be consistent with this σ_n should be set at the value of the normal stress needed to support the weight of the wedge. As an approximation to this, the vertical stress is used, namely

$$\sigma_n = -h\rho g \qquad\qquad 5.4$$

where h is the thickness of the wedge above the relevant point on the base. The applied nodal forces are then calculated using Ch. 3, Section 3.5.1.

If there are superimposed horizontal (or nearly horizontal) stresses, either tensional or compressional, transmitted by the oceanic plate, then these will not only change σ_n but also the other boundary conditions at the base of the wedge (see Section 5.2). For simplicity it is assumed that the only stresses on the wedge are the basal shear and those due to the other boundary conditions as before.

5.4.2 Elastic models

To find the coefficient of friction that produces sufficient basal shear to support the wedge, a similar procedure to that used in the previous section (5.3) is followed.

Elastic analyses are used to narrow down the value for the friction coefficient, and as before the resulting surfaces are roughly straight lines whose orientation depends on the applied shear. Examples are shown in Figs. 5.16 and 5.17, with friction coefficients of 0.05 and 0.20 respectively. In these two cases the rotations are c. 0.1° anti-clockwise and c. 0.2° clockwise.

The displaced surface is roughly parallel to the initial when the friction coefficient is about 0.1.

5.4.3 Visco-elastic models

Figs. 5.18 and 5.19 show the effect of allowing the model to creep visco-elastically for 1 Myr with the same applied shear stresses as in the elastic models of Figs. 5.16 and 5.17 (corresponding to friction coefficients of 0.05 and 0.20 respectively). It is readily seen that a low value allows the wedge to subside at the landward end and move up the basal slope, while a large frictional force drags the seaward end down the slope and lifts up the landward end. The deformation in these two cases is very similar in shape to Figs. 5.8 and 5.9, where the basal shear applied was uniform.

It is impossible to hold the whole surface to zero displacement in this way, but Figs. 5.20 and 5.21 show deformations where parts of the slope do not move (with values of μ, 0.08 and 0.10 respectively).

The best approximation is a friction coefficient of 0.09 (Fig. 5.22) which holds the surface deformation to about 30 m and the resulting

TOE , T=0, MU=0.05

SURFACE FLEXURE

□ Initial surface

o deformed surface

∇ exaggerated deformation
(displacements x5)

Y / METRES

X / KILOMETRES
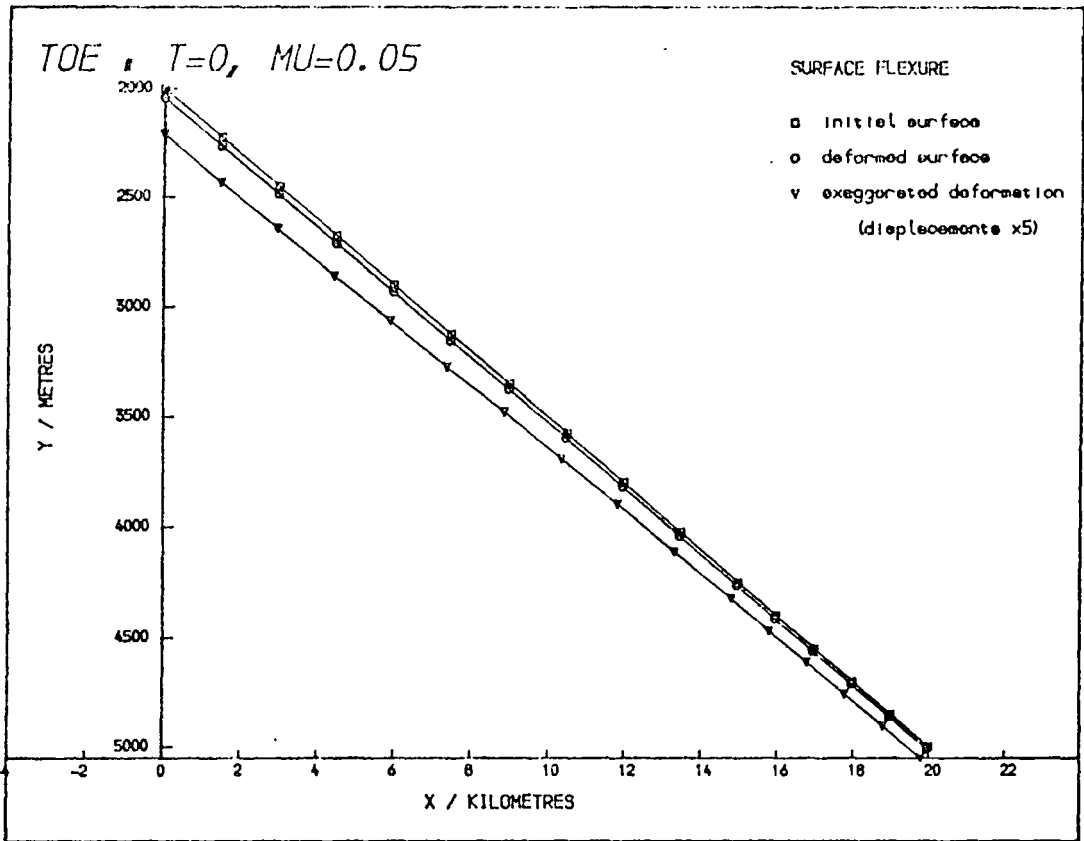
Fig. 5.16:   Elastic displacements of the wedge surface in response to a frictional basal shear stress, coefficient of friction, μ = 0.05.

TOE , T=0, MU=0.2

SURFACE FLEXURE

□ Initial surface

o deformed surface

∇ exaggerated deformation
(displacements x5)

Y / METRES

X / KILOMETRES
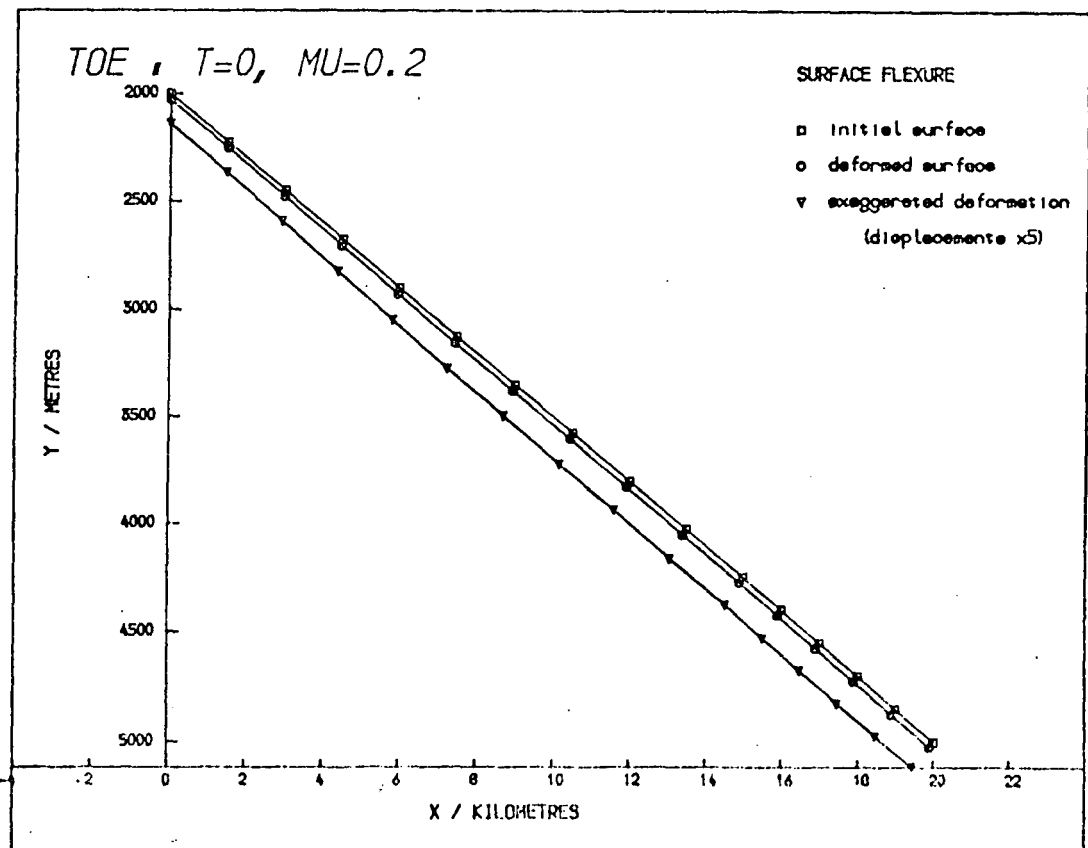
Fig. 5.17:   As above, but μ = 0.20.
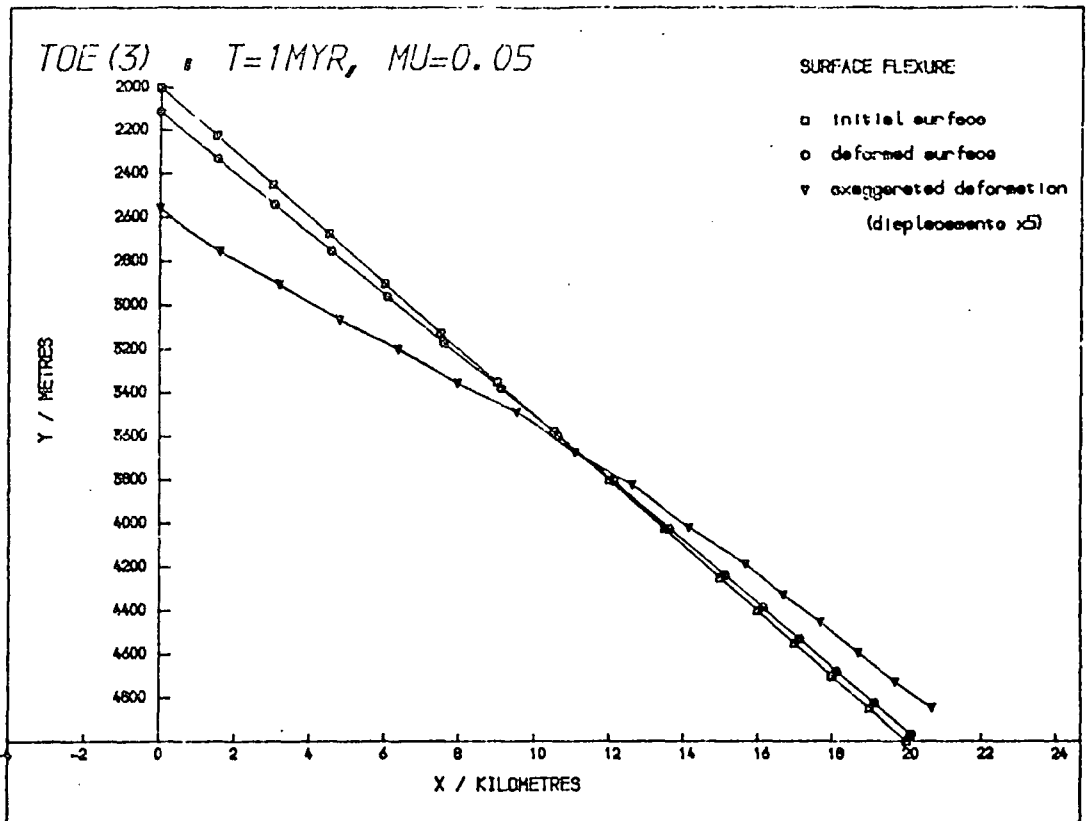
Fig. 5.18: Surface deformation after 1 Myr, in response to a frictional basal shear; μ = 0.05.
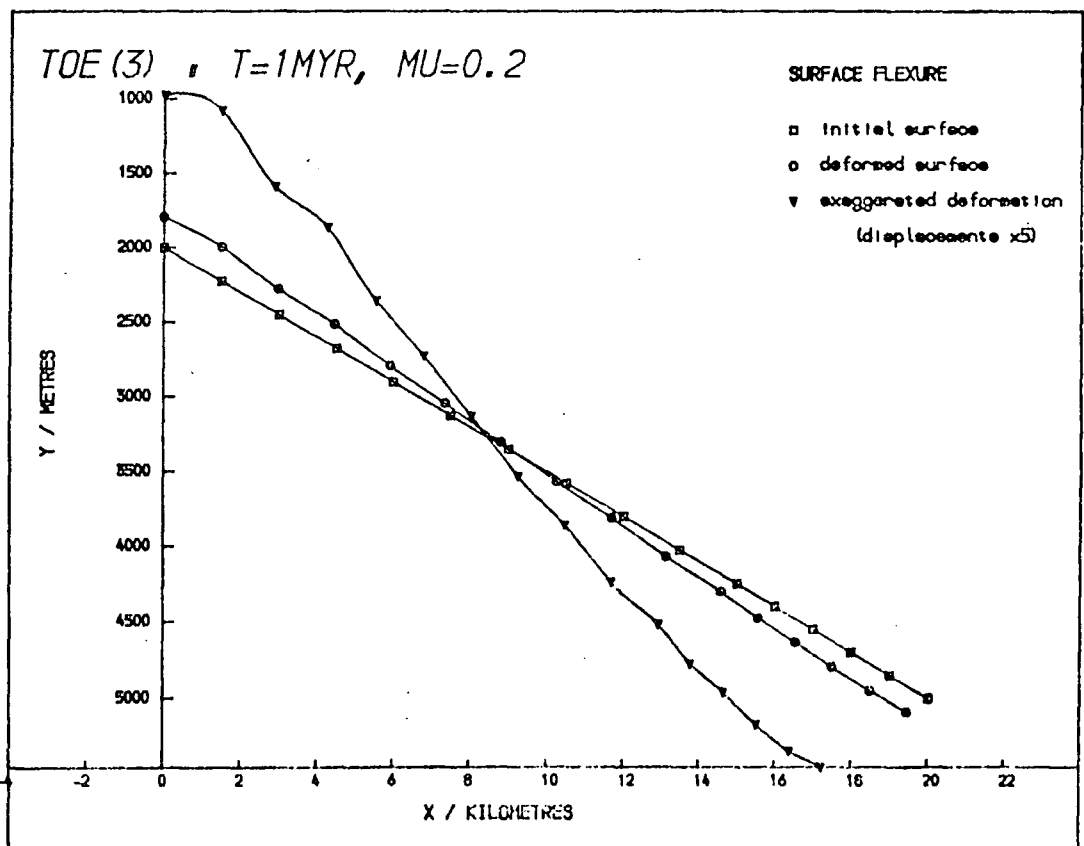
Fig. 5.19: As above, but μ = 0.20.
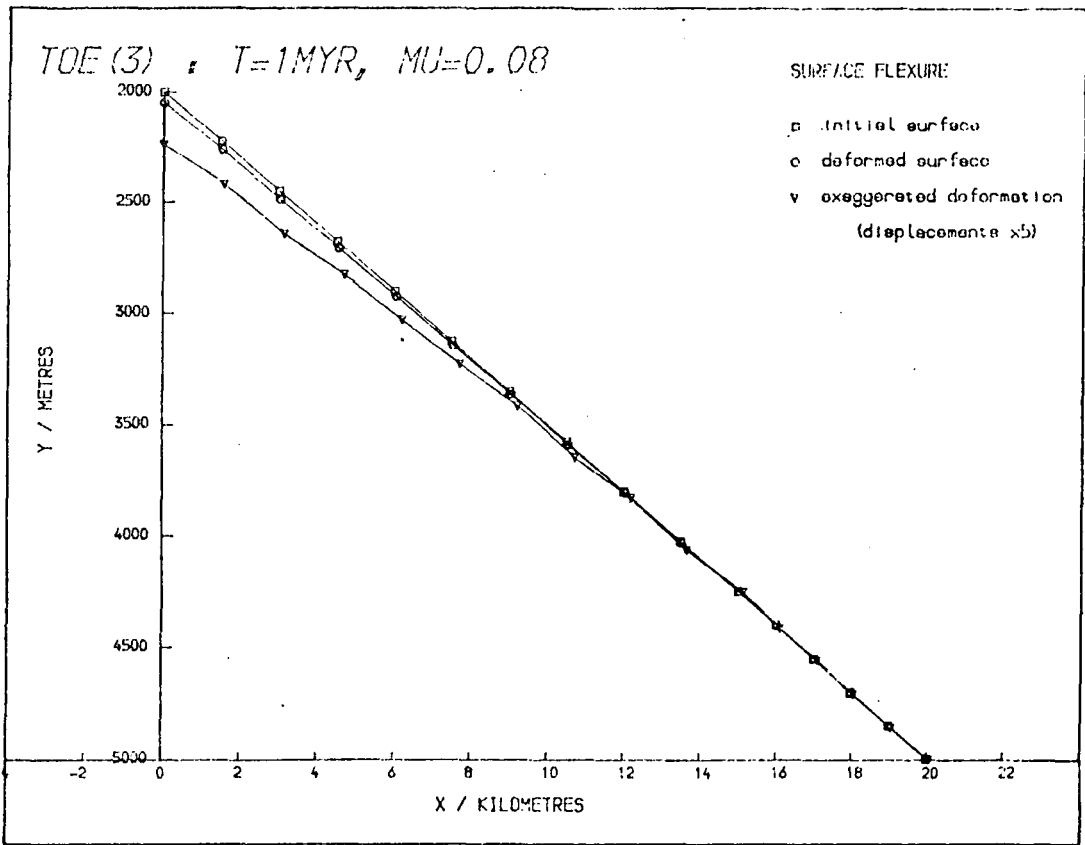
Fig. 5.20: Surface displacements after 1 Myr, with friction at the base
            of the wedge; μ = 0.08.
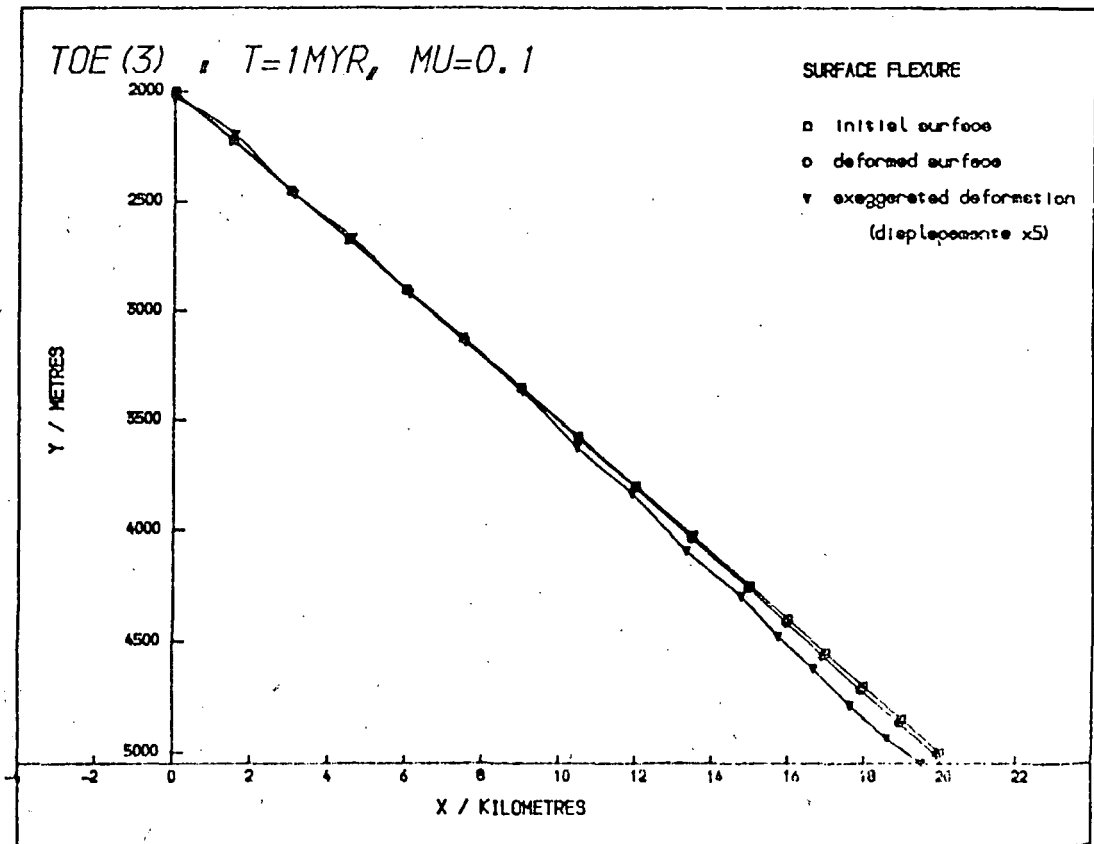
Fig. 5.21: As above, but μ = 0.10.

principal stresses are displayed in Fig. 5.23.

As with the model with a uniform basal shear of 12 MPa (Fig. 5.15), most of the deviatoric stresses present after 1 Myr without any applied stress (Fig. 5.14) are removed by the application of the supporting stress, and there are only small differences between the two resulting stress systems. These differences occur near the base of the model where, because of the increase in frictional stress with depth (Equations 5.3 and 5.4), there is an increase in the deviatoric stresses to the left of the wedge and a decrease to the right, compared with the uniform shear model. However these are small everywhere, rising to 3 MPa at the base of the wedge near to the trench.

5.4.4   Implications of the friction coefficient

The coefficient of friction, obtained as described, namely

$\mu = 0.09$

is significantly smaller than the values given by Byerlee (1978) of

$$\tau = -0.85 \, \sigma_n \qquad ; \qquad |\sigma_n| < 0.2 \text{ GPa}$$

$$\tau = -0.6 \, \sigma_n - 0.05 \text{ GPa} ; \qquad 0.2 \text{ GPa} < |\sigma_n| < 2 \text{ GPa}$$

and the values of Jaeger and Cook (1976) which have an average of

$\mu = 0.62$

both sources including examples of many different rock types. However these coefficients have been found for rock samples without any included gouge, which, Byerlee observes, reduces the friction considerably. Wang and Mao (1979) have performed experiments on small cylindrical granite samples (25.4 mm in diameter, 50.8 mm in length) in which a saw cut is made (at 30° to the axis) and filled with saturated clay, to measure the values of μ for different clays under confining pressures of up to 300 MPa. Their results are quoted in Table 5.2.
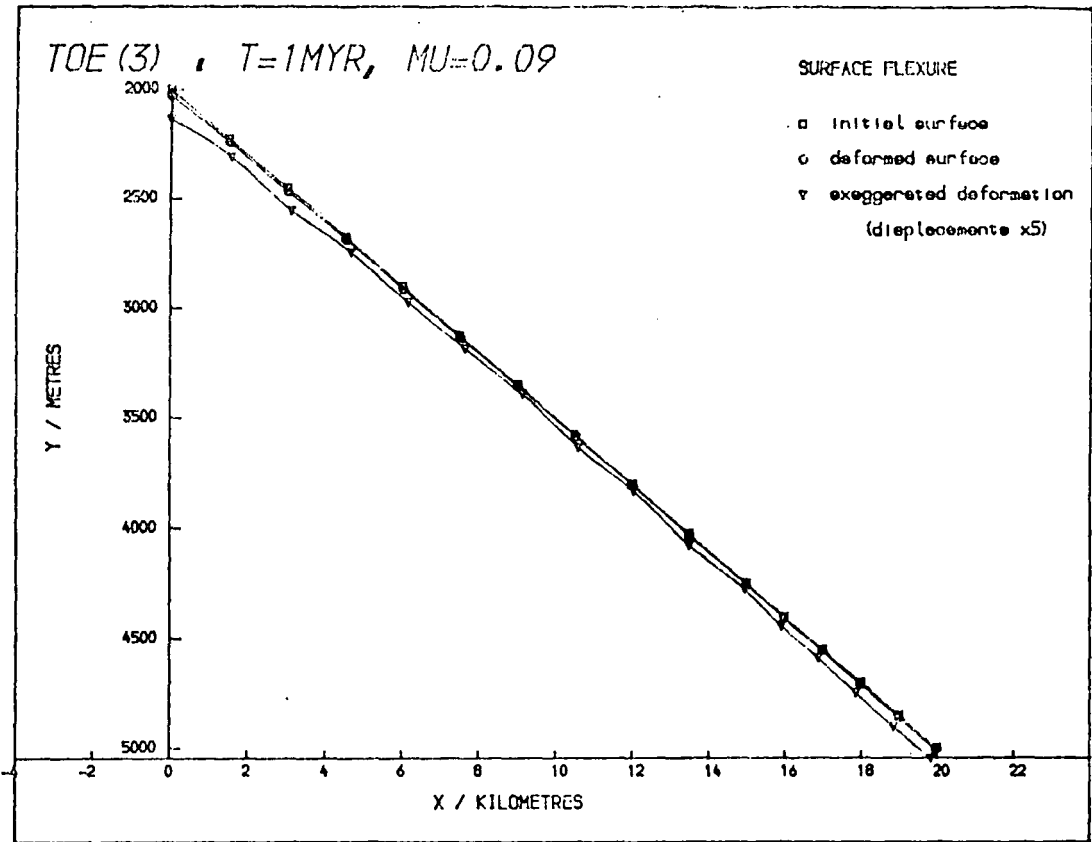
Fig. 5.22: Surface deformation after 1 Myr, with a frictional basal shear, μ = 0.09.
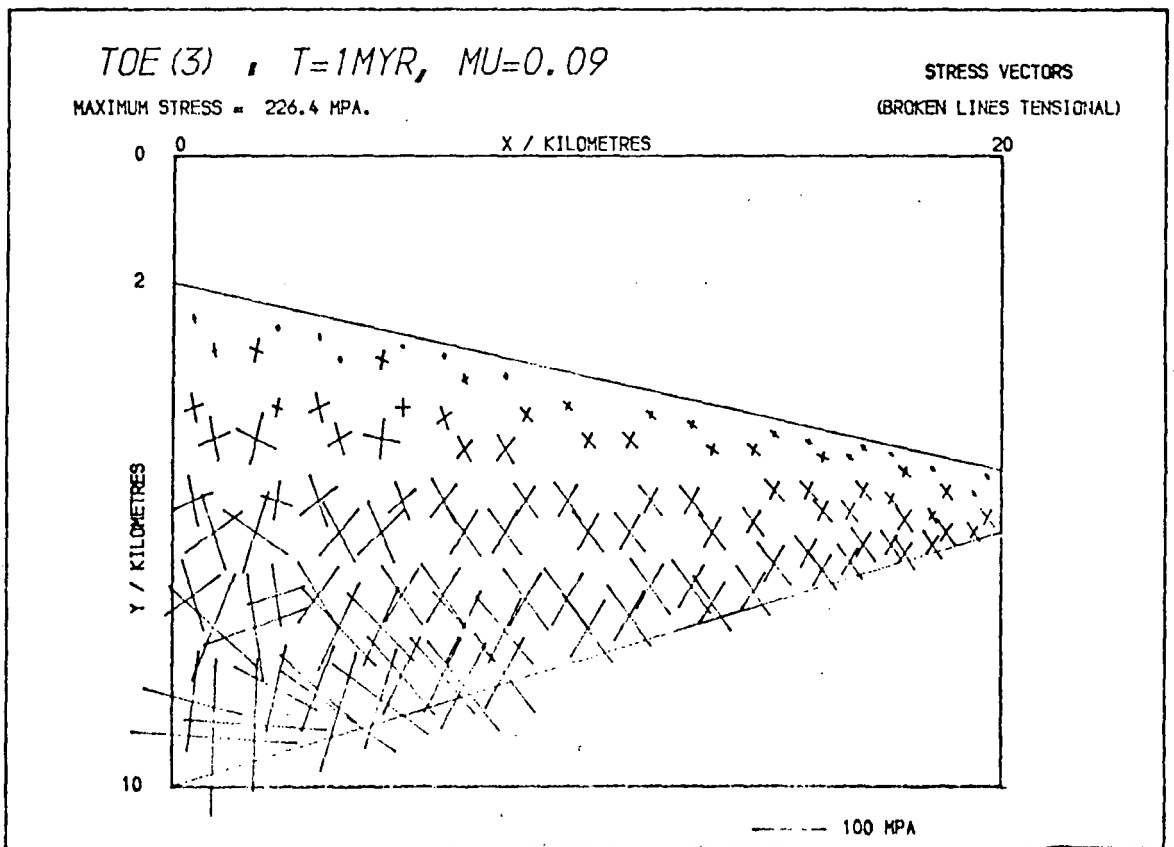
Fig. 5.23: Principal stresses in the same model as above (Fig. 5.22).

Clay	Coefficient of friction, μ
Montmorillonite	0.08 ± 0.01
Chlorite	0.12 ± 0.01
Kaolinite	0.15 ± 0.01
Illite	0.22 ± 0.02

Table 5.2: Friction coefficients for joints in granite filled with various saturated clays.   (Wang and Mao, 1979)

Wang and Mao's experiment was arranged in such a way that the pore pressure of water in the joint, p, could be measured independently from the confining pressure, and their results for μ are based on the effective normal stress across the crack

$$\sigma_{n_{eff}} = \sigma_n + p. \hspace{4cm} 5.5$$

If there is significant pore pressure along the basal thrust of the wedge model, in other words if the sediments there are not dewatered, then the coefficient of friction ~~corresponding to~~ <ins>derived from</ins> the applied shear ᵢₙ ₜₕₑ ₘₒₐₑₗ is larger.

To estimate this increase it is necessary to make some assumptions about the pore pressure on the thrust plane. If pore water is present, the least effect it can have is when all the pores are connected. In this case the pore pressure would be

$$p = h\rho_w g \hspace{4cm} 5.6$$

where h is the depth to the thrust plane and ρ_w is the density of the water. The estimated friction coefficient would then be increased by a factor of

$$\frac{\rho}{(\rho - \rho_w)} = 1.7$$

where ρ is the density of the accreted sediments (as before), giving

$\mu = 0.15$.

However if the pores are not interconnected and the pore water is overpressured, then following Hubbert and Rubey (1959)

$$p = f h \rho g ; \quad 0 \leqslant f \leqslant 1 \tag{5.7}$$

where f indicates the degree of overpressuring. Under these conditions the estimated coefficient of friction (from the finite element model) is increased by a factor of $(1 - f)^{-1}$, a few possible values of which are shown in Table 5.3.

Rubey and Hubbert (1959) report a range of values for f up to 0.9, and it is difficult to put bounds on its value under the conditions of the model. If f is c. 0.9 the estimate for μ is comparable with the results of Byerlee (1978; see above), but if $f \leqslant 0.6$ the estimate is consistent with Wang and Mao's (1979; see Table 5.2, above) values, implying that there is a layer of fault gouge along the thrust plane, as might be expected from observation of faults exposed at the Earth's surface.

f	$(1 - f)^{-1}$	μ
0.5	2.0	0.18
0.6	2.5	0.23
0.7	3.3	0.30
0.8	5.0	0.45
0.9	10.0	0.90

Table 5.3: Some values for the overpressure factor, f, and the corresponding estimates of μ, the coefficient of friction on the basal thrust.

5.5 The Effect of Surface and Basal Gradients

5.5.1 Variations in slope of the model boundaries

To investigate the effects of the gradients of the upper and lower surface boundaries on the basal shear stress, a series of models was run in which all the x co-ordinates were doubled but which were otherwise identical to the uniform shear models of Section 5.3 (Fig. 5.24; cf. Fig. 5.1). An elastic model with a basal shear of 12 MPa (Fig. 5.25) suggests that the same stress is needed to support the new, less steep slope, but in a visco-elastic analysis this does not hold (Fig. 5.26). By trial and error a basal shear of 6 MPa is found to hold the surface best, the displacements being about 50 m on average (Fig. 5.27).

Thus doubling the x co-ordinates of the wedge has the effect of halving (approximately) the basal shear. This effect must be due to some combination of the slopes on the upper and lower surfaces, so to separate their contributions a second model was run with the base returned to its original (steeper) position (Fig. 5.28), but otherwise the same as the previous model.

Again elastic analysis indicates that 12 MPa is the required basal shear (Fig. 5.29), but a visco-elastic model (run for 1 Myr; Fig. 5.30) shows this to be too large, and further investigation leads to the estimate of 8 MPa (Fig. 5.31).

Therefore reductions both in the basal slope and in the surface slope reduce the basal shear necessary to support the model, both effects being of the same order of magnitude (namely c. 5 MPa).
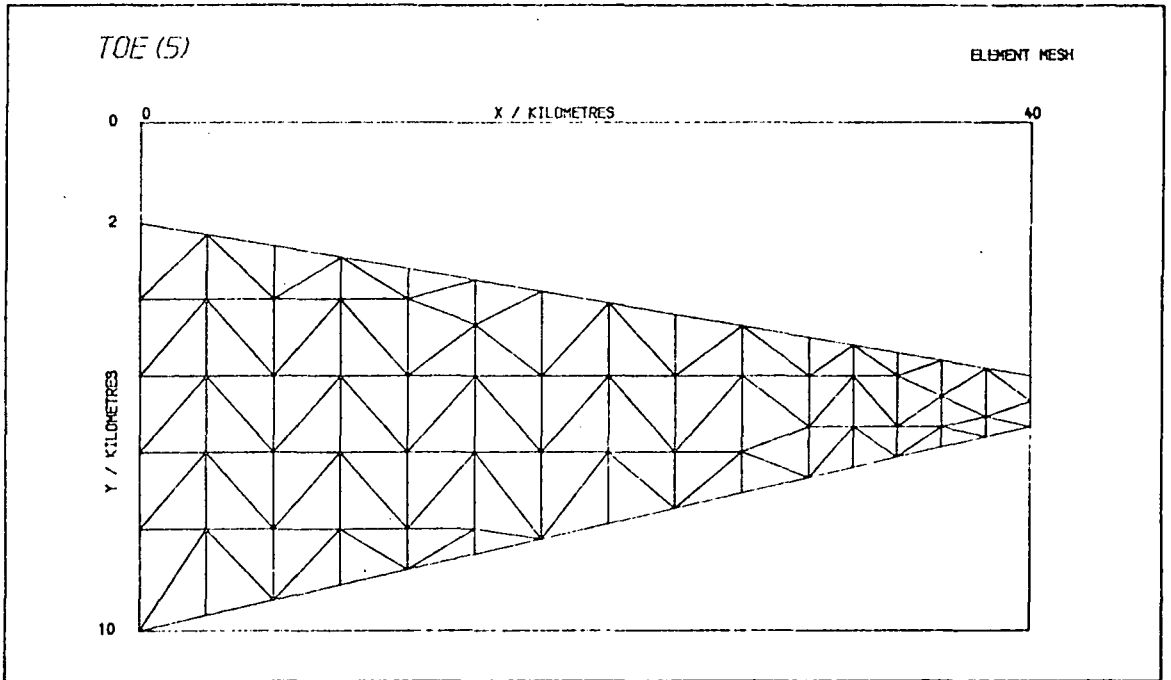
Fig. 5.24: Grid for the extended wedge model, as in Fig. 5.1, but with
all x co-ordinates doubled.
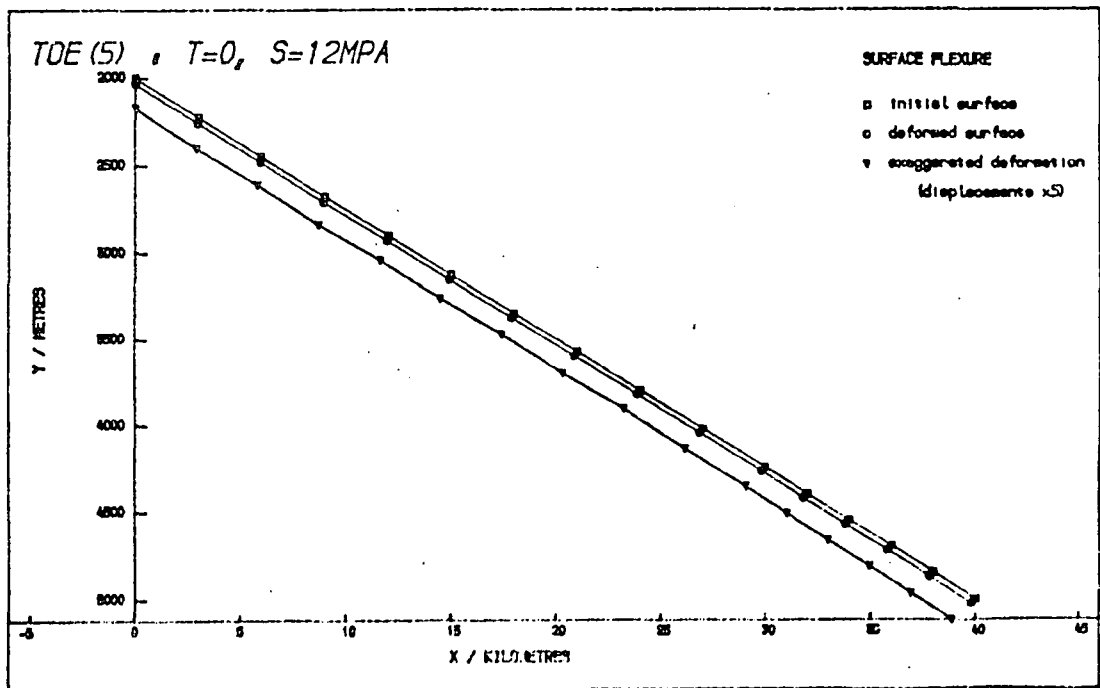
Fig. 5.25: Elastic deformation of the surface of the above model, in response
to a uniform basal shear of 12 MPa.

TOE (5)   T=1MYR, S=12MPA

SURFACE FLEXURE

□ initial surface
o deformed surface
▽ exaggerated deformation
     (displacements x5)
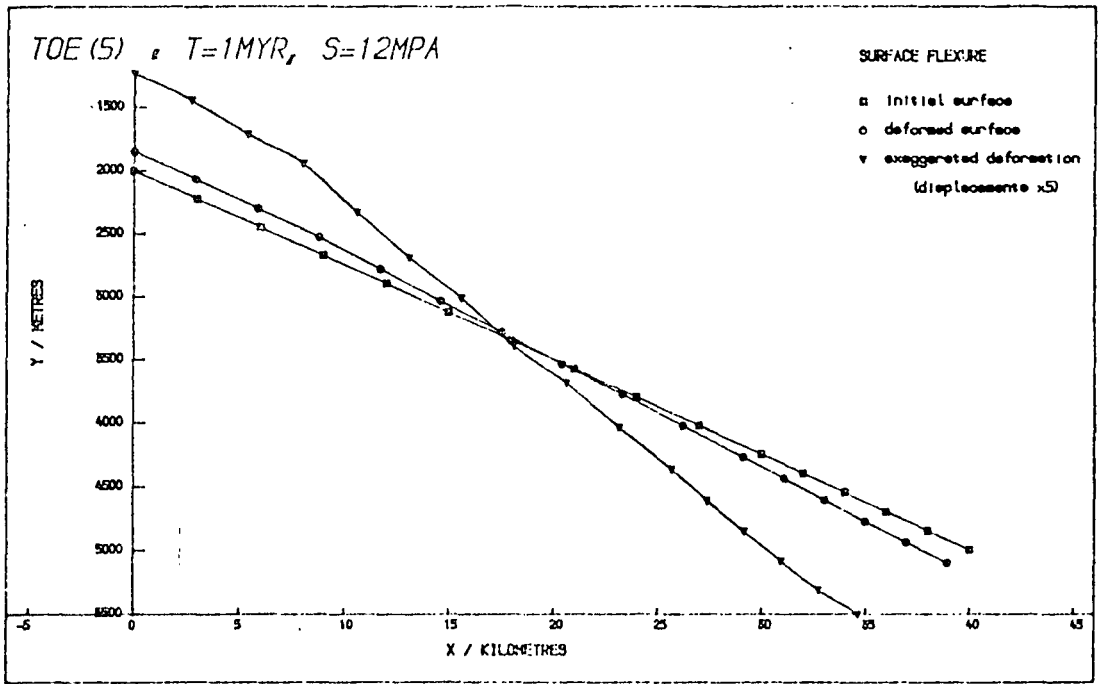
Fig. 5.26:   Surface displacements of the extended wedge (Fig. 5.24) after
             1 Myr of visco-elastic deformation, in response to a uniform
             basal shear of 12 MPa.

TOE (5)   T=1MYR, S=6MPA

SURFACE FLEXURE

□ initial surface
o deformed surface
▽ exaggerated deformation
     (displacements x5)
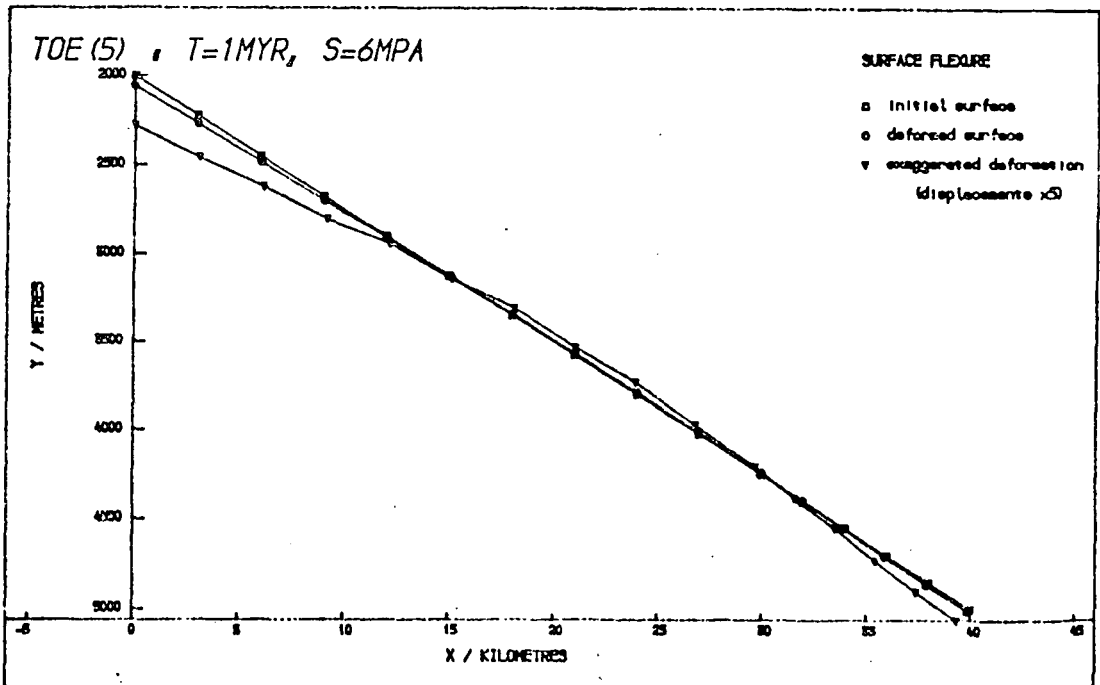
Fig. 5.27:   As above, but with a basal shear stress of 6 MPa.
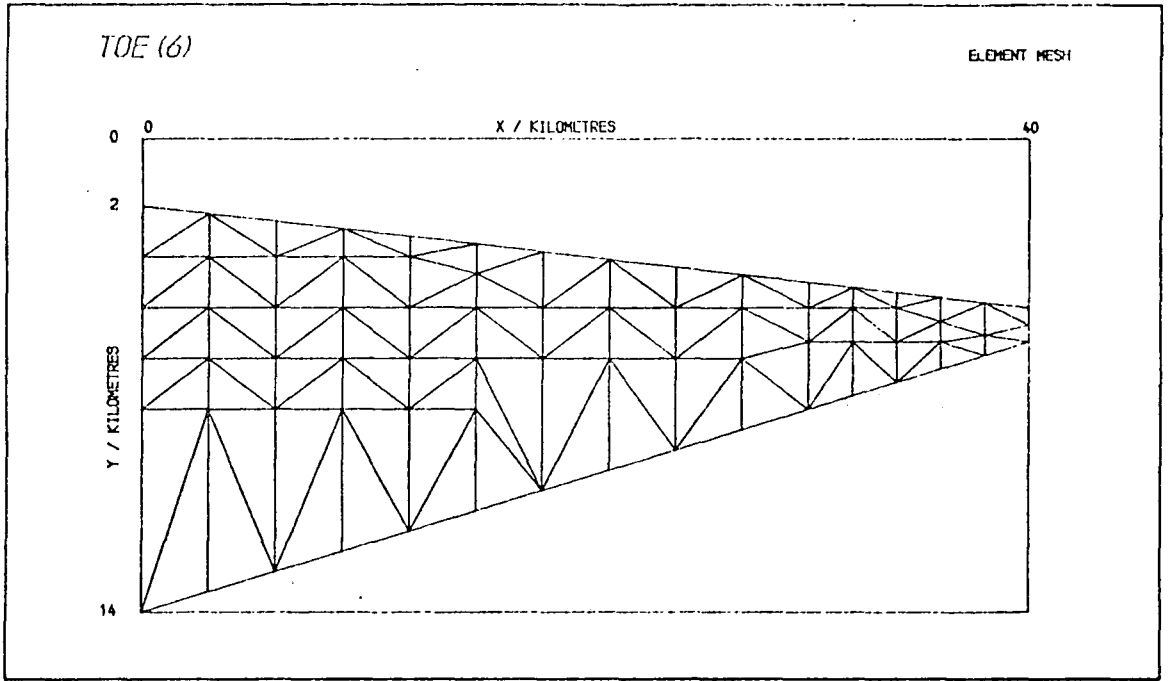
Fig. 5.28: Grid for the extended wedge model (Fig. 5.24), but with the basal gradient restored to that of the original (Fig. 5.1).
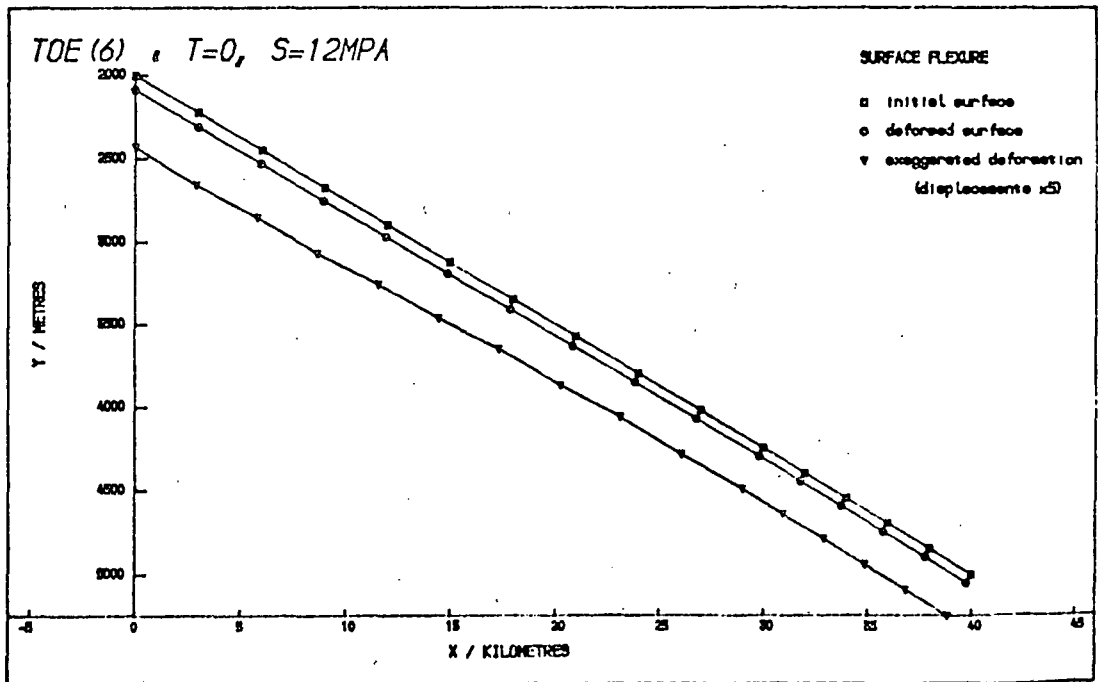
Fig. 5.29: Elastic deformation of the surface of the above model, in response to a uniform basal shear of 12 MPa.
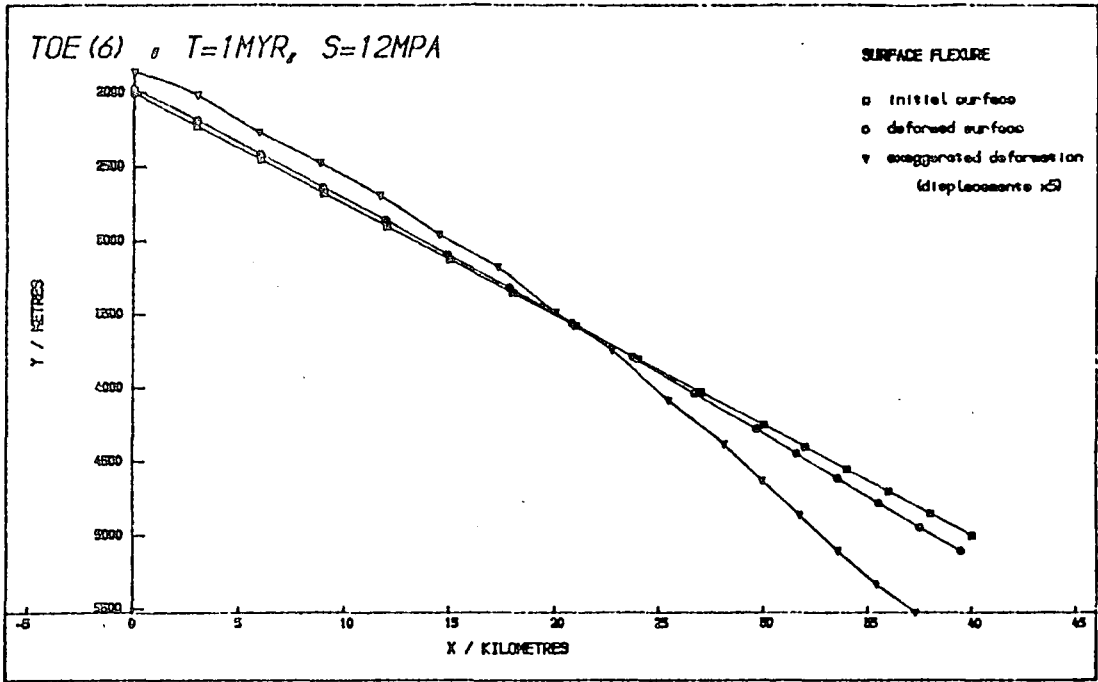
Fig. 5.30: Surface displacements of the wedge of Fig. 5.28 after 1 Myr, in
            response to a uniform basal stress of 12 MPa.
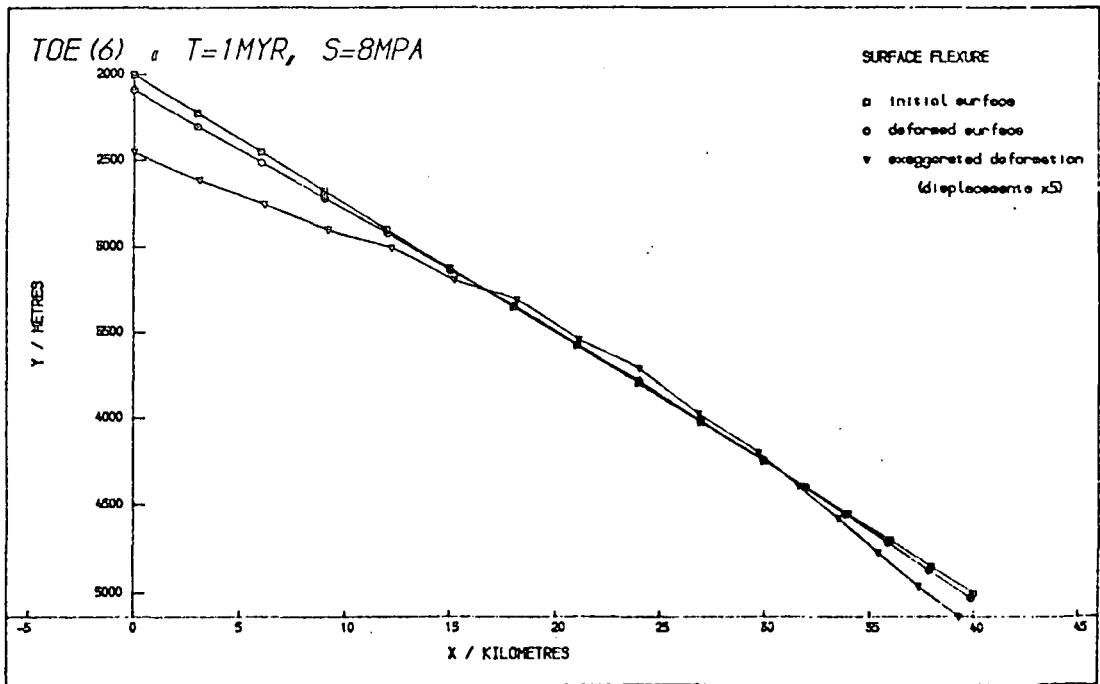
Fig. 5.31: As above for a basal shear stress of 8 MPa.

5.5.2 Comparison with an earlier, analytical model

The result obtained in the previous section is opposed to the conclusions of Elliott (1976) who deduces that,

"It is the surface slope which determines the magnitude and sense of the shearing stress at the base, and not the dip of the base",

but is supported by Seely (1977) who draws a similar conclusion from the presence of seaward-dipping thrust faults (seen on seismic reflection sections) in the sedimentary wedge of the Aleutian trench, where the upper surface is also seaward-dipping, indicating that the sense of shear on the base does not depend on the surface slope.

Elliott finds, analytically, an expression for the shear stress on the base of a thrust wedge, thickness H, surface dip α, given by

$$\tau \simeq \rho g H \alpha \qquad\qquad 5.8$$

where τ is the average basal shear over a length greater than any fluctuations of either surface.

The first derivation given for Equation 5.8 is based on the assumption that longitudinal stress gradients may be neglected. However, this assumption is questionable, since in the finite element solution shown in Fig. 5.15 (where there is a uniform basal shear of 12 MPa) there is a gradient of deviatoric stress, σ_x', of

$$\frac{\partial \sigma_x'}{\partial x} \simeq 1 \text{ MPa km}^{-1}$$

throughout the wedge, which integrated over its thickness H gives

$$\int_H \frac{\partial \sigma_x'}{\partial x} \, dy \simeq \frac{\partial \sigma_x'}{\partial x} . H \simeq 5 \text{ MPa}$$

which is significant with respect to the basal shear of 12 MPa.

Elliott also derives Equation 5.8 by a second method, in which longitudinal stress gradients are accounted for, drawing on the work of

Budd (1970, 1971). There are however two inconsistencies here. Firstly one of the results of Budd (1971) quoted by Elliott is

$$G \simeq \tau \simeq \rho g H \alpha \qquad \qquad 5.9$$

(assuming small variations in the upper surface and smooth variations on the base), but according to Budd (1971, section 1.2(i)) G is the net longitudinal stress gradient

$$G = \frac{\partial \sigma_x{}'}{\partial x} H \qquad \qquad 5.10$$

so that Equation 5.9 contradicts the fundamental assumption of Elliott's first derivation, namely that the longitudinal stress gradient may be neglected.

The second inconsistency arises because Budd's work is concerned with uniform flow (of ice) between two boundaries, the upper surface and the base, whose positions remain fixed with time, whereas an overthrust can move as a single unit. This false assumption has important consequences in the derivation of the change in potential energy of a thrust sheet. To calculate this, following Elliott (1976), a column within the thrust sheet is analysed, as shown in Fig. 5.3 2. Changes in the gravitational potential energy of the column arise because of changes in the height, h, of the centre of mass of the column, which is at a height $(H/2)$ above the base of the thrust sheet.

The height of the centre of mass is a function of several variables, $h(B, \varepsilon_y, x)$, where B is the thickness of material deposited on, or eroded from the surface (measured as negative for erosion), and ε_y is the finite strain of the column vertically (e.g. due to compaction). Thus the rate of change of h with time may be expressed in terms of partial derivatives as

$$\frac{dh}{dt} = \frac{\partial h}{\partial B} \cdot \frac{\partial B}{\partial t} + \frac{\partial H}{\partial \varepsilon_y} \cdot \frac{\partial \varepsilon_y}{\partial t} + v \frac{\partial h}{\partial x} \qquad \qquad 5.11$$
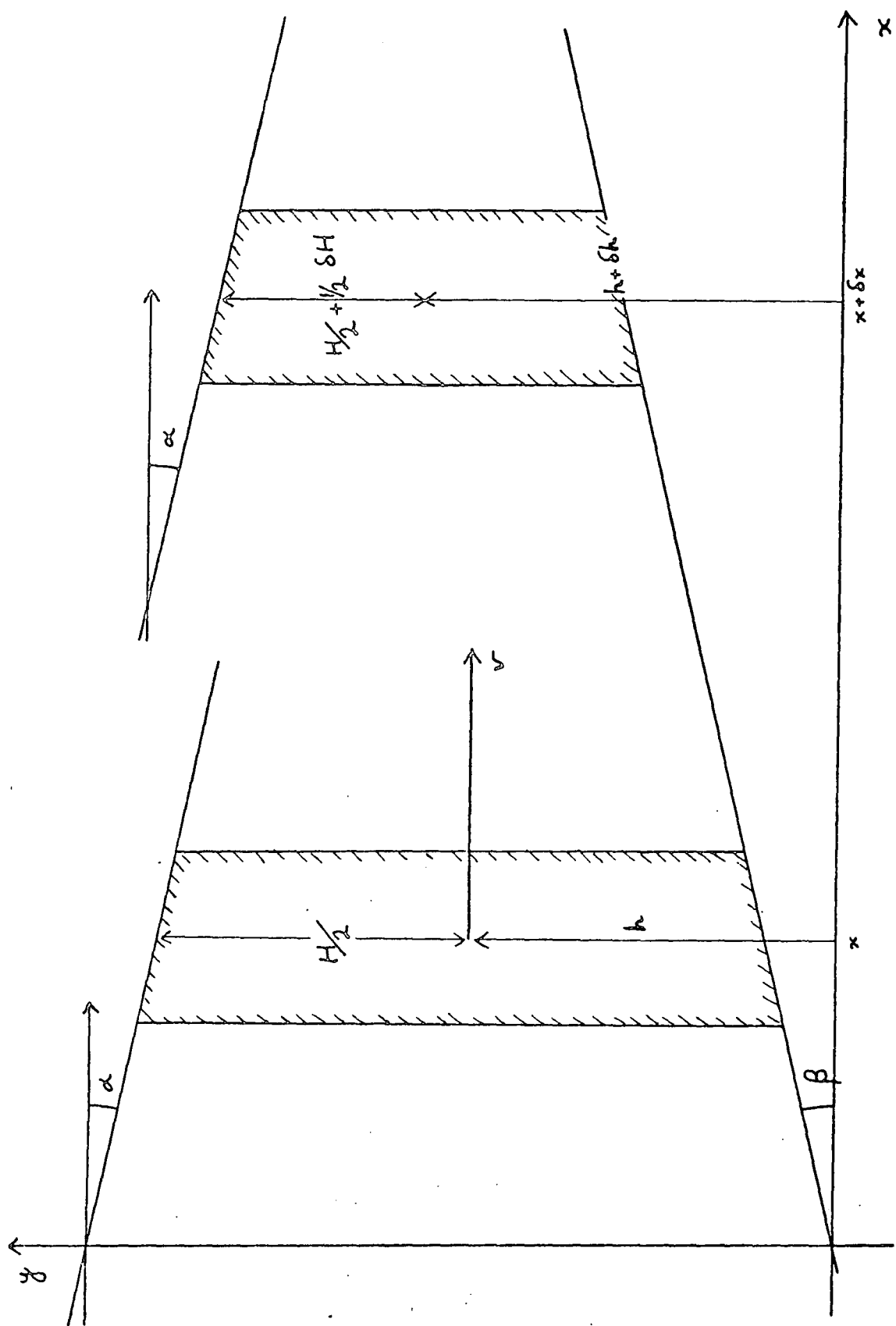
Fig. 5.32: Variables describing the motion of a thrust sheet

where v is the horizontal component of the thrust sheet's velocity
(see any fluid dynamics or advanced calculus text, e.g. Rutherford,
1959; Kaplan, 1962). Now,

$$\frac{\partial h}{\partial B} = \frac{1}{2}\frac{\partial H}{\partial B} = \frac{1}{2} \qquad \qquad 5.12a$$

$$\frac{\partial h}{\partial \varepsilon_y} = \frac{1}{2}\frac{\partial H}{\partial \varepsilon_y} = \frac{H}{2} \qquad \qquad 5.12b$$

(see Elliott, 1976), but the partial derivative of h with respect to
x depends only on the gradient of the base

$$\frac{\partial h}{\partial x} = \tan \beta \qquad \qquad 5.13$$

and not on the surface gradient, α, since the whole overthrust is
free to move as shown, and not confined between the base and a fixed
surface, as mentioned earlier. Thus

$$\frac{dh}{dt} = \frac{\dot{B}}{2} + \frac{H}{2}\dot{\varepsilon}_y + v \tan\beta \quad , \qquad \qquad 5.14$$

which differs from Elliott's expression for dh/dt in being independent
of α.

If sliding on this slope is to be energetically possible, when
the only externally applied force is gravitational, then

$$\frac{dh}{dt} < 0. \qquad \qquad 5.15$$

However, the first two terms in Equation 5.14 are independent of x,
so that the direction of motion of the overthrust is determined by the
last term, namely v tanβ. The most energetically favourable direction
of motion is thus down the basal slope (i.e. v tanβ < 0), and the energy
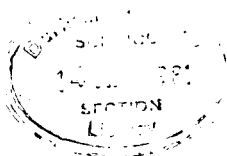
balance (Equations 5.14 and 5.15) is independent of the surface slope.

An overthrust will only move up the basal slope if a sufficient stress (at least equal to the lithostatic stress) is applied to the down-slope (left-hand in Fig. 5.32) end of the thrust wedge, and cannot be driven up-slope by gravity alone. The surface slope may effect the magnitude of the basal shear, but cannot provide the driving stress for the thrust.

A second analytical model is presented by Chapple (1978). He analyses a wedge of sediments above a weaker basal zone, both of which are plastic and in steady-state flow (above their yield stresses). He derives a set of equations (given in Appendix 1) in terms of the upper and lower surface slopes, the thickness, the density and the yield stress, K, of the wedge, which can be used to find the basal shear stress. From these, and using Chapple's value of

$K = 100$ MPa

together with the relevant parameters for the wedge of Section 5.3 (upper and lower surface dips $\tan^{-1}(0.15)$ and $\tan^{-1}(0.2)$, respectively) the basal shear is calculated as

$\tau = 50$ MPa.

This is considerably larger than the 12 MPa obtained in Section 5.3 by finite element analysis. However, Chapple's value for K is very large compared with the values for tensile strength shown in Ch. 2, Section 2.3.4, and if a value is chosen of

$K = 12$ MPa,

good agreement is reached with the finite element results of Sections 5.3 and 5.5.1, as shown in Table 5.4, despite the difference in rheology between Chapple's plastic model and the visco-elastic behaviour assumed in this thesis. The most obvious qualitative agreement is that the basal shear increases with the basal slope.

tan α	tan β	τ(analytic)/MPa	τ(finite element)/MPa
0.15	0.2	12	12
0.075	0.2	9	8
0.075	0.1	7	6

Table 5.4: Comparison of basal stress for various surface and basal slopes, derived using the finite element method and analytically.   (Chapple, 1978)

5.6 The Effects of Variation in Material Properties

The effects of contrasts in the visco-elastic parameters of different parts of an accretionary wedge will be discussed in Ch. 6, but this section (5.6) will describe the effects on the uniform model in this chapter, of variations in material properties.

5.6.1 Viscosity

The viscosity of the material only enters into the finite element calculation in Equations 3.38 (Ch. 3) which show the relationship between creep rate and deviatoric stress in an element.

The whole finite element formulation is linear, for linear creep, so that the value of any component of any relevant variable at time t, q(t) (where q may be a component of displacement, strain or stress), in a body with uniform viscosity, η, may be written as

$$q(t) = q_0 + q_1 \left(\frac{t}{\eta} \right) , \qquad\qquad 5.16$$

where q_0 is the value of q obtained in elastic analysis, q_1 is a function of (t/η), and both q_0 and q_1 depend on the finite element grid, the material properties and the boundary conditions for the model.

Note that this equation depends only on t, and not Δt, the length of the time increment used. To verify this, several models were run with different increments, but for the same total time in each model. In all cases the results agreed to better than 1% for all variables (these differences being caused by the finite convergence criterion in the solution iterations; see Ch. 3 Section 3.4).

Thus η only alters the time-scale of the model. This is readily tested by running the same model with different values of η, but keeping the ratio (Δt/η) constant, and when this was done the results were identical.

5.6.2 Young's modulus

Figs. 5.33 and 5.34 show the effect of altering the Young's modulus of the wedge material from 10 GPa (Fig. 5.12 and Table 5.1) to 100 GPa and 1 GPa, respectively.

The compressibility of a material, κ, is inversely proportional to E,

$$\kappa = \frac{3(1 - 2\upsilon)}{E} \qquad\qquad 5.17$$

(Jaeger and Cook, 1976), where E and υ are the Young's modulus and Poisson's ratio for the material as before, and the change in this is the chief cause of the difference between Figs. 5.33 and 5.34.

The nodal forces are all of the order of 10 GN, both those due to basal shear and those due to weight, and so, in the original model, they were of the same order of magnitude as E (10 GPa). Increasing E to 100 GPa reduces the displacements in the whole wedge by a factor of at least 2, except near the surface at the landward end (Fig. 5.33) where there seem to be some undulations in the displaced surface (see Section 5.7, below).
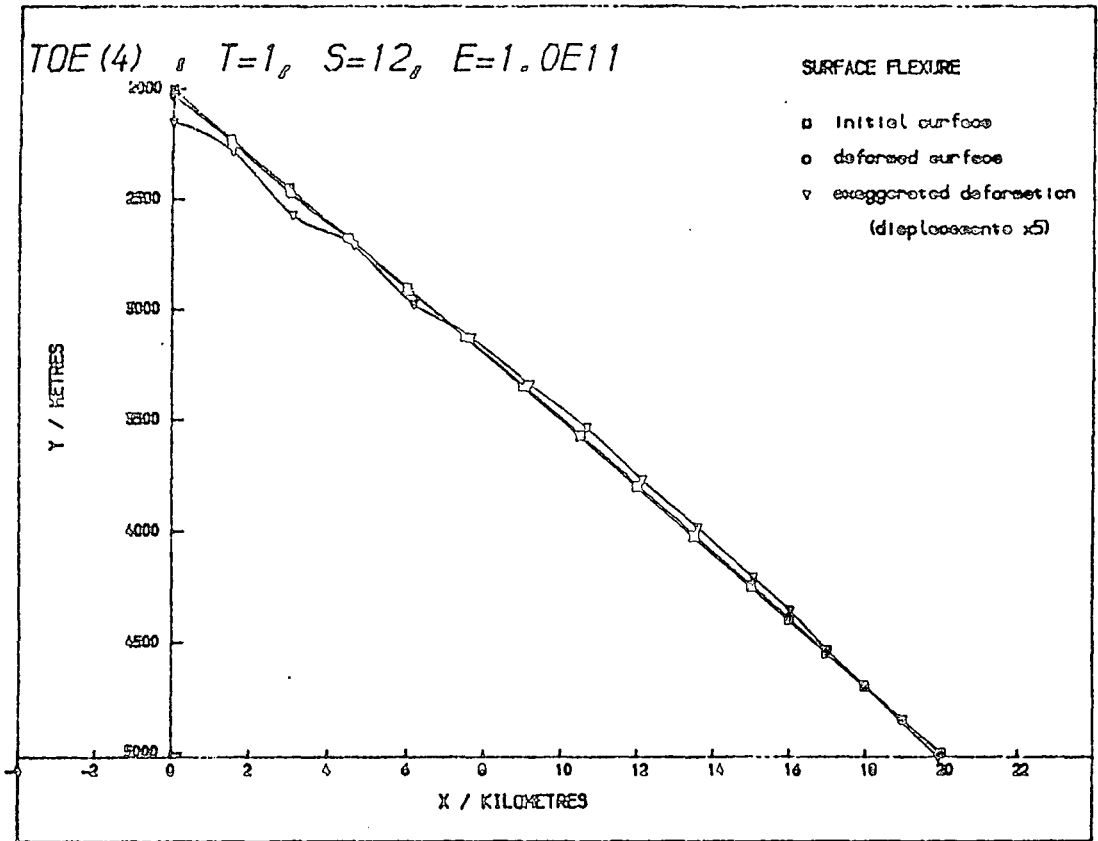
Fig. 5.33: Surface displacements of a wedge (Fig. 5.1) with Young's modulus, E = 100 GPa, after 1 Myr of visco-elastic deformation, with a basal shear of 12 Mpa.
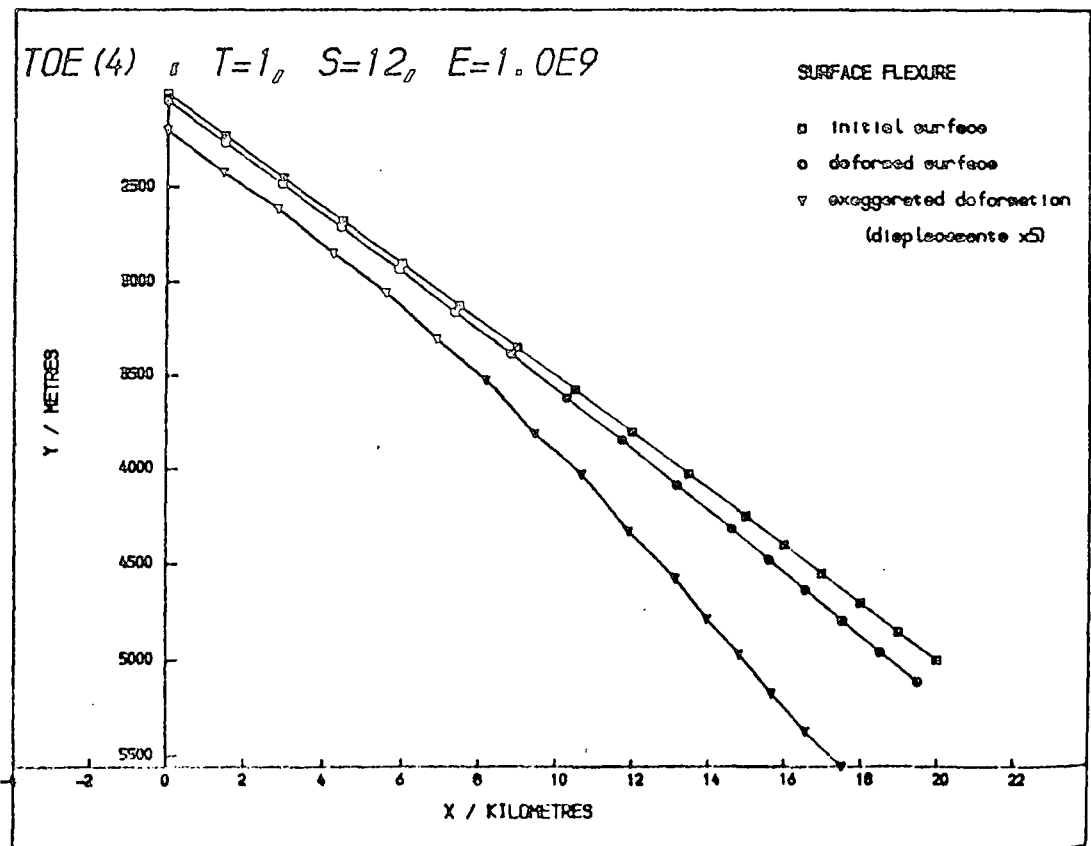
Fig. 5.34: As above, with E = 1 GPa.

Conversely, reducing E by a factor of 10 (Fig. 5.34) increases the displacements in the wedge, particularly at the seaward end, since the landward end is supported somewhat by the boundary condition on the left of the model, namely that there should be no x-displacements (Section 5.2.2). Apart from the nodes near this end, all nodal x-displacements are at least 100 m to the left, reaching over 500 m at the toe of the wedge. Thus with a Young's modulus of 1 GPa, it is impossible to keep the surface displacements as small as in the previous models, but the basal stress required to maintain the average surface slope is still approximately 12 MPa, and is therefore not significantly dependent on E.

5.6.3 Poisson's ratio

Equation 5.17 shows that the compressibility depends not only on Young's modulus but also on Poisson's ratio,ν. However, variations in κ are restricted more because the range of possible values of ν is much smaller than of E.

Figs 5.35 and 5.36 show the visco-elastic deformation after 1 Myr, with a uniform basal shear of 12 MPa, when the Poisson's ratio is 0.4 and 0.15, respectively compared to the previous value, 0.27 (Table 5.1). The similarity between Figs. 5.35 and 5.33 is very marked, indicating that they might be caused through a change in the same parameter (namely κ), though κ is only decreased by a factor of 2.3 in this case, as opposed to 10 in Fig. 5.33.

In both Figs. 5.35 and 5.36, 12 MPa seems to be the best basal shear to hold the model steady, though when ν = 0.15 there are rather larger displacements than before at each end of the wedge. This is probably because, for a lower Poisson's ratio, there is less coupling
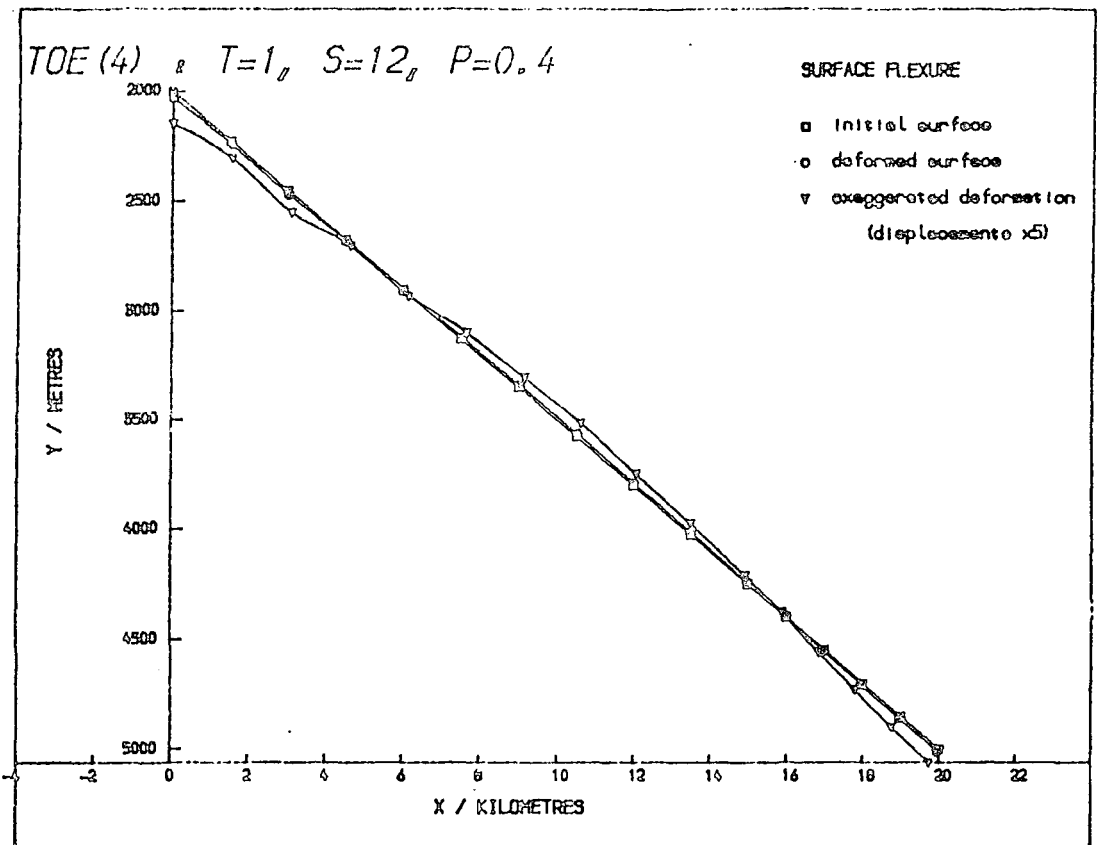
Fig. 5.35: Surface deformation after 1 Myr in a wedge with Poisson's ratio,
ν = 0.4, and a basal stress of 12 MPa.
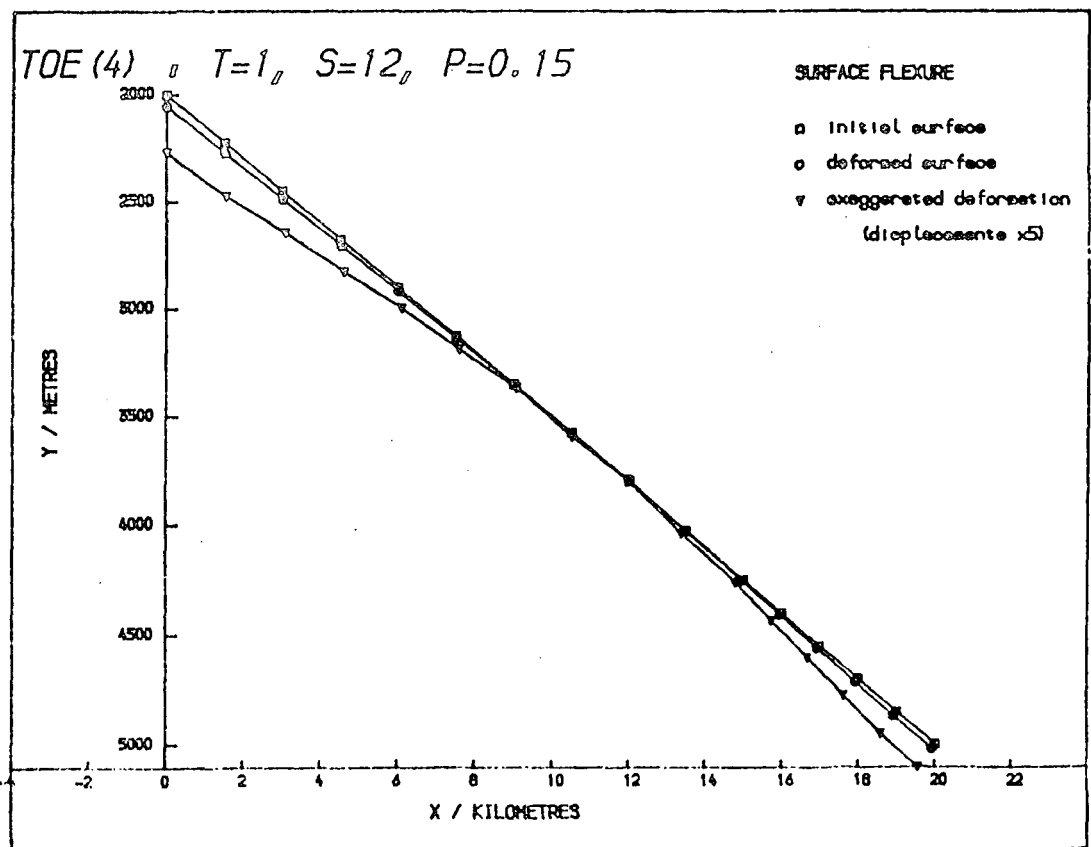
Fig. 5.36: As above, but ν = 0.15.

between vertical and horizontal displacements.

The deviatoric stress system in the wedge does not vary significantly with changes in ν, the deviatoric stresses being overall slightly larger for $\nu = 0.15$ and slightly smaller for $\nu = 0.4$ than for $\nu = 0.27$, but the changes are less than 2 MPa everywhere.

5.6.4 Density

The effects of varying the wedge's density on the results of the model are very straightforward. An increase in density increases the vertical stresses due to the body's weight and so a larger basal shear stress is needed to support it.

A comparison of Fig. 5.37 , where the density is 2700 kg m^{-3} and Fig. 5.38, with $\rho = 2300$ kg m^{-3}, with the original model ($\rho = 2500$ kg m^{-3}) supported by different basal shears as shown in Figs. 5.10 to 5.13, indicates that increasing (or decreasing) the density by 200 kg m^{-3} increases (or decreases) the supporting stress by about 1 MPa.

5.7 A Long-Term Model Instability

If the original model, with properties as listed in Table 5.1, is run for 10 Myr, the solution becomes unstable, as shown in Figs. 5.39 and 5.40. This manifests itself as an undulation in the upper surface (shown together with an exaggerated version in Fig. 5.39), and in the introduction of tensile stresses and unrealistically small compressional stresses into the model (Fig. 5.40).

A similar effect to this is seen if a visco-elastic model is run without the provision of sufficient constraints, for example if one end of a rectangular model is inadvertently left free, although of course when this is done the instability is very much more pronounced.
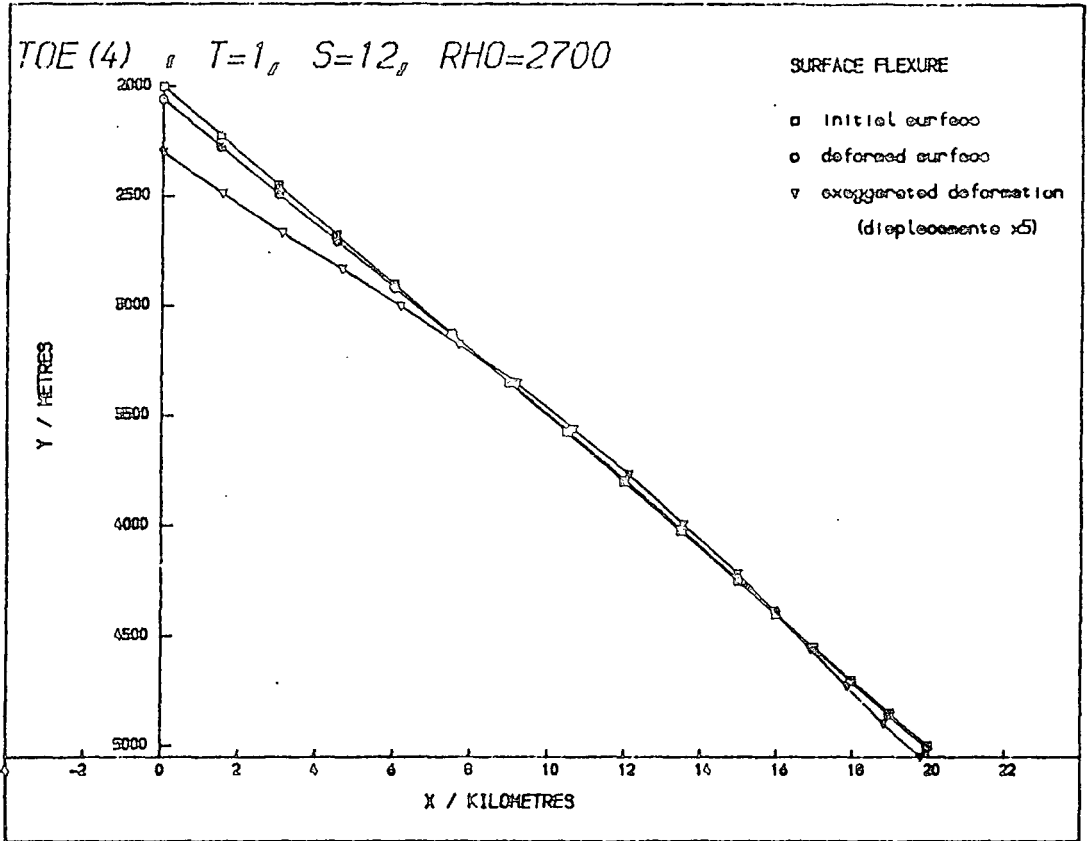
Fig. 5.37: Surface displacements after 1 Myr in a wedge of density, $\rho = 2700$ kg m^{-3}, and a uniform basal shear of 12 MPa.
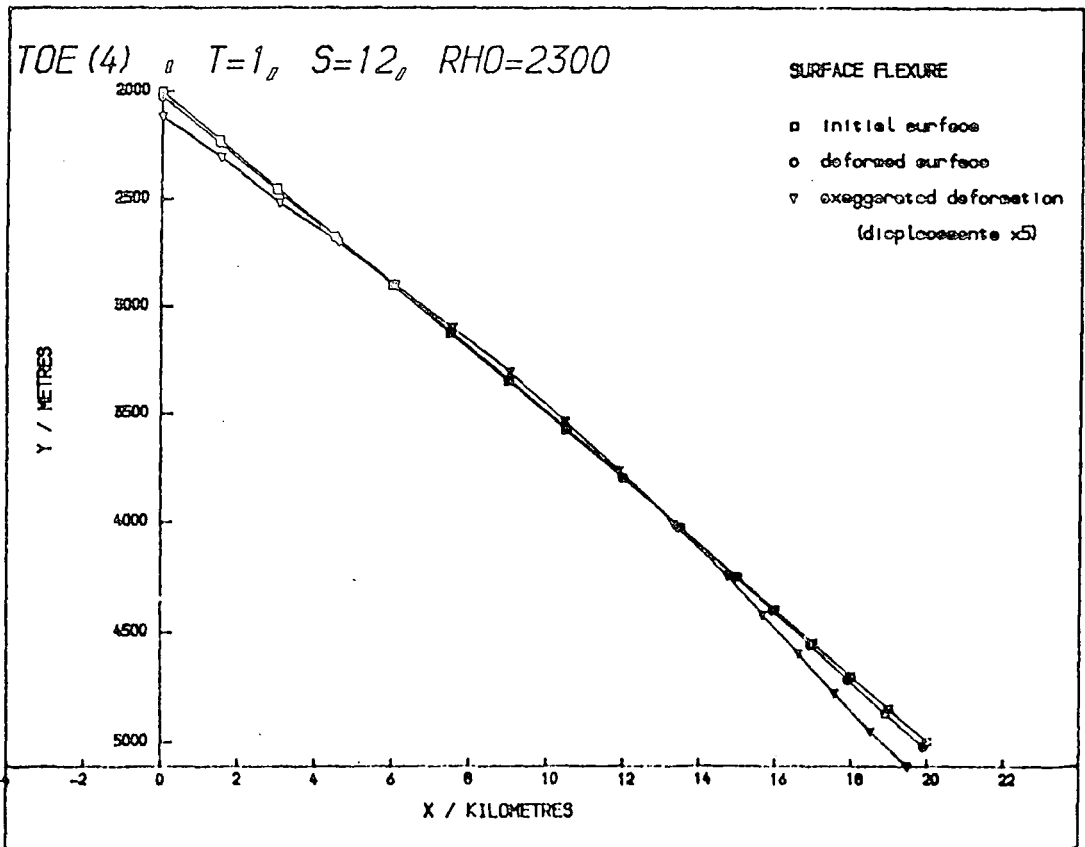
Fig. 5.38: As above for $\rho = 2300$ kg m^{-3}.
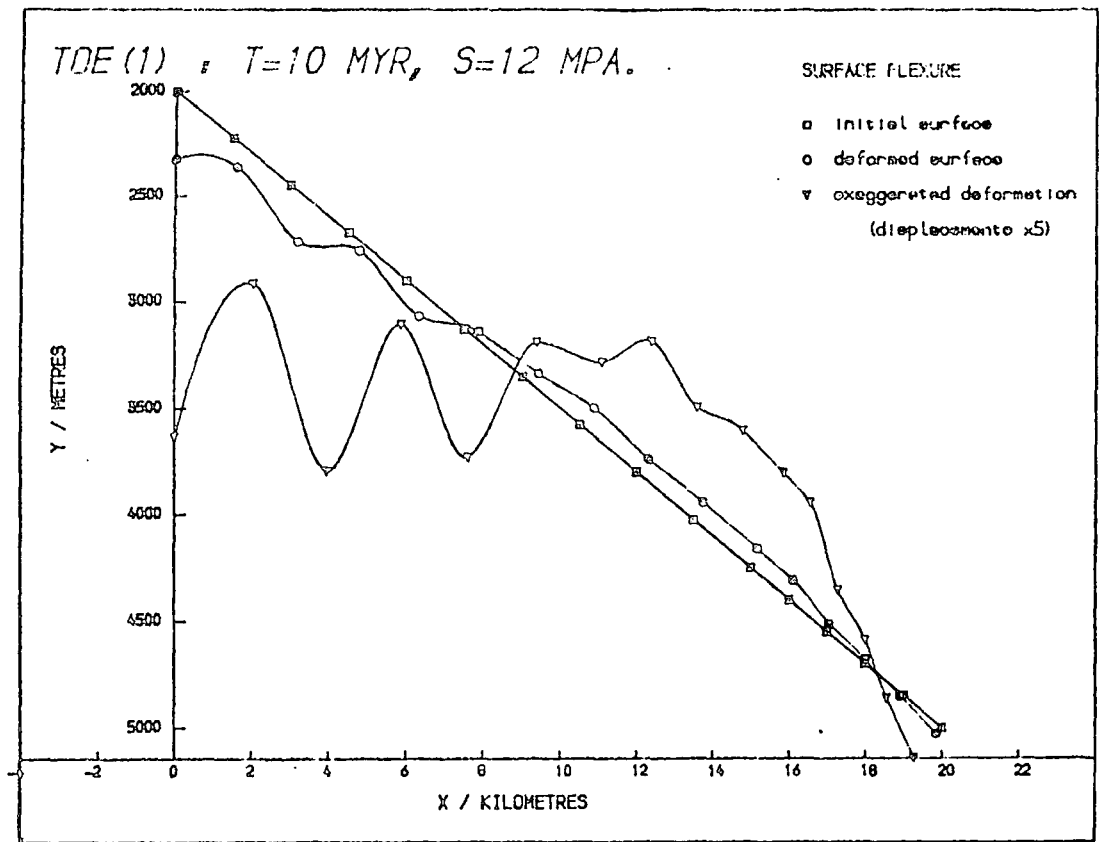
Fig. 5.39: Surface deformation of the wedge after 10 Myr, with a basal stress of 12 MPa.
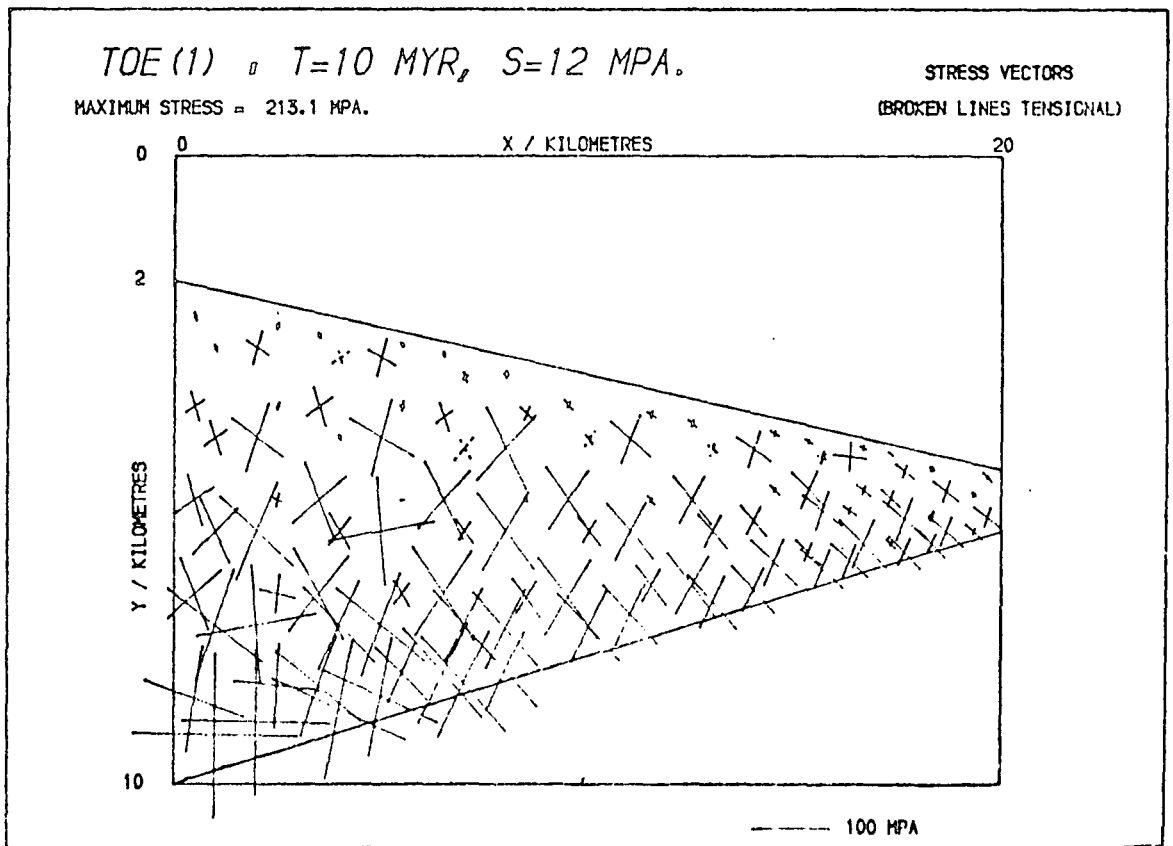
Fig. 5.40: Principal stresses in the same model as above, showing long-term instability in the model.

To find the reason why such a model should become unstable, several test models were run, the first of which was to let the visco-elastic cylinder, used as a test model in Ch. 3 (Section 3.6), relax for 200 time units (compared with the previous maximum of 10 units). This had no significant effect on the stress distribution, which was hydrostatic at the value of the internal pressure, throughout the visco-elastic material.

A second possibility was that the length of the time increments used was too great, but running the same model with the steps reduced by a factor of 10 had no effect above the 1% level.

Finally the importance of the deformation of the grid was considered. The same stiffness matrix (as derived in Section 3.3 of Ch. 3) is used throughout the time over which the model is run, on the assumption that the size and shape of each element does not vary significantly. In the case of the 10 Myr model, the displacements are up to 40% of the dimensions of the element in some places, and so might be significant.

It was more complicated to test this possibility than the previous two, in that the main visco-elastic subroutine had to be restructured to allow a re-definition of the finite element grid at given intervals. However, when this was done it did not provide a solution to the problem. As an example, Fig. 5.41 shows the results of re-running the model of Fig. 5.39, but re-gridding every 1 Myr. The resulting surface is slightly different, but the instability is still present and the stress system shows the same features as before.

Therefore it appears that this instability is due to a combination of the finite element method used (Ch. 3, Section 3.4), the grid used, where the free surface is not horizontal and is not constrained in the x-direction, and the length of time over which the model was run.
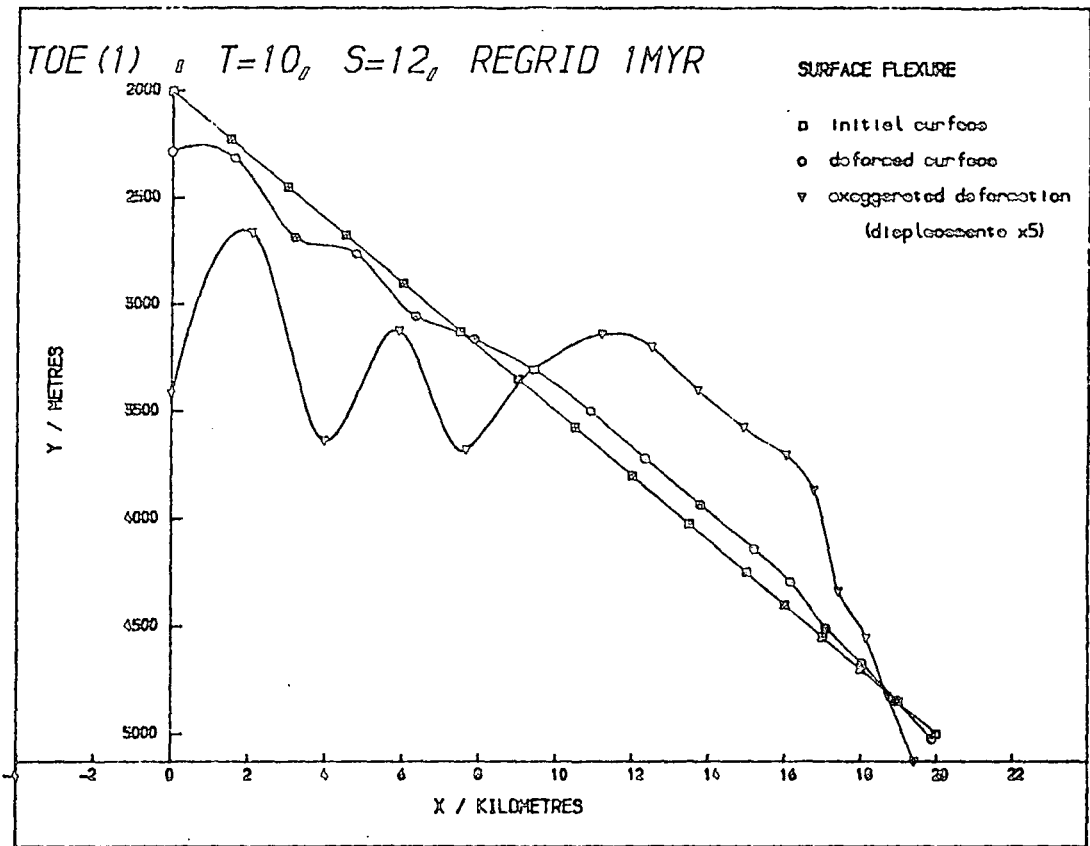
Fig. 5.41: Surface displacements of the wedge model after 10 Myr, with a uniform basal shear of 12 MPa, re-compiling the finite element mesh every 1 Myr.
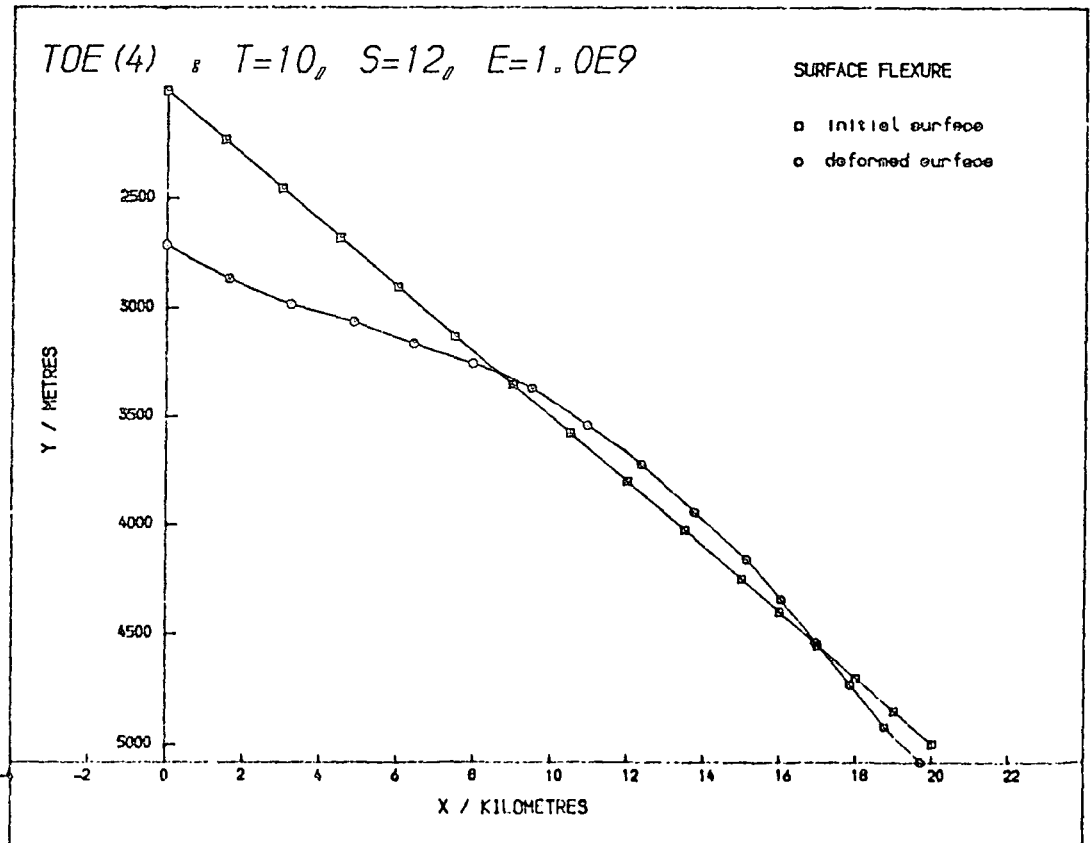
Fig. 5.42: Surface deformation of the wedge after 10 Myr, with a basal stress of 12 MPa, but with a Young's modulus, E = 1 GPa.

The Maxwell time for this model is

$$t_m = \frac{2\eta}{E} \qquad \text{(Equation 3.35)}$$

$$= 0.1 \text{ Myr},$$

so that even after 1 Myr, a rectangular, symmetric model would only have small remaining deviatoric stresses.

In the case where t_m is reduced by a factor of 10 (Fig. 5.33) by increasing E to 100 GPa, the instability can be seen on the upper part of the surface slope, though its effect is smaller because the model is less compressible. Conversely, if t_m is increased by a factor of 10, by decreasing E to 1 GPa, the model is still stable after 10 Myr (see Fig. 5.42; the exaggerated curve is omitted since the displacements are large).

The deviatoric stresses in the model of Fig. 5.12 (run for 1 Myr with a basal stress of 12 MPa) were all below 8 MPa, as mentioned earlier, so that even in this asymmetric model the stresses are nearly hydrostatic. This model was then left to relax for a further 9 Myr (or 90 t_m) to give Fig. 5.39. During this time, because the material has a Maxwell rheology (Ch. 3, Section 3.4), deviatoric stresses in any element tend to relax. However all the elements are interrelated so that the deviatoric stresses in one may only relax at the expense of those in adjacent elements. If some imbalance were set up, perhaps due to the extra degree of freedom of the surface nodes, then it might be accentuated over long periods.

In the first model run for 10 Myr (Figs. 5.39 and 5.40) the deviatoric stresses are at worst the same as after 1 Myr (and mostly reduced by c. 1 MPa), but the creep in each element has resulted in large changes in the hydrostatic stresses. These changes can only occur

in a Maxwell substance because of the restriction to plane strain, which is equivalent to varying stresses perpendicular to the plane of the model.

5.8 Discussion

In this chapter some of the features of deformation beneath trench inner slopes have been isolated by studying simple models. The importance of using visco-elastic, rather than elastic models (Ch. 4) is emphasized by Section 5.5.1, where elastic models could not detect differences between basal shear stresses of 12 MPa and of 6 MPa from the surface displacements, while visco-elastic models could.

When the uniform stress (Section 5.3) and frictional (Section 5.4) boundary conditions are compared, it is apparent that this model cannot distinguish between them. The final surface displacements and principal stress distributions for a shear of 12 MPa and a friction coefficient of 0.09 are very similar. However, both models predict the existence of weaker material in a shear zone along the base of the wedge, and emphasize its importance, in agreement with Seely (1977).

An important difference between the uniform shear and frictional models is their relation to convergence rates. The basal stress applied depends on the relative velocity, v, in the uniform shear model (Equation 5.1), but not according to the frictional model (Equations 5.3 and 5.4) unless there is a dependence of the normal compression, σ_n, across the basal thrust on v. Any such dependence would be reduced because of the shallow dip (c. 11°) of the contact. The former model therefore predicts a correlation between the surface slopes of accretionary prisms and the respective convergence rates (the greater the rate, the steeper the slope), while the latter predicts that rate and slope should be

independent.

However, as Karig and Sharman (1975) point out, the size and consequent shape of the accretionary prism depend more strongly on the rates of sediment input to the subduction zone than on the convergence rate, so it is difficult to distinguish between the two types of model on this basis.

The results of D.S.D.P. Leg 66 (Moore et al., 1979b) show that the whole trench slope has been lifted up (during the Quaternary) at rates varying from 400 m Myr^{-1} at the toe to less than 200 m Myr^{-1} at the landward end of the portion taken for the model. However, none of the models in this chapter shows uplift for the whole of the upper surface, so there must be some important effect other than the shear on the base of the wedge. Watkins et al. (in press) suggest that 50% of the sediment input to the Middle American Trench is subducted, 25% is accreted onto the toe of the slope and 25% is carried down beneath the accretionary prism and then "underplated" onto it. If this were the case, then the effects of accreting more sediments to the toe and of underplating would be superimposed on the effects of the basal shear, and in particular the process of underplating would account for the overall raising of the wedge. A possible mechanism for any underplating is that the basal shear stress may increase with depth beneath the complex, either due to a thinning of the shear zone in the first model (a reduction of d in Equation 5.1), or to an increase in friction coefficient, μ, due to dewatering of the fault gouge (Wang, 1980) in the second. In either case, the effect would be the result of the increase in lithostatic pressure with depth.

The relative vertical movement of the toe and rear of the wedge measured is c.200 m Myr^{-1}, which depends on the effect of any underplating

as well as the basal shear on it. In the simple models of this chapter
the relative vertical displacement after 1 Myr is 25 m for a uniform
shear of 12 MPa, 18 m for a friction coefficient of 0.09, and about
100 m for a uniform shear of 1 MPa. Thus, if all the relative movement
is due to the interaction between weight and basal shear, then the time
scale used is rather too large, i.e. the viscosity used, η (10^{22} N s m^{-2})
is too great (see Section 5.6.1). It was found in the models that the
displacement in the interval 0.1 Myr to 1 Myr was approximately linear,
so that the likely value of η lies in the region

$$10^{21} \leqslant \eta \leqslant 10^{22} \text{ N s m}^{-2}$$

(decreasing η by a factor of 10 will increase the displacements in 1 Myr
by about a factor of 10, also). Underplating may alter the relative
movements considerably, but it is considered that η for the sedimentary
wedge is still within these approximate limits, which are consistent
with the results of Section 5.3.4.

The strains predicted by the finite element model are also of
interest. Fig. 5.4 3 shows the distribution of principal strains in
the model of Section 5.3 (with a uniform basal shear of 12 MPa), which
occur in 1 Myr. The greatest strains are concentrated at the thrust
plane and near the toe of the wedge, and the strains at the surface
on the left of the model are very small (less than 1%).

The magnitudes of the strains are low, all being less than 4%,
which would not be sufficient to produce the deformation observed in
cores taken from the inner trench slope on D.S.D.P. Leg 66 (Moore
et al., 1979a and b; Moore and Watkins, 1979). However, Moore and Watkins,
in their description of drill site 491, note that deformation only occurs
in sediments accumulated in, or near, the trench and in association with
rapid uplift, and that this is followed by an interval of negligible
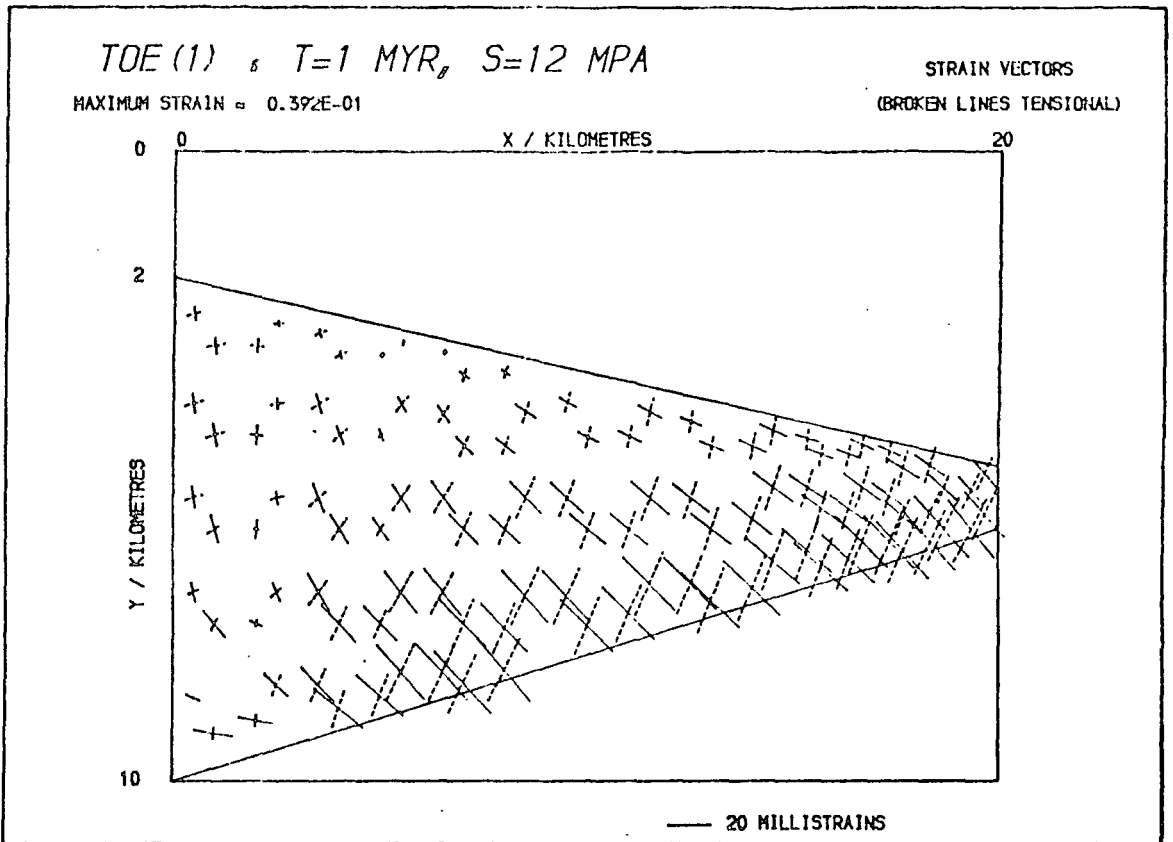
Fig. 5.43: Principal strains after 1 Myr in the equilibrium model with
a basal shear of 12 MPa (Fig. 5.15).
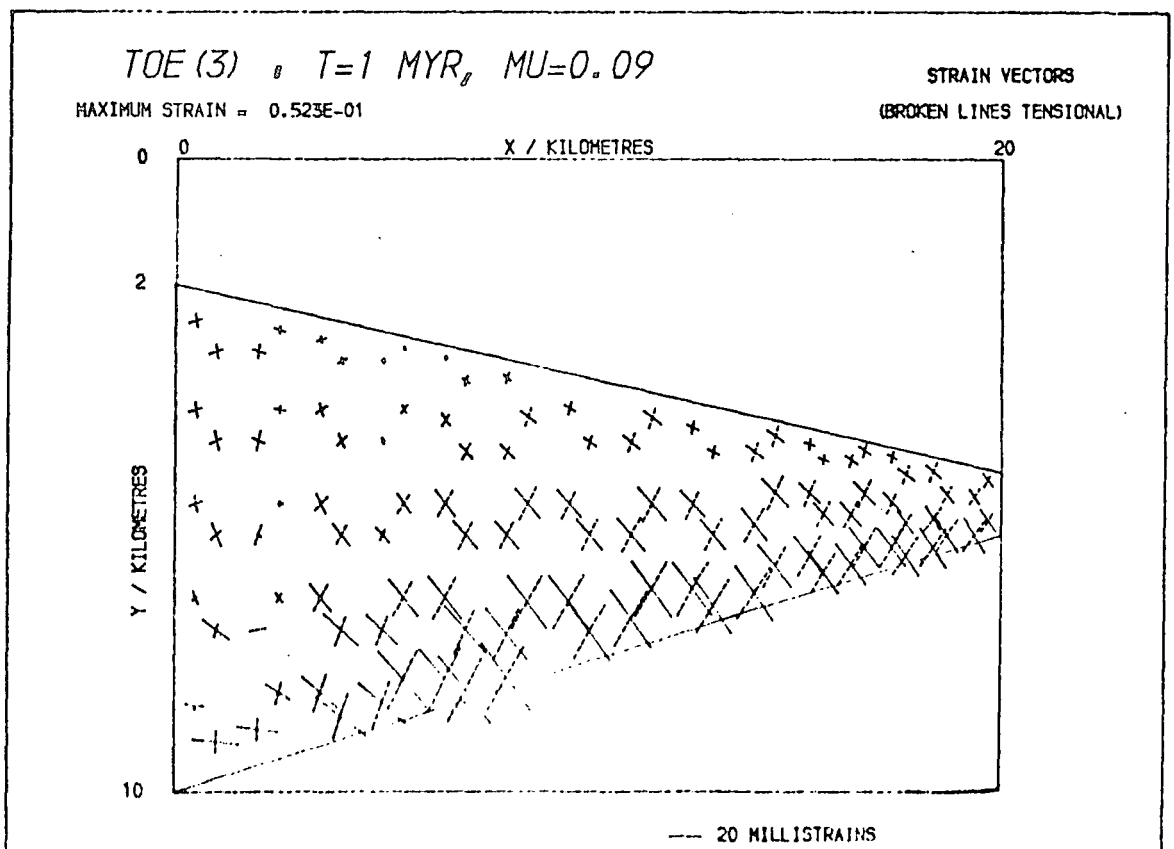
Fig. 5.44: As above for the equilibrium model with a frictional shear at
the base and μ = 0.09 (Fig. 5.23).

deformation (decreasing still more up-slope) and slow uplift. If this were the case, then the greatest strain would occur as the sediments were accreted to the toe of the wedge, and therefore the strains would be much smaller as predicted by the finite element model.

A comparison of Figs. 5.43 and 5.44 (which shows the strains after 1 Myr in the model of Section 5.4 with μ = 0.09) shows that the strain distributions for both types of model are very similar, though the maximum strain for the frictional model is 5% rather than 4%. Thus strain analysis cannot distinguish between the two basal thrust mechanisms presented in this chapter.

A further complicating factor affecting the deformation is the effect of variations in lithology within the wedge, especially the shape of material boundaries such as that between igneous crust and accreted sediments. These variations will be discussed in the next chapter.

CHAPTER 6

THE IMPORTANCE OF THE CONTRAST BETWEEN CRYSTALLINE BASEMENT AND
ACCRETED SEDIMENTS

6.1 Introduction

In the previous chapter, the wedge of accreted sediments forming
the inner wall of the Middle America trench was modelled, assuming that
its landward end remained fixed horizontally, in other words taking the
crust behind it as a fixed frame of reference. In reality, however, the
thicker end of the wedge is supported by more accreted sediments and,
further back, by the crystalline basement rocks of the overriding plate
(continental crust in the case of the Middle America subduction zone, but
igneous oceanic or island arc crust in the case of an ocean-ocean plate
boundary; see Fig. 1.2).

As mentioned in Chapter 1 (Section 1.4), the position and shape of
the lithological boundary between accreted sediments and igneous crust
have not been clearly defined by observations. In this chapter, results
are presented of the analysis of models of two subduction zones where the
shape and extent of the crystalline basement differ appreciably, to
ascertain the effect of these different structures on the stresses
within the accretionary prism and upper slope basin, and on the shape of
their upper surfaces.

The boundary conditions used for these models were the same as those
for the models of Chapter 5 (see Section 5.2.2), except that by holding the
landward end against horizontal displacement, a position further back in
the overriding plate was implicitly taken as a fixed frame of reference.

6.2 A Model of the Middle America Subduction Zone

6.2.1 Description of the model and a first solution

This model was based on the same set of data as the wedge in the previous chapter, namely the D.S.D.P. transect of the Middle America trench (Fig. 1.3, Ch. 1; Moore et al., 1979) and the finite element grid used is shown in Fig. 6.1. The latter also shows the position of the lithological boundary based on Fig. 1.3 (the material type of each element is indicated in Fig. 6.1 by: 1 for crystalline basement, 2 for tectonized sediments), rocks on either side being assigned appropriate properties which are listed in Table 6.1 (see Ch. 2, for the justification of these figures and definition of symbols).

Lithological type	E/GPa	ν	ρ/kgm^{-3}	$\eta/N\ s\ m^{-2}$
Continental basement, 1	90	0.27	2850	10^{25}
Accreted sediments, 2	10	0.27	2500	10^{22}

Table 6.1:   Properties assumed in modelling the Middle America subduction zone.

Figures 6.2 and 6.3 show the surface displacement and principal stress distribution, respectively, obtained by applying a uniform basal shear of 12 MPa to the body and allowing visco-elastic deformation for 1 Myr. This value of basal stress was chosen because it was the equilibrium value for the model in Section 5.3 (Ch. 5) which represents the toe of this model (from x = 22 km, onwards).

Although the boundary conditions on the toe are now different, in
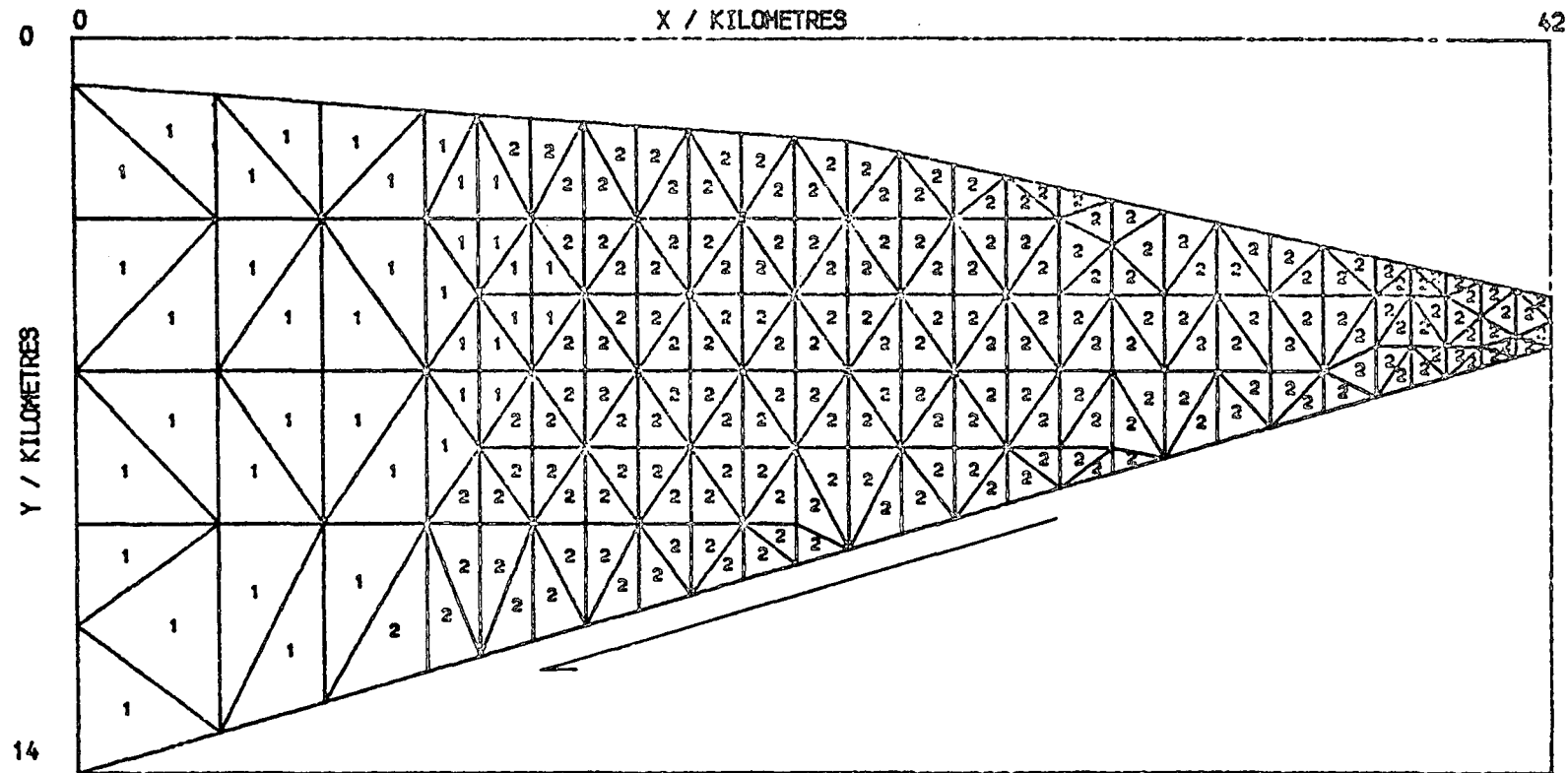
Fig. 6.1: The grid used in Section 6.2.1 for modelling the Middle America
subduction zone. The material type of each element is indicated
at its centroid: 1. Crystalline basement
                      2. Accreted sediments.
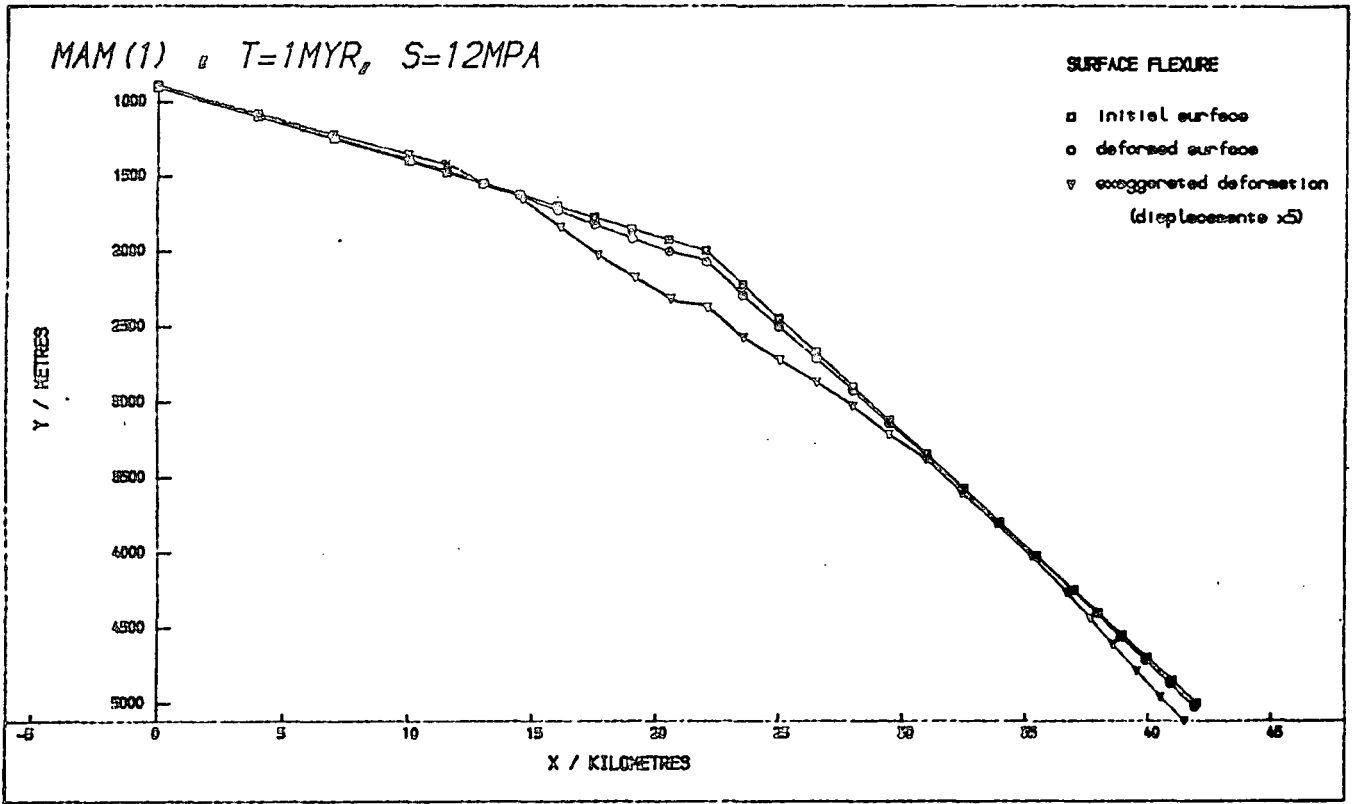
Fig. 6.2:   Surface displacements of the model of Fig. 6.1 after 1 Myr,
            with a basal shear of 12 MPa.
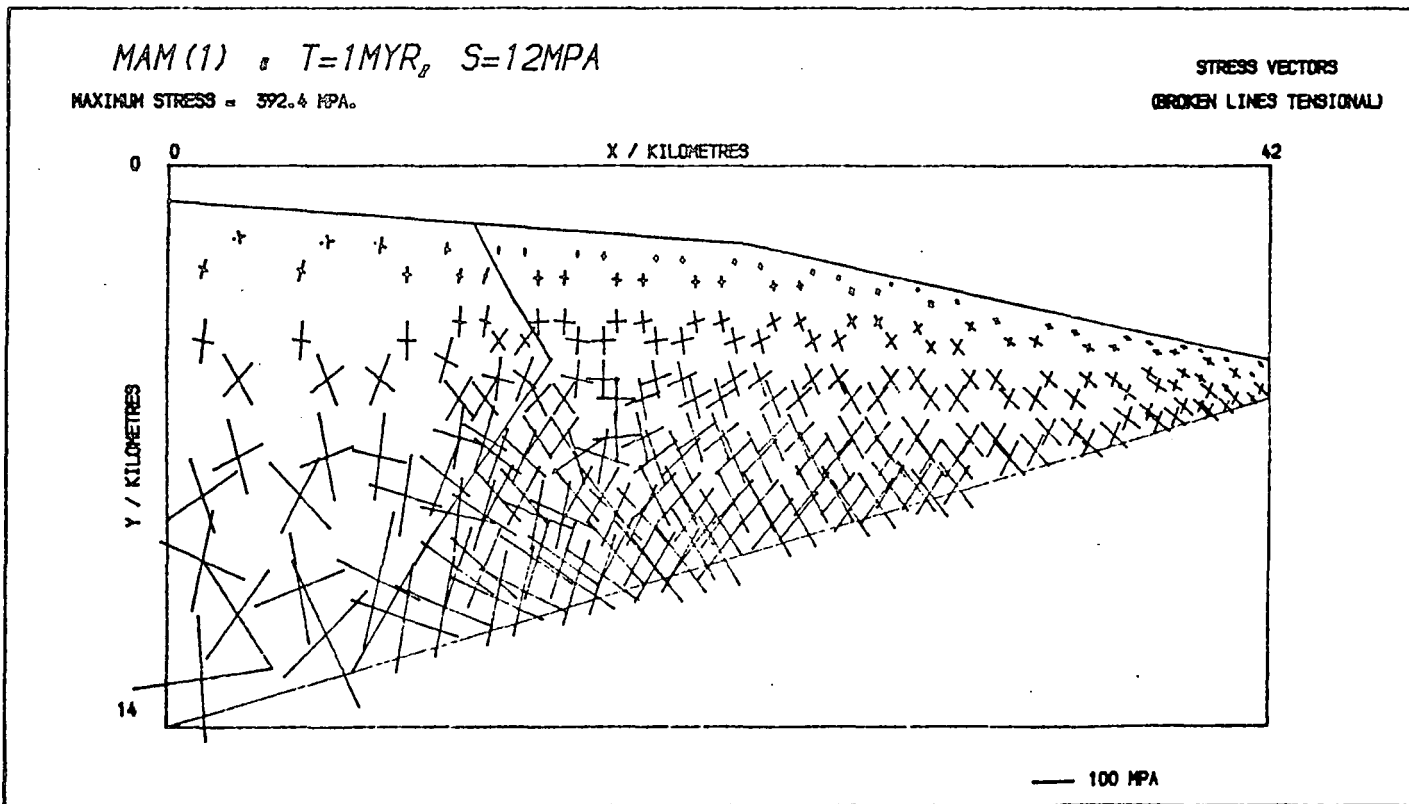
Fig. 6.3:   Principal stresses in the same model as above.

that the boundary of the simpler model (represented by the nodes at
x = 22 km) was fixed, but is now free to move both vertically and
horizontally, the applied stress was still found to keep the slope of
the toe nearest to equilibrium. The average displacement of the
surface is maintained at c. 20 m, although now there are somewhat larger
vertical displacements in places. The displacements near the trench are
similar to the simple toe model, but further back they become greater
(downwards), being about 70 m near the trench slope break (at x = 22 km)
which is a factor of 2 larger than in the previous wedge model.

The most striking feature of the surface deformation (Fig. 6.2) is
the draping of the sediments at the front of the continental section. The
nodes on the continental part of the model show very small displacements,
of up to 10 m upwards and 5 m to the left, while the surface nodes on
the accreted section show increasing subsidence to a maximum of 80 m,
just behind the trench slope break (as defined by the change in surface
slope in Fig. 6.1). The displacements then become smaller again over the toe,
as described above.

The stress system in the accretionary prism is close to hydrostatic,
with deviatoric stresses of less than 12 MPa everywhere. The deviatoric
stresses are largest at the base (where the shear stress is applied) and
drop to less than 5 MPa along the surface, except in the two elements
closest to the continental block where there are (near-horizontal)
deviatoric tensions of c. 7 MPa. Typical deviatoric stresses in the
accreted sediments are c. 6 MPa, indicating that they are close to equilibrium
as expected after 1 Myr (the Maxwell time for these sediments is
$t_m \simeq 0.06$ Myr).

In the continental crust, however, there are deviatoric stresses
of up to 50 MPa. The distribution of these stresses suggests that they are

caused by rotation of the continental crust away from the fixed (landward) boundary, due to the movement exerted by the weight of the undercut part of the basement and by the basal shear stress.

Near the surface, the mean stresses are in the tensional region, as defined by the failure criteria of Section 2.3, Ch. 2, and vary, through the open crack and intermediate regions, to compressional at the base. However, the program does not predict any failure when the tensile strength of the basement rocks is taken to be T = 50 MPa, the closest to fracture being a value for the degree of failure (see Section 2.3) of C $\simeq$ 0.3. On the other hand, if T = 10 MPa for this section, a value which is still consistent with those given in Section 2.3.5, then tensional failure is predicted at the top of the continental crust, the angle of failure being taken between 75° and 80°, corresponding to high-angle normal faulting. There is still no failure at the base of the continental crust, the element closest to failure having C $\simeq$ 0.7, where the dip of the plane where failure would be most favoured is c. 40° landwards.

Failure predictions in the sedimentary wedge are complicated by the presence of pore water, and this will be discussed in Section 7.1 of the next chapter.

As with the models of the toe of the accretionary prism in Ch. 5 (see Section 5.8), the strains in this equilibrium model are all small, being less than 0.3% in the continental basement and rising to a maximum of 5% along the base of the accreted wedge. Strains on the lower slope are between 1% and 2%, the larger values being nearer the toe. This supports the suggestion that most of the strain observed in the accreted sediments occurs as they are being scraped onto the toe of the wedge.

6.2.2 The extent of the continental basement

To find the effect of the edge of the continental crust on the wedge deformation, several models were run in which its position was varied.

Figure 6.4 shows the first of these models, and Fig. 6.5 the surface deformation after 1 Myr, for comparison with the original model of Figs. 6.1 to 6.3. The front of the continental crust has the same shape as before, but has been moved backwards by 3 km at depth, leaving the position where it reaches the surface unchanged (consistent with the D.S.D.P. Leg 66 results; see Fig. 1.3). This change has removed some of the supporting basement from beneath the upper slope, and at the same time allowed more of the accreted sediments to be forced under the overhanging part of the continental crust, with the result that the upper slope has subsided more in front of the continental edge, but that the latter has been lifted up more than in Fig. 6.2. The maximum uplift has been increased from 10 m to 20 m, while the subsidence just behind the trench slope break has increased from 80 m to 90 m, the greatest increase in subsidence being from 50 m to 75 m near the contact with the crystalline basement.

The region of subsidence in model 1 of this section (Fig. 6.4) has therefore deepened and broadened, while the transition from uplift to subsidence at the trailing edge of the upper slope has become sharper. Displacements on the lower slope have all been increased by about 5 m (downwards).

The resulting stress distribution (not shown) is very similar to the original model (Fig. 6.3), the only difference being that the stresses in the continental crust are reduced. This is interpreted as being a result of the reduced weight of the crystalline basement. Tensional failure (normal faulting) is more strongly favoured in the upper crust, because the turning moment (as described in Section 6.2.1) has been
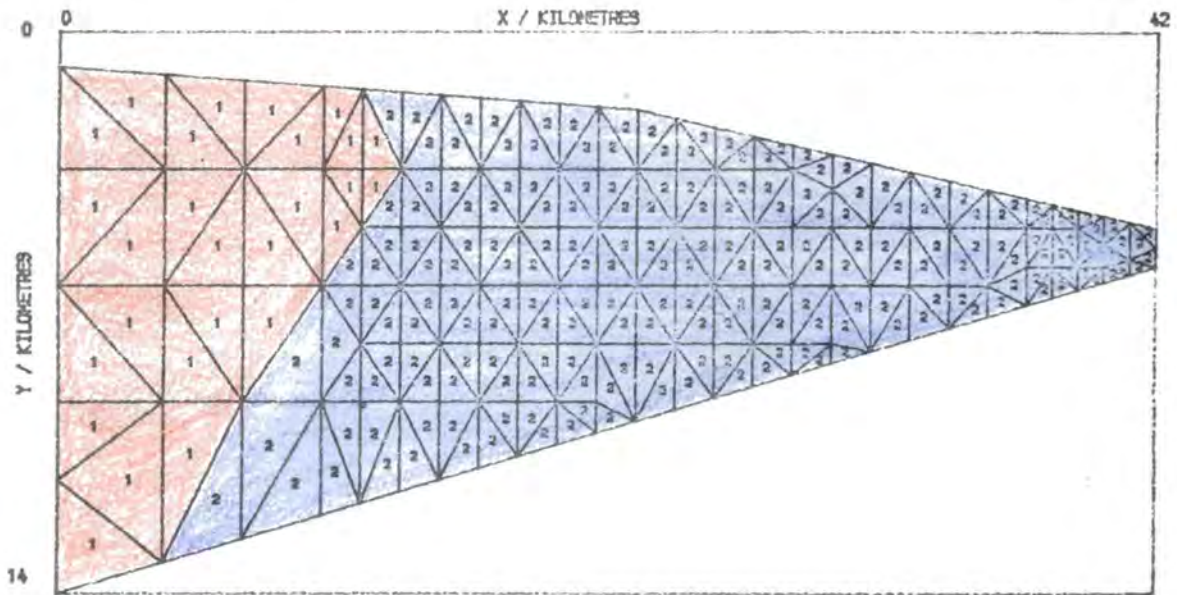
Fig. 6.4: Model 1 of Section 6.2.2, with the edge of the continental
basement moved 34 km landward, at depth, from that of Fig. 6.1.
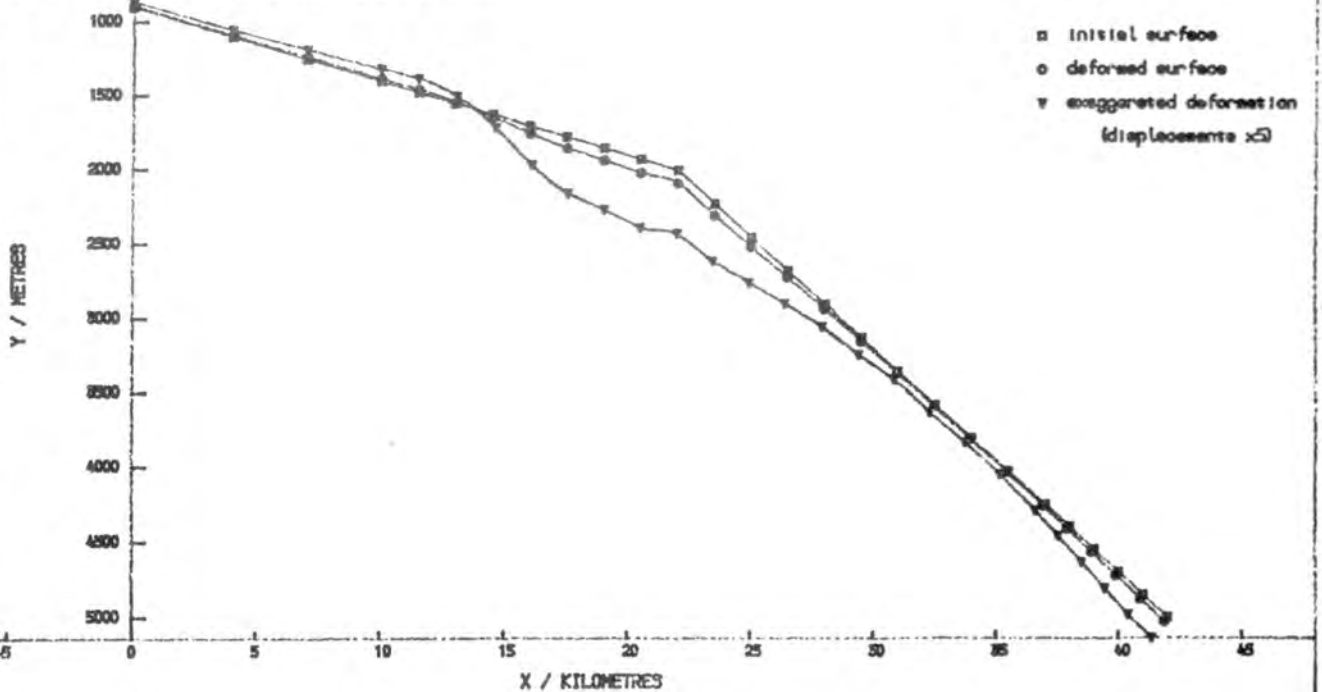
Fig. 6.5: Surface displacements in the above model for 1 Myr, basal shear
12 MPa.

increased by cutting back the lower part of the continental basement, but, because of the reduced weight of crystalline basement present, compressional failure is less likely (i.e. the degree of failure is larger, $C \simeq 0.8$) at the base.

Model 2 of this section is shown in Fig. 6.6 and the resulting surface displacements, under the same conditions as before, in Fig. 6.7. In this case the leading edge of the continental basement has been moved forward 3 km from the initial position of Fig. 6.1, rather than back, and the effects on the surface deformation are as predicted by the previous two models. In other words, the uplift at the top of the continental crust has been reduced, to less than 5 m, the subsidence behind the trench slope break (again as defined by the slope of the model surface) has been reduced, to about 60 m (cf. 80 m in the original model), the draping over the edge of the continental basement has become less steep, and the downward displacements of the lower slope are reduced by c. 5 m (although the latter has kept the same shape).

The principal stress vectors for this model are shown in Fig. 6.8. It can be seen that again they are of the same type as in Fig. 6.3, but with the stress levels (both total and deviatoric) reduced in the crystalline basement, the deviatoric stresses being less than 20 MPa everywhere, except at the contact with the accreted sediments where they rise to 35 MPa.

The tensional failure in the upper part of the model is no longer predicted (the lowest value for C is + 0.6), because the rotation of the basement is counteracted more by the thicker section of igneous rocks. Compressional faulting at the base, on a plane dipping at 30° to 40° landward, is more favourable than before, although the degree of failure is still $C \simeq 0.6$.
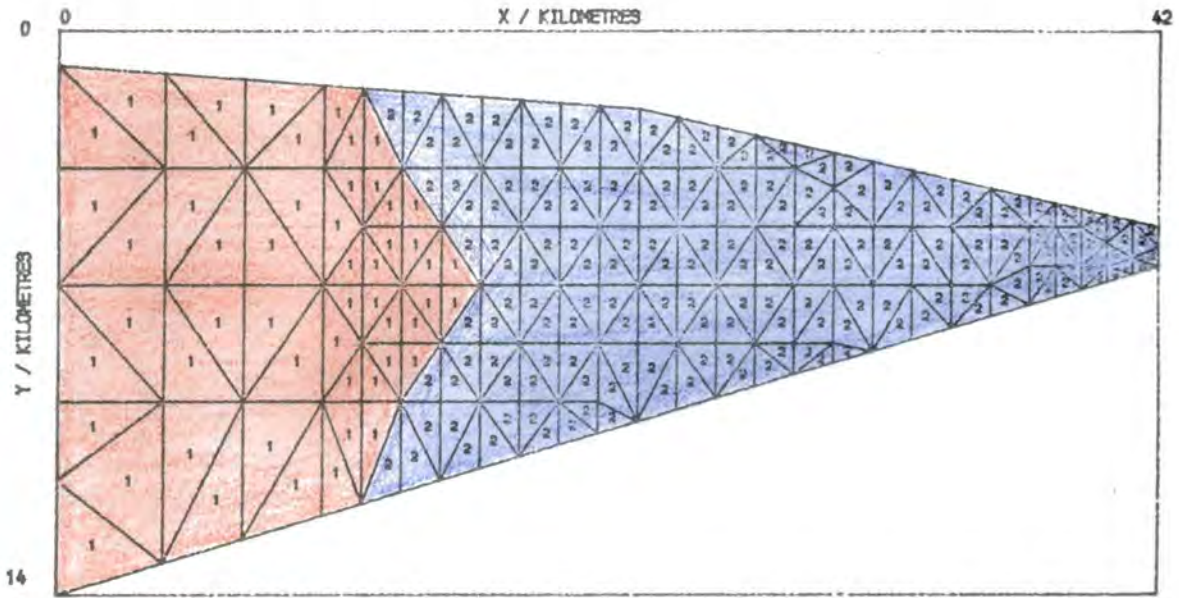
Fig. 6.6: Model 2 of Section 6.2.2, with the edge of the continental
basement moved seaward by 3 km from that of Fig. 6.1.
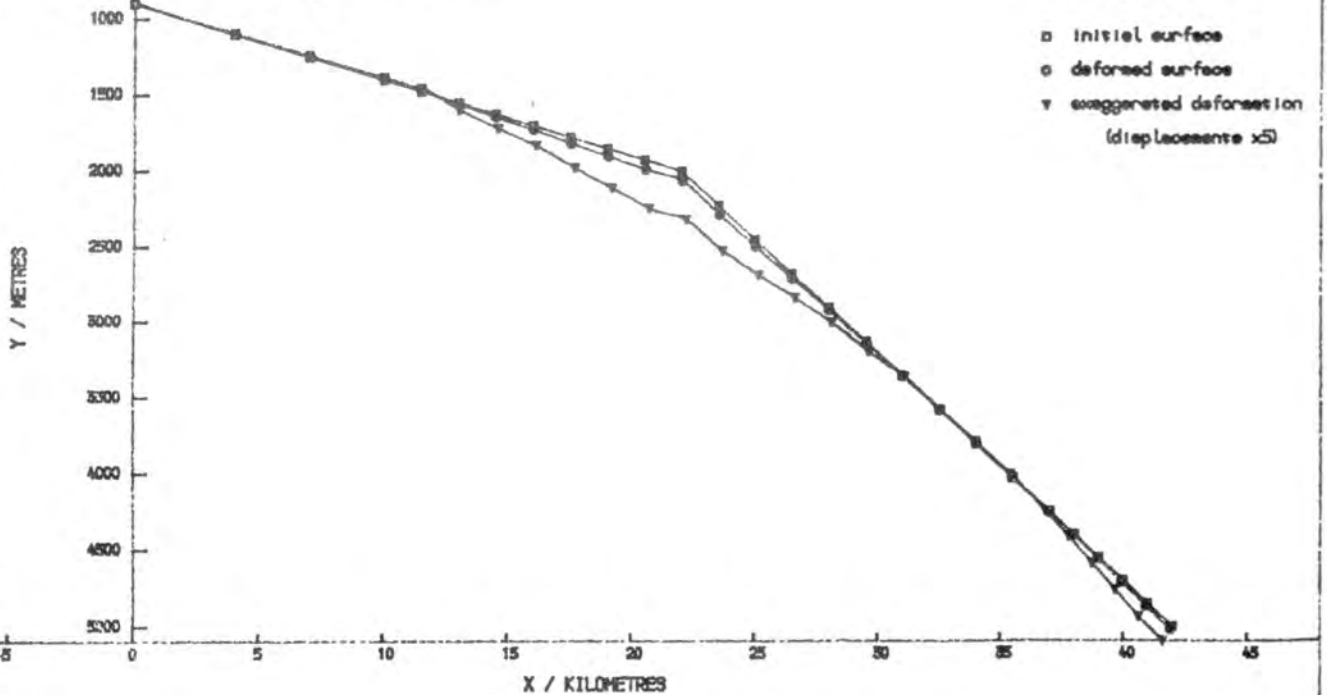
Fig. 6.7: Surface deformation of the above model after 1 Myr, with a basal
stress of 12 MPa.
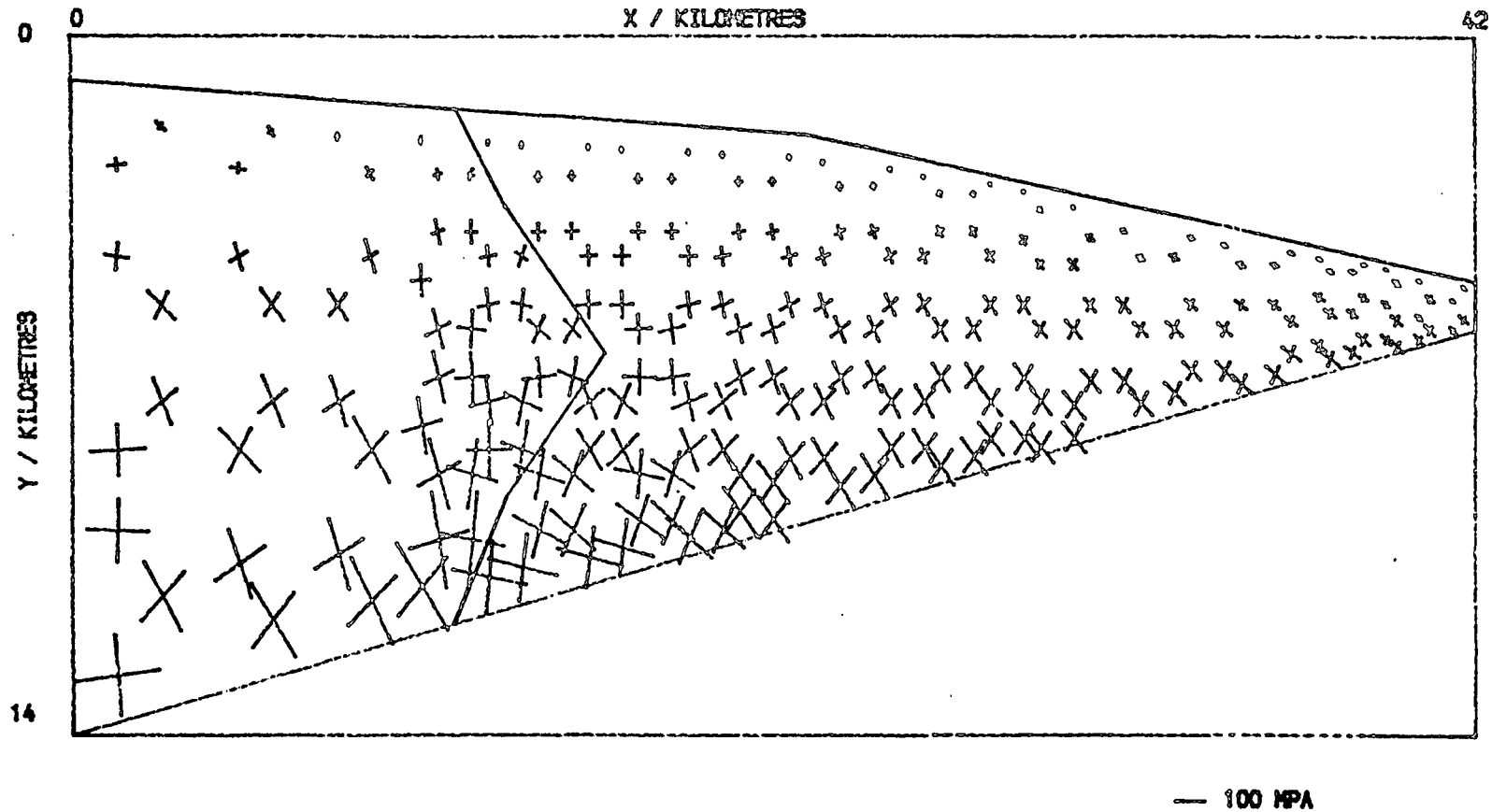
Fig. 6.8: The principal stresses in the second model of Section 6.2.2
(Figs. 6.6 and 6.7).

Figure 6.10 shows the effect of continuing the crystalline basement down to the basal thrust plane, without any overhang (model 3 of this section; Fig. 6.9). The displacement of the upper surface is similar in shape to that of the initial model of Section 6.2.1 (Fig. 6.2), but all displacements are reduced, the maximum subsidence, just behind the model's trench slope break, being c. 60 m.

This effect is increased in model 4 (Figs. 6.11 and 6.12), where the igneous basement has been continued beneath the whole upper slope to the trench slope break, and here the surface is held almost stationary for its whole length. The maximum vertical displacement is c. 30 m over the end of the tongue of continental rocks.

Both the last two models (3 and 4) have significantly different stress distributions from those of the other models in this chapter (see Figs. 6.13 and 6.14), in that the near-horizontal principal stresses at the top of the continental section are compressional, not tensional. The turning moment exerted by the weight of the igneous crust has been nullified by continuing it down to the basal thrust. Thus, in these two models, the basal shear stress is transmitted through the igneous basement as a compression which is approximately parallel to the boundary with the accreted sediments. No fracturing is predicted anywhere within the continental crust in either model.

The strains in all the models of this section are similar to those in the equilibrium model. By bringing the continental basement forward all the strains in the model are reduced, but only by 1% at the most. The greatest strain in the accreted sediments for the model of Fig. 6.11 is 4% (corresponding to shear along the base) rather than 5% in the original model. The strains in the continental basement are reduced to 0.1% and those along the upper part of the inner slope to 0.8% (cf. 0.3% and 1%

MAM.23 . T=1MYR, S=12MPA

ELEMENT MESH
(WITH MATERIAL NUMBERS)
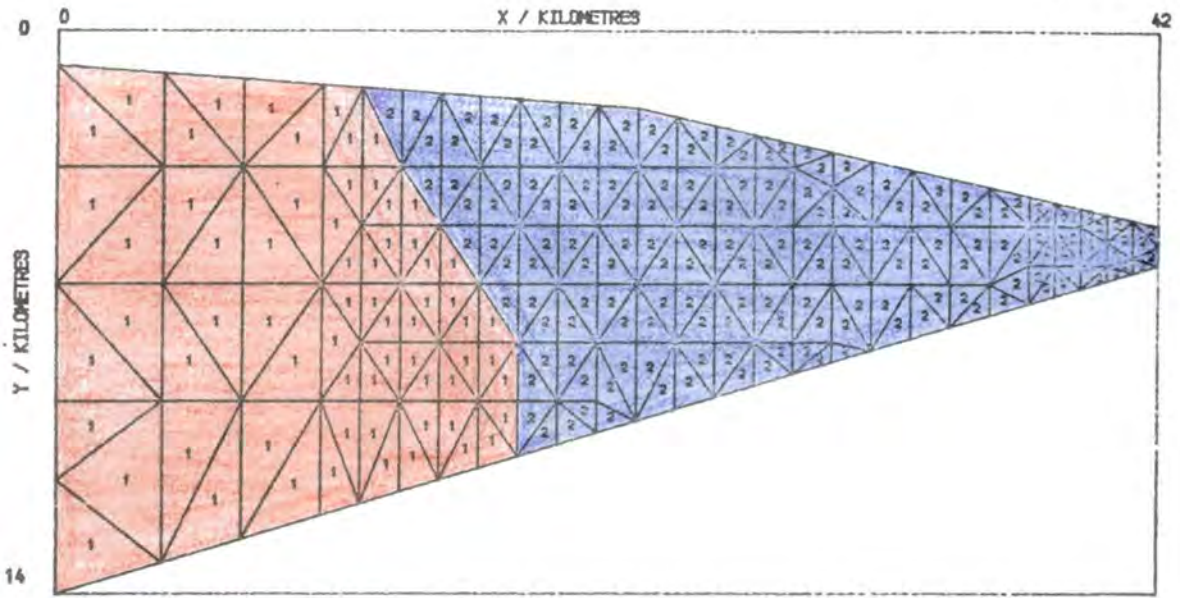
Fig. 6.9: Model 3 of Section 6.2.2, where the continental basement is in
contact with the basal thrust for 10.5 km further than in Fig. 6.1.

MAM.23 . T=1MYR, S=12MPA

SURFACE FLEXURE

□   initial surface
o   deformed surface
▼   exaggerated deformation
       (displacements x5)
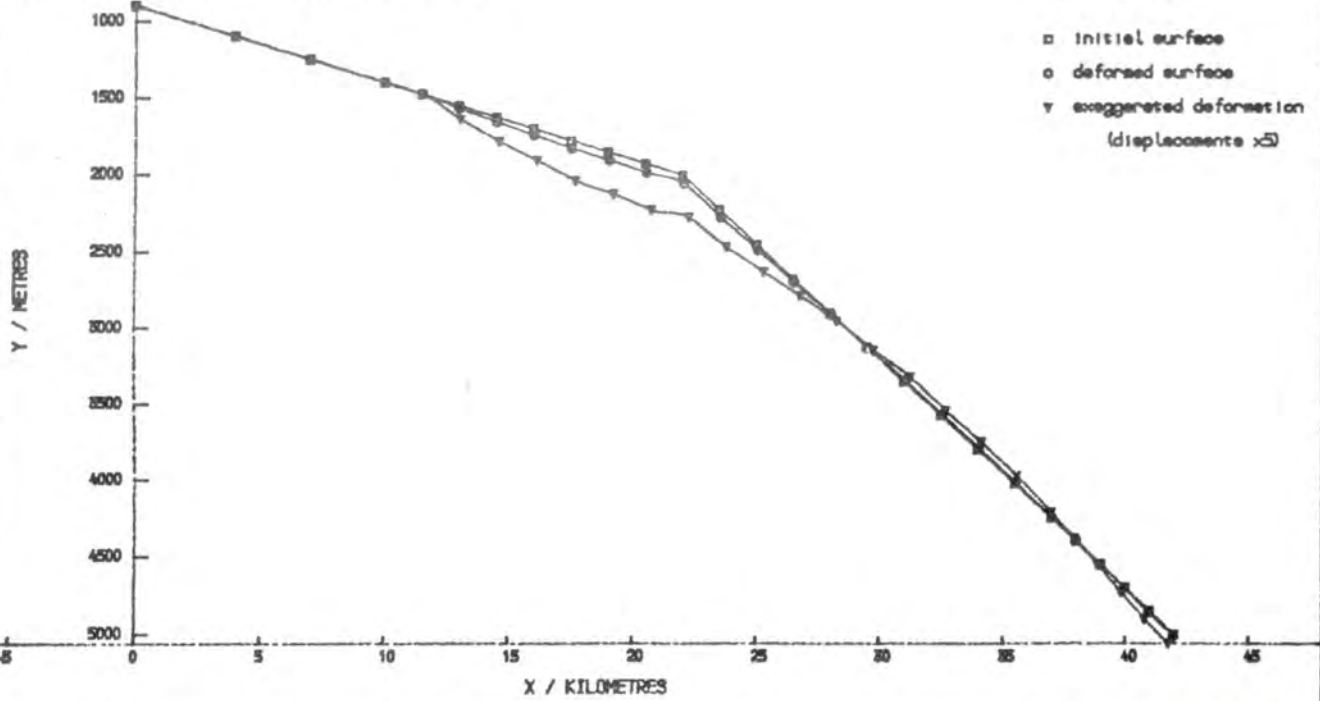
Fig. 6.10: The surface displacements of the above model with a basal
shear of 12 MPa, after 1 Myr.
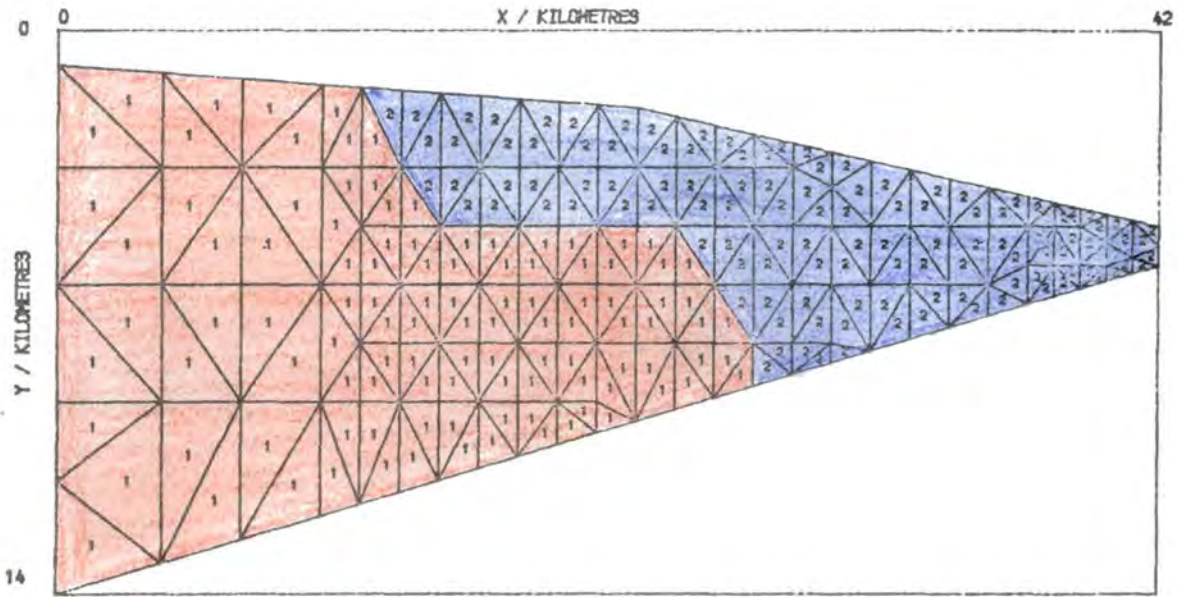
Fig. 6.11: Model 4 of Section 6.2.2, in which continental basement underlies
the whole upper slope.
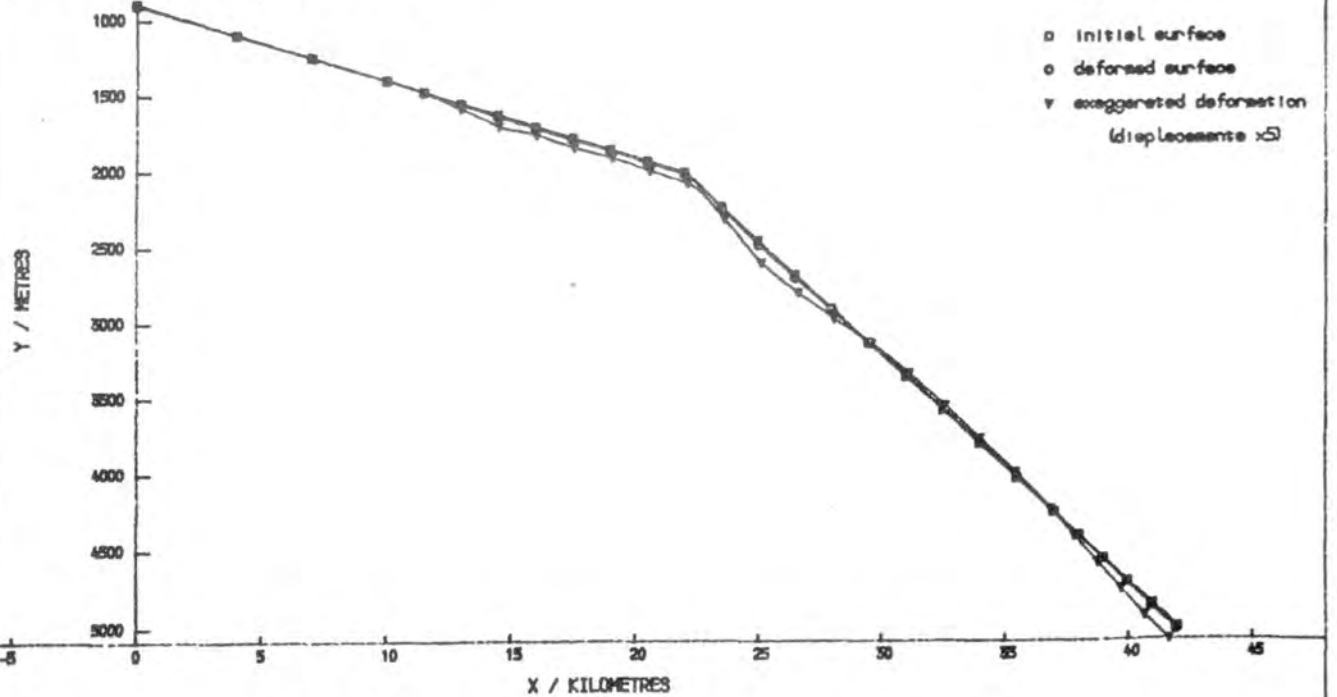
Fig. 6.12: The surface displacements of model 4 (above) after 1 Myr,
with a basal stress of 12 MPa.

STRESS VECTORS
(BROKEN LINES TENSIONAL)

MAXIMUM STRESS = 532.6 KPA.
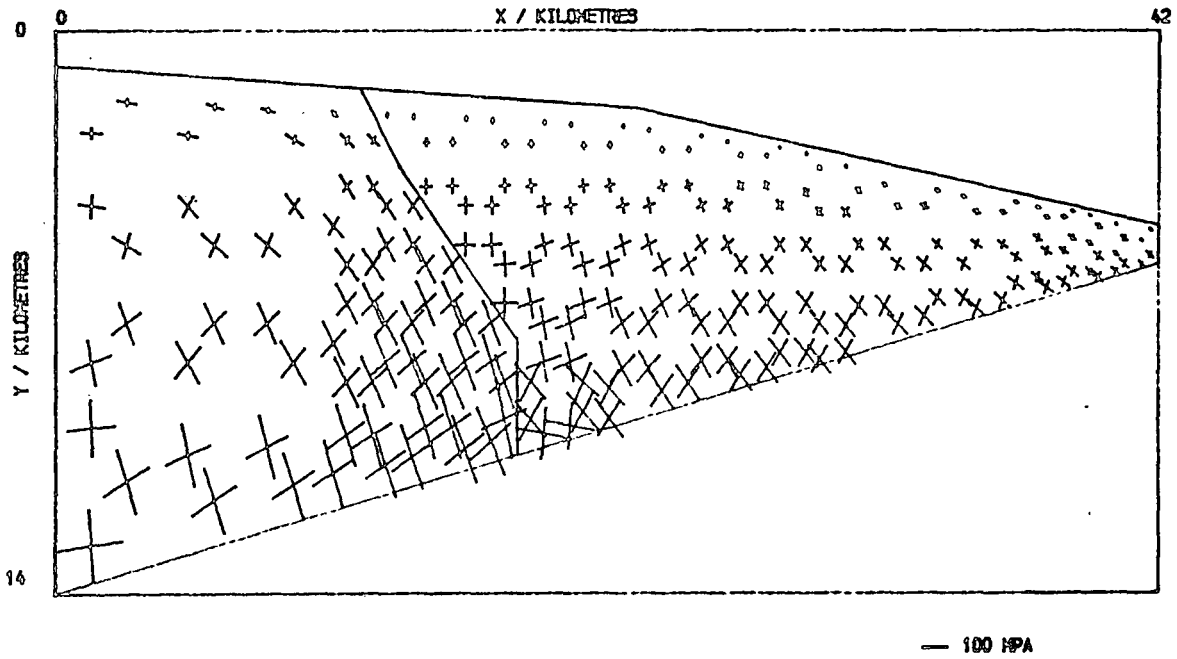
Fig. 6.13:   Principal stresses in model 3 (Figs. 6.9 and 6.10).

MAM. 24 ⍺ T=1, S=12MPA

STRESS VECTORS
(BROKEN LINES TENSIONAL)

MAXIMUM STRESS = 297.1 KPA.
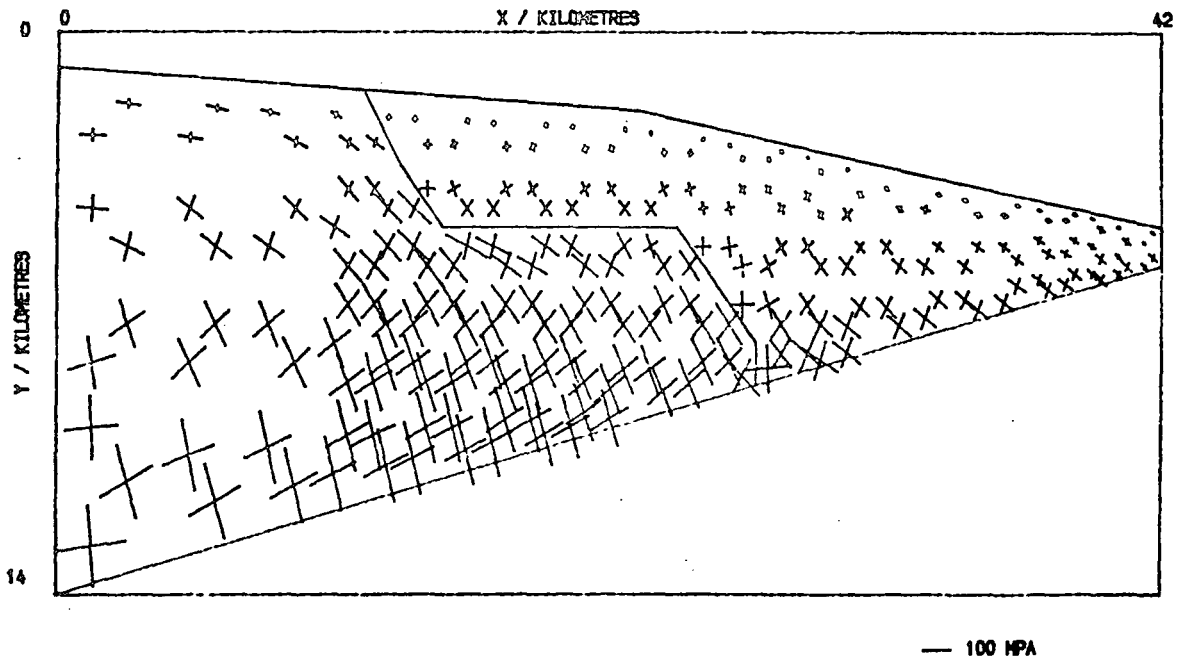
Fig. 6.14:   Principal stresses in model 4 (Figs. 6.11 and 6.12)

respectively, in Section 6.2.1).

6.2.3 The effect of variations in basal stress on the surface flexure

Figures 6.15 and 6.16 show the surface displacements for the original model of Section 6.2.1, with basal shear stresses of 0 and 20 MPa respectively.

In the case where there is no basal shear, the displacements on the upper surface follow a similar pattern to the equilibrium model (with τ = 12 MPa; Fig. 6.2), except that now the upper slope subsides more, by a factor of 3, c. 250 m, and has forced the toe of the prism to slide up the basal thrust (by c. 110 m vertically, 550 m horizontally).

When there is a large basal shear, 20 MPa, Fig. 6.16 shows that the surface displacements change radically. There is uplift (of up to 65 m) of the upper slope, and the lower slope is pushed backwards by c. 550 m and steepened (from 8.5° to 9°). In the light of the observations discussed in Sections 1.3 and 1.4 of Ch. 1, namely that there should be uplift of the lower slope and subsidence of the upper slope, this basal stress is considered to be too large. Even if material were being added to the toe of the prism, which would reduce the angle of the lower slope, the upper slope would still be pushed upwards. From the stress needed to hold the upper slope close to its original position, it may be deduced that the basal shear stress under the accretionary prism of the Middle America trench,

$$\tau \lesssim 15 \text{ MPa}.$$

The principal stress distributions in the first two models of this section are also significantly different from each other. In the first (Fig. 6.17) where there is no basal shear stress, the clockwise rotation of the continental basement is greater than in the original model
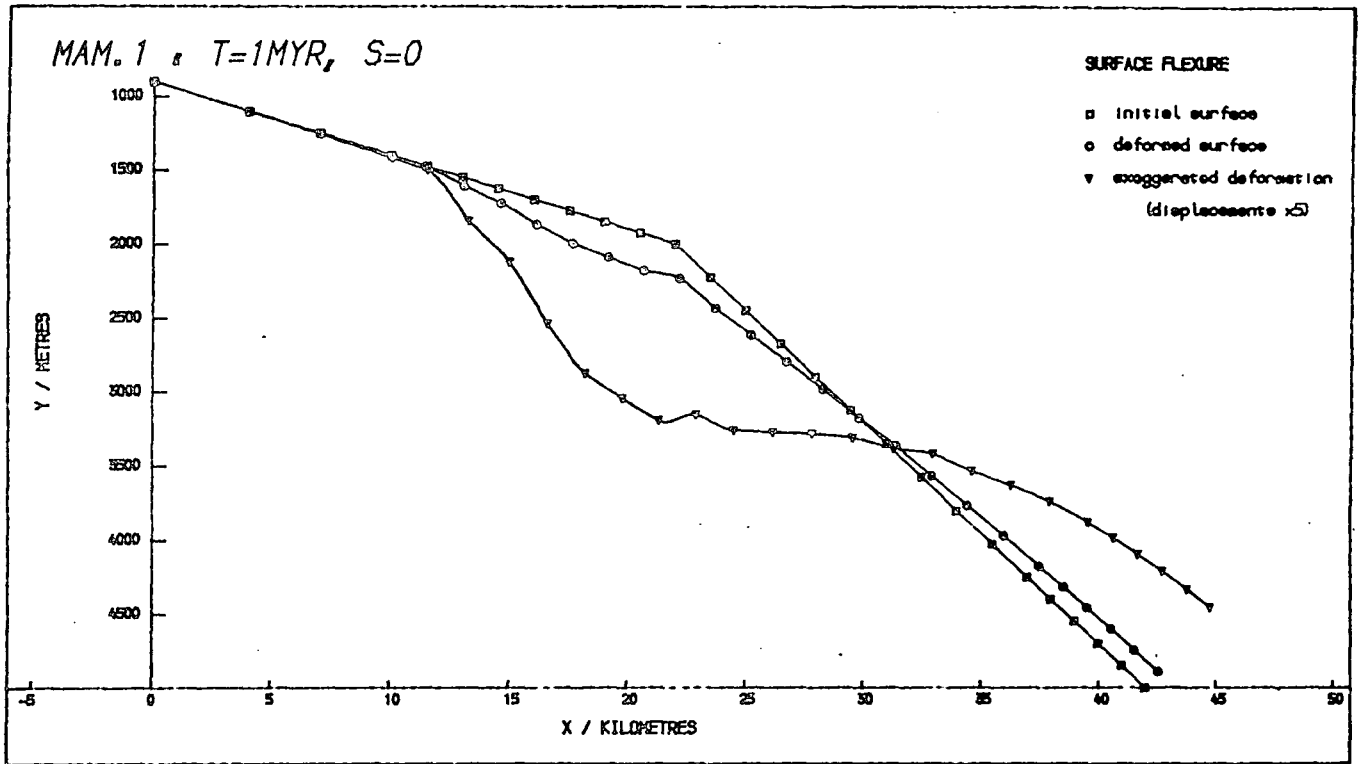
Fig. 6.15: Surface deformation of the original model (Section 6.2.1, Fig. 6.1), after 1 Myr with zero basal shear stress.
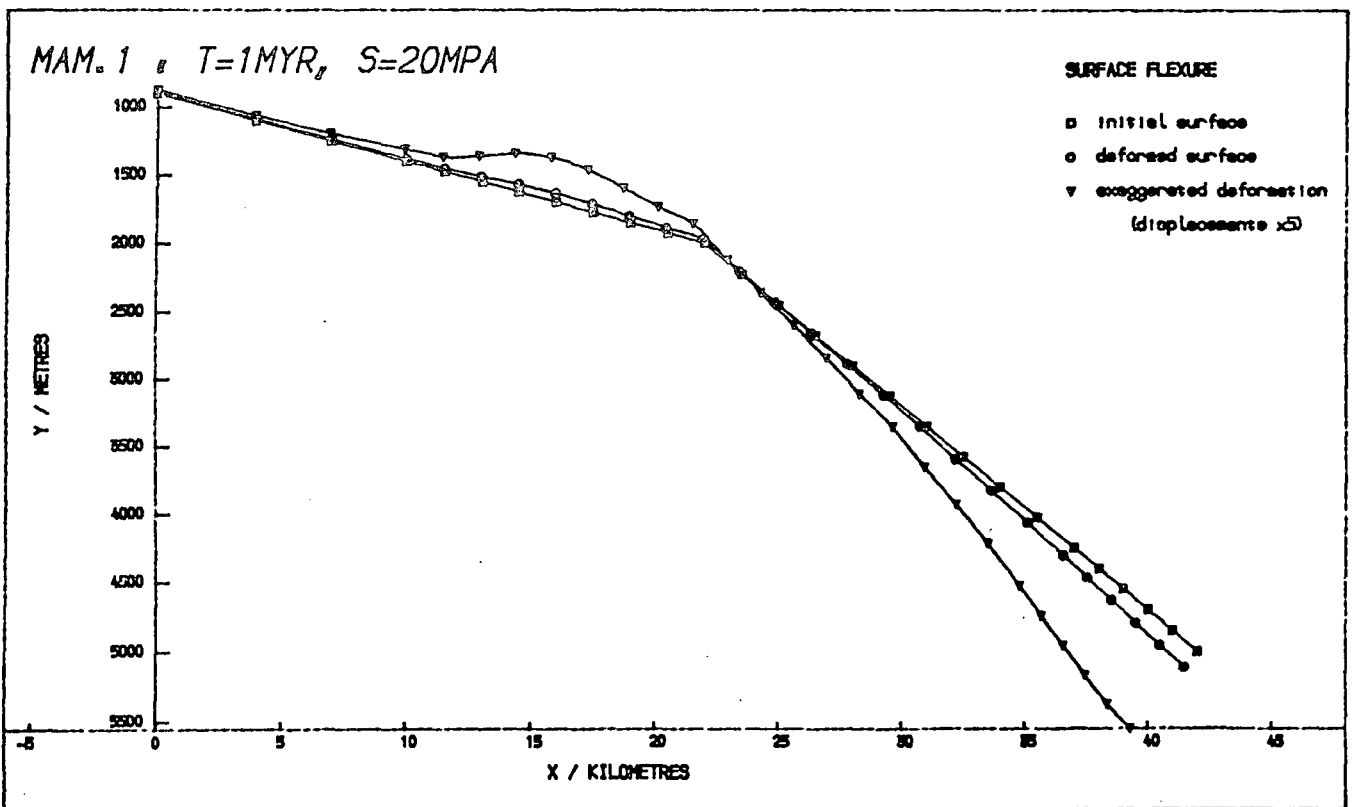
Fig. 6.16: As above with a shear stress of 20 MPa on the basal thrust.

X / KILOMETRES

0   42

Y / KILOMETRES

0

14

— 100 MPA
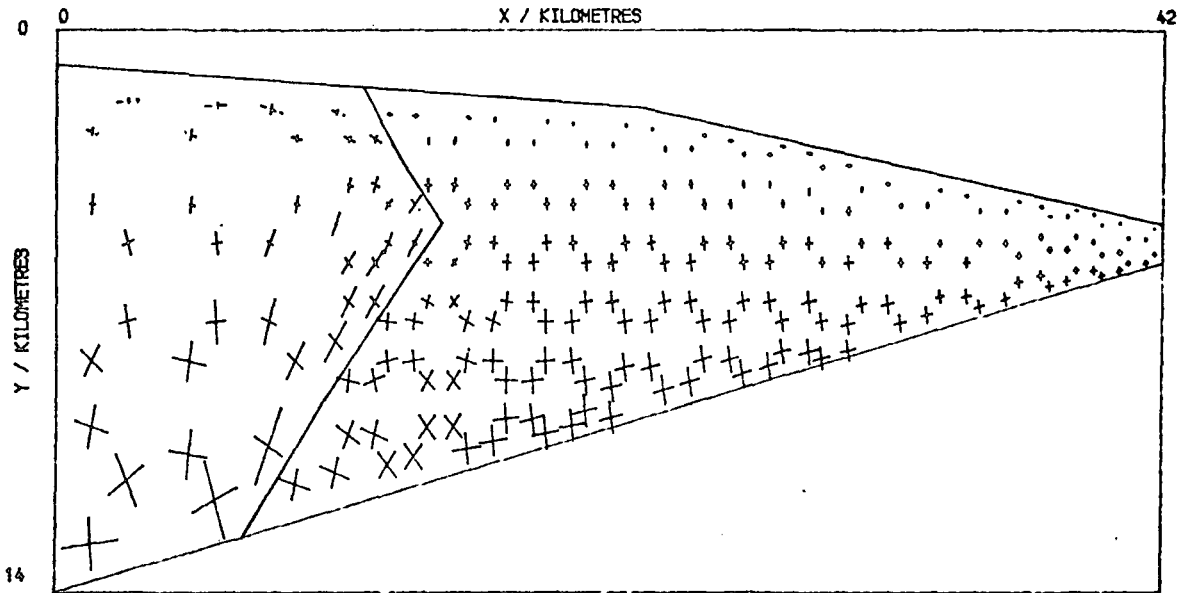
Fig. 6.17: Principal stresses in the model of Fig. 6.15.

X / KILOMETRES

0   42

Y / KILOMETRES

0

14

— 100 MPA
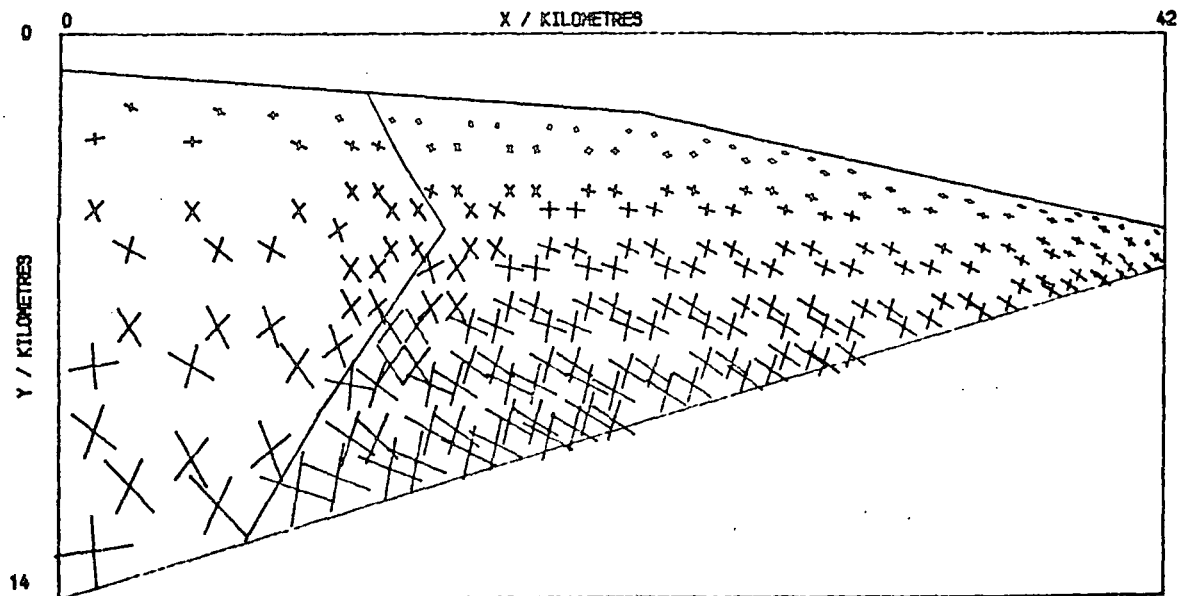
Fig. 6.18: Principal stresses in the model of Fig. 6.16.

(Section 6.2.1), increasing the total compression at the base and the tension near the surface, so that widespread tensional failure is predicted at the top, and the toe of the basement is 20% closer to compressional failure ($C \simeq 0.4$) also. The accreted sediments are not in equilibrium in this model, having deviatoric stresses which are typically 15 MPa and which range up to 25 MPa.

In the second of these models, which has a basal shear of 20 MPa, the rotation of the continental basement is completely counteracted by the effect of pushing accreted sediments down the basal slope, and there is even a tendency to anti-clockwise rotation. This is shown by the principal stresses (Fig. 6.18) which, near the igneous/sedimentary boundary are rotated so that the maximum principal stress (tension positive) is more nearly parallel to the boundary than in the case of zero basal shear (Fig. 6.17), where the minimum principal stress was aligned.

Models may also be run, increasing the basal stress with depth (as suggested by Wang, 1980). However, the same general principles apply as for a uniform basal stress, namely, if the stress is large uplift occurs on the upper slope and the continental basement rotates anti-clockwise, and vice versa for a small basal shear. The results of one of these models, where the average basal stress under the toe of the prism is c. 12 MPa, are shown in Figs. 6.19 and 6.20, and are very similar to those for a uniform basal shear of 20 MPa (Figs. 6.16 and 6.18), the chief difference being that the lower slope remains more nearly parallel to the undeformed position, being rotated by only 0.1°. The form of the basal shear stress as a function of depth is poorly constrained, and the effects of varying that function are not investigated in this thesis.
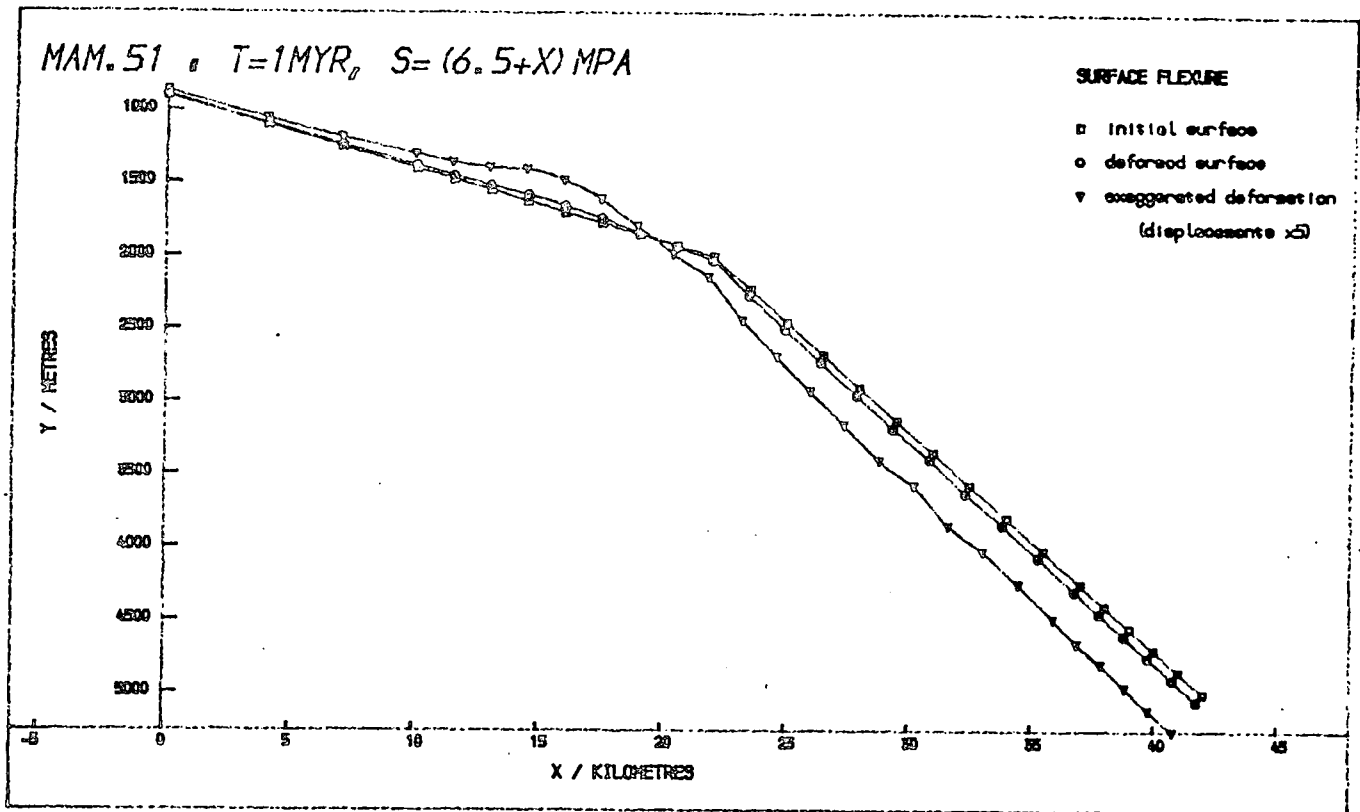
Fig. 6.19: Surface displacements in the original model (Section 6.2.1, Fig. 6.1), after 1 Myr, with a basal shear increasing linearly with depth, (A-Bx) Mpa, where A = 48.5 MPa, B = 1 MPa km⁻
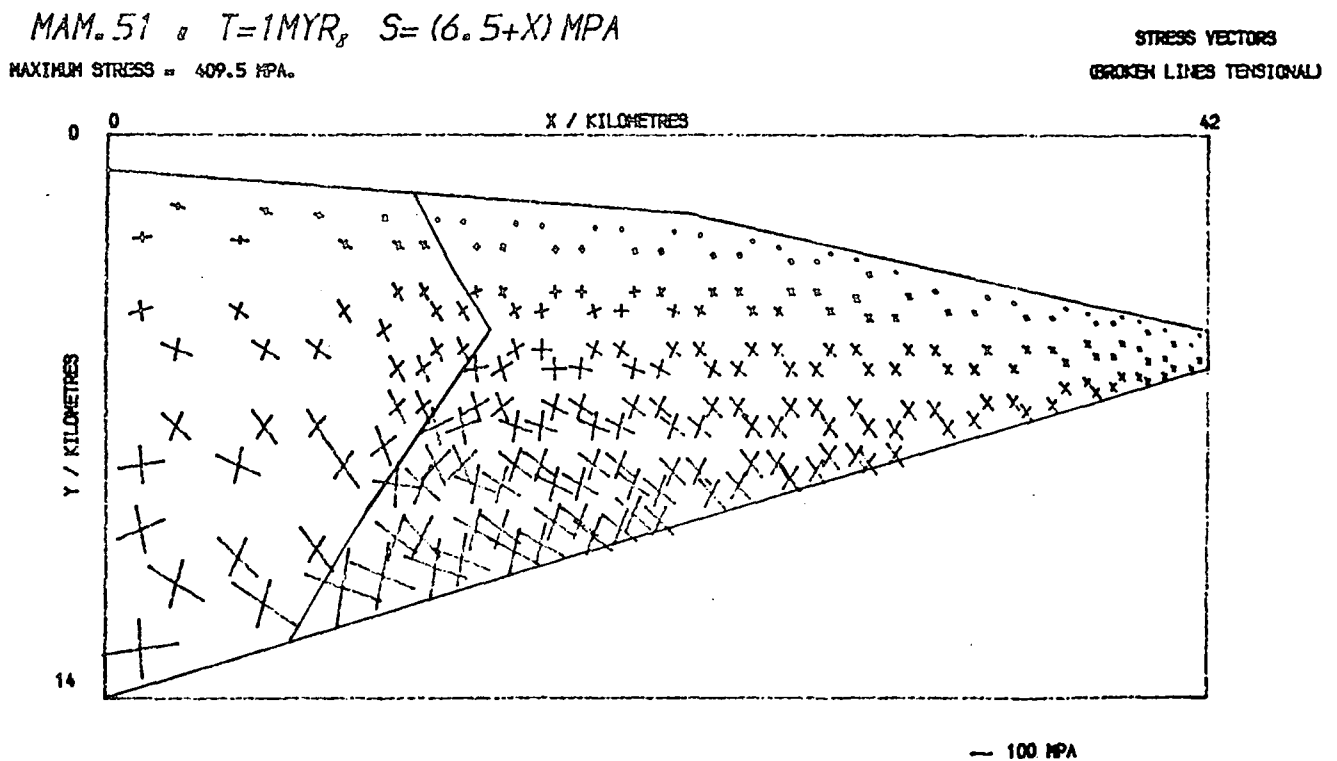
Fig. 6.20: The principal stress distribution for the same model as above.

Finally, the strains in all the models of this section (6.2.3) are still much smaller than those observed in accreted sediments (as were those in the previous two sections and Section 5.8 of Ch. 5) irrespective of the basal shear stress applied. The largest strains (found in each case at the base of the sediment wedge, aligned with the direction of maximum shear approximately parallel to the basal thrust) are 5%, 6% and 7% in the models with zero basal shear, a shear of 20 MPa and a linearly increasing shear, respectively.

6.2.4 Material property contrasts

The effects of changing material properties throughout a finite element model of the wedge type have been examined in Section 5.6, Ch. 5, and so it is only necessary to investigate the effects of changing the contrasts in those properties, in this section. In addition, it was shown that changes in Poisson's ratio ν were only significant in that they altered the compressibility,

$$\kappa = \frac{3(1 - 2\nu)}{E} \qquad \text{(Equation 5.17)}.$$

Increasing ν by a given percentage reduces κ by approximately the same percentage (this relation is exact for changes from $\nu = 0.25$), so that increasing ν by 100% (the greatest possible amount if $\nu = 0.25$) only increases κ by a factor of 2, and the largest feasible decrease in ν (by, say, 50% to $\nu = 0.125$) decreases κ by the same factor. κ is inversely proportional to E_1 which can take a wider range of values than ν, and so variations in Young's moduli are modelled here, rather than in Poisson's ratios.

Figure 6.21 shows the effect on the surface deformation of increasing the Young's modulus (and hence decreasing the compressibility) of the
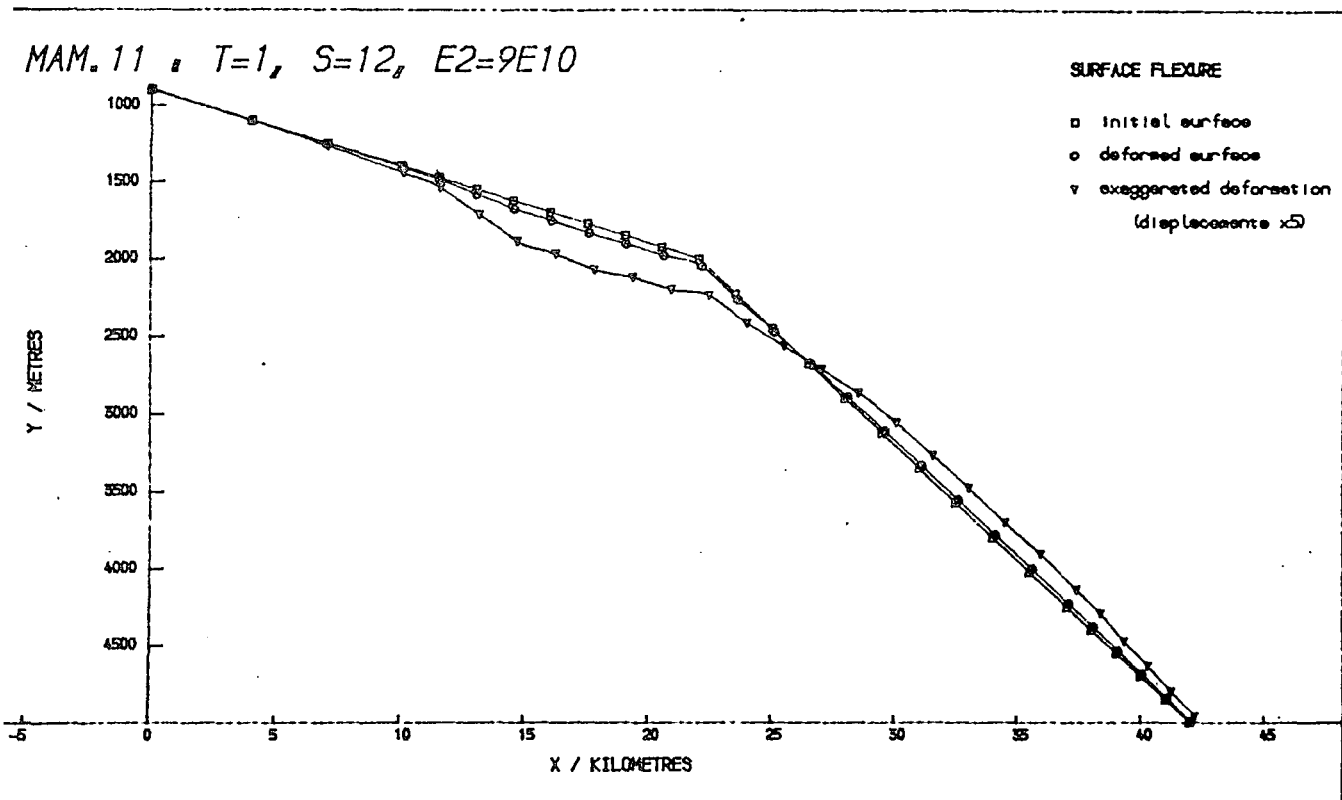
Fig. 6.21: Surface deformation of the original model (Figs. 6.1 to 6.3) with the Young's modulus of the accreted sediments increased to E_2 = 90 GPa.
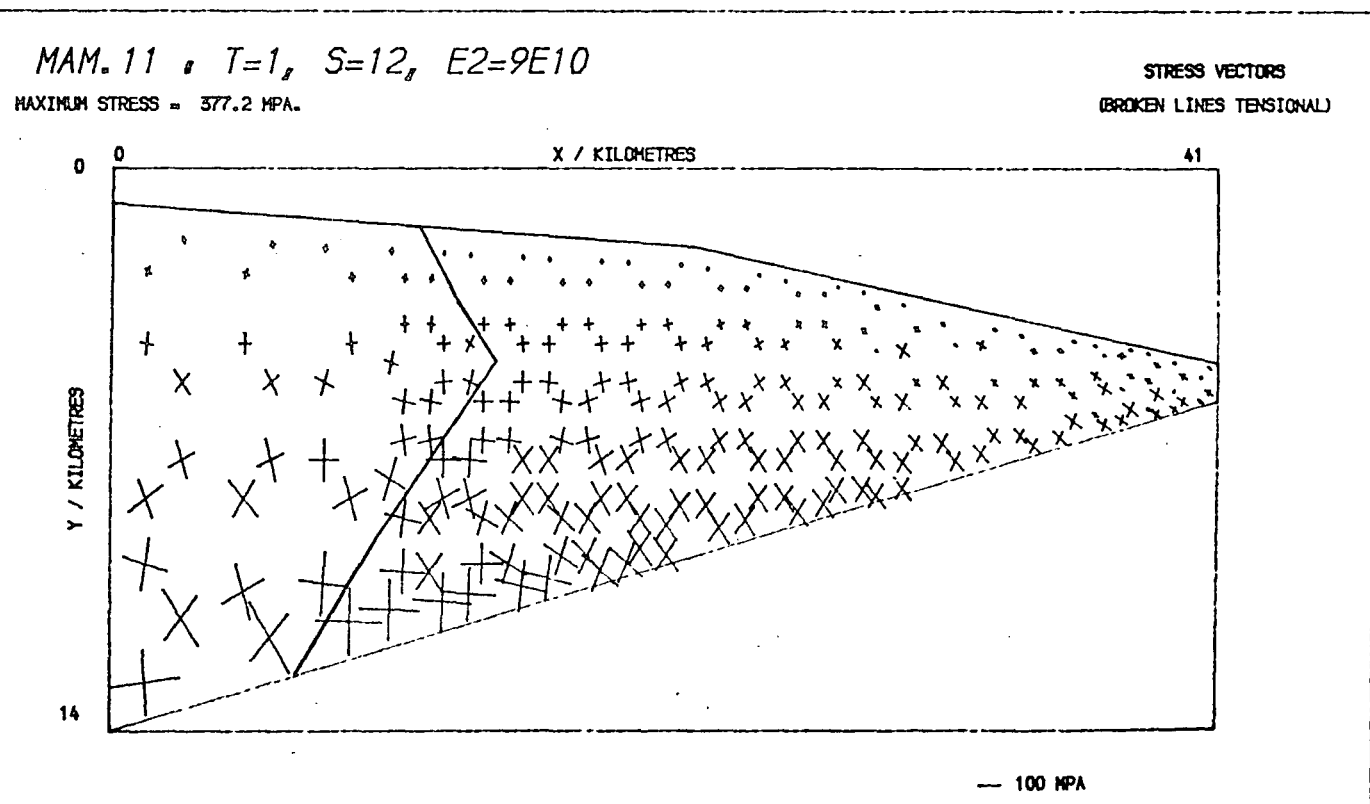
Fig. 6.22: The principal stresses in the above model.

accreted sediments, E_2, by a factor of 9, so that now $E_2 = E_1$, the
Young's modulus of the crystalline basement. The maximum subsidence is
reduced by this change to c. 60 m after 1 Myr (cf. 80 m in the equilibrium
model of Fig. 6.2) and the lower slope moves up by c. 20 m. Both these
effects occur because of the reduced compressibility of the thicker part of
the accreted sediments. This also has the effect of nullifying the boundary-
parallel compressional stresses that were previously within the crystalline
basement and reducing the tensions at its upper surface (Fig. 6.22; cf.
Fig. 6.3).

It should also be noted that, in Fig. 6.22, there are signs of the
instability discussed in Section 5.7, Ch. 5, in that near the toe of the
model some elements have anomalously low hydrostatic stresses.

All the trends in surface displacements and principal stresses are
reversed if the Young's modulus for the accreted sediments, E_2, is reduced
to 1 GPa (Figs. 6.23 and 6.24), except that here the changes are more
marked. The upper slope is lifted up by up to 55 m (after 1 Myr), and the
lower slope is depressed by c. 200 m, while the greatest stresses in the
crystalline basement are concentrated along its boundary. The surface
deformation is inconsistent with all observations of accretionary prisms, and
bearing in mind that the angle of the lower slope in Fig. 6.23 is changed
very little so that the basal stress is still close to the required
equilibrium value, it is concluded that the Young's modulus for accreted
sediments must be significantly greater than 1 GPa.

The effects of varying the viscosity of the accreted sediments, n_2,
with respect to that of the igneous crust, is to change the amount of
viscous deformation in that part of the model. If n_2 is increased to
10^{23} N s m^{-2} (from 10^{22} N s m^{-2}), the surface displacements of the model are
reduced to less than 20 m everywhere, and there are larger deviatoric
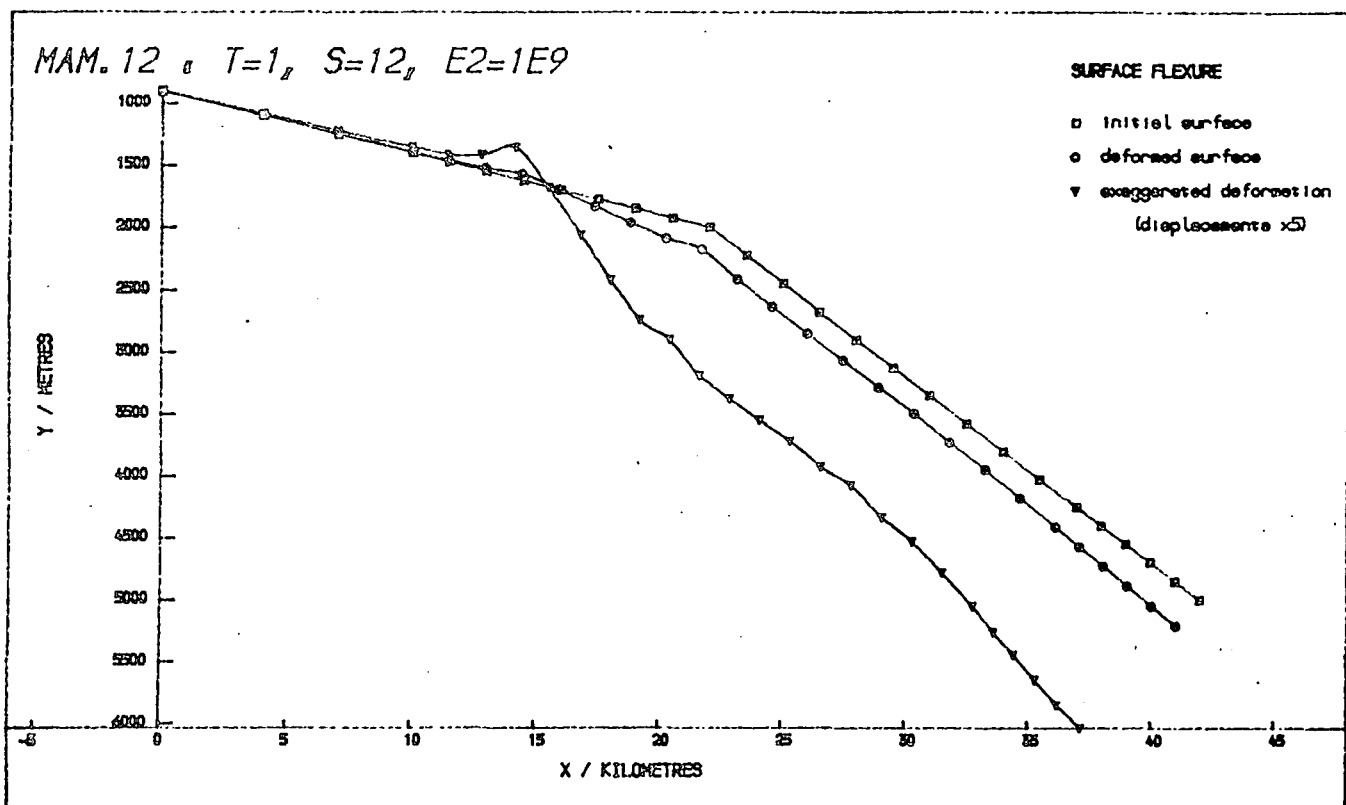
Fig. 6.23:   The same model as in Fig. 6.21, but with E = 1 GPa.
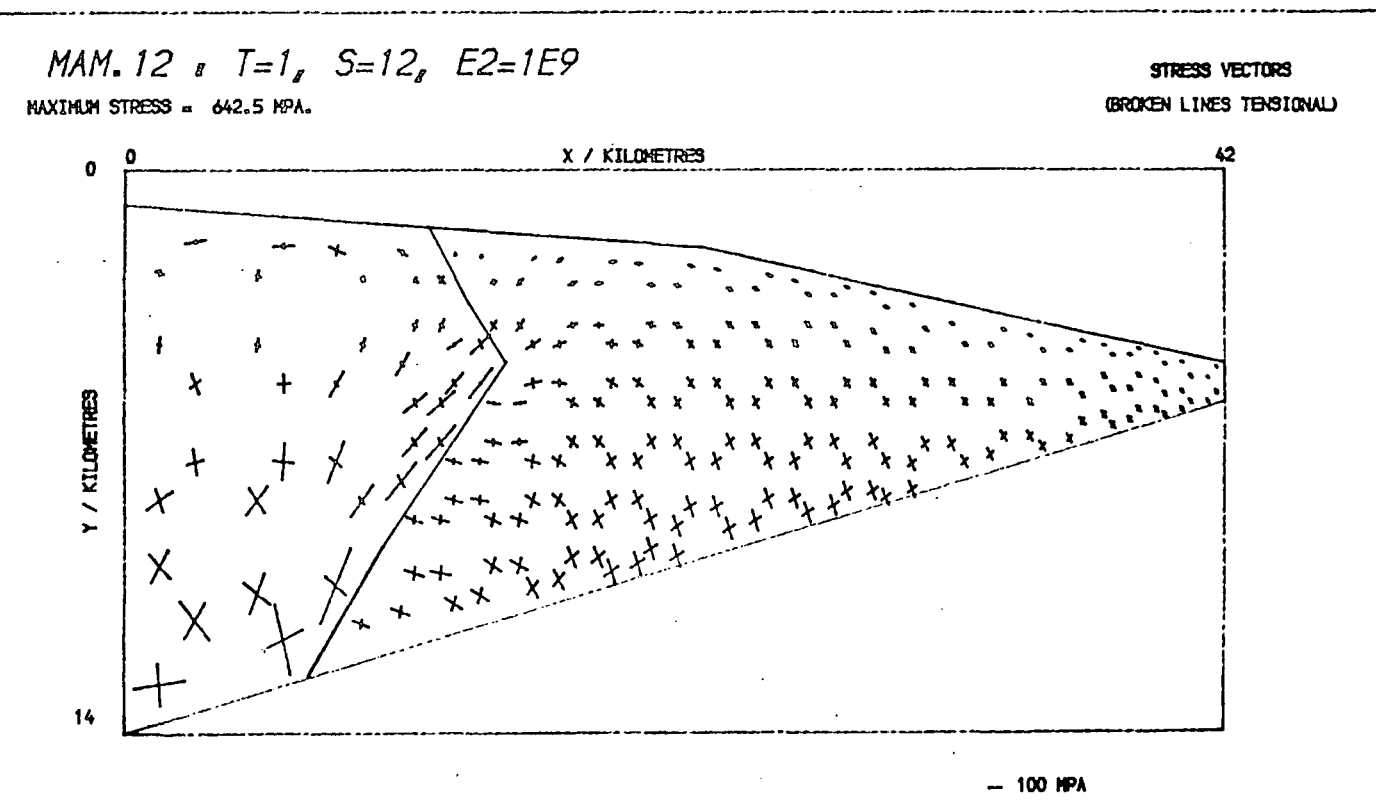
Fig. 6.24:   Principal stresses in the same model (above).

stresses (by a factor of 2) remaining in the accretionary prism. If n_2 is reduced to 10^{21} N s m^{-2}, then the displacements of the original model are amplified, giving a subsidence of c. 600 m in the upper slope and uplift of c. 200 m on the lower slope, after 1 Myr.

Figure 6.25 shows the effect of increasing n_2 and reducing E_2 together. Comparison with Fig. 6.23 shows that the reduction in E_2 has had the same type of effect as before, though the reduction in viscous creep has modified the displacements somewhat. In contrast, Fig. 6.26 shows the effect of decreasing both E_2 and n_2 together. The subsidence of the upper slope is now 1100 m, even larger than obtained by reducing n_2 alone (600 m; see last paragraph), supporting the conclusion reached earlier that $E_2 > 1$ GPa.

The reduction of n_2 to 10^{21} N s m^{-2} reduces the Maxwell time, t_m, for the sediments to an extent where instabilities are noticeable in the stress distribution (Section 5.7, Ch. 5), and increasing E_2 at the same time decreases t_m still further making a solution of this type unstable and so impossible to model over 1 Myr. However, the results of the last two paragraphs indicate that the effective viscosity of the accretionary prism, n_2, must be within the limits

$$10^{21} < n_2 < 10^{23} \text{ N s m}^{-2}$$

whatever the value of the Young's modulus, E_2. This result is consistent with that of Section 5.8, Ch. 5.

The final parameter whose variation is to be studied is the density of the accreted sediments, ρ_2. Figs. 6.27 and 6.28 show the surface displacements when $\rho_2 = 2300$ kg m^{-3} and $\rho_2 = 2700$ kg m^{-3}, respectively (originally $\rho_2 = 2500$ kg m^{-3}). The upper slope subsides more for a higher density and prevents the toe from being pushed so far down the basal slope, and vice versa for a lower density (the displacements of the upper slope are 57 m and 100 m, and of the toe are 32 m and 14 m respectively for $\rho_2 = 2300$
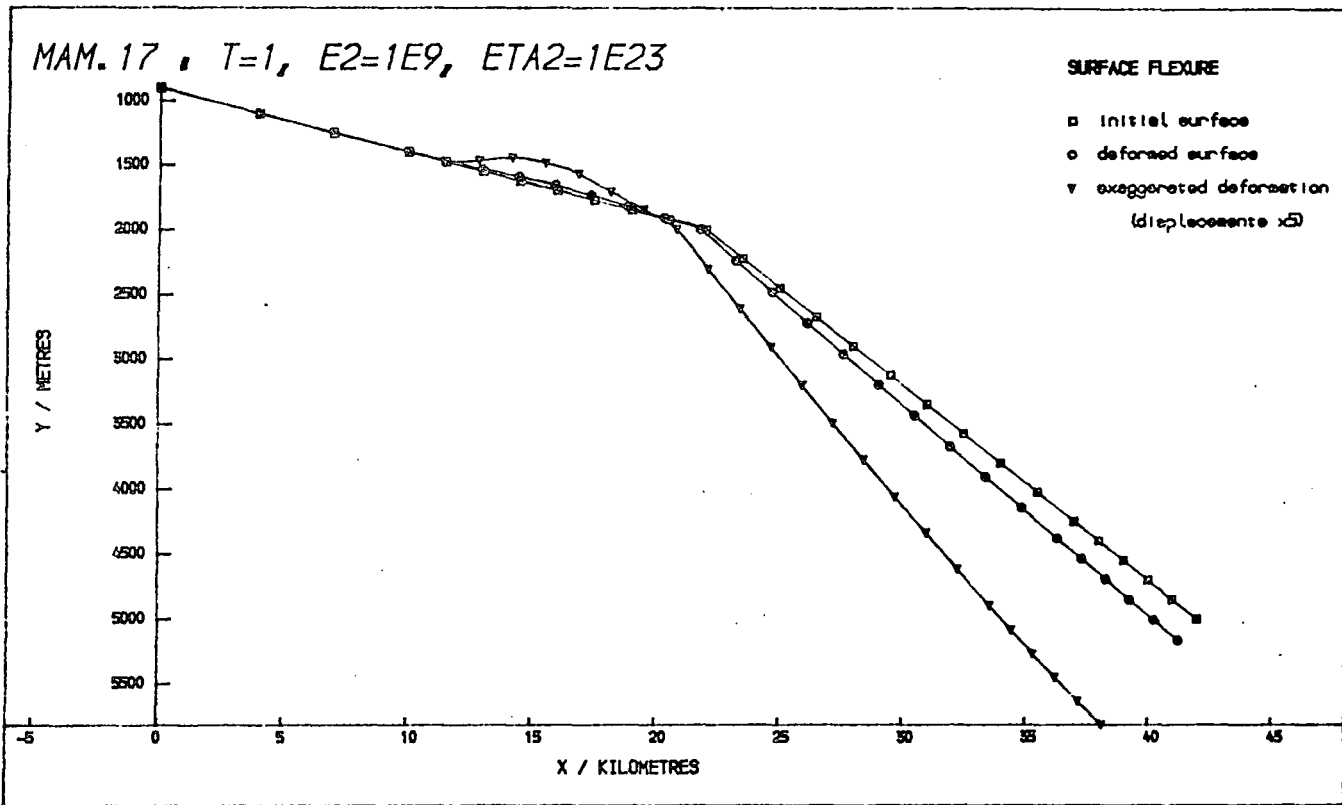
Fig. 6.25:   Surface displacements in the model of Figs. 6.1 to 6.3, with
$E_2 = 1$ GPa and $n_2 = 10^{23}$ N s m^{-2}.
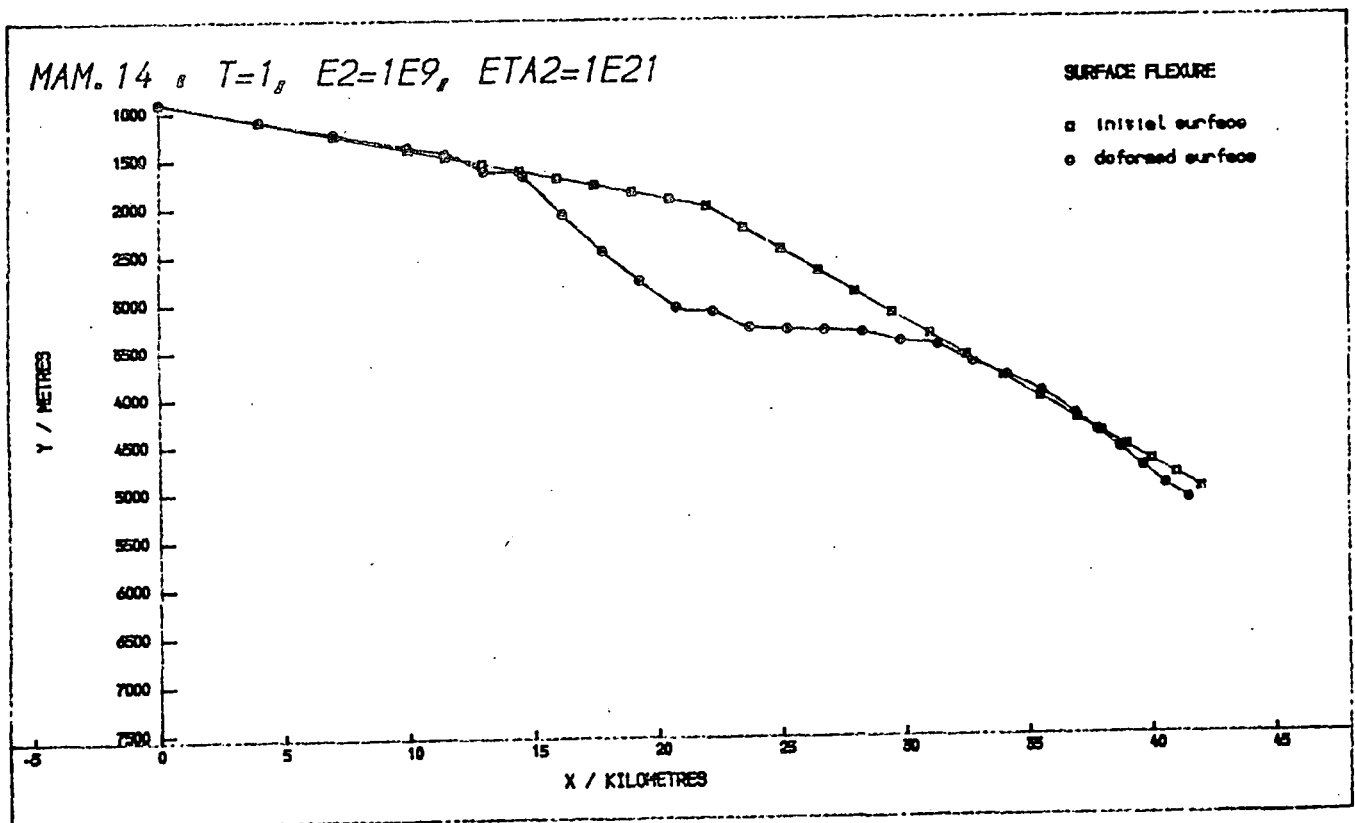
Fig. 6.26:   As above, with $E_2 = 1$ GPa and $n_2 = 10^{21}$ N s m^{-2}.
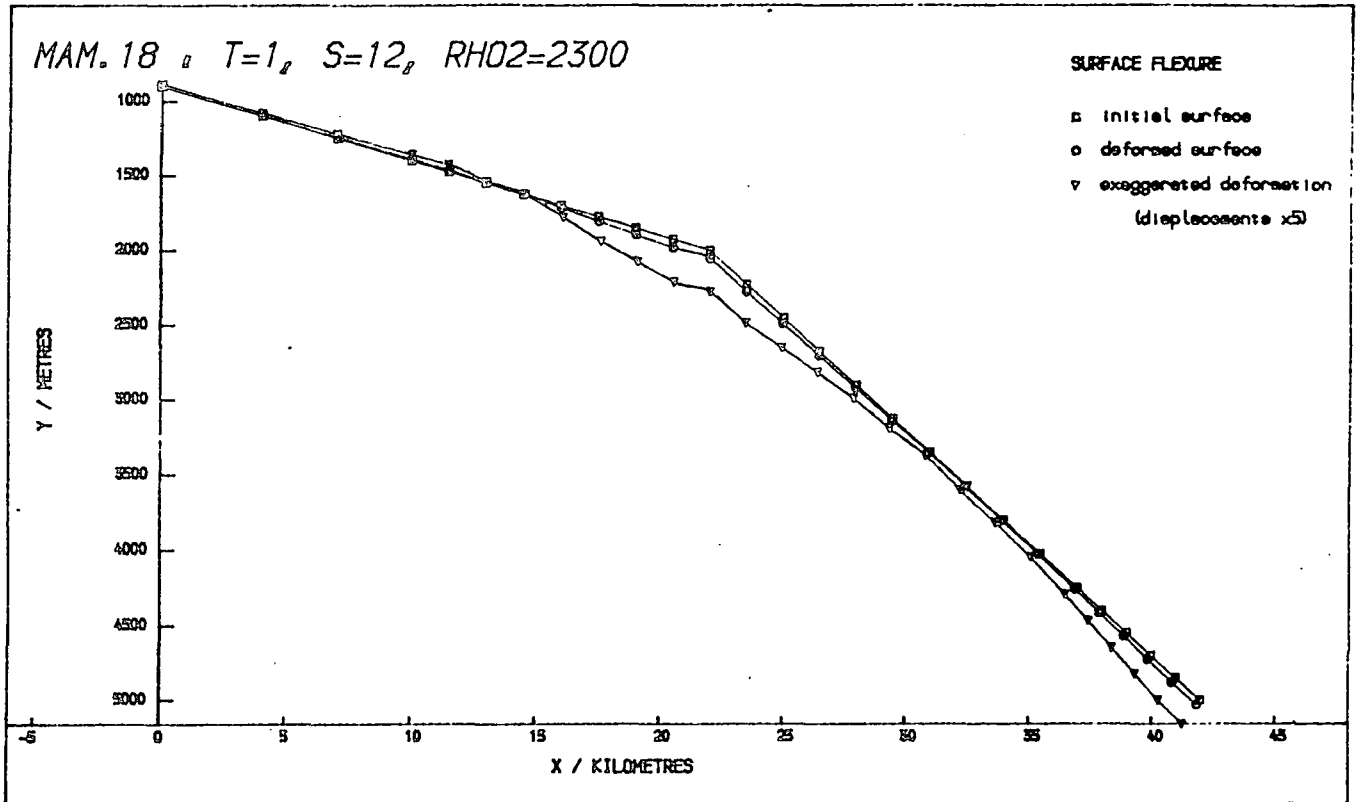
Fig. 6.27: Surface displacements in the original model (Figs. 6.1 to 6.3) with $\rho_2 = 2300$ kg m^{-3}.
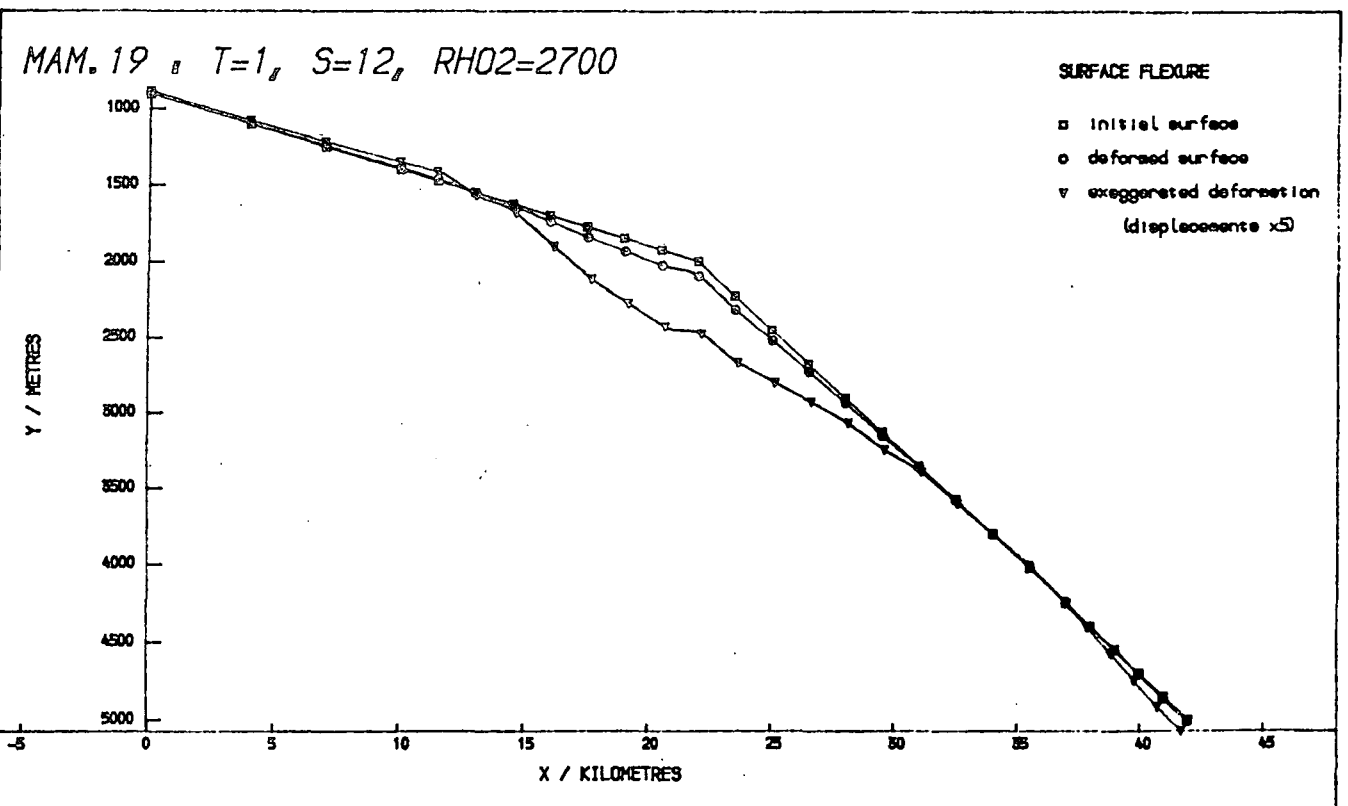
Fig. 6.28: As above, with $\rho_2 = 2700$ kg m^{-3}.

and 2700 kg m^{-3}). The stress systems in the two models are almost identical to the original model (Fig. 6.3), except that the greatest compressions are 395 MPa (ρ_2 = 2300 kg m^{-3}) and 390 MPa (ρ_2 = 2700 kg m^{-3}) as opposed to 392 MPa (ρ_2 = 2500 kg m^{-3}). This stress is within the continental basement and is therefore decreased when the accretionary prism supports it more, which is the case for an increase in ρ_2, although this effect is small.

6.3 A Model of the Inner Wall of the Central Aleutians Trench

6.3.1 The initial model

Figure 6.29 shows the finite element grid and the material properties in each element for a model based on the cross-sections of the central Aleutian Islands subduction zone shown in Fig. 1.8 (Grow, 1973a). The model has been divided into 4 lithological sections, as shown in Table 6.2, although material types 2 and 4 are given the same properties in this initial model.

Lithological type		E/GPa	ν	ρ/kg m^{-3}	η/N s m^{-2}
Terrace sediments	1	0.22	0.38	1900	10^{20}
Older terrace and accreted sediments	2	10	0.27	2500	10^{22}
Igneous oceanic crust	3	35	0.25	2800	10^{23}
More recently accreted sediments	4	10	0.27	2500	10^{22}

Table 6.2: Material properties used in modelling the central Aleutians subduction zone
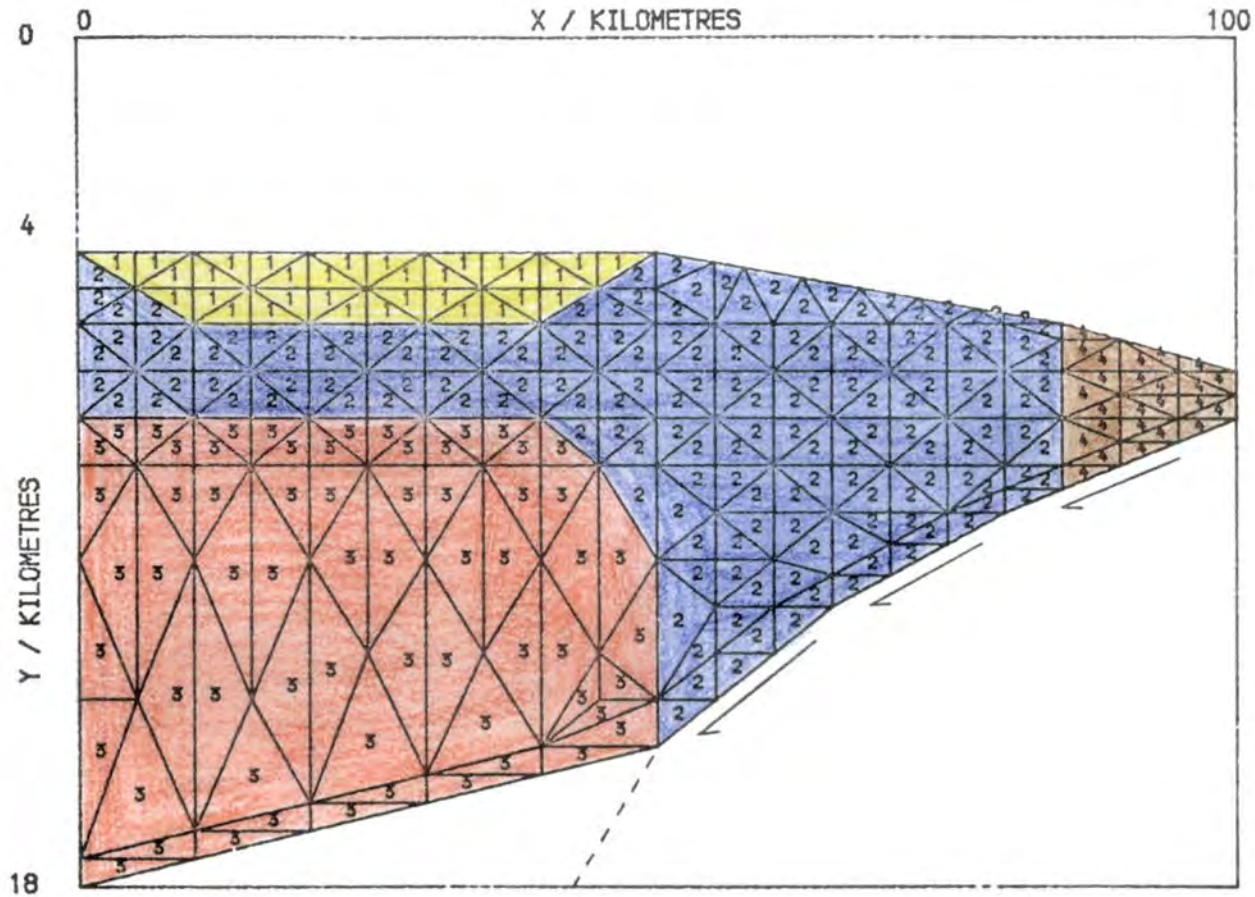
Fig. 6.29: The grid used in Section 6.3.1 for modelling the central Aleutians subduction zone. The material type of each element is indicated at its centroid: 1. terrace sediments; 2. older terrace and accreted sediments; 3. igneous oceanic crust; 4. recently accreted sediments.

The boundary conditions on this model are similar to those on the previous accretionary models, namely; the upper surface is free, the landward end is fixed horizontally, the seaward end has a lithostatic load due to sediments in the trench (of density, 1700 kg m^{-3}), and a shear stress is applied to the base. The base of this model is divided into three straight segments to approximate the curvature of the subducted plate, which is assumed to come into contact with the mantle at 15 km depth. The mantle is assumed to have a low viscosity so that the shear transmitted to the overlying crust from the contact between the subducted plate and the mantle is negligible, and thus only the shear applied directly to the overriding crust need be considered, as indicated in Fig. 6.29. The base of the igneous, oceanic or island arc, crust is supported by the underlying mantle, and since it is impossible to model this support by applied forces (see Section 4.2.2, Ch. 4), those nodes along that part of the base are held in a direction perpendicular to the base, as are the nodes on the thrust plane, but have no applied forces.

The equilibrium basal shear stress is again found by trial and error. Figs. 6.30 and 6.31 show the surface displacements after 1 Myr, when there are no basal stresses and a basal shear of 10 MPa, respectively. These models show very similar features to those of Section 6.2 (especially the subsidence of the upper slope immediately seaward of the edge of the igneous crust, when there is no basal shear), the most obvious difference being the increased subsidence in the terrace region, due to the weak terrace sediments.

The closest model to equilibrium is given by a basal shear of 5 MPa, and the resulting surface deformation (Fig. 6.32) shows several interesting features. There is subsidence of the terrace by up to 25 m forming a depression behind a ridge of accreted sediments which forms the terrace
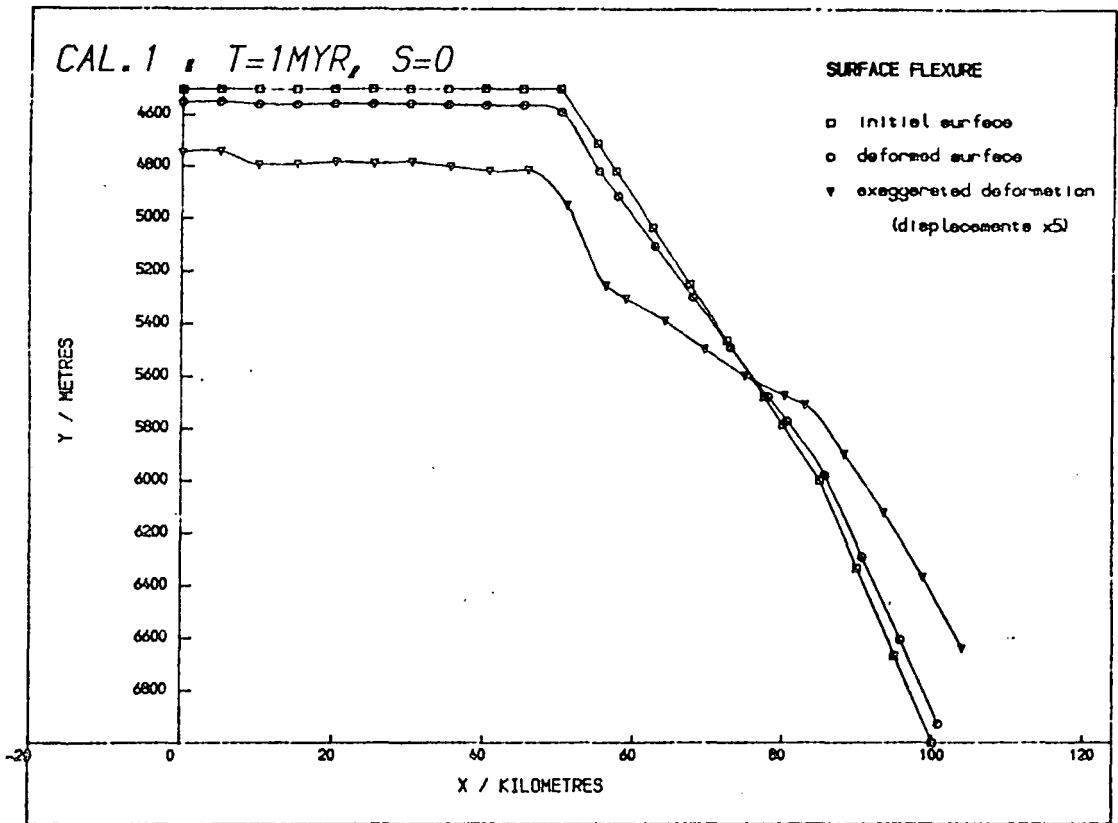
Fig. 6.30:   Surface displacements in the initial central Aleutians model
            (Fig. 6.29), with no basal shear, after 1 Myr.
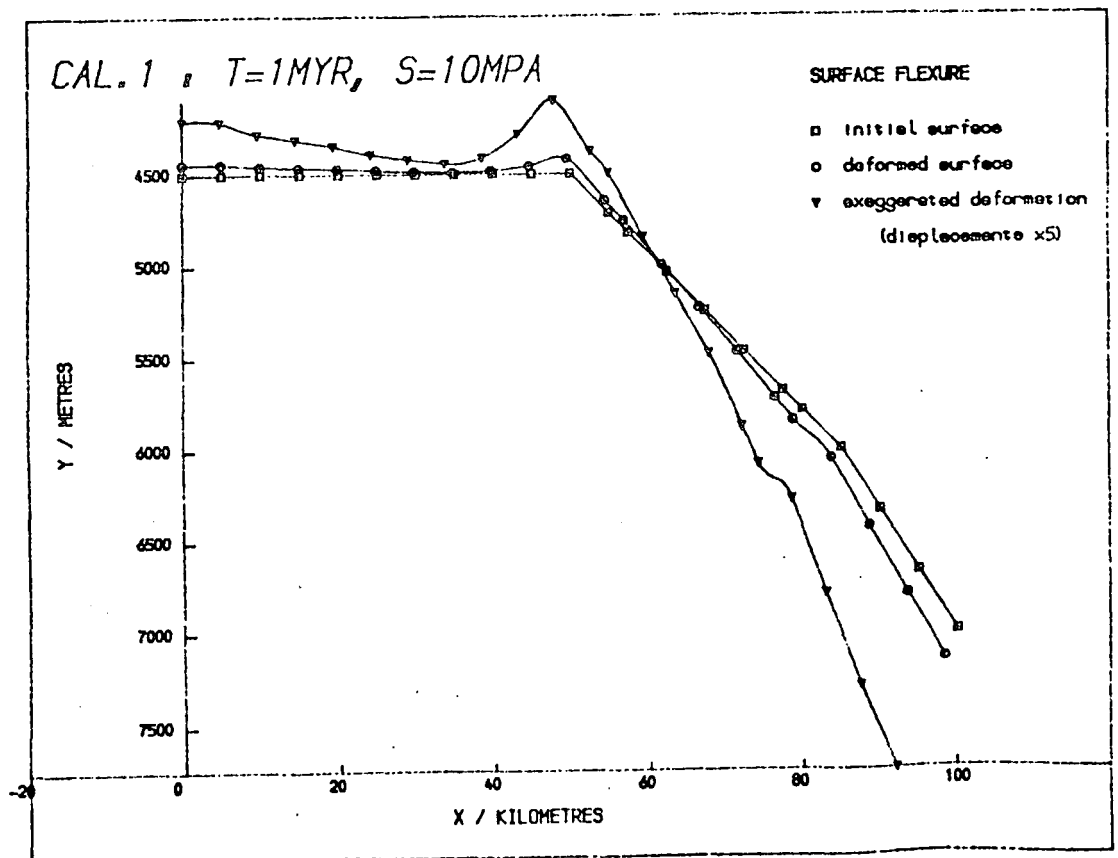
Fig. 6.31: As above with a uniform basal shear of 10 MPa.
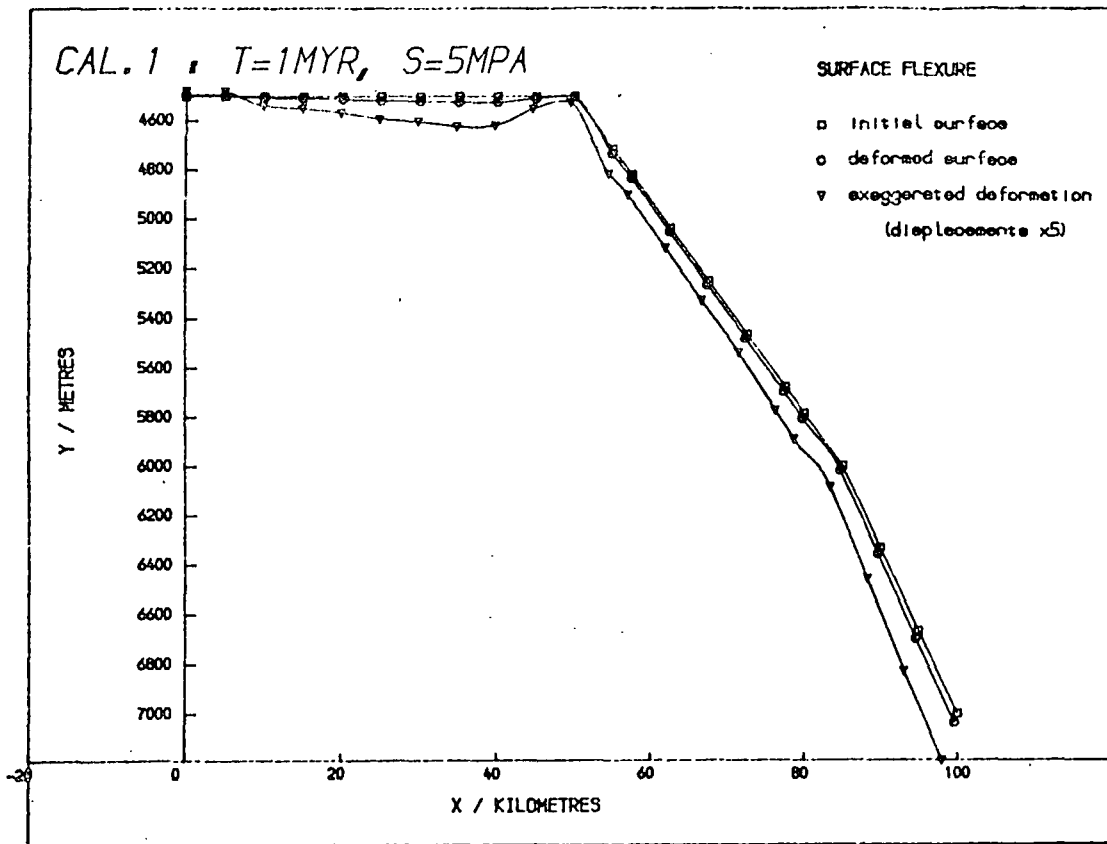
Fig. 6.32: Surface displacements after 1 Myr for the central Aleutians
model with the equilibrium basal shear, 5 MPa.
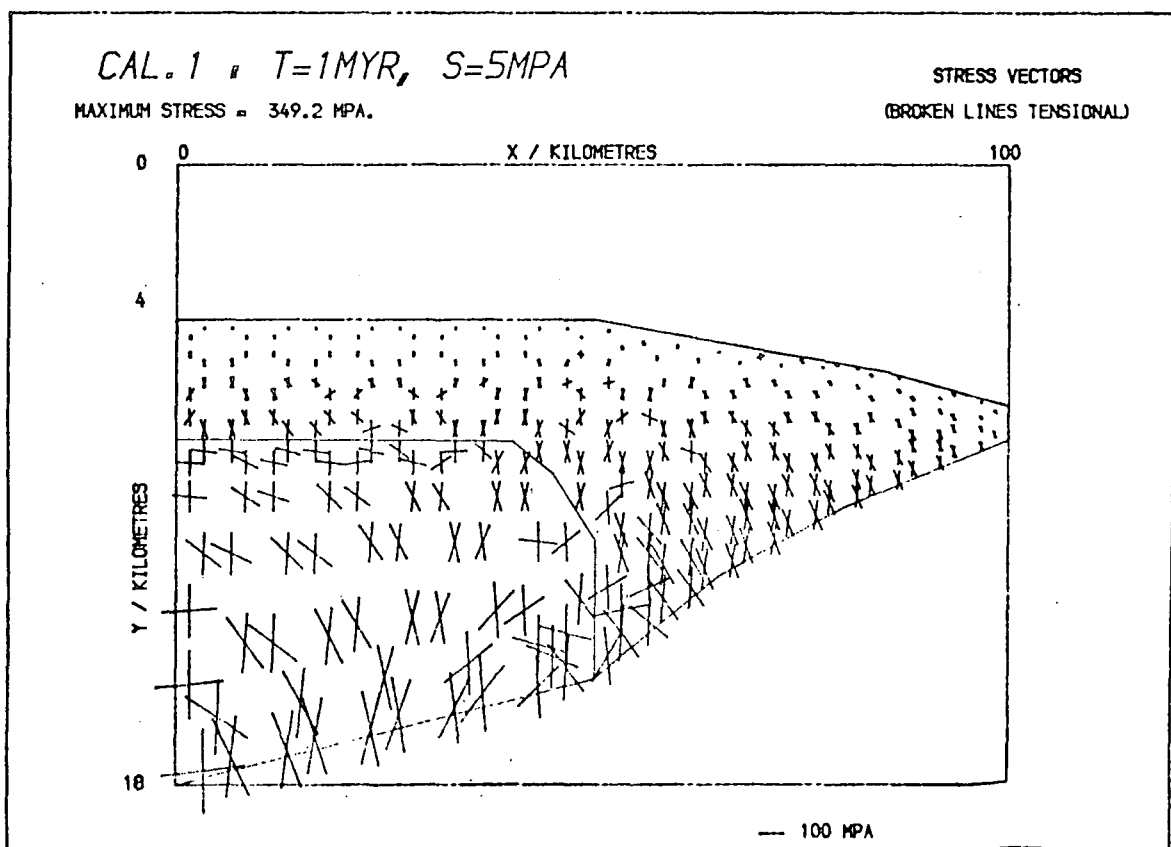
Fig. 6.33: Principal stress vectors in the equilibrium model, above.

edge. Immediately seaward of the terrace edge there is subsidence of
c. 20 m which decreases to 15 m and then remains uniform as far as the
break in the lower trench slope. The subsidence of the toe varies from
20 m at the break in slope to 40 m at the base, thereby increasing the
slope of the lower part and emphasizing the break in slope (at x = 85 km,
i.e. 15 km from the trench).

The stresses in the model (Fig. 6.33) are all close to hydrostatic,
and no failure is predicted anywhere. Deviatoric stresses in the
tectonized sediments are less than 1 MPa, except close to the point of
subduction (where the subducted plate comes into contact with the over-
riding igneous crust) where they reach 5 MPa. They are higher in the
igneous crust, in response to the compression exerted by the accretionary
wedge, at 7 MPa near the surface and up to 12 MPa near the point of
subduction. These low deviatoric stress levels confirm that the model is
close to equilibrium.

The strains in this model are small (as were those in Section 6.2,
and Section 5.8 of Ch. 5), the greatest value being 3% at the base of
the accretionary wedge, representing shear along the basal thrust. This
strain does not depend significantly on the shear stress applied, and is
4% for the case of zero basal shear, and 4.5% when there is a shear of
10 MPa. The strains in the terrace sediments are vertical compactions
of between 1% and 2% in all cases, with horizontal strains of less than
0.3% (tensional for zero basal shear, compressional in the equilibrium
model), consistent with the observation that sediments in upper slope and
terrace basins are not significantly deformed.

6.3.2 Variation in the extent of the overriding igneous crust

Grow (1973a) showed that two models for the position of the igneous crust were consistent with the geophysical data (as shown in Fig. 1.8), so several models were run to find the effect that this has on the surface deformation of the accretionary prism. The most significant result of this modelling is illustrated by Figs. 6.34 to 6.37. These show two models with their resulting surface displacements, one (Figs. 6.34 and 6.35) in which the igneous crust has been moved back 20 km from its original position (Fig. 6.29) and the other forward 20 km (Figs. 6.36 and 6.37).

In both cases, there is uplift of the accreted sediments above, and slightly seaward of the point of lithospheric subduction. This is very clear in Fig. 6.35, where the sediments in that position have been lifted up by 18 m, while the terrace edge of the initial model has subsided by 28 m, giving a relative movement of 46 m (compared with 19 m in the opposite sense found in the original; Fig. 6.32).

The effect is less marked in Fig. 6.37. Here the subsidence of the terrace relative to its leading edge is reduced (to 10 m) because the latter is not held up as effectively as in the original model, and the accreted sediments above the point of subduction have subsided less (5 m, cf. 19 m in Fig. 6.32). In addition, the slope landward of this point has subsided more than in the original model, emphasizing the uplift (reduced subsidence).

The stress systems for these two models are similar, save for elements which change from one lithology to the other, and for the change in position of the edge effects at the point of subduction. The deviatoric stresses are higher in the igneous basement than in the accreted sediments, and there is a stress concentration on both sides of the boundary between the two.

CAL.22 , T=1MYR, S=5MPA

ELEMENT MESH
(WITH MATERIAL NUMBERS)
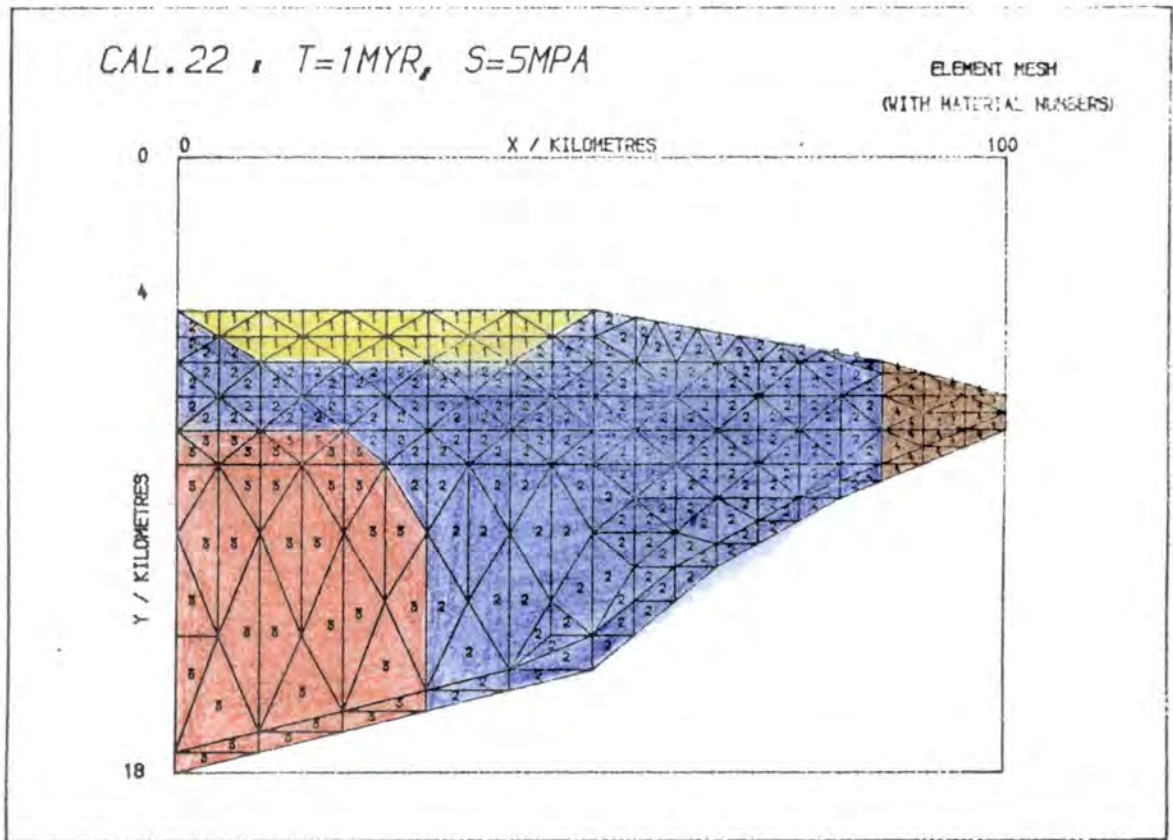
Fig. 6.34: A model of the central Aleutians subduction zone in which the
igneous crust has been moved back 20 km from its original
position (see Fig. 6.29, which also defines material types).

CAL.22 , T=1MYR, S=5MPA

SURFACE FLEXURE

□ initial surface
○ deformed surface
▼ exaggerated deformation
(displacements x5)
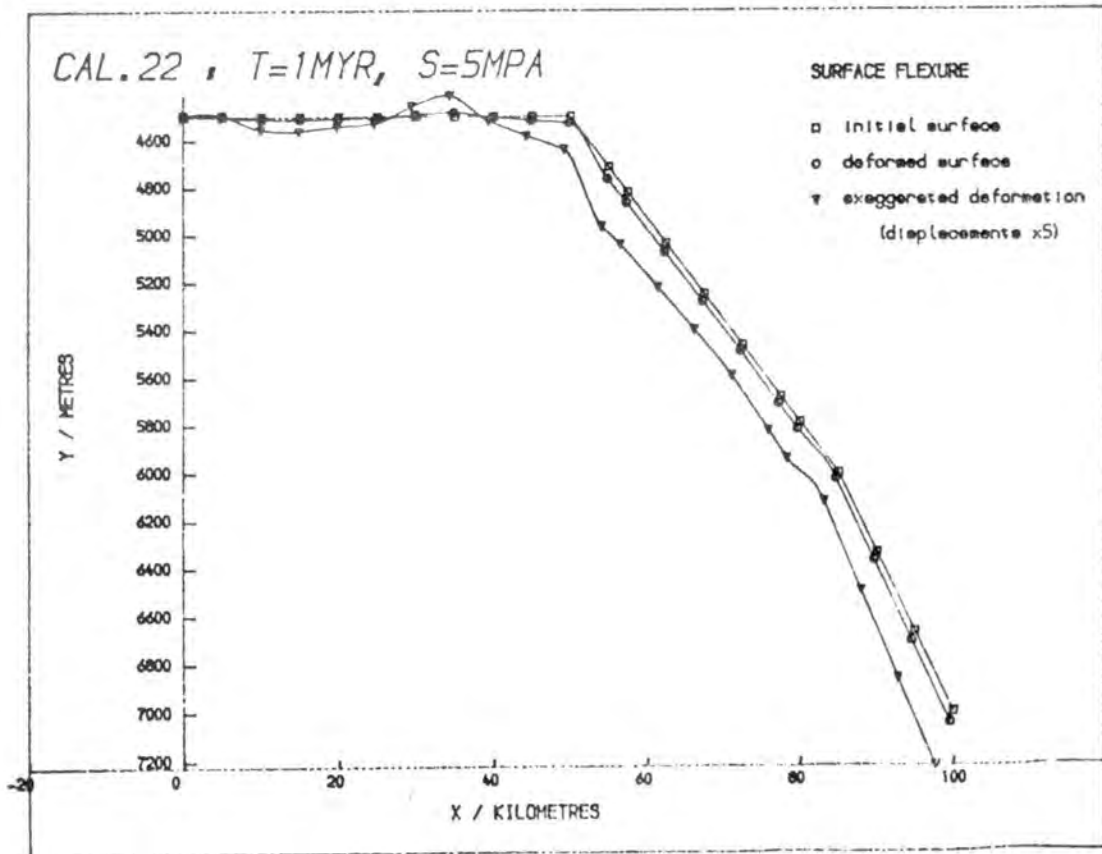
Fig. 6.35: The surface deformation of the above model after 1 Myr, with
a basal shear of 5 MPa.
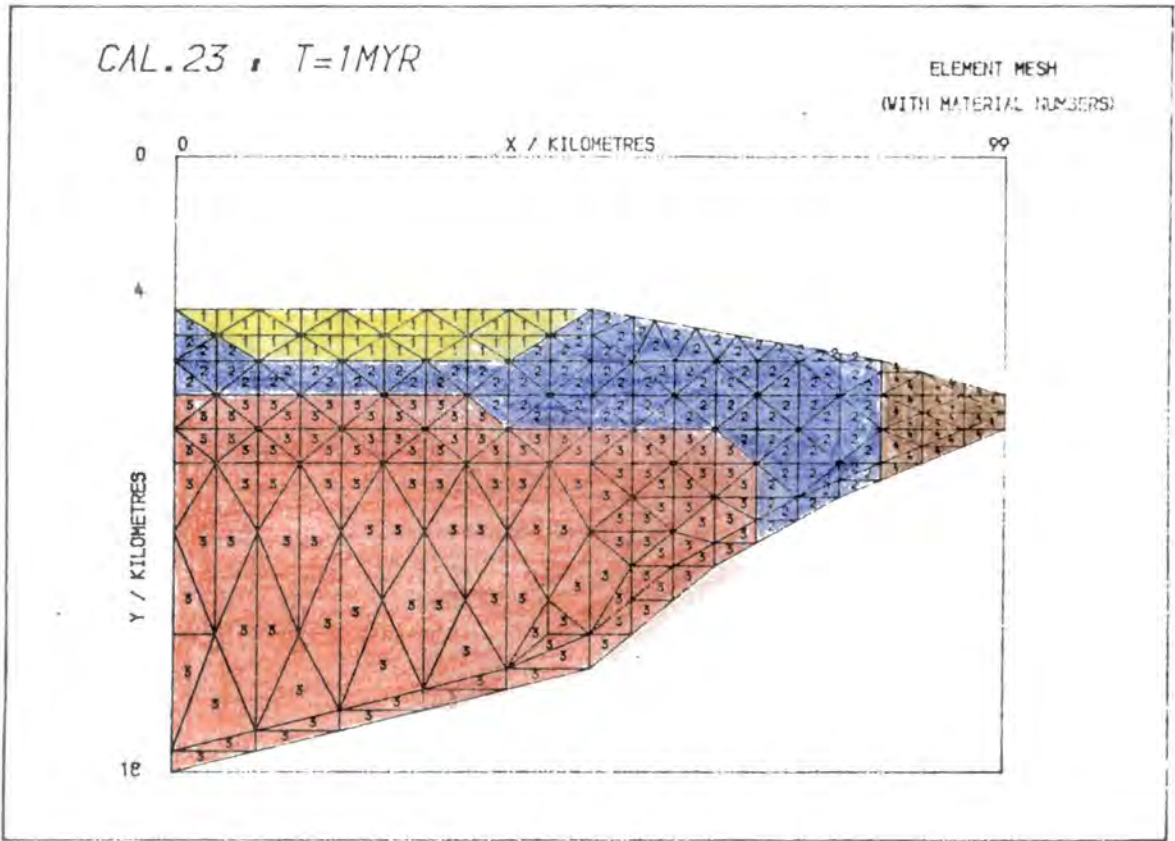
Fig. 6.36: A model of the central Aleutians subduction zone in which the igneous crust has been moved forward 20 km from its original position (see Fig. 6.29).
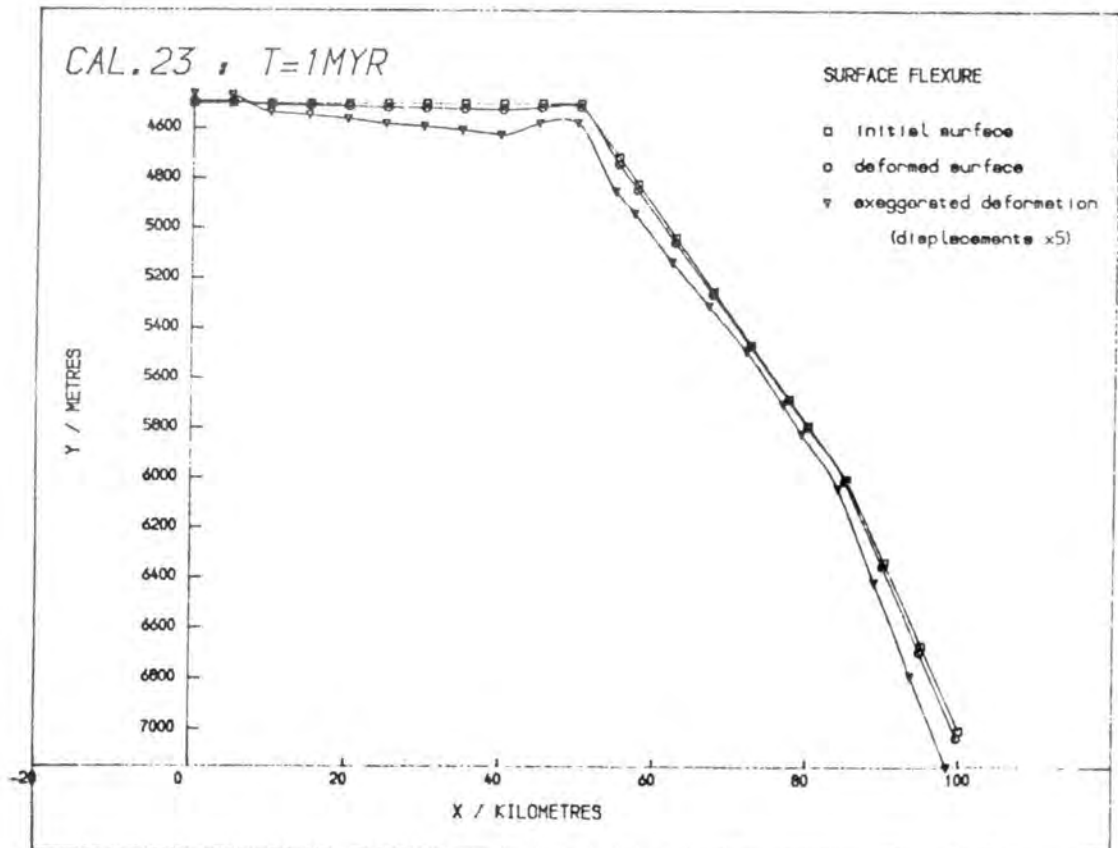
Fig. 6.37: The surface displacements after 1 Myr of the above model with a basal shear of 5 MPa.

Finally, Fig. 6.38 shows a model where the igneous crust has been thickened beneath the terrace by 2 km, and Fig. 6.39 the resulting surface deformation. The displacements are reduced along the upper slope so that it becomes steeper, and subsidence in the terrace is increased. Both these effects result from the lack of more compressible material above the igneous crust, which would allow greater displacement on the upper slope and which would, by being forced landward, also be pushed up, supporting the terrace sediments from beneath. However, this change in displacement pattern is not great enough to distinguish between this and the original model (Fig. 6.32), showing that the finite element model is more sensitive to the lateral extent of the igneous crust than to its thickness.

6.3.3 Variation in material properties of the toe

The model of the central Aleutians subduction zone (Fig. 6.29) was shown with 4 different lithological types, only 3 of which were distinguished in Table 6.1. For this section, models were run in which the accreted sediments at the toe of the wedge were given a lower Young's modulus, $E_4 = 1$ GPa and a lower viscosity, $\eta_4 = 10^{21}$ N s m^{-2}. These reductions are intended to represent the fact that the accreted sediments become more lithified further back from the trench, thereby increasing both these parameters, E and η. The effects of decreasing E_4 and η_4 in the toe are very similar, and the surface displacements are only shown for the reduced value of E_4 (Fig. 6.40). The only significant effect on the model is to steepen the lower slope as shown, but otherwise the deformation of the whole model is unchanged. Fig. 6.41 shows the result of reducing E_4 and η_4 together, which magnifies the effect and shows clearly that, if there is an increase in the rigidity of the accreted sediments with
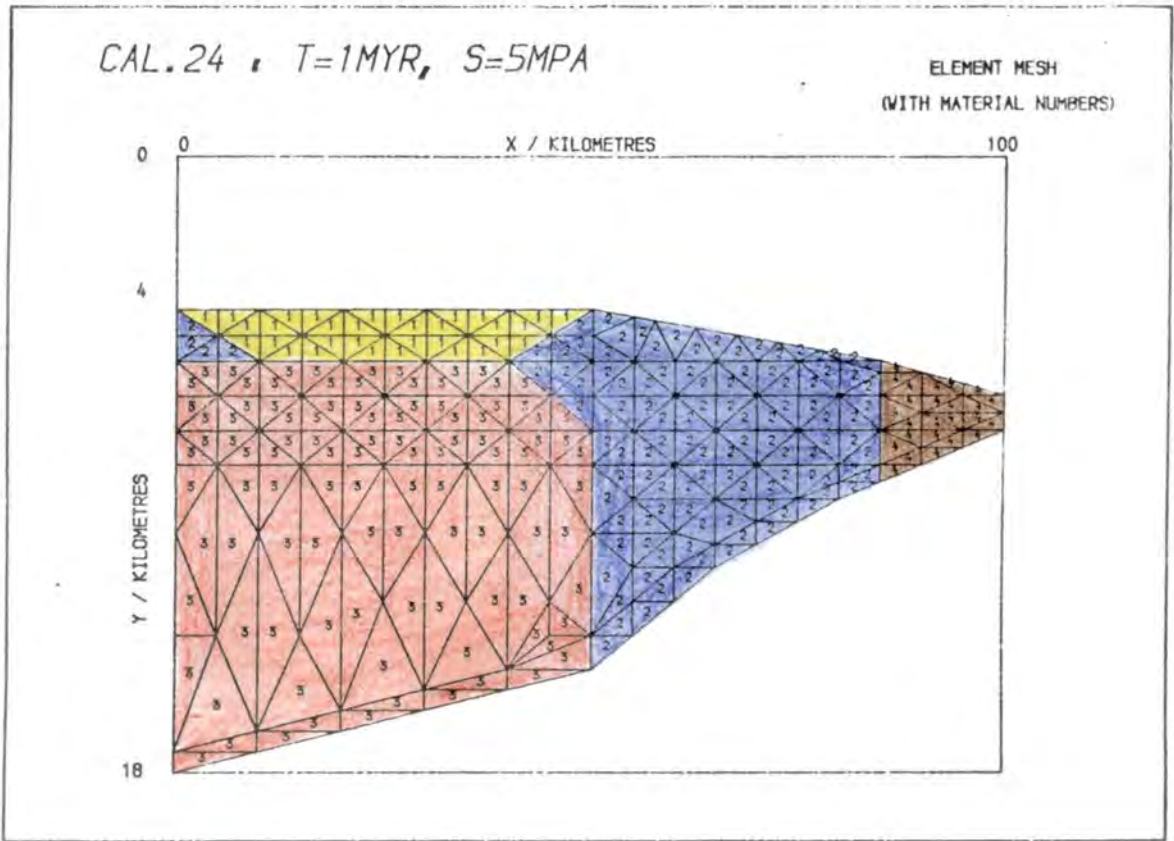
Fig. 6.38: A model of the central Aleutians subduction zone, as Fig. 6.29 but with an additional 2 km thickness of igneous crust.
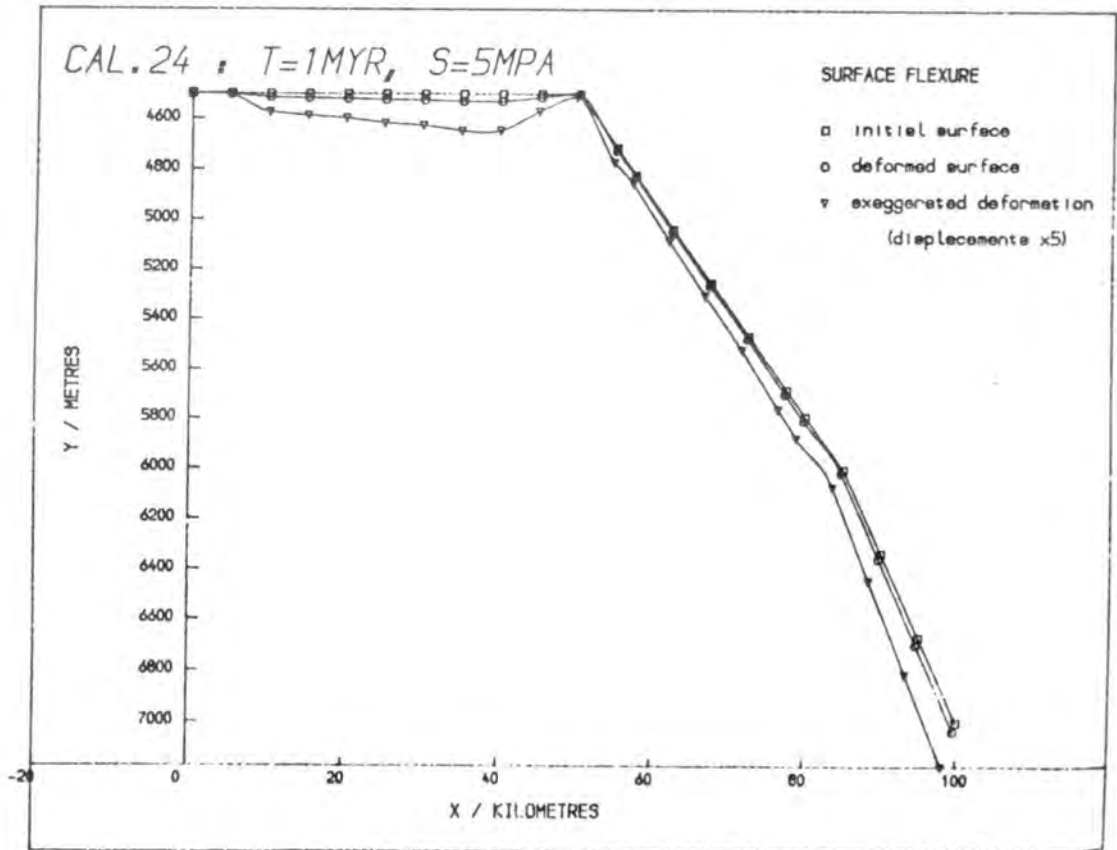
Fig. 6.39: Surface displacements of the above model after 1 Myr, in response to a basal shear of 5 MPa.
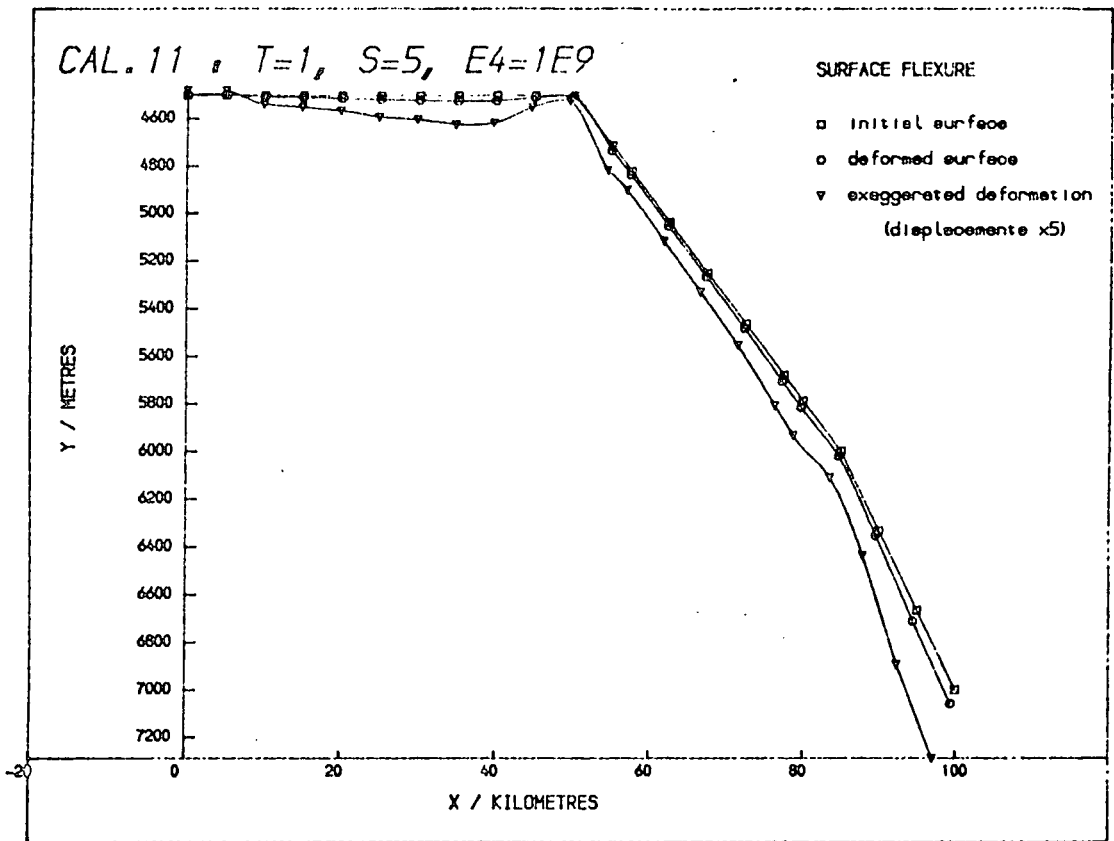
Fig. 6.40: Surface displacements for the original central Aleutians model (Fig. 6.29), with a reduced Young's modulus in the toe, $E_4 = 1$ GPa. Run for 1 Myr with a basal stress of 5 MPa.
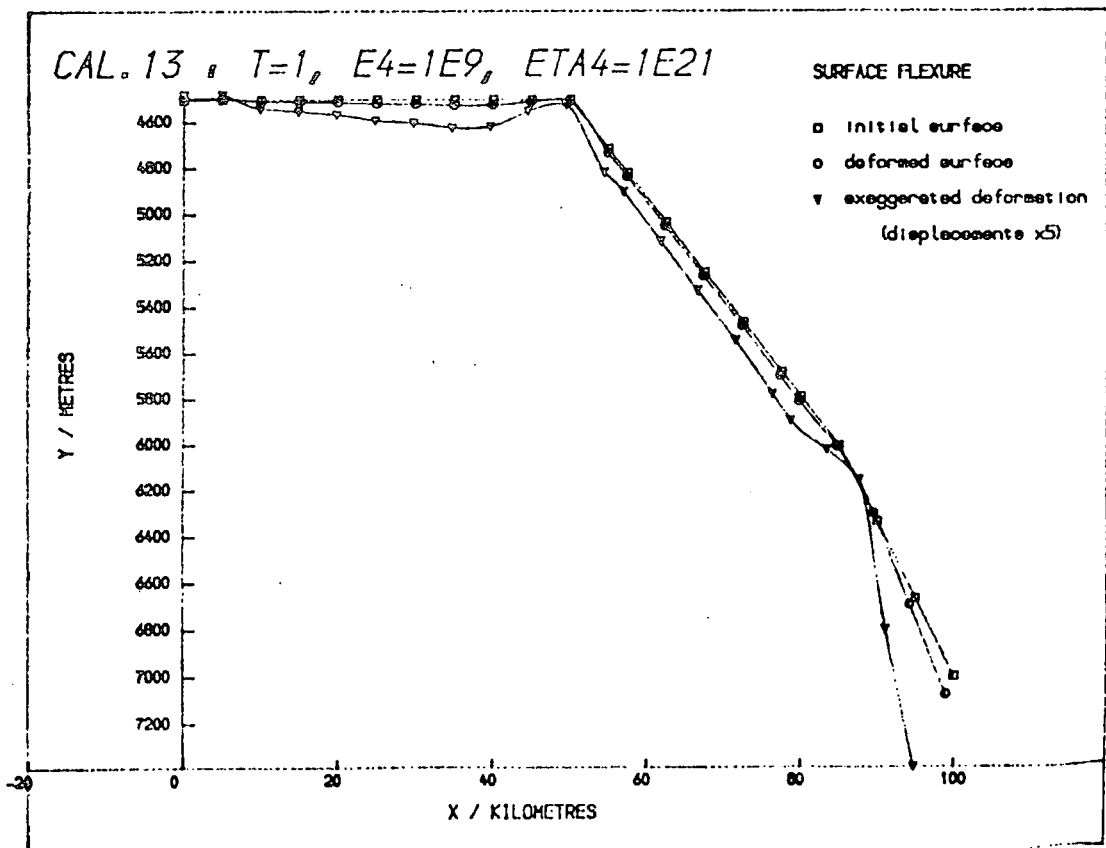
Fig. 6.41: As above, with the viscosity of the toe reduced also, $E_4 = 1$ GPa, $n_4 = 10^{21}$ N s m^{-2}.

distance from the trench, then there will be a corresponding change in the trench inner slope. If this lithification occurs over a comparatively short distance, then a break in the trench slope might appear as a distinct feature, as in Fig. 6.41.

6.4 Discussion

The most important result of this chapter is the contrast between the two plate margins discussed. In the first, the Middle America trench, the stress patterns varied significantly with the shape of the leading edge of the continent, in particular because of the postulated landward-dipping contact between continental crust and accreted sediments, which forms an overhang and can give rise to normal faulting near the surface and the possibility of high angle-compressional failure at the point of lithospheric subduction. These might both be aspects of the type of tectonic erosion postulated by Hussong et al. (1976) and Curray et al. (1977), as described in Section 1.4, Ch. 1 (see Fig. 1.7). This behaviour was not observed at all in the central Aleutian model.

A further difference between the two, is the equilibrium basal shear stress; 12 MPa for the Middle America model, but only 5 MPa for the central Aleutians model. The convergence rate for the first margin is 60 mm yr^{-1} (Karig et al., 1978) and for the second 70 mm yr^{-1}. The latter value is derived from a calculation using the plate motions given by Minster and Jordan (1978), which gives 84 mm yr^{-1} for the rate at an angle of 60° or 50° to the trench axis, or normal convergence of 73 or 64 mm yr^{-1}. So the central Aleutians have a normal convergence rate at least as big, if not greater than that of the Middle America trench, and yet show less than half the basal shear stress.

Using the results of Ch. 5, there are two possibilities, one arising

if a shear zone model is considered, the other for a frictional model of
the basal shear. In the first case, there may be a difference in the material
available to form the shear zone, so that either its viscosity, $n_{s.z.}$,
is lower or its thickness, d, is greater in the Aleutian model (see Equation
5.1). In the second the gouge along the basal thrust may be of a different
composition, reducing the coefficient of friction, μ (Equation 5.3; the
thickness of the two sedimentary complexes are similar so that changes in
σ_n are unlikely to cause the difference in basal shear).

Whatever the mechanism for the difference in basal shear, the latter
is larger for the accretionary prism with the higher angles of dip on the
surface and base, as predicted by Section 5.5, Ch. 5 (the surface and basal
dips for the Middle America prism are 8.5° and 11°, and for the central
Aleutian accretionary prism 4° and 6°, respectively).

A similarity between the two models is the importance of the
position of the overriding basement. In the first set of models it was
shown to dictate the position of the region of subsidence in the upper
slope, which might eventually give rise to an upper slope basin. The draping
of the accreted sediments from the continental basement would then represent
the upper slope discontinuity, although the normal faulting predicted
behind this position might represent this feature instead (see Section 1.4,
Ch. 1).

In the second set of models (of the central Aleutian trench inner slope),
the position of the point of subduction was marked on the surface by a
region of uplift (or reduced subsidence). The model therefore indicates
that the point of subduction defines the seaward edge of the terrace or
upper slope basin, so that in Grow's (1973a) model (Fig. 1.8), the over-
riding igneous crust would extend beneath the terrace to its edge, and meet
the subducted oceanic crust beneath that point.

In Fig. 6.32 it was noted that the break in the lower slope of the model was accentuated by the surface displacement, and even more so if there is an increase in E and η of the accreted sediments as they become more lithified further from the trench (Figs. 6.40 and 6.41; the same type of effect is also shown by several of the models of the Middle America trench in Section 6.2, e.g. Fig. 6.2). This feature might represent the trench slope break, nearer to the trench, where the accreted sediments have been built up to the surface slope dictated by the basal shear stress (as described in Ch. 5). This interpretation predicts that, in an accretionary complex where the point of lithospheric subduction is a long distance from the toe (e.g. over 200 km in the Lesser Antilles), there would be two distinct features; a trench slope break comparatively close to the toe (at 15-20 km), and a second region of uplift above the point of subduction. This is the suggestion made by Westbrook (1975) for the origin of Barbados, as described in Section 1.4.1, Ch. 1.

Finally, the strains in all the models in this chapter are small. The maximum value in each case is at most 7%, and corresponds to shearing along the basal thrust, while the strains along the inner slope are 1-2%. This confirms that most of the deformation observed in accreted sediments occurs while they are being accreted at the toe of the prism, as suggested in Section 5.8, Ch. 5.

CHAPTER 7

FAILURE WITHIN THE UPPER PART OF A SUBDUCTION ZONE, AND DECOUPLING

ON THE BASAL THRUST PLANE

7.1 Pore Pressure and its Effect on Rock Fracture

Hubbert and Rubey (1959) showed that the effective stress within

sediments containing pore water is

$$\sigma_{eff} = \sigma + p \qquad\qquad 7.1$$

(see Ch. 5, Section 5.4.4, Equation 5.5), where p is the pore pressure

and σ is compressive (and therefore negative) at depth. The effective

stress, σ_{eff}, must then be used in the failure criteria of Ch. 2, Section 2.3.

The pore pressure may, in general, take any value between the

hydrostatic value caused by the head of water, $h \rho_w g$ (Equation 5.6), and the

lithostatic pressure $h \rho g$ (Equation 5.7), where ρ_w is the density of water

and ρ the density of rock. The amount of overpressuring (represented by

the factor f in Equation 5.7) depends on the permeability of the rock;

if the permeability is low then the pore pressure will approach the mean

stress at a given point, but if it is high the pore pressure will be close

to $h \rho_w g$.

If this value is assumed to be correct for the accreted sediments in

the models of Section 6.2, in particular for the original equilibrium model

of Figs. 6.1 to 6.3, modelling difficulties arise. The assumption of

$p = h \rho_w g$ implies that the water is self-supporting, that is, that it

permeates the entire sedimentary wedge, and its weight is carried by the

first impermeable layer, taken in this case to be the basal thrust plane.

Therefore no forces are applied to the surface of the model, as mentioned

in Section 4.5, Ch. 4.

However, if sediments are under c. 4 km of water, then at a given point, P, at a depth of less than c. 2 km,

$$p = h_w \rho_w g \quad > \quad h \rho g \qquad\qquad 7.2$$

(where h_w is the depth from sea level to P, and h is the depth from the sea bed to P; see Fig. 7.1).
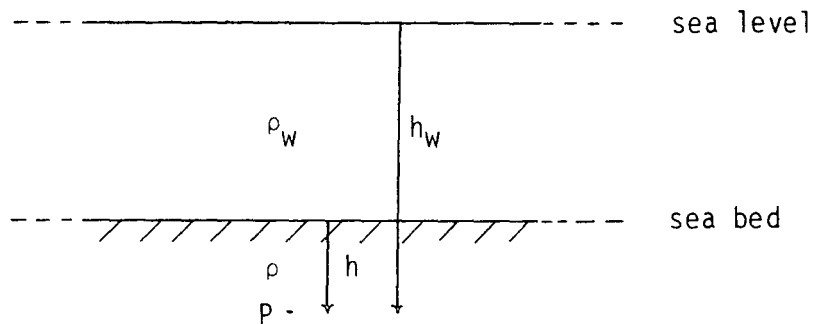
Fig. 7.1: Illustration of parameters used in Section 7.1.

The implication of Equation 7.2 is that when the pore pressure is added to the mean stress ($\sigma_m \simeq -h \rho g$, because the weight of the water is supported by an impermeable layer at greater depth than P), it becomes tensional, so that the upper 2 km of the sediments can support little or no shear stress (they fail in the tensional region with $\sigma_m > 0$; see Section 2.3, Ch. 2). This result cannot apply to the sediments in an accretionary prism, because it implies that a sedimentary structure with surface topography, containing pore water, cannot exist beneath several kilometres of water. It does, however, apply to sediments which are not lithified, and is the physical reason why unconsolidated marine sediments are flat lying (except where there are effects due to currents) and do not accumulate on sloping surfaces.

On the other hand, if sediments under water are well lithified, then the effect of the overlying water is rather different, because now

the sediments are impermeable and so must support the weight of the water above them. Using the ~~same~~ notation as ~~before~~ shown in Fig. 7.1 , the stress at point P must support a depth (h_w - h) of water and a thickness h of sediments, so that if the stresses are lithostatic,

$$\sigma = -(h_w - h)\rho_w g - h\rho g = -h(\rho - \rho_w)g - h_w\rho_w g .$$
7.3

Now, the sediments, even if ~~though~~ impermeable, may still have significant porosity, so that the pore pressure, which will in general be greater than $h_w\rho_w g$, must be added to the stresses to find the effective stresses

$$\sigma_{eff} = \sigma + p$$
(Equation 7.1)

with p = -f σ
7.4

where f is the overpressuring factor, following Hubbert and Rubey (1959). Note that compressional stresses are negative, while pressure, and in particular pore pressure, is conventionally a positive quantity.

When sediments are laid down under several kilometres of water they are at first unconsolidated, and the pore pressure due to the head of water opposes compaction (see Equations 7.1 and 7.3, with $p = h_w\rho_w g$). ~~(Equation 7.2)~~. However, as the sediments become lithified and the pores become isolated, reducing permeability, pore water is excluded and the water above begins to exert a force on them which tends to enhance lithification, until finally, at some depth beneath the sea bed, the entire weight of the water is supported and Equations 7.3 and 7.4 apply.

These factors make a calculation of the effective stresses within the accretionary wedge very difficult. Clearly the accreted sediments are sufficiently lithified to support the surface topography (in Ch. 6 it was concluded that they must have a Young's modulus of at least 1 GPa), but this is not the case for at least the upper 500 m. Lee (1973) presents data for vane shear strengths and water content of the sediments cored on D.S.D.P. Leg 19 (near the Aleutian trench), as do Bouma and Moore (1975)

for Leg 31 (in the Phillipine and Japan Seas), which show that the sediments have a very high water content and are very weak. Leg 19 results show that the shear strength of the sediments is less than 0.4 MPa down to at least 600 m, the limit of the data, and Leg 31 results similarly show that the unconfined shear strength of the sediments is less than 0.1 MPa down to at least 300 m, this last figure being from hole 298 in accreted sediments on the inner trench wall of the Nankai Trough.

It is impossible to say, either at what depth in the accretionary wedge the sediments are sufficiently lithified so that the load of the water should be applied, or what pore pressure should be used to find the effective stresses for failure prediction. In addition it is not clear whether the load of the water should be applied as a set of forces on the body, thereby creating a deviatoric stress system superimposed (non-linearly since the sediments have a visco-elastic rheology) on the tectonic stresses, or as a simple addition of a hydrostatic stress, $-h_w \rho_w g$, at all points in the accretionary prism.

This thesis does not provide a solution to the above problems, and the accretionary wedge was modelled in all cases without any loads due to the water, and the failure criteria of Section 2.3, Ch. 2, could not be applied to the tectonized sediments in the model, because the effective stresses could not be calculated.

However, these problems do not apply to the overriding basement rocks, which are assumed to contain no pore water, and the failure criteria of Section 2.3 are applied to this region both in this chapter and in Ch. 6.

7.2 A New Basal Boundary Condition

All the wedge models analysed so far (Ch. 5, Ch. 6) have had shear stresses applied to their base. This implies that the subducted plate is decoupled from the wedge by the basal thrust plane, with the transmission of stress being either through a weak shear zone, or by frictional contact, and that the basal thrust is in equilibrium with the subducted plate sliding past beneath at a uniform rate.

This type of model is likely to be realistic over a length of time of 1 Myr, but on a shorter time scale it is not such a good approximation. Major earthquakes occur along subduction zones, and Sykes (1971) has shown that these take place in such a way that, although displacement of the subducted plate may vary along the length of the subduction zone at any one time, the gaps between the aftershock regions of major earth-quakes are gradually filled in by others, so that the average displacement rate of the whole plate is preserved.

In order to investigate this type of behaviour, the model of the Middle America trench used in Section 6.2, Ch. 6, was modified to obtain more detail at the base of the overriding basement as shown in Fig. 7.2 (cf. Fig. 6.1), but the material properties and boundary conditions, other than those on the base, were the same as those used in Section 6.2 (Table 6.1).

The model was initialized visco-elastically, as described in Section 4.4, Ch. 4, for 1 Myr with a basal shear of 12 MPa, and was then deformed from this equilibrium position by applying a displacement to the nodes along the thrust plane of 60 mm yr^{-1} (the convergence rate at the Middle America trench, according to Karig et al., 1978) down the basal slope. This displacement boundary condition represents a "locking" of the basal thrust plane, which is then released by failure along or near the
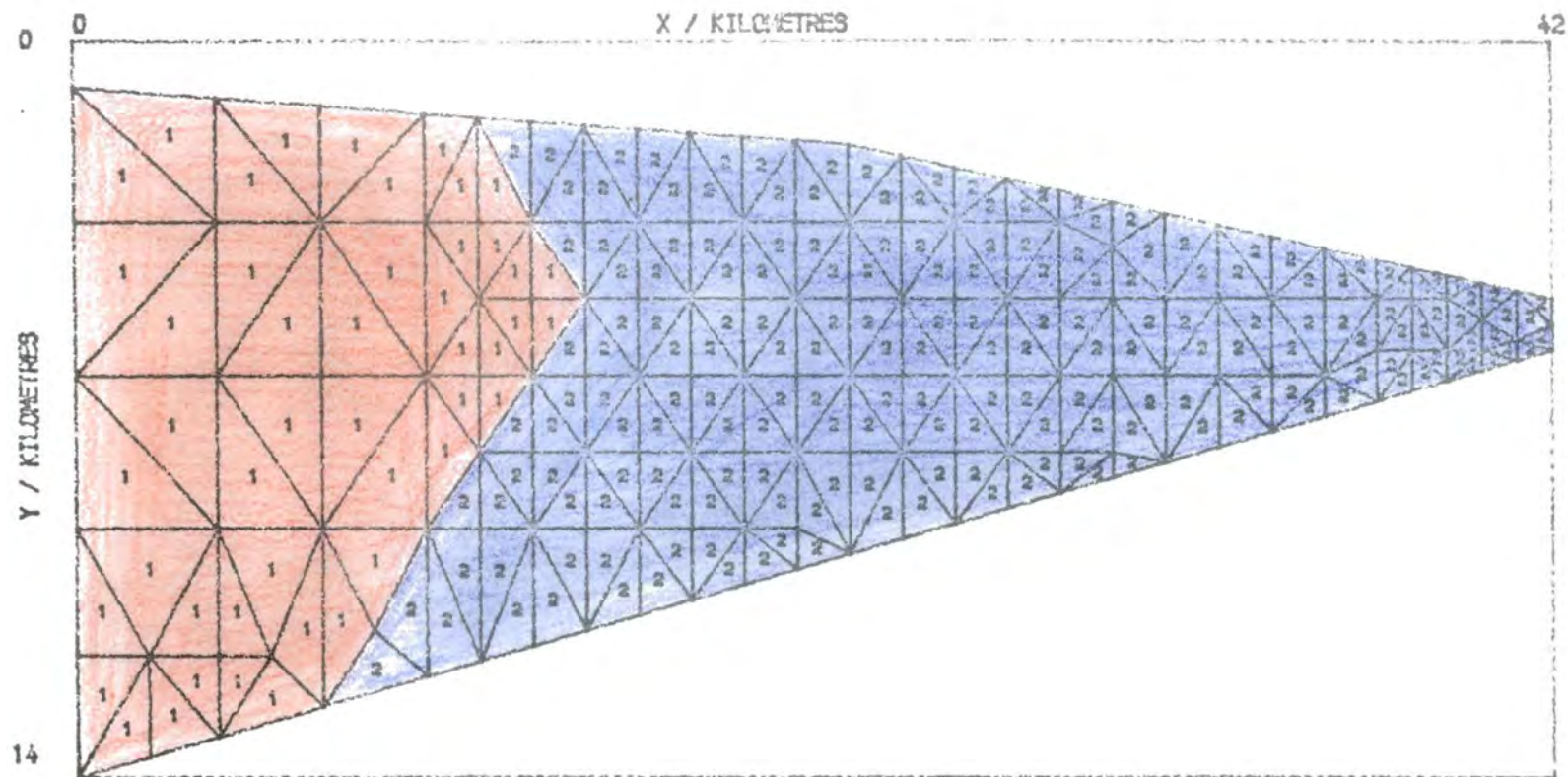
Fig. 7.2: The Middle America trench model of Ch. 6 (Fig. 6.1) with extra
elements inserted at the base of the continental crust to increase
detail. The material type of each element is indicated at its
centroid: 1. Crystalline basement
             2. Accreted sediments.

thrust.

Figure 7.3 shows the stresses in the model after 500 yr. It can be seen that the greatest stresses are concentrated at the base of the continental crust, the greatest compression being very large (2 GPa), while the stresses in the sedimentary wedge are much smaller. Compressional failure is predicted very strongly at the base with a degree of failure, C = -3.1 (as defined in Section 2.3, Ch. 2), as is normal faulting along the surface of the continental section, corresponding once more to a clockwise rotation (cf. Section 6.2, Ch. 6).

Several other models were now run to find out at what stage failure is first predicted at the base of the model. The time taken to fail depends on the tensile strength, T, of the crystalline basement rocks, as shown in Table 7.1, but is approximately 250 yr for T between 10 and 50 MPa. Thus, assuming that the basal stresses are completely relaxed by

Length of time for which model was run/yr	Tensile strength of continental basement T/MPa	Degree of failure C	Type of failure (if any)
200	50	+0.27	Open crack
250	50	+0.07	Open crack
300	50	-0.16	Open crack
200	10	+0.11	Closed crack
250	10	-0.20	Closed crack
300	10	-0.56	Closed crack

Table 7.1: Variation in degree and type of failure for some models with displacement boundary conditions. The degree of failure, C, is negative if failure is predicted.
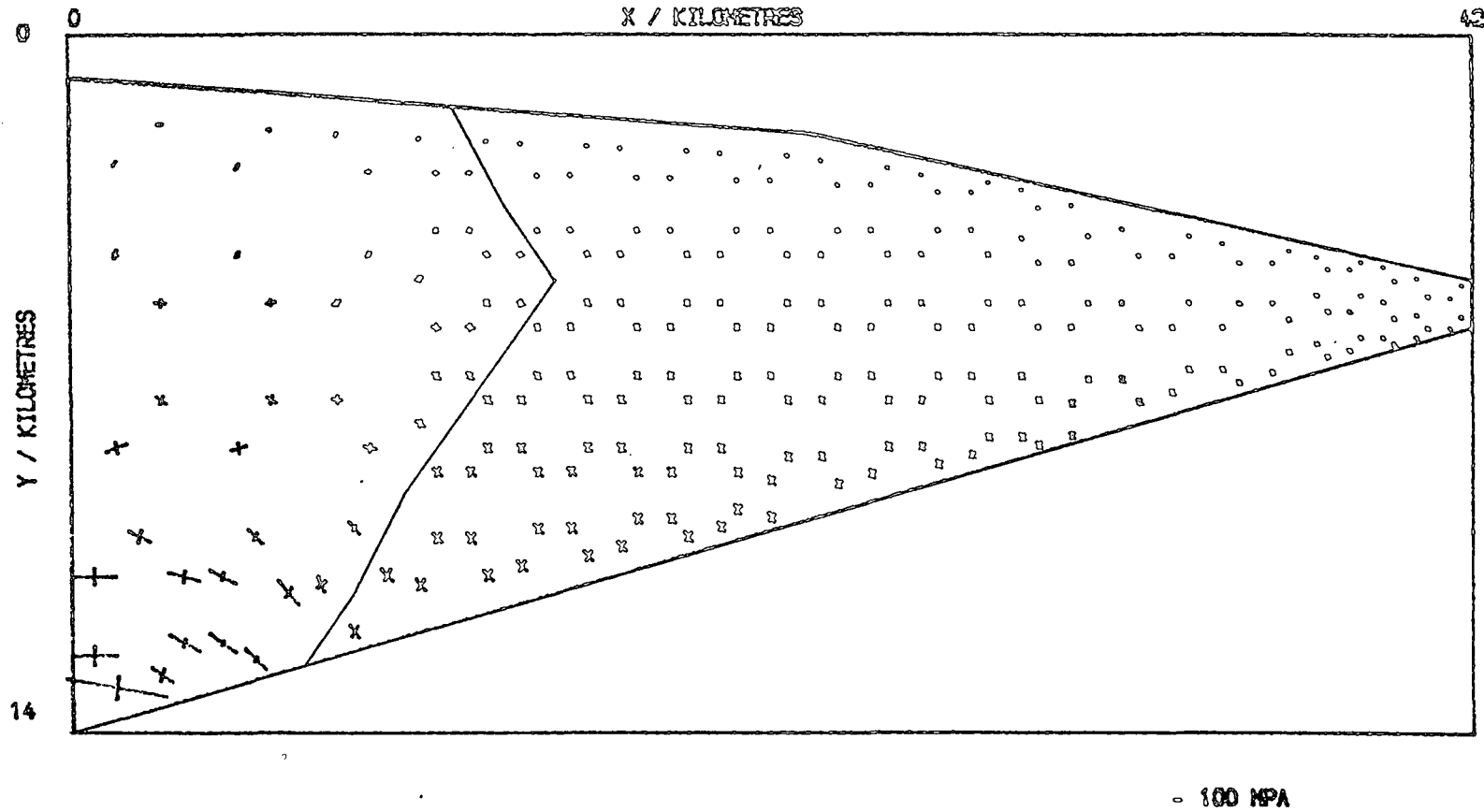
Fig. 7.3: The principal stress distribution in the model of Fig. 7.2, in response to a displacement boundary condition at the base of 60 mm yr^{-1} down slope, after 500 yr.

each event, the model predicts a repeat time for earthquakes in the
upper part of the subduction zone (at the point of subduction) of
c. 250 yr. A shorter repeat time would result if the stresses built up on
the thrust plane are only partially relaxed by the movement during each
event.

However, this does not necessarily represent the repeat time for all
major earthquakes at the subduction zone, since the majority of these, for
most subduction zones, have much deeper hypocentres than the point of
subduction, so that the repeat time must depend more on the interaction
between subducted crust and overriding mantle.

The displacements of the surface after 250 yr (which are not shown
since they are so small) correspond to the rotation of the continental
crust, together with subsidence, of up to 4 m, in the upper slope, and a
general movement of the lower slope parallel to the basal thrust of
c. 60 mm yr^{-1}. However these displacements, which would be large if
continued for 1 Myr, are almost purely elastic (since the Maxwell time
for the sediments $t_m \simeq 6 \times 10^4$ yr $\gg$ 250 yr, the length of time for which
the model was run) and must be released, at least in part, when the basal
thrust "unlocks", that is when there is an earthquake. These displacements
appear to be rather large when compared, for example, with the vertical
displacements recorded in the Japan arc associated with earthquakes (Kato,
1979, gives displacement values of less than 0.4 m for the period 1900-1974).

Another prediction of this model is that there should be widespread
normal faulting in the upper part of the continental basement (in this
part, C $\simeq$ -2.7 after only 50 yr). This prediction casts some doubt on the
method of modelling the basal thrust with displacement boundary conditions,
since extensive normal faulting of this type is not shown on the seismic
reflection profiles published with the D.S.D.P. Leg 66 results (Moore et al.,

1979; Moore and Watkins, 1979; Shipley et al., 1980).

However, if this locking and unlocking of the basal thrust is a valid mechanism for earthquake generation, its time scale is geologically very short. It is proposed that the shape of the accretionary prism is determined by the type of equilibrium shown in Ch. 5 and Ch. 6, and that this type of modelling represents an average of the discontinuous type of basal movement modelled in this section, over times much longer than 500 yr.

CHAPTER 8

SUMMARY AND CONCLUSIONS

The finite element method has been used to model the stresses and deformation within the prism of accreted sediments in a subduction zone.

The application of numerical techniques to model regions, in which physical quantities (e.g. material properties and stress distributions) are so poorly constrained by direct observations, poses many problems, the first of which is to choose a rheology and the associated parameters to represent the behaviour of rocks realistically. A visco-elastic rheology was chosen, and was considered to be more realistic than an elastic one (there were found to be significant differences in the results obtained), but an extension to non-linear viscosities was not thought to be justified, because previous work has shown the consequent changes to be small (Bischke, 1974; Cathles, 1975; Melosh and Raefsky, 1980). A plastic, or elasto-plastic, rheology might also be modelled with finite elements (Zienkiewicz, 1971), but yield stresses and the plastic flow law would be difficult to predict at depth in the crust.

The next difficulty to be faced was how to model correctly the effect of the weight distribution in the lithosphere. Previous finite element models of the lithosphere have not dealt with this problem satisfactorily, and it is particularly important in accretionary prisms where one of the main causes of deformation is the weight of the wedge. A new method for taking these body forces into account was developed, which involves finding, by iteration, a hypothetical starting model which deforms, either elastically or visco-elastically for a prescribed length of time, to give an initial model with the dimensions required. The visco-elastic deformation, resulting

from the application of external tectonic stresses or fixed displacements to this initial model, then gives displacements which are free of deformation occurring before the application of tectonic stresses, such as that due to compaction, but also gives stresses which include the effects of density contrasts within the model.

To illustrate the effects of this initialization, models were run of an Atlantic-type passive margin, where an average shear stress of 60 MPa was found to be set up in the crust due to lateral density variations across the margin.

An analysis was made of a simple model of the toe of the Middle America accretionary prism to investigate the interaction between shear stress along the thrust plane between the wedge and the subducted oceanic crust, and the visco-elastic subsidence of the wedge in response to its weight. Two types of basal stress were modelled, one corresponding to transmission of stress to the base of the wedge through a weak viscous shear zone, the other to frictional shearing on the thrust plane. It was found that these models could not be distinguished by the model used, but that both gave realistic results.

An equilibrium stress was found in each case which supported the wedge sufficiently to hold its surface still. The average basal shear under these conditions was 12 MPa in both models, the viscosity of the shear zone was estimated to be 10^{18} $N\,s\,m^{-2}$, which is consistent with the values obtained from stress-strain curves for sediments, and the coefficient of friction on the thrust was inferred to be c. 0.25 (assuming the fault to contain gouge with a pore pressure of 60% of lithostatic), which is typical for residual shear strengths in clays.

It is considered that this equilibrium position represents the steady state for an accretionary prism, and that a larger basal stress leads to

the building of a larger wedge. If the basal shear is smaller than the equilibrium value, then the wedge tends to subside and flatten out up the basal slope (an example of gravity spreading).

The strains in the equilibrium model are all small (less than 5%), which indicates that most of the strain observed in accreted sediments occurs as they are scraped off onto the toe of the prism, and that thereafter the strain rate drops considerably while they migrate up the trench slope.

It was found that the equilibrium basal shear depends on the slope of both the upper surface and the base, in disagreement with Elliott's (1976) work, and analysis of the potential energy of the wedge (considering it now to represent a thrust sheet) led to the conclusion that, if there is to be motion on a thrust plane up the basal slope, then supporting stresses are needed at the end of the thrust sheet lower down the basal slope. These stresses must be at least equal to lithostatic, in which case gravity spreading of the thrust sheet may occur up the basal slope, but if the thrust sheet is to move as a whole in this direction, then larger, tectonic, driving stresses are required, and such motion cannot be driven by gravity alone.

An instability was discovered in these models when attempting to find the behaviour of sediments with low viscosity. It was found that if a wedge model was run for a time which was much longer than the Maxwell time, t_m, for the sediments, then the stress distribution and surface displacement became unstable (the model was still stable after times of 10 t_m, but 100 t_m was too large). This instability was interpreted as arising from the presence of the free, sloping upper surface of the wedge, combined with the plane strain analysis using a Maxwell rheology, and could not be avoided by any of several methods used.

The model of the Middle America accretionary wedge was extended to

include part of the overriding continental crust, and the basal shear needed to support the toe of the wedge in equilibrium in this model was found to remain unaltered at 12 MPa. By observing the patterns of surface deformation in models of this type where the material properties of the wedge were varied, keeping the better-determined properties of the continental basement constant, it was concluded that the effective viscosity of the sediments is c. 10^{22} N s m^{-2}, and that their Young's modulus is c. 10 GPa.

A comparison was made of this model with one of the accretionary complex in front of the central Aleutian Island arc, where the equilibrium basal stress was found to be only 5 MPa, due to the shallower angle of the basal slope arising from the greater width of the complex. It was deduced in both cases that one of the most significant factors in determining the deformation of the accretionary prism is the shape and extent of the overriding basement, and that this was the cause of marked differences between the two models.

In the Middle America model the basement is undercut and supported in part by the accreted sediments forced underneath it, the degree of support depending on the density and rigidity of the sediments, and on the basal stress. In the Aleutian model, on the other hand, the igneous arc crust underlies the sediments, and it was shown that the latter are pushed upwards immediately above the point of subduction, where subducted crust comes into contact with the leading edge of the overriding basement. It was deduced that this uplift represents the edge of the terrace basins in the central Aleutians, and that the arc crust extends beneath the entire terrace, the point of subduction being immediately below the terrace edge. This feature is thought to be distinct from the trench slope break, which represents the height to which sediments are lifted in response to the basal

shear on the wedge.

Behind this region of uplift, there is subsidence of the terrace sediments, which was also found in the upper slope of the Middle America model, just seaward of the continental crust. This is in agreement with observational evidence that the upper slopes or terraces of many subduction zones are subsiding.

A further difference between the two models was that faulting at the base of the continental basement, of a type thought to lead to tectonic erosion, was only possible in the case where it was undercut. The shape of the underlying crust in the Aleutian model could not give rise to the stresses necessary for this type of compressional faulting.

An attempt was made to investigate the faulting in the accretionary prism and leading edge of the continent by using displacement boundary conditions at the base, instead of shear stresses, with the aim of finding out how much decoupling there is along the basal thrust, and what length of time is needed to cause faulting. However, the water pressure in sediments, at several kilometres depth in the sea, has a complicated effect on the stresses in the sediments, which proved too difficult to model accurately, as far as calculating the degree of failure in them was concerned.

Therefore only the fracture of the continental basement could be investigated, and 250 yr was found to be the time necessary to build stresses up to the point where failure occurs at the base. However, this model also made predictions of the displacements of the surface of the continental crust, and of the degree of failure there, which seem to be unrealistic, and it is thought that the only way to make a realistic model of this type is to include both mantle material in the overriding plate, and at least part of the crust below the basal thrust.

However, despite these difficulties, the visco-elastic finite element

method has produced some interesting results from the models analysed, and there is scope for further work of this kind.

If the problem of pore pressure and effective stresses could be resolved, then modelling might reveal how much of the basal thrust is ever locked together, and over what length motion might occur in earthquakes. The intervals between major earthquakes and their magnitudes might then be modelled as an aid to prediction of seismic risk near subduction zones. The surface displacements predicted might indicate whether tsunamis were likely.

The inclusion of faults in the model would increase its realism, and remove the simplifying assumption of material property isotropy made in the models in this thesis (some work has already been done on the modelling of faults using finite element analysis; see, e.g., Bischke, 1974). It might then be possible, again if effective stresses could be calculated, to predict how the imbricate thrust faults in the sediments at the toe of the wedge propagate, and perhaps to model the shearing of slices of sediment from the subducted plate at depth to discover how under-plating occurs.

There are therefore many more results, essential to the understanding of tectonic processes at subduction zones, that might be obtained from the application of finite-element methods to more sophisticated models of such regions.

APPENDIX 1

ANALYTICAL MODELLING OF A PLASTIC THRUST SHEET

This appendix contains a summary of the equations derived by Chapple (1978) which were referred to in Chapter 5, Section 5.5.2.

A1.1 The Model and Boundary Conditions

Chapple (1978) made an analytical investigation of a model of a thrust sheet, assuming that it consisted of a perfectly plastic material yielding in compressive flow, underlain by a weaker shear zone of the same rheological type.

The plane polar co-ordinate system used (r,θ) is defined by Fig. A1.1, but otherwise notation is as used in Ch. 5.
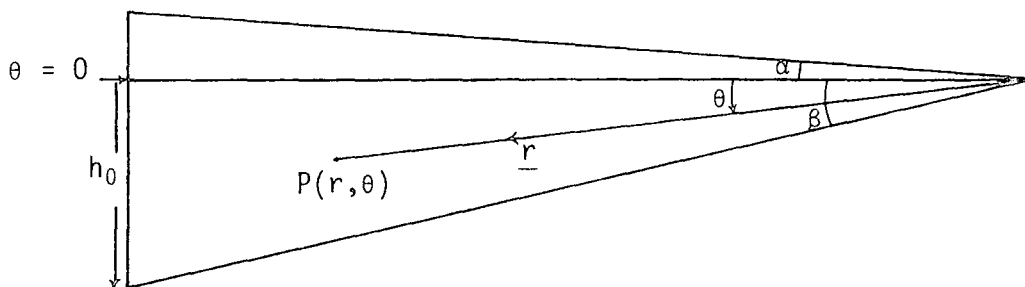
Fig. A1.1: Definition of polar co-ordinates used in modelling a thrust sheet analytically.   (Chapple, 1978)

The boundary conditions used are:

    a)   the top surface is stress free

$$\sigma_\theta = \tau_{r\theta} = 0 \text{ at } \theta = -\alpha \qquad\qquad\qquad \text{A1.1}$$

    b)   the basal shear is constant, and equal to the yield stress of

          the weaker shear zone underlying the wedge

$$\tau_{r\theta} = \tau_0 = \text{constant} \quad \text{at } \theta = \beta \qquad\qquad \text{A1.2}$$

Chapple found that the restraint of maintaining the surface slope fixed, while specifying that the material beneath it was yielding, over-constrained the model. To avoid this, he modelled the wedge in two parts, divided by a horizontal surface which he prescribed to be free of shear stress,

$$\tau_{r\theta} = 0 \quad \text{at } \theta = 0. \qquad\qquad\qquad\qquad \text{A1.3}$$

The lower part was then analysed as supporting plastic flow, and the angle of the surface (α) was found by assuming that the upper part gave rise to the stress distribution derived normal to the dividing boundary, $\theta = 0$.

The condition that the wedge is yielding plastically, implies that

$$|\tau_m| = K \qquad\qquad\qquad\qquad\qquad\qquad \text{A1.4}$$

everywhere, where K is the yield stress of the wedge material and τ_m is the maximum shear stress (see Ch, 2, Section 2.3).

By using similar equations to those in Ch. 2, Section 2.3, Equation A1.4 may be rewritten as

$$(\sigma_r - \sigma_\theta)^2 + 4\tau_{r\theta}^2 = 4K^2 \qquad\qquad\qquad \text{A1.5}$$

which gives

$$\tau_{r\theta} = K \sin2\psi \qquad\qquad\qquad\qquad\qquad \text{A1.6a}$$

$$(\sigma_r - \sigma_\theta) = -2K \cos2\psi \qquad\qquad\qquad \text{A1.6b}$$

for the point P at (r,θ), where $\psi = \psi(\theta)$ is the angle between σ_3 (the minimum principal stress) and $\underline{r}$ at P.

A1.2 Summary of the Analysis and Results

Through application of the boundary conditions (Section A1.1, above) to the equilibrium equations for the wedge,

$$r \frac{\partial \sigma_r}{\partial r} + \frac{\partial \tau_{r\theta}}{\partial \theta} + (\sigma_r - \sigma_\theta) + \rho g r \sin\theta = 0 \qquad \text{A1.7a}$$

$$r \frac{\partial \tau_{r\theta}}{\partial r} + \frac{\partial \sigma_\theta}{\partial \theta} + 2\tau_{r\theta} + \rho g r \cos\theta = 0, \qquad \text{A1.7b}$$

Chapple obtains relations between ψ and θ dependent on a model parameter, C for $C > 1$;

$$\theta = \psi - \frac{C}{\sqrt{C^2 - 1}} \tan^{-1}\left[\sqrt{\frac{C - 1}{C + 1}} \tan\psi\right] \qquad \text{A1.8a}$$

for $-1 < C < 1$;

$$\theta = \psi - \frac{C}{\sqrt{1 - C^2}} \tanh^{-1}\left[\sqrt{\frac{1 - C}{1 + C}} \tan\psi\right] \quad , \qquad \text{A1.8b}$$

$$C = \frac{h_0 \rho g \tan\alpha}{2K \tan\beta} \quad , \qquad \text{A1.9}$$

where h_0 is the depth to the base of the wedge from the boundary at $\theta = 0$ (Fig. A1.1).

The basal shear is taken to be

$$\tau_0 = \chi K \qquad \text{A1.10}$$

where χ is the ratio of the yield stress of the basal shear zone to that of the wedge, and using Equations A1.10 and A1.6a applied to the base of the wedge (where $\psi(\theta) = \psi(\beta) = \psi_0$)

$$\psi_0 = \tfrac{1}{2} \sin^{-1}\chi \quad . \qquad \text{A1.11}$$

Using Equations A1.8 to A1.11, assuming a set of model parameters,

the basal shear stress τ_0 may be found for different values of α and β.

In order to achieve agreement with the finite element results (Ch. 5, Section 5.5), the best value of the yield stress K was found to be 12 MPa, which is consistent with the discussion in Ch. 2, Section 2.3.4. The depth to the base of the wedge (h_0) was taken to be 5 km, and its density was taken to be the reduced value, ρ = 1500 kg m^{-3} (being the total density, 2500 kg m^{-3}, less the density of water, following the rheological assumptions made by Chapple).

An apparent inconsistency arose in using these values, because the yield stress calculated for Chapple's shear zone is close to that for the whole wedge, i.e. $\chi \simeq 1$, so that the shear zone is no longer a well-defined region, distinct from the rest of the wedge. However the analysis is nonetheless valid and the results are presented (to the nearest 1 MPa) in Ch. 5, Section 5.5.2, Table 5.4.

It should be emphasized that the agreement between Chapple's results and those using the finite element method can only be regarded as qualitative, because of the difference in rheology between the two models (the finite element analysis was visco-elastic; see Ch. 3).

APPENDIX 2

COMPUTER PROGRAMS

A2.1 <u>Introduction</u>

The finite element program developed for this research uses the methods described in Chapter 3. It was written (in IBM FORTRAN IV) in modular form, with a main calling program (filename FEVER) and a subroutine library (PRIMA). The advantage of this system is that the sequence of subroutines called may be changed easily, by using comment characters (C in column 1 of the relevant line in FEVER), and only the main program need be recompiled.

The external subroutines required are MAØ7BD (in the Harwell subroutine library; Hopper, 1973), an inversion routine for banded matrices, and the graphical subroutines in the GHOST library. In addition, contour plots require the CALCOMP General Purpose Contouring Package (GPCP). These are commonly available at computing centres.

It has been assumed that S.I. units will be used for all input, but any consistent set of units may be used (bearing in mind the default values of certain variables, e.g. the gravitational field strength, and that the nodal coordinates (X,Y) are multiplied by 10^3 on input to convert from km to m).

A2.2 <u>Input</u>

The program reads data from 4 device numbers:

1. Initial stresses, σ_0 (see Ch. 3), generated by a previous program run (unformatted).

3. Unformatted input of all variables necessary to perform further

time increments on a model. This file must be generated by a

previous run of FEVER or by the initialization program, SETUP

(see Section A2.6).

4. All input data describing the model and its boundary conditions.

5. Interactive input for controlling each job, e.g. the title and

the number and length of time increments.

The input on Devices 4 and 5 is shown below, in detail. All integers

are read in under Format (I4), all real numbers under (E10.3).

Device 4

NNOD, NEL, MOHO, G: number of nodes, number of elements, flag for

Moho, gravitational field strength. MOHO determines whether the Moho will

be drawn on plots of rectangular models, and must be the number of the

node on the Moho at the left-hand side of the model. Its default value is

0, in which case the Moho is not drawn. G defines the direction of the

y-axis (if G is positive, y is measured downwards), and defaults to + 9.81.

IMESH, NNODB, NELB, WIDB, NSID, NNODA, NELA: Information for the

regular rectangular mesh generating subroutine, MESH. If IMESH is

positive then MESH is called. NNODB, NELB are the numbers of nodes and

elements whose properties are to be read in, WIDB is the width of the

block to be repeated, NSID is the number of nodes down each end of the

model (if different from the main part of it), and NNODA, NELA are the

repeat numbers for nodes and elements, respectively (see comment cards

in the listing of subroutine MESH). If IMESH is set to zero, the mesh

generating subroutine is not called, and the rest of the card may be

left blank.

JNOD, X(JNOD), Y(JNOD): The number of each node, together with its

x and y coordinates in km.

NMAT: The number of different material types in the model.

EM(IMAT), PM(IMAT), RHOM(IMAT), ETAM(IMAT), TS(IMAT), IPORE(IMAT): The Young's modulus, Poisson's ratio, density, viscosity, tensile strength and pore pressure marker for each material type. If ETAM is zero, the material is elastic. The default value for TS is 5×10^7 (corresponding to T = 50 MPa). If IPORE = 1, then pore pressure, due to the head of water above the centroid of the element, is added, using Subroutine PORE, to all the stresses (reducing compressional stresses) before application of failure criteria.

JEL, (NODEL (KEL, JEL), KEL = 1,3), ITYP(JEL): The number of each element, the numbers of the three nodes at its corners, and the material type.

NLOAD: The number of nodes at which external forces are applied.

LOAD(ILD), FLOAD(2*ILD - 1), FLOAD(2*ILD): The number of each node at which a force is applied, and the x and y components of that force.

NFIX: The number of nodes at which displacements are to be fixed.

NOFIX(IFIX), (IFLAG(JFIX, IFIX), DFIX(JFIX, IFIX), JFIX = 1,2), ANGLE(IFIX): The number of each node whose displacement is to be fixed, the marker and value of the fixed displacement for each component, and the angle of the coordinates in which the displacements are given. If, for a particular component, IFLAG is

Ø that component is not fixed;

1 it is a fixed displacement in global coordinates (x,y);

2 it has a fixed velocity of DFIX per time increment, in global coordinates;

3 it is a fixed displacement in coordinates which make an angle to (x,y) given by ANGLE;

4 it has a fixed velocity, DFIX per time increment, in rotated coordinates.

If Subroutine ISOS has been called, it reads in information on the isostatic compensation to be applied at this stage, and if Subroutine HYDRA has been called, it also reads in the relevant data here (for details of these options, see subroutine listings).

NOUT(IOUT): A list of the numbers of the nodes forming the outline of the body to be drawn on the graphical output. The list must be closed by making the last number equal to the first, and must be taken anticlockwise if y is measured downwards. If NOUT(1) = $\emptyset$, then the body is assumed to be rectangular.

Device 5

TITLE: The title of the job in Format (4A8).

NTIME, DTIME: The number of time increments and the length of each. If NTIME = $\emptyset$ an elastic solution is given. These variables may be given in the main program before the call to Subroutine VISEL, in which case they are not read in.

ITCON: If a time increment does not converge, the program prompts (on Device 6) for the entry of the number of extra iterations.

A2.3 Output

The program produces output on 7 device numbers:

$\emptyset$. A file for input to the contouring package, GPCP.

2. Unformatted output of stresses for input to the next run on Device 1.

3. Unformatted continuation data written out by Subroutine MORE.

6. Interactive output, prompting for input to Device 5, and giving information on the progress of the job, including error messages.

7. Written output echoing input and presenting results.

8. Information on the convergence of each time increment.

9. Plotfile containing graphical output generated.

The output on Device 7 includes verification of the input to the program and of which subroutines were called, but the main part of it consists of tables of the results calculated. The first of these is a table of the nodal displacements, and the second of the resultant stresses and failure states for each element. The two principal stresses in the plane of the model are given together with the angle that the first makes with the x-axis. Following that is the stress in the z-direction (perpendicular to the plane) σ_z, and a marker, MZ, which is -1, $\emptyset$ or +1 according to whether σ_z is the minimum, intermediate or maximum principal stress. The final three columns show the failure state of the element (calculated by Subroutine FAIL according to Section 2.3, Ch. 2); CFAIL, the degree of failure, IFAIL, the type of failure, and θ, the angle of failure (stored in array FANGL).

Finally if Subroutine STRAIN has been called it writes out the principal strains in the plane of the model with their angle of orientation, for each element.

A2.4 Subroutine Calling Sequence

The sequence of subroutine calls from the main program is shown below. Those subroutines which are optional are indented.

Solution Phase

READ   reads in data from Device 4.

         READ2   as an alternative to READ, reads in data from a previous run, on Device 3.

	ECHO1	echoes nodal coordinates and element topologies.
ECHO2		echoes material properties and boundary conditions.
KFORM		forms the stiffness matrix.
	INSTRS	incorporates an initial stress distribution (from Device 1).
	FBODY	applies body forces due to the weight of the model.
	ISOS	applies isostatic compensation.
BOUNDS		applies fixed displacement or velocity boundary conditions in global coordinates.
	ROTOR	as BOUNDS, but in rotated coordinates.
VISEL		solves for the visco-elastic displacements.
	SOLVE	solves for elastic displacements, as an alternative to VISEL (it is called by VISEL if the number of time increments input is $\emptyset$).
STRESS		finds the principal stresses in the body, from the displacements.
	HYDRA	adds a lithostatic stress distribution.
	PORE	takes off pore pressure.
FAIL		applies the failure criteria of Section 2.3, Ch. 2 to each element.
	ZERO	subtracts the initial displacements at the end of a previous run (e.g. using SETUP; see Section A2.6).
OUTPUT		writes resulting displacements and stresses in Device 7.
	STRAIN	calculates principal strains and writes them on Device 7.
	MORE	writes information for continuation on Device 3.

Plotting Phase

PSCALE	calculates plot scaling factors, reads in the outline array from Device 4 and initializes the plotfile.

SCON   writes out (on Device Ø) input data for GPCP to plot contours of maximum shear stress.

PLON   writes out data for contours of minimum principal stress.

OUTLIN   draws an outline of the body prior to the plotting of vectors.

VECPLT   plots principal stress vectors or principal strains if STRAIN has been called previously.

SURF   plots the displaced surface of the body.

DISTRT   plots the deformed outline of the whole body.

GRDPLT   plots the finite element grid, with element numbers.

PROPS   plots the grid with material property numbers.

GREND   a GHOST subroutine to close the plotfile.

A2.5 Common Block Organisation

Variables are passed to all the major subroutines in common blocks, as part of the modular arrangement of the program.

There are 11 common blocks, listed below with the most important arrays within them.

Common Block	Principal Contents
NOD	nodal coordinates (X,Y); the displacement vector (DISP); the force vector (FORCE).
EL	the material type of each element (ITYP); a list of the nodes on each element (NODEL).
MAT	material properties.
FIX	fixed displacement data.
SØ	initial stresses (STRØ). This block is also used to transfer failure information from Subroutine FAIL to OUTPUT.

K	the global stiffness matrix (GLOBK); libraries containing the element areas (DELIB), B matrices (BLIB) and D matrices (DLIB).
ST	the principal stresses and their orientation (PRINC).
CR	the creep vector (CREEP); information on time increments.
WK	used to provide work space, but also to transfer applied force data from READ to ECHO2, and to store scale factors during the plotting phase of the program.
IN	initial displacements (DISPØ) and nodal coordinates (XØ, YØ) for continuation runs.
MIS	miscellaneous arrays, including the title (TITLE) and date (IDATE) of the job.

A2.6 The Initialization Program

The initialization program based on the theory developed in Chapter 4 is in file SETUP. This program solves for an initial model, using the Subroutines in PRIMA, and writes all the information necessary for continuation onto Device 3 by calling Subroutine MORE (the continuation run should then call ZERO, to subtract the initializing displacements, before OUTPUT, but after STRESS).

The input for this program is exactly as for the main finite element program (read in by READ), except that the number of solution iterations, NSOL, is read in from Device 5 (NSOL = 5 is found to be the maximum necessary for the models in this thesis). The output is also the same, with the addition of information on convergence to the initialized model.

A2.7 Program Listings

The subroutines in the library file PRIMA are listed in the order given by the main program FEVER, and are followed by a listing of the initialization program, SETUP.

```
***  FEVER : FINITE ELEMENT VISCO-ELASTIC ROUTINE           *****
***          FOR USE WITH SUBROUTINE LIBRARY PRIMA          *****
***                                                         *****
***                    WRITTEN AT DURHAM UNIVERSITY BY JOHN PARK  *****
***                                    1978 - 1990          *****
***                                                         *****
***  MAIN PROGRAM                                           *****

      IMPLICIT REAL*8 (A-H,O-W)
      COMMON /NOD/ ZCOM1(600),COM1(1001),NCOM1(2)
      COMMON /EL/   NCOM2(2001)
      COMMON /MAT/  COM3(60),NCOM3(11)
      COMMON /FIX/  COM4(300),NCOM4(301)
      COMMON /SO/   COM5(2000),INST
      COMMON /K/    COM6(125000),NCOM6(3)
      COMMON /ST/   COM7(2001),NCOM7(1002)
      COMMON /CR/   COM8(2000),DTIME,COMR1,NCOM8,NTIME
      COMMON /WK/   COM9(5089)
      COMMON /IN/   COM10(900),ISET
      COMMON /MIS/  COM0(7),NCOM0(4)

      CALL TIME(0,1)
      CALL READ
      CALL READ2
      CALL ECHO1
      CALL ECHO2
      CALL KFORM
      CALL INSTRS
      INST=1
      CALL REDDY
      CALL ISOS
      CALL BOUNCS
      CALL ROTOF
      CALL SOLVF
      NTIME=20
      DTIME=5.0D4
      CALL VISEL
      CALL STRESS
      CALL HYDRA
      CALL PORE
      CALL FAIL
      CALL ZERO
      CALL OUTPUT
      CALL STRAIN
      CALL MORE

      CALL PSCALE
      CALL SCON
      CALL PCON
      CALL OUTLIN
      CALL VECPLT
      CALL FRAME
      CALL STRAIN
      CALL OUTLIN
      CALL VECPLT
      CALL FRAME
      CALL SURF
      CALL FRAME
      CALL FRAME
      CALL DISTRT
      CALL FRAME
      CALL GRDPLT
      CALL PROPS
      CALL GREND

      STOP
      END
```

```
****  PRIMA : A SUBROUTINE LIBRARY FOR USE WITH FEVER, A          *****
****          VISCO-ELASTIC FINITE ELEMENT PROGRAM FOR            *****
****          FINDING LITHOSPHERIC STRESS DISTRIBUTIONS.          *****
****                                                              *****
****                    WRITTEN AT DURHAM UNIVERSITY BY JOHN PARK  *****
****                                             1979 - 1980       *****

      SUBROUTINE READ
      ===============
****  TO SET UP MODEL                                             *****

      IMPLICIT REAL*8 (A-H,O-W)
      COMMON /NOD/ X(300),Y(300),DISP(600),FORCE(600),G,NNOD,NNOD2
      COMMON /EL/  ITYP(500),NODEL(3,500),NEL
      COMMON /MAT/ EM(10),PM(10),RHOM(10),ETAM(10),TS(10),IPORE(10),NMAT
      COMMON /FIX/ DFIX(2,100),ANGLE(100),IFLAG(2,100),NOFIX(100),NFIX
      COMMON /SO/  COM5(2000),INST
      COMMON /ST/  COM7(2000),NCOM7(1001),ISTR
      COMMON /CR/  COM8(2001),TOTIME,KTIME,NTIME
      COMMON /WK/  FLOAD(600),LOAD(300),NLOAD,NCOM9,COM9(4538)
      COMMON /IN/  COM10(600),X0(300),Y0(300),ISET
      COMMON /MIS/ PI,TITLE(4),ZUF(4),IDATE(3),MOHO

      CALL TIME(5,0,IDATE)

****  READ TITLE AND WRITE IT WITH DATE                           *****

      WRITE(6,199)
  199 FORMAT(1H0,'PLEASE GIVE TITLE (4A8)'/
     1           ' -----------------------')
      READ(5,198) TITLE
  198 FORMAT(4A8)
      WRITE(7,187)IDATE,TITLE
  187 FORMAT(1H0,12X,3A4,34X,'OUTPUT FROM FEVER'/
     1           1H+,58X,'_____'/1H0,55X,4A8)

****  READ NODE COORDINATES                                       *****

      READ(4,197)NNOD,NEL,MOHO,G

****  ASSIGN DEFAULT VALUE OF G                                   *****

      IF (G.EQ.0.0) G=9.81
      READ(4,197)IMESH,NNODB,NELB,WIDE,NSID,NNODA,NELA
  197 FORMAT(3I4,D10.3,3I4)
      NNOD2=NNOD*2
      IF (IMESH.EQ.0) NNODB=NNOD
      DO 110 INOD=1,NNODB
      READ(4,196)JNOD,X(JNOD),Y(JNOD)
  196 FORMAT(I4,2F10.3)
      X(JNOD)=X(JNOD)*1.0E3
      Y(JNOD)=Y(JNOD)*1.0E3
  110 CONTINUE

****  READ ELEMENT TOPOLOGIES AND PROPERTIES                      *****

      READ(4,197)NMAT
      DO 120 IMAT=1,NMAT
      READ(4,195) EM(IMAT),PM(IMAT),RHOM(IMAT),ETAM(IMAT),
     1            TS(IMAT),IPORE(IMAT)
  195 FORMAT(D10.3,2F10.3,2D10.3,I4)

****  ASSIGN DEFAULT VALUE OF TENSILE STRENGTH                    *****

      IF (TS(IMAT).LE.0.0) TS(IMAT)=0.508
  120 CONTINUE

      IF (IMESH.EQ.0) NELB=NEL
      DO 121 IEL=1,NELB
      READ(4,194)JEL,(NODEL(KEL,JEL),KEL=1,3),ITYP(JEL)
  194 FORMAT(5I4)
  121 CONTINUE
      IF (IMESH.GT.0) CALL MESH(IMESH,NNODB,NELB,WIDE,NSID,NNODA,NELA)

****  READ APPLIED FORCES FIRST ZEROING 'FORCE'                   *****
```

```
      DO 130 IFO=1,NNOD2
  130 FORCE(IFO)=0.0
      READ(4,194)NLOAD
      IF(NLOAD.EQ.0) GO TO 132
      DO 131 ILD=1,NLOAD
      READ(4,193) LOAD(ILD),FLOAD(2*ILD-1),FLOAD(2*ILD)
  193 FORMAT(I4,2D10.3)
      FORCE(2*LOAD(ILD)-1)=FLOAD(2*ILD-1)
      FORCE(2*LOAD(ILD))  =FLOAD(2*ILD)
  131 CONTINUE

C**** READ FIXED DISPLACEMENTS                                          *****

  132 READ(4,194)NFIX
      IF(NFIX.EQ.0) GO TO 142

      DO 141 IFIX=1,NFIX
      READ (4,192) NOFIX(IFIX),(IFLAG(JFIX,IFIX),DFIX(JFIX,IFIX),
     1             JFIX=1,2),ANGLE(IFIX)
  192 FORMAT(I4,2(I4,F10.3),F10.3)
      ANGLE(IFIX)=ANGLE(IFIX)*PI/180.0
  141 CONTINUE

C**** SET FLAGS AND COUNTERS                                            *****

      INST =0
      ISTR =0
      NTIME=0
      KTIME=0
      TOTIME=0.0
      ISET =0

C**** INITIALIZE ARRAYS XO AND YO                                       *****

      DO 143 IXO=1,NNOD
      XO(IXO)=X(IXO)
      YO(IXO)=Y(IXO)
  143 CONTINUE

  142 CONTINUE

      WRITE(6,190)
  190 FORMAT('OREADING OF DATA COMPLETED')
      CALL TIME(1,1)

      RETURN
      END

C*************************************************************************************

      SUBROUTINE READ2
      ================
C**** TO CONTINUE WITH A PREVIOUS MODEL                                 *****

      IMPLICIT REAL*8 (A-H,O-W)
      COMMON /NOD/ X(300),Y(300),DISP(600),FORCE(600),G,NNOD,NNOD2
      COMMON /EL/   ITYP(500),NODEL(3,500),NEL
      COMMON /MAT/  EM(10),PM(10),RHOM(10),ETAM(10),TS(10),IPORE(10),NMAT
      COMMON /FIX/  DFIX(2,100),ANGLE(100),IFLAG(2,100),NOFIX(100),NFIX
      COMMON /SO/   COM5(2000),INST
      COMMON /ST/   COM7(2001),NCOM7(1001),ISTR
      COMMON /CR/   CREEP(4,500),DTIME,TOTIME,KTIME,NTIME
      COMMON /WK/   FLOAD(600),LOAD(300),NLOAD,NCOM9,COM9(4538)
      COMMON /IN/   DISPO(600),XO(300),YO(300),ISET
      COMMON /MIS/  PI,TITLE(4),ZUF(4),IDATE(3),MOHO

      CALL TIME(5,0,IDATE)

C**** READ TITLE AND WRITE IT WITH DATE                                 *****

      WRITE(6,199)
  199 FORMAT(1H0,'PLEASE GIVE TITLE (4A8)'/
```

```
      1                 ' ------------------------')
        READ(5,198) TITLE
  198 FORMAT(4A8)
        WRITE(7,187)IDATE,TITLE
  187 FORMAT(1H0,12X,3A4,34X,'OUTPUT FROM FEVER'/
      1          1H+,58X,'_____'/1H0,55X,4A8)

**** READ PARAMETERS AND NODAL COORDINATES                              *****

      READ (3) G,NNOD,NNOD2,TOTIME,KTIME,ISET
      READ (3) X,Y,DISP

**** WRITE INFORMATION ON INITIAL GRID                                  *****

      IF (KTIME.LE.0) GO TO 133
      TOTIME=TOTIME/3.1607
      WRITE (7,196) KTIME,TOTIME
  196 FORMAT (1H0,30X,'*** INITIAL MODEL REACHED AFTER',I4,
      1               ' ITERATIONS, TOTAL ',D10.3,' YRS.')
      TOTIME=TOTIME*3.1607

**** READ IN PREVIOUS CREEP, IF ANY                                     *****

      READ (3) CREEP
      GO TO 134

  133 WRITE (7,195)
  195 FORMAT (1H0,30X,'*** INITIAL MODEL REACHED AFTER ',
      1               'AN ELASTIC SOLUTION')
  134 CONTINUE

**** READ ELEMENT TOPOLOGIES AND PROPERTIES                             *****

      READ (3) EM,PM,RHOM,ETAM,TS,IPORE,NMAT
      READ (3) ITYP,NODEL,NEL

**** READ FORCES                                                        *****

      READ (3) FORCE

**** IF MODEL HAS BEEN INITIALIZED USING SETUP,                         *****
****     READ IN DISPLACEMENTS AND WRITE INFORMATION TO #7              *****

      IF (ISET.LT.1) GO TO 135

      READ (3) DISPO

      WRITE(7,191) ISET
  191 FORMAT (1H0,30X,'*** USING SETUP, FOR',I4,' ITERATIONS')

**** READ ANY SUPERIMPOSED FORCES FROM DEVICE #4                        *****

  135 READ(4,194)NLOAD
      IF(NLOAD.EQ.0) GO TO 132
      DO 131 ILD=1,NLOAD
      READ(4,193) LOAD(ILD),FLOAD(2*ILD-1),FLOAD(2*ILD)
  193 FORMAT(I4,2D10.3)
      JLD=2*LOAD(ILD)-1
      FORCE(JLD)=FORCE(JLD)+FLOAD(2*ILD-1)
      JLD=JLD+1
      FORCE(JLD)=FORCE(JLD)+FLOAD(2*ILD)
  131 CONTINUE

**** READ FIXED DISPLACEMENTS                                           *****

  132 READ(4,194)NFIX
  194 FORMAT(I4)
      IF(NFIX.EQ.0) GO TO 142
      DO 141 IFIX=1,NFIX
      READ (4,192) NOFIX(IFIX),(IFLAG(JFIX,IFIX),DFIX(JFIX,IFIX),
      1              JFIX=1,2),ANGLE(IFIX)
  192 FORMAT(I4,2(I4,F10.3),F10.3)
      ANGLE(IFIX)=ANGLE(IFIX)*PI/180.0
  141 CONTINUE
```

```
****  SET FLAGS AND COUNTERS                                           ******

      MOHO =0
      IMESH=0
      INST =0
      ISTR =0
      NTIME=0
****  INITIALIZE ARRAYS X0 AND Y0                                      *****

      DO 143 IX0=1,NNOD
      X0(IX0)=X(IX0)
      Y0(IX0)=Y(IX0)
  143 CONTINUE

  142 WRITE(6,190)
  190 FORMAT('0READING OF DATA COMPLETED')
      CALL TIME(1,1)

      RETURN
      END

*************************************************************************

      BLOCK DATA
      ==========
****  TO INITIALIZE SUFFIX ARRAY, AND PI                               *****

      IMPLICIT REAL*8 (A-H,O-W)
      COMMON /MIS/ PI,COMO(4),ZUF(4),NCOMO(4)

      DATA ZUF /'ST. ','ND. ','RD. ','TH. '/
      DATA PI  /3.1415926535897931DO/

      END

*************************************************************************

      SUBROUTINE ECHO1
      ================
****  ECHO MESH INPUT TO DEVICE 7                                      *****

      IMPLICIT REAL*8 (A-H,O-W)
      COMMON /NOD/ X(300),Y(300),COM1(1201),NNOD,NNOD2
      COMMON /EL/  ITYP(500),NODEL(3,500),NEL
      COMMON /MIS/ PI,TITLE(4),ZUF(4),IDATE(3),MOHO

      WRITE(7,189)
  189 FORMAT(1H0,9X,'** DATA INPUT **')
      WRITE(7,188)NNOD,NEL
  188 FORMAT(1H0,10X,'NUMBER OF NODES = ',I4,
     1        10X,'NUMBER OF ELEMENTS = ',I4)

      WRITE(7,185)
  185 FORMAT(1H0,10X,'NODAL COORDINATES'/
     1        1H+,10X,'                 '/
     2        1H0,30X,'NODE',14X,'X(I): M',15X,'Y(I): M'/1H0)
      DO 160 IECN=1,NNOD
  160 WRITE(7,184) IECN,X(IECN),Y(IECN)
  184 FORMAT(31X,I4,2(12X,D10.3))

      WRITE(7,183)
  183 FORMAT(1H0/1H0,10X,'ELEMENT PROPERTIES'/
     1        1H+,10X,'                  '/
     2        1H0,12X,'ELEMENT',10X,'NODE1',11X,'NODE2',
     3        11X,'NODE3',11X,'MATERIAL'/1H0)
      DO 161 IECEL=1,NEL
  161 WRITE(7,182) IECEL,(NODEL(JECEL,IECEL),JECEL=1,3),ITYP(IECEL)
  182 FORMAT(14X,I4,4(12X,I4))

      WRITE(6,175)
```

```
  178 FORMAT('0ECHO1 COMPLETED')
      CALL TIME(1,1)

      RETURN
      END
```

****

```
      SUBROUTINE ECHO2
      ================
**** ECHO BOUNDARY CONDITIONS TO DEVICE 7                              *****

      IMPLICIT REAL*8 (A-H,O-W)
      COMMON /NOD/ ZCOM1(600),COM1(1200),G,NCOM1(2)
      COMMON /MAT/ EM(10),PM(10),RHOM(10),ETAM(10),TS(10),NCOM3(10),NMAT
      COMMON /FIX/ DFIX(2,100),ANGLE(100),IFLAG(2,100),NOFIX(100),NFIX
      COMMON /WK/ FLOAD(600),LOAD(300),NLOAD,NCOM9,COM9(4528)
      COMMON /MIS/ PI,COMO(5),NCOMO(4)

**** WRITE OUT MATERIAL PROPERTIES                                     *****

      WRITE(7,177)
  177 FORMAT(1H0/1H0,10X,'MATERIAL PROPERTIES'/
     1               1H+,10X,'                   '/
     2               1H0,8X,'MATERIAL NUMBER',3X,15HYOUNG'S MODULUS,
     3                7X,15HPOISSON'S RATIO,7X,'DENSITY',
     4               12X,'VISCOSITY',10X,'TENSILE STRENGTH'/
     5               17X,'I',11X,'E(I): N/SQ.M',12X,'NU(I)',
     6                9X,'RHO(I): KG/CU.M',5X,'ETA(I): NS/SQ.M',
     7                9X,'T(I): N/SQ.M'/1H0)
      DO 165 JMAT=1,NMAT
      WRITE(7,176) JMAT,EM(JMAT),PM(JMAT),RHOM(JMAT),ETAM(JMAT),TS(JMAT)
  176 FORMAT(14X,I4,12X,D10.3,12X,F6.3,12X,F7.1,2(12X,D10.2))
  165 CONTINUE

**** WRITE OUT EXTERNAL FORCES APPLIED, IF ANY                         *****

      IF (NLOAD.GT.0) GO TO 167
      WRITE(7,175)
  175 FORMAT(1H0/1H0,10X,'NO EXTERNAL FORCES')
      GO TO 168
  167 WRITE(7,174) NLOAD
  174 FORMAT(1H0/1H0,10X,'EXTERNAL FORCES'/
     1               1H+,10X,'               ',3X,I4,' IN TOTAL'/
     2               1H0,14X,'NODE',9X,'APPLIED FORCES'/
     3               14X,'NUMBER',12X,'FX: N',17X,'FY: N'/1H0)
      DO 169 JLD=1,NLOAD
      WRITE(7,173) LOAD(JLD),FLOAD(2*JLD-1),FLOAD(2*JLD)
  173 FORMAT(14X,I4,2(12X,D10.3))
  169 CONTINUE
  168 CONTINUE

**** WRITE OUT FIXED DISPLACEMENTS, IF ANY                             *****

      IF(NFIX.GT.0) GO TO 162
      WRITE(7,181)
  181 FORMAT(1H0/1H0,10X,'NO FIXED DISPLACEMENTS')
      GO TO 164
  162 WRITE(7,180)NFIX
  180 FORMAT(1H0/1H0,10X,'FIXED DISPLACEMENTS'/
     1               1H+,10X,'                   ',2X,I4,' IN TOTAL'/
     2               1H0,13X,'NODE',12X,'X FLAG',5X,'X DISPLACEMENT',
     3                6X,'Y FLAG',6X,'Y DISPLACEMENT',
     4                5X,'ANGLE OF CO-ORDINATES'/1H0)
      DO 163 IECFIX=1,NFIX
      ANG=ANGLE(IECFIX)*180.0/PI
      WRITE (7,179) NOFIX(IECFIX),(IFLAG(JECFIX,IECFIX),
     1               DFIX(JECFIX,IECFIX),JECFIX=1,2),ANG
  179 FORMAT (14X,2(I4,12X),D10.3,6X,I4,12X,D10.3,10X,F7.2)
  163 CONTINUE
  164 CONTINUE

      WRITE(7,186) G
```

```
  186 FORMAT(1H0/1H0,10X,'GRAVITY : ',F5.2,' N PER KG.')

      WRITE(6,172)
  172 FORMAT('0ECHO2 COMPLETED')
      CALL TIME(1,1)

      RETURN
      END
```

```
******************************************************************************
```

```
      SUBROUTINE KFORM
      ================
**** TO SET UP THE GLOBAL STIFFNESS MATRIX KGLOB                              *****

      IMPLICIT REAL*8 (A-H,O-W)
      COMMON /NOD/ X(300),Y(300),COM1(1200),G,NNOD,NNOD2
      COMMON /EL/ ITYP(500),NODEL(3,500),NEL
      COMMON /MAT/ EM(10),PM(10),RHOM(10),COM3(20),NCOM3(10),NMAT
      COMMON /K/ GLOBK(600,185),DELTE(500),BLIB(6,3,500),
     1           DLIB(3,3,500),KBW,KSIZE
      DIMENSION B(3,6),D(3,3),DB(3,6),BT(6,3),ELK(6,6)

**** TO CALCULATE THE BANDWIDTH,KBW,AND THE SECOND DIMENSION                  *****
**** OF THE GLOBAL STIFFNESS,GLOBK(NNOD2,KSIZE)                               *****

      DO  206 IBW=1,NEL
      IAB1=IABS(NODEL(1,IBW)-NODEL(2,IBW))
      IAB2=IABS(NODEL(1,IBW)-NODEL(3,IBW))
      IAB3=IABS(NODEL(2,IBW)-NODEL(3,IBW))
  206 MAX=MAXO(IAB1,IAB2,IAB3,MAX)
      KBW=2*(MAX+1)
      KSIZE=2*KBW-1
      WRITE(7,298) KBW
  298 FORMAT(1H0,10X,'BANDWIDTH = ',I4)

**** TO CONSTRUCT THE STIFFNESS MATRIX,K.                                     *****

      DO  207 JKO=1,KSIZE
      DO  207 IKO=1,NNOD2
  207 GLOBK(IKO,JKO)=0.0
      DO 210 IKEL=1,NEL
      E=EM(ITYP(IKEL))
      P=PM(ITYP(IKEL))

**** FORM THE ELASTICITY MATRIX,D,ASSUMING PLANE STRAIN                       *****

      D(1,1)=E*(1-P)/(1+P)/(1-2*P)
      D(1,2)=D(1,1)*P/(1-P)
      D(1,3)=0.0
      D(2,1)=D(1,2)
      D(2,2)=D(1,1)
      D(2,3)=0.0
      D(3,1)=0.0
      D(3,2)=0.0
      D(3,3)=E/2.0/(1+P)

**** FORM THE ELEMENT AREA,DELTA,AND STRAIN MATRIX,B                          *****

      DXI=X(NODEL(1,IKEL))
      DXJ=X(NODEL(2,IKEL))
      DXM=X(NODEL(3,IKEL))
      DYI=Y(NODEL(1,IKEL))
      DYJ=Y(NODEL(2,IKEL))
      DYM=Y(NODEL(3,IKEL))
      DELTA=(DXJ*DYM-DXM*DYJ-DXI*DYM+
     1       DXM*DYI+DXI*DYJ-DXJ*DYI)/2.0
      B(3,1)=(DXM-DXJ)/2.0/DELTA
      B(3,2)=(DYJ-DYM)/2.0/DELTA
      B(3,3)=(DXI-DXM)/2.0/DELTA
      B(3,4)=(DYM-DYI)/2.0/DELTA
      B(3,5)=(DXJ-DXI)/2.0/DELTA
      B(3,6)=(DYI-DYJ)/2.0/DELTA
```

```
      DO 200 JB=1,3
      B(1,(2*JB-1))=B(3,(2*JB))
      B(1,(2*JB))=0.0
      B(2,(2*JB-1))=0.0
  200 B(2,(2*JB))=B(3,(2*JB-1))
```

**** STORE B,D AND DELTA IN THE ARRAYS BLIB,DLIB AND DELIB   *****

```
      DELIB(IKEL)=DELTA
      DO 201 JDSTOR=1,3
      DO 201 IDSTOR=1,3
  201 DLIB(IDSTOR,JDSTOR,IKEL)=D(IDSTOR,JDSTOR)
```

**** FOR ACCESSING EFFICIENCY B IS STORED IN BLIB AS (6,2)   *****

```
      DO 202 IBSTOR=1,3
      DO 202 JBSTOR=1,6
  202 BLIB(JBSTOR,IBSTOR,IKEL)=B(IBSTOR,JBSTOR)
```

**** TO FORM THE TRANSPOSE OF B,BT,AND THE PRODUCT (BT)(D)(B)   *****

```
      DO 203 IBT=1,6
      DO 203 JBT=1,3
  203 BT(IBT,JBT)=B(JBT,IBT)
      CALL MATPRD(D,B,DB,3,3,6)
      CALL MATPRD(BT,DB,ELK,6,3,6)
```

**** THE ELEMENT STIFFNESS, ELK=(BT)(D)(B)*DELTA   *****
**** (FOR UNIT ELEMENT THICKNESS)   *****

```
      DO 204 JELK=1,6
      DO 204 IELK=1,6
  204 ELK(IELK,JELK)=ELK(IELK,JELK)*DABS(DELTA)
```

**** TO LOAD THE ELEMENT STIFFNESS,ELK,   *****
**** INTO THE GLOBAL STIFFNESS MATRIX,GLOBK   *****

```
      DO 205 JKFORM=1,3
      DO 205 LKFORM=1,2
      DO 205 IKFORM=1,3
      DO 205 KKFORM=1,2
      IGLOB=2*(NODEL(IKFORM,IKEL))+KKFORM-2
      JGLOB=2*(NODEL(JKFORM,IKEL))+LKFORM-2
     1      -IGLOB+KBW
      MKFORM=2*IKFORM+KKFORM-2
      NKFORM=2*JKFORM+LKFORM-2
      GLOBK(IGLOB,JGLOB)=GLOBK(IGLOB,JGLOB)+ELK(MKFORM,NKFORM)
  205 CONTINUE
  210 CONTINUE

      WRITE(6,299)
  299 FORMAT('0GLOBAL STIFFNESS MATRIX FORMED')
      CALL TIME(1,1)

      RETURN
      END
```

****

```
      SUBROUTINE MATPRD(A,B,C,L,M,N)
      ==============================
```
**** TO FIND THE MATRIX PRODUCT C(L,N)=A(L,M)*B(M,N)   *****

```
      IMPLICIT REAL*8 (A-H,O-W)
      DIMENSION A(L,M),B(M,N),C(L,N)

      DO 2 JPROD=1,N
      DO 2 IPROD=1,L
      C(IPROD,JPROD)=0.0
      DO 1 KPROD=1,M
    1 C(IPROD,JPROD)=C(IPROD,JPROD)+A(IPROD,KPROD)*B(KPROD,JPROD)
    2 CONTINUE
```

```
      RETURN
      END


**************************************************************************

      SUBROUTINE INSTRS
      =================
****  TO ACCOUNT FOR AN INITIAL STRESS DISTRIBUTION                    ****

      IMPLICIT REAL*8 (A-H,O-W)
      COMMON /NOD/ ZCOM1(600),DISP(600),FORCE(600),G,NCOM1(2)
      COMMON /EL/   NCOM2(500),NODEL(3,500),NEL
      COMMON /SO/   STRO(4,500),INST
      COMMON  /K/   COM6(111000),DELIB(500),BLIB(6,3,500),
     1              COM61(4500),NCOM6(2)

****  UNFORMATTED READ OF INITIAL STRESS SYSTEM FROM DEVICE 1          ****

      DO 232 INS=1,NEL
      READ(1) (STRO(JSO,INS),JSO=1,4)

****  CALCULATE INITIAL STRESS 'FORCE' VECTOR AND ADD INTO FORCE       ****

      DO 233 JNS=1,3
      FISX=(BLIB((2*JNS-1),1,INS)*STRO(1,INS)
     1     +BLIB((2*JNS-1),3,INS)*STRO(3,INS)) * DABS(DELIB(INS))
      FISY=(BLIB( (2*JNS) ,2,INS)*STRO(2,INS)
     1     +BLIB( (2*JNS) ,3,INS)*STRO(3,INS)) * DABS(DELIB(INS))
      NFINS=2*NODEL(JNS,INS)
      FORCE(NFINS-1)=FORCE(NFINS-1) - FISX
      FORCE( NFINS )=FORCE( NFINS ) - FISY
  233 CONTINUE

  232 CONTINUE

      WRITE (7,238)
  238 FORMAT(1H0,10X,'INITIAL STRESS SYSTEM SUBTRACTED')

      RETURN
      END


**************************************************************************

      SUBROUTINE FBODY
      =================
****  INTRODUCE BODY FORCES ; Y AXIS DEFINED BY G                      ****

      IMPLICIT REAL*8 (A-H,O-W)
      COMMON /NOD/ ZCOM1(600),DISP(600),FORCE(600),G,NCOM1(2)
      COMMON /EL/   ITYP(500),NODEL(3,500),NEL
      COMMON /MAT/ COM3(20),RHOM(10),COM31(20),NCOM3(11)
      COMMON /K/   COM6(111000),DELIB(500),COM64(13500),NCOM6(2)

      DO  350 IBOD=1,NEL
      RHO=RHOM(ITYP(IBOD))
      DELTA=DABS(DELIB(IBOD))
      FP=RHO*G*DELTA/3.0
      DO  351 JBOD=1,3
  351 FORCE(2*NODEL(JBOD,IBOD))=FORCE(2*NODEL(JBOD,IBOD))+FP
  350 CONTINUE

      WRITE(7,359)
  359 FORMAT(1H0,10X,'BODY FORCES APPLIED')

      RETURN
      END


**************************************************************************
```

```
      SUBROUTINE ISOS
      ===============
:**** TO INCLUDE ISOSTATIC COMPENSATION IN GLOBK                        *****

      IMPLICIT REAL*8 (A-H,O-W)
      COMMON /NOD/ X(300),Y(300),COM1(1000),G,NNOD,NNOD2
      COMMON /K/ GLOBK(600,165),COMA(14000),KBW,KSIZE
      COMMON /WK/ FISOS(100),YDATUM(2),RHOI(2),NODAT(100),
     1            IS(2),COM4(5135)

:**** READ DENSITIES,FLAGS AND DATUMS                                   *****

      READ(4,308) (IS(JS),JS=1,2)
  308 FORMAT (2I4)
      DO 310 JSOS=1,2
      IF (IS(JSOS)-1) 303,304,305

:**** IF IS=1, THEN COMPENSATION IS INTRODUCED                          *****
:****   AT ALL NODES WITH Y=DATUM                                       *****

  304 READ (4,307) RHOI(JSOS),YDATUM(JSOS)
  307 FORMAT (2F10.3)
      YDATUM(JSOS)=1.0E3*YDATUM(JSOS)
      IF (JSOS.EQ.1) RHOI(JSOS)=-RHOI(JSOS)

:**** TO FIND NODES ON DATUM                                            *****

      KDATUM=0
      DO 300 IDATUM=1,NNOD
      IF (Y(IDATUM).NE.YDATUM(JSOS)) GO TO 300
      KDATUM=KDATUM+1
      NODAT(KDATUM)=IDATUM
  300 CONTINUE
      GO TO 312

:**** IF IS IS GREATER THAN 1, A LIST OF IS NODES IS                    *****
:****    READ IN WHERE COMPENSATION IS TO BE APPLIED                    *****

  305 READ (4,307) RHOI(JSOS)
      IF (JSOS.EQ.1) RHOI(JSOS)=-RHOI(JSOS)
      KDATUM=IS(JSOS)
      READ (4,306) (NODAT(JDATUM),JDATUM=1,KDATUM)
  306 FORMAT (5I4)

:**** TO CALCULATE FISOS FOR END NODES                                  *****

  312 IDAT=NODAT(1)
      KDAT=NODAT(2)
      FISOS(1)=(X(KDAT)-X(IDAT))/2.0*RHOI(JSOS)*G
      IDAT=NODAT(KDATUM-1)
      KDAT=NODAT(KDATUM)
      FISOS(KDATUM)=(X(KDAT)-X(IDAT))/2.0*RHOI(JSOS)*G

:**** FOR OTHER NODES ON DATUM                                          *****

      JOMAX=KDATUM-1
      DO 301 JDAT=2,JOMAX
      IDAT=NODAT(JDAT-1)
      KDAT=NODAT(JDAT+1)
  301 FISOS(JDAT)=(X(KDAT)-X(IDAT))/2.0*RHOI(JSOS)*G

:**** MODIFY THE APPROPRIATE ELEMENTS OF THE STIFFNESS MATRIX           *****

      DO 302 JISOS=1,KDATUM
      IISOS=2*NODAT(JISOS)
  302 GLOBK(IISOS,KBW)=GLOBK(IISOS,KBW)+FISOS(JISOS)
      GO TO 311
  303 RHOI(JSOS)=0.0
  311 CONTINUE
  310 CONTINUE

      WRITE(7,309) RHOI
  309 FORMAT(1H0,10X,'ISOSTATIC COMPENSATION INCLUDED :',
     1            ' RHOI(1) =',F7.1,', RHOI(2) =',F7.1)
```

```
      RETURN
      END


***************************************************************************


      SUBROUTINE BOUNDS
      =================
****  TO INSERT BOUNDARY CONDITIONS IN GLOBAL CO-ORDINATES            *****
****      ACCORDING TO : IFLAG=0: FREE DISPLACEMENT                   *****
****                     IFLAG=1: FIXED DISPLACEMENT                  *****
****                     IFLAG=2: FIXED VELOCITY                      *****

      IMPLICIT REAL*8 (A-H,O-W)
      COMMON /NOD/ X(300),Y(300),COM1(600),FORCE(600),G,NNOD,NNOD2
      COMMON /FIX/ DFIX(2,100),COM4(100),IFLAG(2,100),NOFIX(100),NFIX
      COMMON /K/  GLOBK(600,185),COM5(14000),KBW,KSIZE
      COMMON /IN/  DISPO(600),XCOM10(600),ISET

      IF (NFIX.EQ.0) GO TO 324

      DO 323 IBOUND=1,NFIX
      IF (IFLAG(1,IBOUND).GT.2.OR.IFLAG(2,IBOUND).GT.2) GO TO 323
      DO 322 JBOUND=1,2
      IF (IFLAG(JBOUND,IBOUND).LE.0) GO TO 322
      KBOUND=2*NOFIX(IBOUND)+JBOUND-2

****  ZERO APPROPRIATE ROW OF GLOBK                                   *****

      DO 320 LBOUND=1,KSIZE
  320 GLOBK(KBOUND,LBOUND)=0.0

****  SET THE DIAGONAL VALUE OF K TO A LARGE VALUE AND                *****
****  REPLACE FORCE(J) BY DISP(J)*(THAT VALUE)                        *****

      GLOBK(KBOUND,KBW)=1.0D12
      IF(IFLAG(JBOUND,IBOUND).EQ.1) FORCE(KBOUND)=DFIX(JBOUND,IBOUND)
     1                                            *1.0D12
      IF(IFLAG(JBOUND,IBOUND).EQ.2) FORCE(KBOUND)=0.0
      IF(ISET.GE.1) FORCE(KBOUND)=FORCE(KBOUND)+DISPO(KBOUND)*1.0D12
  322 CONTINUE
  323 CONTINUE

  324 CONTINUE

      WRITE(6,399)
  399 FORMAT('0BOUNDARY CONDITIONS APPLIED'/' IN GLOBAL CO-ORDS')
      CALL TIME(1,1)

      RETURN
      END


***************************************************************************


      SUBROUTINE ROTOR
      ================
****  TO FIX NODAL DISPLACEMENTS IN A ROTATED CO-ORDINATE SYSTEM      *****
****      ACCORDING TO : IFLAG=3: FIXED DISPLACEMENT                  *****
****                     IFLAG=4: FIXED VELOCITY                      *****

      IMPLICIT REAL*8 (A-H,O-W)
      COMMON /NOD/ ZCOM1(600),COM1(600),FORCE(600),G,NNOD,NNOD2
      COMMON /FIX/ DFIX(2,100),ANGLE(100),IFLAG(2,100),NOFIX(100),NFIX
      COMMON  /K/  GLOBK(600,185),COM5(14000),KBW,KSIZE
      COMMON /WK/ COM5(5269),R(2,2),RT(2,2),F(2),RF(2),SUBK(2,2),RS(2,2)
     1            ,D(2),RD(2)
      COMMON /IN/  DISPO(600),XCOM10(600),ISET

      IF (NFIX.LE.0) GO TO 404

      ANGL=31.42
      DO 400 IFIX=1,NFIX
```

```
      IF (IFLAG(1,IFIX).LT.3.AND.IFLAG(2,IFIX).LT.3) GO TO 400
C**** SKIP THE FIRST SECTION IF THE ANGLE OF ROTATION IS THE SAME   *****
C****   AS BEFORE  (ANGL WAS INITIALIZED AT AN UNLIKELY VALUE)       *****
C
      IF (ANGLE(IFIX).EQ.ANGL) GO TO 403
C**** FORM ROTATION MATRIX, R, AND ITS TRANSPOSE, RT                 *****
C
      ANGL=ANGLE(IFIX)
      R(1,1)=DCOS(ANGL)
      R(2,2)=R(1,1)
      R(1,2)=DSIN(ANGL)
      R(2,1)=-R(1,2)
      DO 401 IRT=1,2
      DO 401 JRT=1,2
      RT(IRT,JRT)=R(JRT,IRT)
  401 CONTINUE
C**** ROTATE FORCE VECTOR TO RF                                      *****
C
  403 MROT=NOFIX(IFIX)
      F(1)=FORCE(2*MROT-1)
      F(2)=FORCE(2*MROT)
      CALL MATPRD(R,F,RF,2,2,1)
C**** TAKE THE MATRIX RELATING NODES M AND N FROM THE GLOBAL         *****
C**** STIFFNESS MATRIX AND PUT IN SUBK,                              *****
C**** FOR EACH VALUE OF N IN THE BAND                                *****
C
      NRMAX=MROT+(KBW/2-1)
      NRMIN=MROT-(KBW/2-1)
      IF (NRMAX.GT.NNOD) NRMAX=NNOD
      IF (NRMIN.LT.1) NRMIN=1
      DO 410 NROT=NRMIN,NRMAX
      DO 411 IROT=1,2
      DO 411 JROT=1,2
      KROT=2*MROT+IROT-2
      LROT=2*NROT+JROT-2-KROT+KBW
      SUBK(IROT,JROT)=GLOBK(KROT,LROT)
  411 CONTINUE
C**** ROTATE SUBK TO GIVE (R)(SUBK)(RT)                              *****
C
      CALL MATPRD(R,SUBK,RS,2,2,2)
      CALL MATPRD(RS,RT,SUBK,2,2,2)
C**** FIND THE COMPONENTS OF ANY INITIALIZING DISPLACEMENTS          *****
C****         IN ROTATED CO-ORDINATES                                *****
C
      IF (ISET.LT.1) GO TO 414
      D(1)=DISP0(2*MROT-1)
      D(2)=DISP0(2*MROT)
      CALL MATPRD(R,D,RD,2,2,1)
  414 CONTINUE
C**** ZERO ROW OF STIFFNESS MATRIX CORRESPONDING TO                  *****
C**** DISPLACEMENT TO BE FIXED                                       *****
C
      DO 412 JFIX=1,2
      IF (IFLAG(JFIX,IFIX).EQ.0) GO TO 412
      SUBK(JFIX,1)=0.0
      SUBK(JFIX,2)=0.0
C**** SET THE DIAGONAL TERM TO A LARGE NUMBER AND                    *****
C**** THE MTH. ROW OF THE FORCE VECTOR TO THAT NUMBER                *****
C**** TIMES THE DISPLACEMENT TO BE FIXED. (ZERO FOR FIXED VELOCITY)  *****
C
      IF (NROT.NE.MROT) GO TO 412
      SUBK(JFIX,JFIX)=1.0D12
      IF (IFLAG(JFIX,IFIX).EQ.3) RF(JFIX)=DFIX(JFIX,IFIX)*1.0D12
      IF (IFLAG(JFIX,IFIX).EQ.4) RF(JFIX)=0.0
C**** IF MODEL HAS BEEN INITIALIZED WITH SETUP,                      *****
C****     ADD IN PREVIOUS DISPLACEMENTS                              *****
```

```
      IF (ISET.LT.1) GO TO 412
      RF(JFIX)=RF(JFIX) + RD(JFIX)*1.0012
  412 CONTINUE
```
***** ROTATE SUBK BACK TO GLOBAL CO-ORDS AND REPLACE IN GLOBK   *****
```
      CALL MATPRD(RT,SUBK,RS,2,2,2)
      CALL MATPRD(RS,R,SUBK,2,2,2)
      DO 413 IRER=1,2
      DO 413 JRER=1,2
      KROT=2*MROT+IRER-2
      LROT=2*NROT+JRER-2-KROT+KBW
      GLOBK(KROT,LROT)=SUBK(IRER,JRER)
  413 CONTINUE
  410 CONTINUE
```
***** ROTATE BACK AND REPLACE THE FORCE VECTOR   *****
```
      CALL MATPRD(RT,RF,F,2,2,1)
      FORCE(2*MROT-1)=F(1)
      FORCE(2*MROT)  =F(2)
  400 CONTINUE

  404 CONTINUE

      WRITE(6,499)
  499 FORMAT('0BOUNDARY CONDITIONS APPLIED'/' IN ROTATED CO-ORDS')
      CALL TIME(1,1)

      RETURN
      END
```

****

```
      SUBROUTINE SOLVE
      ================
```
***** SOLVE THE EQUATION K*DISP=FORCE   *****
```
      IMPLICIT REAL*8 (A-H,O-W)
      COMMON /NOD/ ZCOM1(600),DISP(600),FORCE(600),G,NNOD,NNOD2
      COMMON /K/   GLOBK(600,125),COM4(14000),KBW,KSIZE
```
***** COPY FORCE INTO DISP, AND SOLVE THE STIFFNESS EQUATION   *****
```
      DO 1000 ISOL=1,NNOD2
      DISP(ISOL)=FORCE(ISOL)
 1000 CONTINUE
      NUM=600
      PT=1.0
      CALL MA07BD(GLOBK,DISP,NUM,NNOD2,KSIZE,PT)
```
***** SOLUTION VECTOR IS IN DISP(600)   *****
```
      WRITE(7,1909)
 1909 FORMAT(1H0,10X,'ELASTIC ANALYSIS')
      WRITE(6,1908)
 1908 FORMAT('0EQUATION SOLVED')
      CALL TIME(1,1)

      RETURN
      END
```

****

```
      SUBROUTINE VISEL
      ================
**** TO SOLVE FOR VISCO-ELASTIC STRESSES AND STRAINS                    *****

      IMPLICIT REAL*8 (A-H,O-W)
      COMMON /NOD/ ZCOM1(600),DISP(600),FORCE(600),G,NNOD,NNOD2
      COMMON /EL/  ITYP(500),NODEL(3,500),NEL
      COMMON /MAT/ EM(10),PM(10),COM3(10),ETAM(10),COM31(10),NCOM3(11)
      COMMON /FIX/ DFIX(2,100),ANGLF(100),IFLAG(2,100),NCFIX(100),NFIX
      COMMON /K/   GLOBK(600,185),DELIB(500),RLIB(5,3,500),
     1             DLIB(3,3,500),KBW,KSIZE
      COMMON /ST/  STREBN(4,500),STMAX,NCOMT(1002)
      COMMON /CP/  CREEP(4,500),DTIME,TOTIME,KTIME,NTIME
      COMMON /WK/  FINIT(600),DCREEP(4,500),PRESTR(4,500),FCREEP(600),
     1             DIS(6),B(3,6),C(3,3),BT(6,3),STRN(4),STRES(4),
     2             STINIT(4),DS(4),DFCR(6),STRIT(4),
     3             R(2,2),RT(2,2),E(2),EE(2)
      COMMON /MIS/ PI,TITLE(4),ZUF(4),IDATE(3),NCOMO

**** IF THEY HAVE NOT ALREADY BEEN GIVEN, READ IN NTIME AND DTIME *****

      IF (NTIME.GT.0) GO TO 1002
      WRITE(5,1909)
1909 FORMAT('0NTIME(I4) AND DTIME(D10.3)?'/'....----------')
      READ(5,1908) NTIME,DTIME
1908 FORMAT(I4,D10.3)

**** IF NTIME.LE.0 AN ELASTIC SOLUTION IS GIVEN                         *****

      IF (NTIME) 1001,1001,1002
1001 CALL SOLVE
      RETURN

**** ASSIGN PARAMETER VALUES                                            *****

1002 PT=1.0
      NJM=600
      NITER=20
      VERGE=1.004
      WRITE (7,1906) NTIME,DTIME,VERGE
1906 FORMAT(1H0/1H0,I4,' TIME INCREMENTS, EACH OF ',D7.1,' YRS.'/
     1            1H0,5X,'CONVERGENCE LIMIT =',D7.1,' N PER SQ.M'/1H0)
      DTIME=DTIME*3.16D7
      WRITE (8,1905) IDATE,TITLE
1905 FORMAT (1H0,12X,3A4,30X,4A8/1H0)

**** ZERO CREEP, IF THERE HAVE BEEN NO PREVIOUS TIME STEPS              *****

      IF (KTIME.GT.0) GO TO 1004
      DO 1005 JCRO=1,NEL
      DO 1005 ICRO=1,4
1005 CREEP(ICRO,JCRO)=0.0
1004 CONTINUE

**** STORE INITIAL FORCES IN FINIT                                      *****

      DO 1006 IFIN=1,NNOD2
1006 FINIT(IFIN)=FORCE(IFIN)

**** START LOOP OVER NTIME TIME INCREMENTS                              *****

      DO 1010 ITIME=1,NTIME
      TOTIME=TOTIME+DTIME
      MTIM=ITIME-100*(ITIME/100)
      LTIM=MTIM-10*(MTIM/10)
      IF (MTIM.LT.14) LTIM=MTIM
      IF (LTIM.GT.4.OR.LTIM.EQ.0) LTIM=4
      WRITE(8,1919) ITIME,ZUF(LTIM),TOTIME
1919 FORMAT(1H0/1H0,I4,A4,'TIME INCREMENT, ENDING AT ',D9.3,' S.'/1H )
      DO 1011 JDCO=1,NEL
      DO 1011 IDCO=1,4
      DCREEP(IDCO,JDCO)=0.0
1011 PRESTR(IDCO,JDCO)=0.0

**** START SOLUTION ITERATIONS                                          *****
```

```
      ITERO=1
      ITMAX=NITER
1014  DO 1020 ITER=ITERO,ITMAX
```

***** COPY FORCE INTO DISP, AND SOLVE THE STIFFNESS EQUATION   *****

```
      DO 1000 ISOL=1,NNOD2
      DISP(ISOL)=FORCE(ISOL)
1000  CONTINUE
      CALL MA07RD(GLOBK,DISP,NUM,NNOD2,KSIZE,PT)
      PT=0.0
```

***** SOLUTION VECTOR IS IN DISP(600)   *****

```
      DO 1021 IFCRO=1,NNOD2
1021  FCREEP(IFCRO)=0.0
      CONV=0.0
```

***** START LOOP OVER NEL ELEMENTS   *****

```
      DO 1030 ICREEP=1,NEL
```

***** ASSIGN PROPERTIES TO CURRENT ELEMENT   *****

```
      ITY=ITYP(ICREEP)
      E=EM(ITY)
      P=PM(ITY)
      ETA=ETAM(ITY)
      DO 1031 IDIS=1,3
      DIS(2*IDIS-1)=DISP(2*NODEL(IDIS,ICREEP)-1)
1031  DIS(2*IDIS)=DISP(2*NODEL(IDIS,ICREEP))
      DO 1032 IBGET=1,3
      DO 1032 JBGET=1,6
      B(IBGET,JBGET)=BLIB(JBGET,IBGET,ICREEP)
1032  BT(JBGET,IBGET)=B(IBGET,JBGET)
      DO 1033 JDGET=1,3
      DO 1033 IDGET=1,3
1033  D(IDGET,JDGET)=DLIB(IDGET,JDGET,ICREEP)
      CALL MATPRD(B,DIS,STRN,3,6,1)
      STRN(4)=0.0D0
```

***** FORM ELASTIC STRAINS AND STRESSES   *****

```
      DO 1034 ILAS=1,4
1034  STRN(ILAS)=STRN(ILAS)-CREEP(ILAS,ICREEP)-DCREEP(ILAS,ICREEP)
      STRN(1)=STRN(1)+P*STRN(4)
      STRN(2)=STRN(2)+P*STRN(4)
      CALL MATPRD(D,STRN,STRES,3,3,1)
      STRES(4)=P*(STRES(1)+STRES(2))+E*STRN(4)
```

***** STORE STRESSES AT START OF TIME INCREMENT   *****

```
      IF (ITER.GT.1) GO TO 1036
      DO 1035 IBGN=1,4
1035  STRBGN(IBGN,ICREEP)=STRES(IBGN)
1036  CONTINUE
```

***** FIND CREEP STRAIN FROM DEVIATORIC STRESSES   *****

```
      DO 1037 ISTAV=1,4
1037  STRES(ISTAV)=(STRES(ISTAV)+STRBGN(ISTAV,ICREEP))/2.0D0
      STHYD=(STRES(1)+STRES(2)+STRES(4))/3.0D0
      STRES(1)=STRES(1)-STHYD
      STRES(2)=STRES(2)-STHYD
      STRES(4)=STRES(4)-STHYD
      STRES(3)=STRES(3)*2.0D0
      IF(ETA.EQ.0.0) GO TO 1039
      DO 1038 JCREEP=1,4
      STINIT(JCREEP)=STRES(JCREEP)*DTIME/(2.0D0*ETA)
1038  DCREEP(JCREEP,ICREEP)=STINIT(JCREEP)
      STINIT(1)=STINIT(1)+P*STINIT(4)
      STINIT(2)=STINIT(2)+P*STINIT(4)
```

***** FORM CREEP 'FORCE' VECTOR = (BT)(D)(CREEP)*DELTA   *****

```
      CALL MATPRD(D,STINIT,DS,3,3,1)
      CALL MATPRD(BT,DS,DFCR,6,3,1)
      DO 1930 JFCR=1,3
      FCREEP(2*NODEL(JFCR,ICREEP)-1)=FCREEP(2*NODEL(JFCR,ICREEP)-1)
     1                      +DFCR(2*JFCR-1)*DABS(DELIB(ICREEP))
 1930 FCREEP(2*NODEL(JFCR,ICREEP))=FCREEP(2*NODEL(JFCR,ICREEP))
     1                      +DFCR(2*JFCR)*DABS(DELIB(ICREEP))
```

**** CALCULATE CONV, A MEASURE OF CONVERGENCE   *****

```
 1039 DO 1931 JTEST=1,4
      STRES(JTEST)=DABS(STRES(JTEST))
      STRDIF(JTEST)=DABS(STRES(JTEST)-PRESTR(JTEST,ICREEP))
      CONV=DMAX1(CONV,STRDIF(JTEST))
 1931 PRESTR(JTEST,ICREEP)=STRES(JTEST)
 1030 CONTINUE
```

**** END OF LOOP OVER ELEMENTS   *****

**** ENSURE THAT 'FIXED' DISPLACEMENTS REMAIN FIXED   *****

```
      IF (NFIX.EQ.0) GO TO 1027
      ANGL=31.42
      DO 1040 IBOUN=1,NFIX
      IF (ANGLE(IBOUN).NE.0.0) GO TO 1044
```

**** NODES FIXED IN GLOBAL CO-ORDINATES   *****

```
      DO 1041 JBOUN=1,2
      IF (IFLAG(JBOUN,IBOUN)-1) 1041,1042,1043
```

**** FIXED DISPLACEMENTS   *****

```
 1042 KBOUN=2*NOFIX(IBOUN)+JBOUN-2
      FCREEP(KBOUN)=0.0
      GO TO 1041
```

**** FIXED VELOCITIES   *****

```
 1043 IF (IFLAG(JBOUN,IBOUN).EQ.3) GO TO 1042
      KBOUN=2*NOFIX(IBOUN)+JBOUN-2
      FCREEP(KBOUN)=DFIX(JBOUN,IBOUN)*1.0D12
 1041 CONTINUE
      GO TO 1040
```

**** NODES FIXED IN ROTATED CO-ORDINATES   *****

```
 1044 IF (ANGLE(IBOUN).EQ.ANGL) GO TO 1047
```

**** FORM ROTATION MATRIX, R, AND ITS TRANSPOSE, RT   *****

```
      ANGL=ANGLE(IBOUN)
      R(1,1)=DCOS(ANGL)
      R(2,2)=R(1,1)
      R(1,2)=DSIN(ANGL)
      R(2,1)=-R(1,2)
      DO 1046 IRT=1,2
      DO 1046 JRT=1,2
      RT(IRT,JRT)=R(JRT,IRT)
 1046 CONTINUE
```

**** ROTATE FCREEP TO RF AND SET APPROPRIATE VALUES   *****
**** IFLAG=3 GIVES FIXED DISPLACEMENT, 4 FIXED VELOCITY   *****

```
 1047 MROTF=NOFIX(IBOUN)
      F(1)=FCREEP(2*MROTF-1)
      F(2)=FCREEP(2*MROTF)
      CALL MATPRD(R,F,RF,2,2,1)
      DO 1048 JROTF=1,2
      IF (IFLAG(JROTF,IBOUN).EQ.3) RF(JROTF)=0.0
      IF (IFLAG(JROTF,IBOUN).EQ.4) RF(JROTF)=DFIX(JROTF,IBOUN)*1.0D12
 1048 CONTINUE
```

**** ROTATE RF BACK TO GLOBAL CO-ORDS AND REPLACE IN FCREEP   *****

```
      CALL MATPPD(RT,RF,F,2,2,1)
      FCREEP(2*MROTF-1)=F(1)
      FCREEP(2*MROTF)  =F(2)

1040 CONTINUE
```

```
1027 IF (ITER.EQ.1) GO TO 1024
      CONV=CONV/VERGE
      LTER=ITER-10*(ITER/10)
      IF (ITER.LT.14) LTER=ITER
      IF (LTER.GT.4.OR.LTER.EQ.0) LTER=4
```

**** WRITE INFORMATION ON CONVERGENCE ON DEVICE ?   *****

```
      IF (CONV.GE.999.999) GO TO 1025
      WRITE(8,1929) ITER,ZUF(LTER),CONV
1929 FORMAT(1H ,I4,A4,'ITERATION; NORMALISED STRESS DIFFERENCE=',F7.3)
      GO TO 1026
1025 WRITE(8,1928) ITER,ZUF(LTER),CONV
1928 FORMAT(1H ,I4,A4,'ITERATION; NORMALISED STRESS DIFFERENCE=',D11.3)
```

**** IF CONVERGENCE IS SUCCESSFUL LEAVE ITERATION LOOP   *****

```
1026 IF (CONV.LT.1.0) GO TO 1019
```

**** INCORPORATE TOTAL CREEP STRAIN INTO FORCE VECTOR   *****

```
1024 DO 1023 LBOUN=1,NNOD2
1023 FORCE(LBOUN)=FINIT(LBOUN)+FCREEP(LBOUN)
1020 CONTINUE
```

**** END OF ITERATION LOOP   *****

**** CONVERGENCE HAS FAILED   *****
**** ITERATION MAY BE CONTINUED IF REQUIRED   *****

```
      WRITE(6,1917)ITIME,ZUF(LTIM),CONV
1917 FORMAT(1H0,I4,A4,'TIME INCREMENT HAS NOT CONVERGED'/
     1        9X,'RESIDUAL= ',D10.3/
     2        9X,'ENTER NUMBER OF EXTRA ITERATIONS (I4)'/' ....')
      READ(5,1916) ITCON
1916 FORMAT(I4)
      IF (ITCON.LE.0) GO TO 1015
      ITERO=ITMAX+1
      ITMAX=ITMAX+ITCON
      GO TO 1014
1015 WRITE(7,1915)
1915 FORMAT(1H0,10X,'** RUN ABORTED **')
      CALL TIME(1,1)
      STOP

1019 CONTINUE
```

**** END OF SOLUTION ITERATIONS   *****

**** INCORPORATE INCREMENTAL CREEP INTO TOTAL CREEP VECTOR   *****

```
      DO 1013 JCRT=1,NEL
      DO 1013 ICRT=1,4
1013 CREEP(ICRT,JCRT)=CREEP(ICRT,JCRT)+DCREEP(ICRT,JCRT)
```

**** SET UP FORCE VECTORS FOR NEXT TIME INCREMENT   *****

```
      DO 1016 NEXTF=1,NNOD2
      FINIT(NEXTF)=FINIT(NEXTF)+FCREEP(NEXTF)
      FORCE(NEXTF)=FINIT(NEXTF)
1016 CONTINUE

      WRITE(6,1918) ITIME,ZUF(LTIM)
1918 FORMAT(1H0,I4,A4,'TIME INCREMENT COMPLETE')
      CALL TIME(1,1)
```

```
1010 CONTINUE

**** END OF TIME ITERATIONS                                              ******

      DTIME=DTIME/3.16D7

      RETURN
      END


********************************************************************************


      SUBROUTINE STRESS
      =================
**** TO OBTAIN STRESSES FROM DISPLACEMENTS                               *****

      IMPLICIT REAL*8 (A-H,O-W)
      COMMON /NOD/ X(300),Y(300),DISP(600),FORCE(600),G,NCOM1(2)
      COMMON /EL/ ITYP(500),NODEL(3,500),NEL
      COMMON /MAT/ EM(10),PM(10),COM3(30),NCOM3(11)
      COMMON /SO/ STRO(4,500),INST
      COMMON /K/ COM6(111500),BLIB(6,3,500),DLIB(3,3,500),NCOM6(2)
      COMMON /ST/ PRINC(4,500),STMAX,MZ(500),IFAIL(500),MAXEL,ISTR
      COMMON /CR/ CREEP(4,500),CCM8(2),KTIME,NTIME
      COMMON /WK/ B(3,6),D(3,3),DB(3,6),STRES(4),STRN(4),
     1            DIS(6),COM9(5230)
      COMMON /MIS/ PI,COMO(5),NCOMO(4)

      STMAX=0.0
      MAXEL=1
      ISTR=1

      DO 510 IST=1,NEL

**** ASSIGN PROPERTIES TO CURRENT ELEMENT                                *****

      ITY=ITYP(IST)
      E=EM(ITY)
      P=PM(ITY)
      DO 500 IDIS=1,3
      DIS(2*IDIS-1)=DISP(2*NODEL(IDIS,IST)-1)
  500 DIS(2*IDIS)=DISP(2*NODEL(IDIS,IST))
      DO 501 IBGET=1,3
      DO 501 JBGET=1,6
  501 B(IBGET,JBGET)=BLIB(JBGET,IBGET,IST)
      DO 502 JDGET=1,3
      DO 502 IDGET=1,3
  502 D(IDGET,JDGET)=DLIB(IDGET,JDGET,IST)
      CALL MATPRD(B,DIS,STRN,3,6,1)
      STRN(4)=0.0
      IF((KTIME+NTIME).EQ.0) GO TO 506

**** FORM ELASTIC STRAINS AND STRESSES                                   *****

      DO 505 ILAS=1,4
  505 STRN(ILAS)=STRN(ILAS)-CREEP(ILAS,IST)
      STRN(1)=STRN(1)+P*STRN(4)
      STRN(2)=STRN(2)+P*STRN(4)
  506 CALL MATPRD(D,STRN,STRES,3,3,1)
      STRES(4)=P*(STRES(1)+STRES(2))+E*STRN(4)

**** WRITE OUT STRESSES FOR CONTINUATION (UNFORMATTED, ON #2)            *****

      WRITE (2) (STRES(JSO),JSO=1,4)

**** ADD ON INITIAL STRESSES, IF INST=1                                  *****

      IF (INST.NE.1) GO TO 508
      DO 507 ISO=1,4
      STRES(ISO)=STRES(ISO) + STRO(ISO,IST)
  507 CONTINUE

**** TO OBTAIN PRINCIPAL STRESSES                                        *****
**** ( PRINC(1) IS AT THETA TO THE X AXIS )                              *****
```

```fortran
508 IF (STRES(2).NE.STRES(1)) GO TO 503
    THETA=PI/4.0
    GO TO 504
503 THETA=DATAN(2.0*STRES(3)/(STRES(1)-STRES(2)))/2.0
    IF (THETA.LT.0.0) THETA=THETA+PI/2.0
504 PRINC(1,IST)=(STRES(1)*(DCOS(THETA)**2))
   1             +(STRES(2)*(DSIN(THETA)**2))
   2             +(STRES(3)*DSIN(2.0*THETA))
    PRINC(2,IST)=STRES(1)+STRES(2)-PRINC(1,IST)
    PRINC(3,IST)=STRES(4)
    PRINC(4,IST)=THETA*180.0/PI
```

```fortran
**** TO FIND THE MAXIMUM STRESS (IN THE BODY) AND TO TEST       *****
**** WHETHER THE Z STRESS IS AN EXTREMUM (FOR THIS ELEMENT)     *****

    DMAX=DMAX1(PRINC(1,IST),PRINC(2,IST),PRINC(3,IST))
    DMIN=DMIN1(PRINC(1,IST),PRINC(2,IST),PRINC(3,IST))
    MZ(IST)=0
    IF (PRINC(1,IST).EQ.PRINC(3,IST)) GO TO 509
    IF (PRINC(2,IST).EQ.PRINC(3,IST)) GO TO 509
    IF (DMAX.EQ.PRINC(3,IST)) MZ(IST)=1
    IF (DMIN.EQ.PRINC(3,IST)) MZ(IST)=-1
509 DMAX=DABS(DMAX)
    DMIN=DABS(DMIN)
    DMAX=DMAX1(DMAX,DMIN)
    IF (STMAX.GE.DMAX) GO TO 510
    STMAX=DMAX
    MAXEL=IST
510 CONTINUE

    WRITE(6,599)
599 FORMAT('0PRINCIPAL STRESSES CALCULATED')
    CALL TIME(1,1)

    RETURN
    END
```

```fortran
***********************************************************************

    SUBROUTINE HYDRA
    ================
**** TO ADD LITHOSTATIC PRESSURE                                 *****
****    TO THE FINAL STRESS SYSTEM IN A MODEL                    *****

    IMPLICIT REAL*8 (A-H,O-W)
    COMMON /NOD/ XCOM1(600),COM1(1200),G,NCOM1(2)
    COMMON /EL/  NCOM2(500),NODEL(3,500),NEL
    COMMON /ST/  PRINC(4,500),STMAX,NCOM7(1000),MAXEL,NCOM71
    COMMON /WK/  RO(5),YRO(5),NRO,COM9(5291)
    COMMON /IN/  COM10(600),X(300),Y(300),ISET

    YSIGN=G/DABS(G)

**** READ IN DENSITY OF LAYERS, AND DEPTH TO THE TOP OF EACH      *****

    READ(4,569) NRO
569 FORMAT(I4)
    DO 561 IRO=1,NRO
    READ(4,568) YRO(IRO),RO(IRO)
568 FORMAT(2F10.3)
    YRO(IRO)=YRO(IRO)*1.0E3*YSIGN
561 CONTINUE

    DO 570 IHYD=1,NEL

**** FIND THE DEPTH TO THE CENTROID OF EACH ELEMENT              *****

    PHYD=0.0
    YCEN=(Y(NODEL(1,IHYD))+Y(NODEL(2,IHYD))+Y(NODEL(3,IHYD)))
   1      *YSIGN/3.0
    IF (YCEN.LE.YRO(1)) GO TO 570
```

```
C**** APPLY CONTRIBUTION TO HYDROSTATIC PRESSURE                    *****
C****    FROM ALL LAYERS ABOVE THE CENTROID                         *****

      DO 573 JRO=1,NRO
      KRO=JRO+1
      IF (JRO.EQ.NRO) GO TO 571
      IF (YCEN.GE.YRO(KRO)) GO TO 572
  571 PHYD=PHYD+(YCEN-YRO(JRO))*RO(JRO)
      GO TO 574
  572 PHYD=PHYD+(YRO(KRO)-YRO(JRO))*RO(JRO)
  573 CONTINUE

  574 CONTINUE
      PHYD=PHYD*DABS(G)

C**** ADD HYDROSTATIC PRESSURE TO ALL THREE PRINCIPAL STRESSES      *****

      DO 575 JHYD=1,3
      PRINC(JHYD,IHYD)=PRINC(JHYD,IHYD)-PHYD

C**** RE-COMPUTE STMAX AND MAXEL                                    *****

      DMAX=DABS(PRINC(JHYD,IHYD))
      IF (STMAX.GE.DMAX) GO TO 575
      STMAX=DMAX
      MAXEL=IHYD
  575 CONTINUE

  570 CONTINUE

      WRITE(7,567)
  567 FORMAT(1H0,10X,'HYDROSTATIC PRESSURE ADDED AS FOLLOWS :'/
     1       1H0/15X,'TOP OF LAYER (M)',5X,'DENSITY')
      DO 562 IH=1,NRO
      YRO(IH)=YRO(IH)*YSIGN
      WRITE(7,566) YRO(IH),RO(IH)
  566 FORMAT(18X,E10.3,8X,F7.1)
  562 CONTINUE

      RETURN
      END
```

`*****************************************************************************`

```
      SUBROUTINE PORE
      ===============
C**** TO SUBTRACT PRESSURE DUE TO WATER, WHOSE SURFACE IS AT Y=0,   *****
C****    FROM THE PRINCIPAL STRESSES , GIVING THE PRINCIPAL         *****
C****    EFFECTIVE STRESSES (IN REGIONS WITH IPORE=1)               *****

      IMPLICIT REAL*8 (A-H,O-W)
      COMMON /NOD/ X(300),Y(300),COM1(1200),G,NCOM1(2)
      COMMON /EL/  ITYP(500),NODEL(3,500),NEL
      COMMON /MAT/ COM3(50),IPORE(10),NMAT
      COMMON /ST/  PRINC(4,500),STMAX,NCOM7(1002)

      DIMENSION JP(10)

C**** ASSIGN WATER DENSITY                                          *****

      RHOW=1030.0

      DO 220 IPO=1,NEL

      IF (IPORE(ITYP(IPO)).NE.1) GO TO 220

C**** FIND THE WATER PRESSURE AT THE ELEMENT CENTRE                 *****

      YCEN=(Y(NODEL(1,IPO))+Y(NODEL(2,IPO))+Y(NODEL(3,IPO)))/3.0
      PP=YCEN*RHOW*G

C**** SUBTRACT THE PORE PRESSURE FROM EACH OF THE PRINCIPAL         *****
C****    STRESSES (NOTE: PP IS +VE, WHILE PORE PRESSURE IS -VE)     *****
```

```
      DO 221 JPO=1,3
      PRINC(JPO,IPO) = PRINC(JPO,IPO) + PP
  221 CONTINUE

  220 CONTINUE

**** WRITE INFORMATION ON PORE PRESSURE INCLUDED                        *****

      KP=0
      DO 222 IP=1,NMAT
      IF (IPORE(IP).NE.1) GO TO 222
      KP=KP+1
      JP(KP)=IP
  222 CONTINUE

      IF (KP.EQ.0) GO TO 223

      WRITE(7,229) (JP(NP),NP=1,KP)
  229 FORMAT (1H0/1H0,10X,'PORE PRESSURE SUBTRACTED, '/
     1             11X,'IN MATERIALS ',10I3)
      GO TO 224

  223 WRITE(6,228)
  228 FORMAT('0ERROR : PORE WAS CALLED BUT NO MATERIALS HAD IPORE=1')

  224 CONTINUE

      RETURN
      END


*********************************************************************************


      SUBROUTINE FAIL
      ===============
**** TO PREDICT FAILURE IN ELEMENTS                                     *****

      IMPLICIT REAL*8 (A-H,O-W)
      COMMON /EL/   ITYP(500),NCOM2(1500),NEL
      COMMON /MAT/  COM3(40),TS(10),NCOM3(11)
      COMMON /SO/   CFAIL(500),FANGL(500),COM5(1000),NCOM5
      COMMON /ST/   PRINC(4,500),COM7,NCOM7(500),IFAIL(500),NCOM71(2)
      COMMON /MIS/  PI,COM0(6),NCOM0(4)

**** CONSTANTS : T,THE TENSILE STRENGTH; SC,THE STRESS REQUIRED         *****
**** TO CLOSE CRACKS; FMU,THE COEFFICIENT OF FRICTION.                  *****

**** IN ALL CASES FAILURE OCCURS IF CFAIL IS LESS THAN 0,               *****
****     THE DIRECTION OF FAILURE BEING AT FANGL TO S3                  *****
****        (I.E.TO THE GREATEST COMPRESSION)                           *****

      FMU=1.09
      PHI=DATAN(1.0/FMU)*90.0/PI

      DO 550 IF=1,NEL

**** ASSIGN VALUES OF T AND SC FOR ELEMENT                              *****

      T = TS(ITYP(IF))
      SC=-4.19*T

**** S1,S3 ARE THE MAXIMUM AND MINIMUM PRINCIPAL STRESSES               *****
**** RESPECTIVELY, IN THE X,Y PLANE                                     *****

      S1=DMAX1(PRINC(1,IF),PRINC(2,IF))
      S3=DMIN1(PRINC(1,IF),PRINC(2,IF))

**** THE MODE OF FAILURE DEPENDS ON THE MEAN STRESS, SM                 *****
**** AND ITS DEGREE DEPENDS ON THE MAXIMUM SHEAR STRESS, TM             *****

      SM=(S1+S3)/2.0
      TM=(S1-S3)/2.0
```

```
****  TENSIONAL REGION                                                      *****

      IF (SM.LT.T) GO TO 551
      IFAIL(IF)=-1
      CFAIL(IF)=(T-SM)/T
      FANGL(IF)=0.0
      GO TO 555
  551 IF (SM.LT.-T) GO TO 552
      IFAIL(IF)=1
      CFAIL(IF)=(T-S1)/(T-SM)
      FANGL(IF)=0.0
      GO TO 555

****  OPEN CRACK COMPRESSIONAL REGION                                       *****

  552 SA=SC-2.0*T
      IF (SM.LT.SA) GO TO 553
      IFAIL(IF)=2
      TF=DSQRT(-4.0*T*SM)
      CFAIL(IF)=1.0 - TM/TF
      FANGL(IF)=DARCOS(-TF/SM/2.0)*90.0/PI
      GO TO 555

****  INTERMEDIATE REGION                                                   *****

  553 BETA=2.0/FMU*DSQRT(1.0-SC/T) + SC/T
      SB=SC*(1.0+FMU*FMU) + BETA*FMU*FMU*T
      TC=BETA*FMU*T - FMU*SC
      IF (SM.LT.SB) GO TO 554
      IFAIL(IF)=3
      CFAIL(IF)=1.0 - TM/DSQRT((SM-SC)*(SM-SC)+TC*TC)
      FANGL(IF)=DATAN(TC/(SC-SM))*90.0/PI
      GO TO 555

****  CLOSED CRACK COMPRESSIONAL REGION                                     *****

  554 ALPHA=DSQRT(1.0+FMU*FMU)/FMU
      IFAIL(IF)=4
      CFAIL(IF)=1.0 - ALPHA*TM/(BETA*T-SM)
      FANGL(IF)=PHI
  555 CONTINUE
  550 CONTINUE

      RETURN
      END


************************************************************************************


      SUBROUTINE ZERO
      ===============
****  TO TAKE OFF INITIAL DISPLACEMENTS CALCULATED BY SETUP                 *****

      IMPLICIT REAL*8 (A-H,O-W)
      COMMON /NOD/ ICOM1(600),DISP(600),COM1(600),G,NNOD,NNOD2
      COMMON /IN/  DISP0(600),X0(300),Y0(300),ISET

****  TEST WHETHER ZERO CAN BE USED                                         *****

      IF (ISET.GE.1) GO TO 2101
      WRITE (6,2109)
 2109 FORMAT ('0** ERROR: MODEL WAS NOT INITIALIZED USING SETUP'/
     1            11X,'ZERO CANNOT BE USED')
      RETURN
 2101 CONTINUE

****  TAKE INITIAL DISPLACEMENTS FROM DISP                                  *****

      DO 2100 ISUB=1,NNOD2
      DISP(ISUB)=DISP(ISUB)-DISP0(ISUB)
 2100 CONTINUE

****  CORRECT GRID TO GIVE X0,Y0                                            *****
```

```
      DO 2001 IADD=1,NNOD
      XO(IADD)=XO(IADD)+DISPO(2*IADD-1)
      YO(IADD)=YO(IADD)+DISPO(2*IADD)
2001  CONTINUE

      WRITE (7,2108)
2108  FORMAT (1H0,10X,'INITIAL DISPLACEMENTS SUBTRACTED')
      RETURN
      END
```

```
      SUBROUTINE OUTPUT
      =================
****  TO OUTPUT RESULTS                                             *****

      IMPLICIT REAL*8 (A-H,O-W)
      COMMON /NOD/ XCOM1(600),DISP(600),FORCE(600),G,NNOD,NNOD2
      COMMON /EL/  NCOM2(2000),NEL
      COMMON /SO/  CFAIL(500),FANGL(500),COM5(1000),NCOM5
      COMMON /ST/ PRINC(4,500),STMAX,MZ(500),IFAIL(500),MAXEL,ISTR
      COMMON /MIS/ PI,TITLE(4),ZUF(4),IDATE(3),MCHO

      WRITE(7,699) IDATE,TITLE
699   FORMAT(1H1,7X,'** RESULTS **',11X,3A4,12X,4A8/
     1       1H0/1H0,10X,'NODAL DISPLACEMENTS'/
     2       1H+,10X,'                    '/
     3       1H0,30X,'NODE',12X,'DISP(X): M',12X,'DISP(Y): M'/1H0)
      DO 510 IDOUT=1,NNOD
      WRITE(7,698) IDOUT,DISP(2*IDOUT-1),DISP(2*IDOUT)
698   FORMAT(31X,I4,2(12X,D10.3))
510   CONTINUE

      IF (ISTR.EQ.1) GO TO 613
      WRITE (6,695)
695   FORMAT('0NO STRESSES WRITTEN : ISTR.NE.1')
      GO TO 612

613   WRITE(7,697) STMAX,MAXEL
697   FORMAT(1H0/1H0,10X,'STRESSES AND FAILURE PREDICTIONS'/
     1       1H+,10X,'                               '/
     2       1H0,10X,'MAXIMUM STRESS =',D10.3,'N/SQ.M (ABSOLUTE VALUE)',
     3       ', IN ELEMENT NO.',I4/1H0/
     4       1H0,10X,'ELEMENT',11X,'PRINCIPAL STRESSES',14X,'ANGLE',
     5       11X,'ZSTRESS',6X,'MZ',7X,'CFAIL',4X,'IFAIL',5X,'THETA'/1H0)
      DO 611 ISTOUT=1,NEL
      WRITE(7,696) ISTOUT,PRINC(1,ISTOUT),PRINC(2,ISTOUT),
     1             PRINC(4,ISTOUT),PRINC(3,ISTOUT),MZ(ISTOUT),
     2             CFAIL(ISTOUT),IFAIL(ISTOUT),FANGL(ISTOUT)
696   FORMAT(11X,I4,2(8X,D10.3),8X,F3.3,8X,D10.3,
     1       5X,I2,5X,F7.3,5X,I2,5X,F7.2)
611   CONTINUE

612   WRITE(6,692)
692   FORMAT('0OUTPUT COMPLETED')
      CALL TIME(1,1)

      RETURN
      END
```

```fortran
      SUBROUTINE STRAIN
      =================
****  TO OBTAIN TOTAL STRAINS FROM DISPLACEMENTS                          *****
****       (INCLUDING ANY CREEP STRAINS)                                  *****

      IMPLICIT REAL*8 (A-H,O-W)
      COMMON /NOD/ XCOM1(600),DISP(600),COM1(601),NCOM1(2)
      COMMON /EL/ ITYP(500),NODEL(3,500),NEL
      COMMON /K/ COM6(111500),BLIB(6,3,500),DLIB(3,3,500),NCOM6(2)
      COMMON /ST/ PRINC(4,500),STMAX,NE(500),IFAIL(500),MAXEL,ISTR
      COMMON /WK/ COM9(5220),B(3,6),D(3,3),DB(3,6),
     1                    STRES(4),STRN(4),DIS(6)
      COMMON /MIS/ PI,COMO(5),NCOMO(4)

      STMAX=0.0
      MAXEL=1
      ISTP=2

      DO 510 IST=1,NEL

****  ASSIGN PROPERTIES TO CURRENT ELEMENT                                *****

      DO 500 IDIS=1,3
      DIS(2*IDIS-1)=DISP(2*NODEL(IDIS,IST)-1)
  500 DIS(2*IDIS)=DISP(2*NODEL(IDIS,IST))
      DO 501 IBGET=1,2
      DO 501 JBGET=1,6
  501 B(IBGET,JBGET)=BLIB(JBGET,IBGET,IST)
      CALL MATPRO(3,DIS,STRN,3,6,1)
      STRN(4)=0.0

****  TO OBTAIN PRINCIPAL STRAINS                                         *****
****  ( PRINC(1) IS AT THETA TO THE X AXIS )                              *****

  508 IF (STRN(2).NE.STRN(1)) GO TO 503
      THETA=PI/4.0
      GO TO 504
  503 THETA=DATAN(STRN(3)/(STRN(1)-STRN(2)))/2.0
      IF (THETA.LE.0.0) THETA=THETA+PI/2.0
  504 PRINC(1,IST)=(STRN(1)*(DCOS(THETA)**2))
     1            +(STRN(2)*(DSIN(THETA)**2))
     2            +(STRN(3)*DSIN(2.0*THETA))
      PRINC(2,IST)=STRN(1)+STRN(2)-PRINC(1,IST)
      PRINC(3,IST)=STRN(4)
      PRINC(4,IST)=THETA*180.0/PI

****  TO FIND THE MAXIMUM STRAIN IN THE BODY                              *****

      DMAX=DMAX1(PRINC(1,IST),PRINC(2,IST),PRINC(3,IST))
      DMIN=DMIN1(PRINC(1,IST),PRINC(2,IST),PRINC(3,IST))
      DMAX=DABS(DMAX)
      DMIN=DABS(DMIN)
      DMAX=DMAX1(DMAX,DMIN)
      IF (STMAX.GE.DMAX) GO TO 510
      STMAX=DMAX
      MAXEL=IST
  510 CONTINUE

      WRITE(7,598) STMAX,MAXEL
  598 FORMAT(1H0,10X,'TOTAL STRAINS'/
     1       1H+,10X,'             '/
     2       1H0,10X,'MAXIMUM STRAIN = ',D10.3,' (ABSOLUTE VALUE)',
     3       ', IN ELEMENT NO.',I4/1H0/
     4       1H0,30X,'ELEMENT',11X,'PRINCIPAL STRAINS',15X,'ANGLE'/1H0)
      DO 520 JST=1,NEL
      WRITE(7,597) JST,PRINC(1,JST),PRINC(2,JST),PRINC(4,JST)
  597 FORMAT(31X,I4,2(8X,D10.3),8X,F8.3)
  520 CONTINUE

      WRITE(6,599)
  599 FORMAT('0PRINCIPAL STRAINS CALCULATED')
      CALL TIME(1,1)

      RETURN
      END
```

```
********************************************************************************

      SUBROUTINE MORE
      ===============
****  WRITE OUT INFORMATION FOR MORE TIME INCREMENTS                   *****
****  (UNFORMATTED, TO BE READ IN BY SR READ2)                         *****

      IMPLICIT REAL*8 (A-H,O-W)
      COMMON /NOD/  X(300),Y(300),DISP(600),FORCE(600),G,NNOD,NNOD2
      COMMON /EL/   ITYP(500),NODEL(2,500),NEL
      COMMON /MAT/  EM(10),PM(10),RHOM(10),ETAM(10),TS(10),IPORE(10),NMAT
      COMMON /CR/   CREEP(4,500),DTIME,TOTIME,KTIME,NTIME
      COMMON /IN/   DISP0(600),XCOM10(600),ISET

      KTIME=KTIME+NTIME

      WRITE (3)  G,NNOD,NNOD2,TOTIME,KTIME,ISET
      WRITE (3)  X,Y,DISP

      IF (KTIME.GT.0) WRITE (3) CREEP

      WRITE (3)  EM,PM,RHOM,ETAM,TS,IPORE,NMAT
      WRITE (3)  ITYP,NODEL,NEL
      WRITE (3)  FORCE

      IF (ISET.GE.1) WRITE (3) DISP0

      RETURN
      END


********************************************************************************


      SUBROUTINE PSCALE
      =================
****  TO CALCULATE PLOT SCALES AND PARAMETERS                          *****

      IMPLICIT REAL*8 (A-H,O-W)
      REAL*4 RAMAX,RAMIN
      COMMON /NOD/  XCOM1(600),COM1(1200),G,NNOD,NNOD2
      COMMON /WK/   XMAX,XMIN,YMAX,YMIN,XSC,YSC,XSP,YSP,
     1              XMAP1,XMAP2,YMAP1,YMAP2,SIGN,NOUT(51),KNOUT,COM9(5256)
      COMMON /IN/   COM10(600),X(300),Y(300),ISET

****  READ NUMBERS OF OUTER NODES FOR USE IN OUTLIN                    *****

      READ (4,709) NOUT(1)
  709 FORMAT (I4)
      IF (NOUT(1).LE.0) GO TO 702
      DO 703 IOUT=2,51
      READ (4,709) NOUT(IOUT)
      IF (NOUT(IOUT).NE.NOUT(1)) GO TO 703
      KNOUT=IOUT
      GO TO 702
  703 CONTINUE
      WRITE (6,708)
  708 FORMAT('0** ERROR : OUTLINE ARRAY CONTAINS MORE THAN 50 NODES')
  702 CONTINUE

****  START PLOTFILE                                                   *****

      CALL PAPER(1)

****  ASSIGN MAXIMUM AND MINIMUM VALUES OF X AND Y                     *****
****   YMAX BEING THE GREATEST DEPTH (WHETHER +VE OR -VE)              *****

      XMAX=RAMAX(X,NNOD)
      YMAX=RAMAX(Y,NNOD)
      XMIN=RAMIN(X,NNOD)
      YMIN=RAMIN(Y,NNOD)
      IF (G.GT.0.0) GO TO 713
```

```
      YMA=YMAX
      YMAX=YMIN
      YMIN=YMA
  713 CONTINUE
```

**** CALCULATE PLOT SCALES   *****

```
      XSC=1.0E5
      IF (XMAX.LE.5.0E4) XSC=1.0E4
      IX=IFIX(XMAX/2.0/XSC)+1
      XSC=FLOAT(IX)*XSC
      XMAP1=-0.2*XSC
      XMAP2=XMAX-XMAP1
      XSP=XMAX/XSC+0.4
```

**** THE PLOT ORIENTATION DEPENDS ON THE SIGN OF G   *****
****   (IF VARIABLE 'SIGN' IS +VE, Y IS +VE UPWARDS)   *****

```
      SIGN=1.0D0
      SIGN=-DSIGN(SIGN,G)
      IY=ABS(YMAX-YMIN)/5.0E3
      IF (IY.GT.10) IY=(IY/10)*10
      YSC=FLOAT(IY)*1.0E3
      YMAP2=SIGN*YSC
      YMAP1=YMAX-YMAP2
      YSP=0.9

      RETURN
      END
```

****

```
      FUNCTION RAMAX(X,N)
      ===================
```
**** TO FIND THE MAXIMUM VALUE OF AN ARRAY   *****

```
      DIMENSION X(N)
      RAMAX=X(1)
      DO 700 IMAX=2,N
      RAMAX=AMAX1(RAMAX,X(IMAX))
  700 CONTINUE

      RETURN
      END
```

****

```
      FUNCTION RAMIN(X,N)
      ===================
```
**** TO FIND THE MINIMUM VALUE OF AN ARRAY   *****

```
      DIMENSION X(N)
      RAMIN=X(1)
      DO 701 IMIN=2,N
      RAMIN=AMIN1(RAMIN,X(IMIN))
  701 CONTINUE

      RETURN
      END
```

****

```
      SUBROUTINE SCON
      ================
****  TO SET UP A FILE ON DEVICE 9 FOR USE WITH GPCP         *****
****    (THE CALCOMP GENERAL PURPOSE CONTOURING PACKAGE)     *****
****      GIVING CONTOURS OF MAXIMUM SHEAR STRESS            *****

      IMPLICIT REAL*8 (A-H,O-W)
      REAL*4 ALEVEL,DALEV
      COMMON /ND/ XCOM1(600),COM1(1200),G,NNOD,NNOD2
      COMMON /EL/ NCOM2(500),NODEL(3,500),NEL
      COMMON /ST/ PRINC(4,500),COM7,NCOM7(1001),ISTR
      COMMON /WK/ XMAX,XMIN,YMAX,YMIN,XSC,YSC,COM8(6),SIGN,
     1            NOUT(51),KNOUT,XN(51),YM(51),COM9(5205)
      COMMON /IN/ COM10(600),X(300),Y(300),ISET
      COMMON /MIS/ PI,TITLE(4),ZUF(4),IDATE(3),MCHO

      PMAX=0.0
      PMIN=0.0
      X1=X(1)/1.0E3
      Y1=Y(1)/1.0E3
      XMA=XMAX/1.0E3
      YMA=YMAX/1.0E3

****  FIND THE CO-ORDINATES OF THE OUTLINE, XN,YN,           *****
****    NUMBERING CLOCKWISE (FOR PHASE 3), ASSUMING          *****
****     THAT NOUT IS GIVEN ANTI-CLOCKWISE                   *****

      DO 800 IN=1,KNOUT
      JN=KNOUT-IN+1
      NN=NOUT(IN)
      XN(JN)=X(NN)/1.0E3
      YN(JN)=Y(NN)/1.0E3
  800 CONTINUE
****  PHASE 1                                                *****

      WRITE(0,899) TITLE
  899 FORMAT('JOBX ',4A8/'FLEX')
      IF(G.GT.0.0) WRITE(0,898)
  898 FORMAT('ANGL 180.0  0.0')

****  PHASE 2 : PARAMETERS                                   *****

      XS=XSC/1.0E4
      YS=YMA/8.0
      XINC=(XMAX-XMIN)/2.0E4
      YINC=(YMAX-YMIN)/2.0E4
      WRITE(0,897) XS,YS,XINC,XMA,YINC,YMA
  897 FORMAT('SIZX ',2F5.1,'  1.0     0.5       0.0  ',F5.1,
     1         F10.3,'       0.0  ',F5.1,F10.3/
     2         'CNTL 0.075 0.15   -1     1')

****  PHASE 2 : POINTS AND VALUES TO BE CONTOURED            *****

      DO 820 ICON=1,NEL
      XCON=(X(NODEL(1,ICON))+X(NODEL(2,ICON))+X(NODEL(3,ICON)))/3.0E3
      YCON=(Y(NODEL(1,ICON))+Y(NODEL(2,ICON))+Y(NODEL(3,ICON)))/3.0E3
      P=DABS(PRINC(1,ICON)-PRINC(2,ICON))/2.0

****  SCALE STRESSES AND STRAINS ACCORDINGLY                 *****

      IF (ISTR.EQ.1) P=P/1.0D9
      IF (ISTR.EQ.2) P=P*1.0D3

      PMAX=DMAX1(PMAX,P)
      PMIN=DMIN1(PMIN,P)
      WRITE(0,896) XCON,YCON,P
  896 FORMAT('CNTL ',2F10.3,F10.5)
  820 CONTINUE

****  PHASE 3 : DEFINE AREA TO BE CONTOURED                  *****

      WRITE(0,895)  KNOUT
  895 FORMAT('BEND'/'SAMF'/'BLNK     1',I5)
      WRITE (0,887) (XN(IBND),YN(IBND),IBND=1,KNOUT)
```

```
  887 FORMAT ('BND  ',6F10.3)
```

**** PHASE 4 : PLOT CONTOURS   *****

```
      CALL LEVEL(PMAX,PMIN,ALEVEL,DALEV,NLEVS)
      WRITE(0,894) ALEVEL,ALEVEL,DALEV,DALEV,NLEVS
  894 FORMAT ('PHS4'/'LEVS ',2F5.2,'  3.0  0.1  0.2  0.0 0.05  0.0',
     1       '    0    5    2',2F5.2,I5,'    5'/
     2       'SKIP   0.1'/'BRDR')
```

**** PHASE 5 : DRAW MODEL   *****

```
      WRITE(0,884) (XN(ILIN-1),YN(ILIN-1),
     1              XN(ILIN)  ,YN(ILIN)  ,ILIN=2,KNOUT)
  884 FORMAT ('LINE',5X,'1',4F5.1,'   0.0  0.0  0.0    1')
```

**** PHASE 5 : DRAW BORDER   *****

```
      WRITE(0,893)
  893 FORMAT('LINE',5X,'0  0.0  0.0  0.0 10.5  0.0  0.0  0.0    1'/
     1       'LINE',5X,'0  0.0 10.5 15.0 10.5  0.0  0.0  0.0    1'/
     2       'LINE',5X,'0 15.0 10.5 15.0  0.0  0.0  0.0  0.0    1'/
     3       'LINE',5X,'0 15.0  0.0  0.0  0.0  0.0  0.0  0.0    1')
```

**** PHASE 5 : ANNOTATE PLOT   *****

```
      XT1=-0.4*XS
      XT2=-0.9*XS
      WRITE(0,892) XT1,XT2,YMA,YMA
  892 FORMAT('SYMB',5X,'1',F5.1,'   0.0  0.0 0.15  1.0',15X,'0'/
     1       'SYMB',5X,'1',2F5.1,'   0.0 0.15  5.0',15X,F5.1)
      IF (Y1.NE.0.0) WRITE(0,881) XT2,Y1,Y1
  881 FORMAT ('SYMB',5X,'1',2F5.1,'   0.0 0.15  5.0',15X,F5.1)
      WRITE(0,891) TITLE
  891 FORMAT('SYMB',5X,'0  0.5 10.0  0.0  0.3 32.0',15X,4A8/
     1       'SYMB',5X,'0 10.5  9.4  0.0  0.2 19.0',15X,
     2       'CONTOURS OF MAXIMUM')
```

```
      IF (ISTR.EQ.2) GO TO 852
```

**** HEADINGS FOR STRESS CONTOURS   *****

```
      WRITE(0,886)
  886 FORMAT('SYMB',5X,'0 11.1  9.0  0.0  0.2 12.0',15X,
     1       'SHEAR STRESS')
      WRITE(0,885)PMAX,PMIN
  885 FORMAT('SYMB',5X,'0  1.0  9.4  0.0  0.2 30.0',15X,
     1       'MAXIMUM STRESS = ',F7.3,' KBAR.'/
     2       'SYMB',5X,'0  1.0  9.0  0.0  0.2 30.0',15X,
     3       'MINIMUM STRESS = ',F7.3,' KBAR.')
      GO TO 851
```

**** HEADINGS FOR STRAIN CONTOURS   *****

```
  852 CONTINUE
      WRITE(0,879)
  879 FORMAT('SYMB',5X,'0 11.1  9.0  0.0  0.2 12.0',15X,
     1       'SHEAR STRAIN')
      PMAX=PMAX/1.0D3
      PMIN=PMIN/1.0D3
      WRITE(0,878)PMAX,PMIN
  878 FORMAT('SYMB',5X,'0  1.0  9.4  0.0  0.2 27.0',15X,
     1       'MAXIMUM STRAIN = ',E10.3/
     2       'SYMB',5X,'0  1.0  9.0  0.0  0.2 27.0',15X,
     3       'MINIMUM STRAIN = ',E10.3)
  851 CONTINUE
```

```
      WRITE(0,833)
  833 FORMAT('END ')
      WRITE(0,890)
  890 FORMAT('STOP')
```

```
      WRITE(7,889)
  889 FORMAT(1H0,10X,'SHEAR CONTOUR FILE GENERATED')
      WRITE(6,838)
```

```
888 FORMAT('OSHEAR CONTOUR FILE GENERATED')
    CALL TIME(1,1)

    RETURN
    END


********************************************************************

    SUBROUTINE PCON
    ===============
***** TO SET UP A FILE ON DEVICE 0 FOR USE WITH GPCP              *****
*****    (THE CALCOMP GENERAL PURPOSE CONTOURING PACKAGE)         *****
*****      GIVING CONTOURS OF MINIMUM PRINCIPAL STRESS            *****

    IMPLICIT REAL*8 (A-H,O-W)
    REAL*4 ALEVEL,DALEV
    COMMON /NOD/ XCOM1(600),COM1(1200),G,NNOD,NNOD2
    COMMON /EL/  NCOM2(500),NODEL(3,500),NEL
    COMMON /ST/  PRINC(4,500),COM7,NCOM7(1001),ISTR
    COMMON /WK/  XMAX,XMIN,YMAX,YMIN,XSC,YSC,ZCOM9(6),SIGN,
   1             NOUT(51),KNOUT,XN(51),YN(51),COM9(5205)
    COMMON /IN/  COM10(600),X(300),Y(300),ISET
    COMMON /MIS/ PI,TITLE(4),ZUF(4),IDATE(3),MOHO

    PMAX=0.0
    PMIN=0.0
    X1=X(1)/1.0E3
    Y1=Y(1)/1.0E3
    XMA=XMAX/1.0E3
    YMA=YMAX/1.0E3

***** FIND THE CO-ORDINATES OF THE OUTLINE, XN,YN,               *****
*****  NUMBERING CLOCKWISE (FOR PHASE 3), ASSUMING               *****
*****  THAT NOUT IS GIVEN ANTI-CLOCKWISE                         *****

    DO 800 IN=1,KNOUT
    JN=KNOUT-IN+1
    NN=NOUT(IN)
    XN(JN)=X(NN)/1.0E3
    YN(JN)=Y(NN)/1.0E3
800 CONTINUE

**** PHASE 1                                                     *****

    WRITE(0,899) TITLE
899 FORMAT('JOBX ',4A8/'FLEX')
    IF(G.GT.0.0) WRITE(0,898)
898 FORMAT('ANGL 130.0  0.0')

**** PHASE 2 : PARAMETERS                                        *****

    XS=XSC/1.0E4
    YS=YMA/8.0
    XINC=(XMAX-XMIN)/2.0E4
    YINC=(YMAX-YMIN)/2.0E4
    WRITE(0,897) XS,YS,XINC,XMA,YINC,YMA
897 FORMAT('SIZX ',2F5.1,'  1.0  8.5      0.0  ',F5.1,
   1         F10.3,'     0.0  ',F5.1,F10.3/
   2         'CNTL 0.075 0.15   -1    1')

**** PHASE 2 : POINTS AND VALUES TO BE CONTOURED                 *****

    DO 820 ICON=1,NEL
    XCON=(X(NODEL(1,ICON))+X(NODEL(2,ICON))+X(NODEL(3,ICON)))/3.0E3
    YCON=(Y(NODEL(1,ICON))+Y(NODEL(2,ICON))+Y(NODEL(3,ICON)))/3.0E3
    P=DMIN1(PRINC(1,ICON),PRINC(2,ICON))

**** SCALE STRESSES AND STRAINS ACCORDINGLY                      *****

    IF (ISTR.EQ.1) P=P/1.0D8
    IF (ISTR.EQ.2) P=P*1.0D3

    PMAX=DMAX1(PMAX,P)
```

```
      PMIN=DMIN1(PMIN,P)
      WRITE(0,896) XCON,YCON,P
  896 FORMAT('CNTL ',2F10.3,F10.5)
  320 CONTINUE
C**** PHASE 3 : DEFINE AREA TO BE CONTOURED                        *****
C
      WRITE(0,895) KNOUT
  895 FORMAT('BEND'/'SAME'/'BLNK      1',I5)
      WRITE (0,887) (XN(IBND),YN(IBND),IBND=1,KNOUT)
  887 FORMAT ('BND ',6F10.3)
C**** PHASE 4 : PLOT CONTOURS                                      *****
C
      CALL LEVEL(PMAX,PMIN,ALEVEL,DALEV,NLEVS)
      WRITE(0,894) ALEVEL,ALEVEL,DALEV,DALEV,NLEVS
  894 FORMAT ('PHS4'/'LEVS ',2F5.1,'   3.0   0.1  0.2  0.0 0.05  0.0',
     1        '       0     5    2',2F5.2,I5,'     5'/
     2        'SKIP   0.1'/'DROP')
C**** PHASE 5 : DRAW MODEL                                         *****
C
      WRITE(0,884) (XN(ILIN-1),YN(ILIN-1),
     1              XN(ILIN)  ,YN(ILIN)  ,ILIN=2,KNOUT)
  884 FORMAT ('LINE',5X,'1',4F5.1,'   0.0  0.0  0.0      1')
C**** PHASE 5 : DRAW BORDER                                        *****
C
      WRITE(0,893)
  893 FORMAT('LINE',5X,'0  0.0   0.0  0.0 10.5   0.0  0.0  0.0      1'/
     1       'LINE',5X,'0  0.0  10.5 15.0 10.5   0.0  0.0  0.0      1'/
     2       'LINE',5X,'0 15.0  10.5 15.0  0.0   0.0  0.0  0.0      1'/
     3       'LINE',5X,'0 15.0   0.0  0.0  0.0   0.0  0.0  0.0      1')
C**** PHASE 5 : ANNOTATE PLOT                                      *****
C
      XT1=-0.4*XS
      XT2=-0.9*XS
      WRITE(0,892) XT1,XT2,YMA,YMA
  892 FORMAT('SYMB',5X,'1',F5.1,'   0.0  0.0 0.15  1.0',15X,'0'/
     1       'SYMB',5X,'1',2F5.1,'   0.0 0.15  5.0',15X,F5.1)
      IF (Y1.NE.0.0) WRITE(0,881) XT2,Y1,Y1
  881 FORMAT ('SYMB',5X,'1',2F5.1,'   0.0 0.15  5.0',15X,F5.1)
      WRITE(0,891) TITLE
  891 FORMAT('SYMB',5X,'0  0.5 10.0   0.0  0.3 32.0',15X,4A8/
     1       'SYMB',5X,'0 10.5  9.4   0.0  0.2 19.0',15X,
     2       'CONTOURS OF MINIMUM')
C
      IF (ISTR.EQ.2) GO TO 852
C**** HEADINGS FOR STRESS CONTOURS                                 *****
C
      WRITE(0,886)
  886 FORMAT('SYMB',5X,'0 10.7  9.0   0.0  0.2 15.0',15X,
     1       'PRINCIPAL STRESS')
      WRITE(0,885)PMAX,PMIN
  885 FORMAT('SYMB',5X,'0  1.0  9.4   0.0  0.2 30.0',15X,
     1       'MAXIMUM STRESS = ',F7.3,' KBAR.'/
     2       'SYMB',5X,'0  1.0  9.0  0.0  0.2 30.0',15X,
     3       'MINIMUM STRESS = ',F7.3,' KBAR.')
      GO TO 851
C**** HEADINGS FOR STRAIN CONTOURS                                 *****
C
  852 CONTINUE
      WRITE(0,879)
  879 FORMAT('SYMB',5X,'0 10.7  9.0   0.0  0.2 16.0',15X,
     1       'PRINCIPAL STRAIN')
      PMAX=PMAX/1.0D3
      PMIN=PMIN/1.0D3
      WRITE(0,878)PMAX,PMIN
  878 FORMAT('SYMB',5X,'0  1.0  9.4  0.0  0.2 27.0',15X,
     1       'MAXIMUM STRAIN = ',E10.3/
     2       'SYMB',5X,'0  1.0  9.0  0.0  0.2 27.0',15X,
     3       'MINIMUM STRAIN = ',E10.3)
```

```
  851 CONTINUE

      WRITE(0,883)
  883 FORMAT('END ')
      WRITE(0,890)
  890 FORMAT('STOP')

      WRITE(7,889)
  889 FORMAT(1H0,10X,'PRINCIPAL CONTOUR FILE GENERATED')
      WRITE(6,838)
  838 FORMAT('0PRINCIPAL CONTOUR FILE GENERATED')
      CALL TIME(1,1)

      RETURN
      END


***************************************************************************

      SUBROUTINE LEVEL(PMAX,PMIN,ALEVEL,DALEV,NLEVS)
      =================
**** TO CALCULATE CONTOUR LEVELS                                     *****

      REAL*8 PMAX,PMIN

**** IF MINIMUM STRESS IS ZERO, SET ALEVEL TO ZERO                   *****

      IF(PMIN.NE.0.0) GO TO 840
      ALEVEL=0.0
      GO TO 843

**** SET ALEVEL TO PMIN, TO 1 SIGNIFICANT FIGURE                     *****

  840 KAL=0
      IAL=PMIN
  841 IF(IAL.NE.0) GO TO 842
      KAL=KAL+1
      IAL=PMIN*(10.0**KAL)
      GO TO 841
  842 CONTINUE
      ALEVEL=FLOAT(IAL)*10.0**(-KAL)

**** FIND CONTOUR INTERVAL, DALEV, TO 1 SIG. FIG.                    *****

  843 DALEV=(PMAX-ALEVEL)/20.0
      KDA=0
      IDA=DALEV
  844 IF(IDA.NE.0) GO TO 845
      KDA=KDA+1
      IDA=DALEV*(10.0**KDA)
      GO TO 844
  845 CONTINUE
      DALEV=FLOAT(IDA)*10.0**(-KDA)

**** CONTOUR INTERVAL CANNOT BE LESS THAN 0.1, OR IT WILL            *****
****    BE WRITTEN AS 0.00 TO CONTOUR FILE (PHASE 4)                 *****

      IF (DALEV.LT.0.01) DALEV=0.01

**** SET NO. OF CONTOURS, NLEVS, TO INCLUDE ALL STRESS VALUES        *****

      NLEVS=22
  846 IF((ALEVEL-DALEV).LE.PMIN) GO TO 847
      NLEVS=NLEVS+1
      ALEVEL=ALEVEL-DALEV
      GO TO 846
  847 CONTINUE
  848 IF((ALEVEL+FLOAT(NLEVS)*DALEV).GE.PMAX) GO TO 849
      NLEVS=NLEVS+1
      GO TO 848
  849 CONTINUE

      RETURN
      END
```

```
******************************************************************************

      SUBROUTINE OUTLIN
      =================
****  TO DRAW THE OUTLINE OF A BODY OF IRREGULAR SHAPE                  *****
****      FOR USE WITH STRESS VECTOR PLOT                               *****

      IMPLICIT REAL*8 (A-H,O-W)
      COMMON /WK/ XMAX,XMIN,YMAX,YMIN,XSC,YSC,XSP,YSP,
     1            XMAP1,XMAP2,YMAP1,YMAP2,SIGN,NOUT(51),KNOUT,COM9(5256)
      COMMON /IN/  COM10(600),X(300),Y(300),ISET

      CALL PSPACE(0.0,XSP,0.0,YSP)
      CALL MAP(XMAP1,XMAP2,YMAP1,YMAP2)
****  DRAW OUTLINE (IF NOUT HAS BEEN GIVEN)                             *****

      IF (NOUT(1).LE.0) GO TO 705
      CALL POSITN (X(NOUT(1)),Y(NOUT(1)))
      DO 704 JOUT=2,KNOUT
      CALL JOIN(X(NOUT(JOUT)),Y(NOUT(JOUT)))
  704 CONTINUE
  705 CONTINUE

      RETURN
      END


******************************************************************************


      SUBROUTINE VECPLT
      =================
****  TO PLOT VECTORS OF PRINCIPAL STRESSES OR STRAINS                  *****

      IMPLICIT REAL*8 (A-H,O-W)
      COMMON /NOD/ XCOM1(600),COM1(1200),G,NNOD,NNOD2
      COMMON /EL/   NCOM2(500),NODEL(3,500),NEL
      COMMON /ST/   PRINC(4,500),STMAX,NCOM7(1001),ISTP
      COMMON /WK/   XMAX,XMIN,YMAX,YMIN,XSC,YSC,XSP,YSP,
     1              XMAP1,XMAP2,YMAP1,YMAP2,SIGN,COM9(5232)
      COMMON /IN/   COM10(600),X(300),Y(300),ISET
      COMMON /MIS/  PI,TITLE(4),ZUF(4),IDATE(3),MOHO

      IF (STMAX.NE.0.0) GO TO 715
      WRITE(6,797)
  797 FORMAT('0** ERROR : STMAX=0.0 - NO VECTOR PLOT PRODUCED')
      RETURN

  715 CALL CSPACE(0.0,XSP,0.0,1.0)
      CALL PSPACE(0.0,XSP,0.0,1.0)
      CALL MAP(0.0,1.0,0.0,1.0)
      CALL BORDER
      CALL PSPACE(0.0,XSP,0.0,YSP)
      CALL MAP(XMAP1,XMAP2,YMAP1,YMAP2)
****  DRAW A BOX ROUND THE MODEL                                        *****

      CALL BOX(0.0,XMAX,0.0,YMAX)
****  DRAW THE MOHO, UNLESS MOHO=0                                      *****

      IF(MOHO.LE.0) GO TO 712
      CALL POSITN(X(1),Y(MOHO))
      CALL JOIN(XMAX,Y(MOHO))
  712 CONTINUE
****  SCALE VECTORS EQUALLY IN X AND Y DIRECTIONS                       *****

      XVECS=ABS(XMAP2-XMAP1)/10.0/XSP
      YVECS=ABS(YMAP2-YMAP1)/10.0/YSP
```

```
**** PLOT VECTORS                                                        *****

     DO 710 IPLT=1,NEL
     XCEN=(X(NODEL(1,IPLT))+X(NODEL(2,IPLT))+X(NODEL(3,IPLT)))/3.0
     YCEN=(Y(NODEL(1,IPLT))+Y(NODEL(2,IPLT))+Y(NODEL(3,IPLT)))/3.0
     KPLT=1
**** ADJUST ANGLES FOR PLOTTING, SO THAT ANGLES OF STRESS                *****
**** VECTORS CAN BE COMPARED DIRECTLY WITH ANGLES ON MODEL               *****

     IF (DABS(PRINC(4,IPLT)-90.0).LT.1.0E-7) GO TO 713

     TTHETA=DTAN(PRINC(4,IPLT)*PI/180.0) * XVECS/YVECS
     CTHETA=1.0/DSQRT(1.0+TTHETA*TTHETA)
     STHETA=TTHETA*CTHETA
     GO TO 714

 713 CTHETA=0.0
     STHETA=1.0
 714 CONTINUE

     XPLT=XCEN+(PRINC(1,IPLT)*CTHETA/STMAX*XVECS)
     YPLT=YCEN+(PRINC(1,IPLT)*STHETA/STMAX*YVECS)
 711 CALL POSITN(XPLT,YPLT)
     XPLT=2.0*XCEN-XPLT
     YPLT=2.0*YCEN-YPLT

**** IF THE STRESS IS TENSIONAL THE VECTOR IS A BROKEN LINE              *****

     IF (PRINC(KPLT,IPLT).GT.0.0) CALL BROKEN(5,5,5,5)
     CALL JOIN(XPLT,YPLT)
     CALL FULL
     IF (KPLT.EQ.2) GO TO 710

**** ADJUST ANGLE OF PRINC(2)

     IF (CTHETA.EQ.0.0) GO TO 718
     TTHETA=1.0/DTAN(PRINC(4,IPLT)*PI/180.0) * XVECS/YVECS
     CTHETA=1.0/DSQRT(1.0+TTHETA*TTHETA)
     STHETA=TTHETA*CTHETA
 718 XPLT=XCEN-(PRINC(2,IPLT)*CTHETA/STMAX*XVECS)
     YPLT=YCEN+(PRINC(2,IPLT)*STHETA/STMAX*YVECS)
     KPLT=KPLT+1
     GO TO 711
 710 CONTINUE

**** ANNOTATE PLOT                                                       *****

     CALL CTRMAG(15)
     IPLACE=(XSP*77.0)-25
     CALL PLACE(IPLACE,6)
     CALL TYPECS('(BROKEN LINES TENSIONAL)',24)
     CALL LINEFD(-2)
     CALL SPACE(-19)
     IF (ISTR.EQ.2) GO TO 716

**** HEADINGS FOR STRESS VECTORS                                         *****

     CALL TYPECS('STRESS VECTORS',14)
     CALL PLACE(7,6)
     CALL TYPECS('MAXIMUM STRESS = ',17)
     ST=STMAX/1.0D6
     CALL TYPENF(ST,1)
     CALL TYPECS(' MPA.',5)

     XLABEL=XMAX - XVECS*3.0
     YLABEL=YMAX - YMAP2*0.7
     CALL POSITN(XLABEL,YLABEL)
     XLABEL=XLABEL + 2.0E8/STMAX*XVECS
     CALL JOIN(XLABEL,YLABEL)
     CALL PLOTCS(XLABEL,YLABEL,'  100 MPA',9)
     GO TO 717

**** HEADINGS FOR STRAIN VECTORS                                         *****
```

```
716 CALL TYPECS ('STRAIN VECTORS',14)
    CALL PLACE (7,6)
    CALL TYPECS ('MAXIMUM STRAIN = ',17)
    CALL TYPENE (STMAX,3)

    XLABEL=XMAX - XVECS*4.0
    YLABEL=YMAX - YMAP2*0.7
    CALL POSITN(XLABEL,YLABEL)
    XLABEL=XLABEL + 0.02/STMAX*XVECS
    CALL JOIN(XLABEL,YLABEL)
    CALL PLOTCS(XLABEL,YLABEL,'  10 MILLISTRAINS',17)
717 CONTINUE
```

**** WRITE TITLE AND LABEL AXES   *****

```
    CALL LABEL

    WRITE(7,798)
798 FORMAT(1H0,10X,'VECTOR PLOT PRODUCED')
    WRITE(6,799)
799 FORMAT('0VECTOR PLOT PRODUCED')
    CALL TIME(1,1)

    RETURN
    END
```

****

```
    SUBROUTINE LABEL
    ================
```
**** TO WRITE TITLE AND LABEL AXES ON PLOTS   *****

```
    IMPLICIT REAL*8 (A-H,O-W)
    COMMON /WK/   XMAX,XMIN,YMAX,YMIN,XSC,YSC,XSP,YSP,
   1              XMAP1,XMAP2,YMAP1,YMAP2,SIGN,COM9(5292)
    COMMON /IN/   COM10(600),XCOM10(300),Y(300),ISET
    COMMON /MIS/  PI,TITLE(4),ZUF(4),IDATE(3),MOHO
```
**** WRITE OUT TITLE   *****

```
    CALL CTRMAG(30)
    CALL PLACE(4,2)
    CALL ITALIC(1)
    CALL TYPECS(TITLE,32)
    CALL ITALIC(0)
```
**** LABEL Y-AXIS   *****

```
    CALL CTRMAG(15)
    XLABEL=-0.04*XSC
    YLABEL=(YMAX+YMIN)*0.6
    CALL CTRORI(1.0)
    CALL PLOTCS(XLABEL,YLABEL,'Y / KILOMETRES',14)
    CALL CTRORI(0.0)
    IY=YMIN/1.0E3
    XLABEL=-0.03*XSC
    YLABEL=IY*1.0E3
    IF (IY.NE.0) CALL PLOTNI(XLABEL,YLABEL,IY)
    CALL PLOTNI(XLABEL,0.0,0)
    IY=YMAX/1.0E3
    YLABEL=IY*1.0E3
    CALL PLOTNI(XLABEL,YLABEL,IY)
    IF (MOHO.LE.0) GO TO 714
    XLABEL=-0.14*XSC
    CALL PLOTCS(XLABEL,Y(MOHO),'MOHO',4)
714 CONTINUE
```
**** LABEL X-AXIS   *****

```
    YLABEL=SIGN*0.15*YSC
    XLABEL=XMAX*0.4
    CALL PLOTCS(XLABEL,YLABEL,'X / KILOMETRES',14)
```

```
      XLABEL=0.02*XSC
      CALL PLOTNI(XLABEL,YLABEL,0)
      IX=XMAX/1.0E3
      XLABEL=IX*1.0E3+XLABEL
      CALL PLOTNI(XLABEL,YLABEL,IX)

      RETURN
      END
```

****

```
      SUBROUTINE SURF
      ===============
```
**** TO PLOT THE SURFACE DEFLECTION OF A MODEL   *****

```
      IMPLICIT REAL*8 (A-H,O-W)
      COMMON /NOD/ XCOM1(600),DISP(600),COM1(601),NCOM1(2)
      COMMON /WK/  XMAX,XMIN,YMAX,YMIN,XSC,YSC,XSP,YSP,
     1             XMAP1,XMAP2,YMAP1,YMAP2,SIGN,NOUT(51),KNOUT,
     2             XTOP(30),YTOP(30),XD(30),YD(30),XDO(30),YDO(30),
     3             NODTOP(30),COM9(5151)
      COMMON /IN/  COM10(600),X(300),Y(300),ISET
      COMMON /MIS/ PI,TITLE(4),ZCOM3(9)
```

**** TO FIND THE NODES ON THE UPPER SURFACE,   *****
****   ASSUMING THAT 'NOUT' HAS BEEN GIVEN,   *****
****   NUMBERING ANTI-CLOCKWISE FROM THE TOP LEFT-HAND CORNER   *****

**** THE FIRST NODE   *****

```
      NT=NOUT(KNOUT)
      NODTOP(1)=NT
      XTOP(1)=X(NT)/1.0E3
      YTOP(1)=Y(NT)
      XDO(1)=XTOP(1) + DISP(2*NT-1)/1.0E3
      YDO(1)=YTOP(1) + DISP(2*NT)
      XD(1)=XTOP(1) + 5.0 * DISP(2*NT-1)/1.0E3
      YD(1)=YTOP(1) + 5.0 * DISP(2*NT)
      XDMAX=AMAX1(XTOP(1),XD(1))
      YDMAX=AMAX1(YTOP(1),YD(1))
      YDMIN=AMIN1(YTOP(1),YD(1))
      KTOP=1
      MULTI=0
```

**** THE REMAINING SURFACE NODES   *****

```
      DO 730 ITOP=2,KNOUT
      NT=NOUT(KNOUT+1-ITOP)
      XTOP(ITOP)=X(NT)/1.0E3
      IF(XTOP(ITOP).LE.XTOP(ITOP-1)) GO TO 731
      IF((XTOP(ITOP)-XTOP(ITOP-1)).LE.1.0E-2) GO TO 731
      NODTOP(ITOP)=NT
      YTOP(ITOP)=Y(NT)
      XDO(ITOP)=XTOP(ITOP) + DISP(2*NT-1)/1.0E3
      YDO(ITOP)=YTOP(ITOP) + DISP(2*NT)
      XD(ITOP)=XTOP(ITOP) + 5.0 * DISP(2*NT-1)/1.0E3
      YD(ITOP)=YTOP(ITOP) + 5.0 * DISP(2*NT)
      XDMAX=AMAX1(XDMAX,XTOP(ITOP),XD(ITOP))
      YDMAX=AMAX1(YDMAX,YTOP(ITOP),YD(ITOP))
      YDMIN=AMIN1(YDMIN,YTOP(ITOP),YD(ITOP))
```

**** TEST IF THE DEFORMED SURFACE IS MULTI-VALUED   *****

```
      IF (XD(ITOP).LE.XD(ITOP-1)) MULTI=1

      KTOP=ITOP
  730 CONTINUE

  731 IF (KTOP.GT.2) GO TO 732
      WRITE (6,739) KTOP
  739 FORMAT('0** ERROR: THE NUMBER OF TOP SURFACE NODES'/
     1         11X,'IS TOO SMALL (KTOP=',I3,')'/
```

```
      2           11X,'NO PLOT OF SURFACE DRAWN')
        RETURN
  732 CONTINUE

**** SET UP PLOT LIMITS                                                    *****

      XS=XDMAX*1.0E3/XSC+0.4
      CALL CSPACE(0.0,XS,0.0,1.0)
      CALL PSPACE(0.1,XS,0.0,1.0)
      CALL MAP(0.0,1.0,0.0,1.0)
      CALL BORDER
      CALL PSPACE(0.1,XS,0.1,0.9)

**** YDMAX REPRESENTS THE GREATEST DEPTH, IRRESPECTIVE OF SIGN             *****
****    (IF SIGN IS +VE, Y IS +VE UPWARDS)                                 *****

      IF (SIGN.LT.0.0) GO TO 733
      YDM=YDMAX
      YDMAX=YDMIN
      YDMIN=YDM
  733 XM1=XMAP1/1.0E3
      XM2=XDMAX-XM1
      CALL MAP(XM1,XM2,YDMAX,YDMIN)

**** DRAW AXES                                                             *****

      CALL CTRMAG(10)
      CALL AXES

**** LABEL X-AXIS                                                          *****

      CALL CTRMAG(15)
      IPLACE=XS*35.0
      IF (SIGN.GT.0.0.AND.YDMIN.LT.0.0) GO TO 735
      IF (SIGN.LT.0.0.AND.YDMIN.GT.0.0) GO TO 736
      JPLACE=36.0*YDMIN/(YDMIN-YDMAX) + 4.0
      GO TO 737
  736 JPLACE=45
  737 CALL PLACE(IPLACE,JPLACE)
      CALL TYPECS('X / KILOMETRES',14)

**** LABEL Y-AXIS                                                          *****

      CALL PLACE(12,25)
      CALL CTRORI(1.0)
      CALL TYPECS('Y / METRES',10)
      CALL CTRORI(0.0)

**** DRAW INITIAL SURFACE                                                  *****

      CALL PTPLOT(XTOP,YTOP,1,KTOP,-3)
      CALL CTRSET(2)
      CALL PTPLOT(XTOP,YTOP,1,KTOP,62)

**** DRAW DEFORMED SURFACE (XD0,YD0),                                      *****
**** AND EXAGGERATED DEFORMATION (XD,YD)                                   *****
**** IF THEY ARE MULTI-VALUED, NMCURV MUST BE USED (NOT NSCURV)            *****

      CALL PTPLOT(XD0,YD0,1,KTOP,25)
      CALL PTPLOT(XD,YD,1,KTOP,61)
      IF (MULTI.EQ.1) GO TO 734
      CALL NSCURV(XD0,YD0,1,KTOP)
      CALL NSCURV(XD,YD,1,KTOP)
      GO TO 735
  734 CALL NMCURV(XD0,YD0,1,KTOP)
      CALL NMCURV(XD,YD,1,KTOP)
  735 CONTINUE

**** ANNOTATE PLOT                                                         *****

      CALL CTRSET(1)
      CALL CTRMAG(30)
      CALL PLACE(5,2)
      CALL ITALIC(1)
```

```
      CALL TYPECS(TITLE,32)
      CALL ITALIC(0)

      CALL CTRMAG(15)
      IPLACE=(XS*77.0)-25
      CALL PLACE(IPLACE,4)
      CALL TYPECS('SURFACE FLEXURE',15)
C
      CALL LINEFD(3)
      CALL SPACE(-15)
      CALL CTRSET(2)
      CALL TYPENC(62)
      CALL TYPECS('   INITIAL SURFACE',17)
C
      CALL LINEFD(2)
      CALL SPACE(-18)
      CALL TYPENC(25)
      CALL TYPECS('   DEFORMED SURFACE',18)
C
      CALL LINEFD(2)
      CALL SPACE(-19)
      CALL TYPENC(61)
      CALL TYPECS('   EXAGGERATED DEFORMATION',25)
      CALL LINEFD(2)
      CALL SPACE(-20)
      CALL TYPECS('(DISPLACEMENTS X5)',18)
C
      CALL CTRSET(1)
C
      WRITE(7,738)
  738 FORMAT(1H0,10X,'PLOT OF SURFACE FLEXURE PRODUCED')
      WRITE (6,729)
  729 FORMAT('0PLOT OF SURFACE FLEXURE PRODUCED')
      CALL TIME(1,1)
C
      RETURN
      END


****************************************************************************

      SUBROUTINE DISTRT
      =================
****  TO SHOW THE DISTORTION OF THE BODY                                 *****

      IMPLICIT REAL*8 (A-H,O-W)
      COMMON /NOD/ XCOM1(600),DISP(600),FORCE(600),G,NNOD,NNOD2
      COMMON /WK/   XMAX,XMIN,YMAX,YMIN,XSC,YSC,XSP,YSP,XMAP1,
     1              XMAP2,YMAP1,YMAP2,SIGN,NOUT(51),KNOUT,COM9(5256)
      COMMON /IN/   COM10(600),X(300),Y(300),ISET
C
      CALL CSPACE(0.0,XSP,0.0,1.0)
      CALL PSPACE(0.0,XSP,0.0,1.0)
      CALL MAP(0.0,1.0,0.0,1.0)
      CALL BORDER
      CALL PSPACE(0.0,XSP,0.0,YSP)
      CALL MAP(XMAP1,XMAP2,YMAP1,YMAP2)

****  DRAW A BOX ROUND THE MODEL                                         *****

      CALL BLUPEN
      CALL BOX(0.0,XMAX,0.0,YMAX)
      CALL OUTLIN

****  CALCULATE AND DRAW DISTORTED SHAPE                                 *****

      DO 720 JDIS=2,KNOUT
      X(NOUT(JDIS))=X(NOUT(JDIS))+DISP(2*NOUT(JDIS)-1)
      Y(NOUT(JDIS))=Y(NOUT(JDIS))+DISP(2*NOUT(JDIS))
  720 CONTINUE
      CALL REDPEN
      CALL OUTLIN

      CALL BLKPEN
```

```
***** ANNOTATE PLOT                                                      *****

      CALL CTRMAG(15)
      IPLACE=(XSP*77.0)-20
      CALL PLACE(IPLACE,4)
      CALL BLUPEN
      CALL TYPECS('DISPLACEMENTS',13)

***** WRITE TITLE AND LABEL AXES                                         *****

      CALL LABEL

      RETURN
      END


***************************************************************************


      SUBROUTINE GROPLT
      =================
***** TO PLOT GRID FOR REFERENCE WITH ELEMENT NUMBERS                    *****

      IMPLICIT REAL*8 (A-H,O-W)
      COMMON /NOD/ XCOM1(600),COM1(1200),G,NNOD,NNOD2
      COMMON /EL/  NCOM2(500),NODEL(3,500),NEL
      COMMON /WK/  XMAX,XMIN,YMAX,YMIN,XSC,YSC,XSP,YSP,
     1             XMAP1,XMAP2,YMAP1,YMAP2,SIGN,COM9(5232)
      COMMON /IN/  COM10(600),X(300),Y(300),ISET

***** DRAW A BORDER AND A BOX ROUND THE MODEL                            *****

      CALL CSPACE(0.0,XSP,0.0,1.0)
      CALL PSPACE(0.0,XSP,0.0,1.0)
      CALL MAP(0.0,1.0,0.0,1.0)
      CALL BORDER
      CALL PSPACE(0.0,XSP,0.0,YSP)
      CALL MAP(XMAP1,XMAP2,YMAP1,YMAP2)
      CALL BOX(0.0,XMAX,0.0,YMAX)

***** DRAW ELEMENTS                                                      *****

      DO 750 IGRID=1,NEL
      IF (IGRID.EQ.1) GO TO 752
      IF (NODEL(1,IGRID).EQ.NODEL(1,(IGRID-1))) GO TO 751
  752 CALL POSITN(X(NODEL(1,IGRID)),Y(NODEL(1,IGRID)))
  751 CALL JOIN(X(NODEL(2,IGRID)),Y(NODEL(2,IGRID)))
      CALL JOIN(X(NODEL(3,IGRID)),Y(NODEL(3,IGRID)))
      CALL JOIN(X(NODEL(1,IGRID)),Y(NODEL(1,IGRID)))
  750 CONTINUE

***** WRITE ELEMENT NUMBERS                                              *****

      CALL CTRMAG(8)
      DO 760 INUM=1,NEL
      XCEN=((X(NODEL(1,INUM))+X(NODEL(2,INUM))+X(NODEL(3,INUM)))
     1      /3.0)+(XSC/100.0)
      YCEN=(Y(NODEL(1,INUM))+Y(NODEL(2,INUM))+Y(NODEL(3,INUM)))/3.0
      CALL PLOTNI(XCEN,YCEN,INUM)
  760 CONTINUE

***** ANNOTATE PLOT                                                      *****

      CALL CTRMAG(15)
      IPLACE=(XSP*77.0)-20
      CALL PLACE(IPLACE,4)
      CALL TYPECS('ELEMENT MESH',12)
      CALL LINEFD(2)
      CALL SPACE(-17)
      CALL TYPECS('(WITH ELEMENT NUMBERS)',22)

***** WRITE TITLE AND LABEL AXES                                         *****

      CALL LABEL
```

```
      WRITE(7,795)
  795 FORMAT(1H0,10X,'PLOT OF GRID PRODUCED')
      WRITE(6,794)
  794 FORMAT('0PLOT OF GRID PRODUCED')
      CALL TIME(1,1)

      RETURN
      END


**************************************************************************


      SUBROUTINE PROPS
      ================
C**** TO PLOT GRID FOR REFERENCE WITH MATERIAL PROPERTIES                *****

      IMPLICIT REAL*8 (A-H,O-W)
      COMMON /NOD/ XCOM1(600),COM1(1200),G,NNOD,NNOD2
      COMMON /EL/  ITYP(500),NODEL(3,500),NEL
      COMMON /WK/  XMAX,XMIN,YMAX,YMIN,XSC,YSC,XSP,YSP,
     1             XMAP1,XMAP2,YMAP1,YMAP2,SIGN,COM3(5282)
      COMMON /IN/  COM10(600),X(300),Y(300),ISE*
C**** DRAW A BORDER AND A BOX ROUND THE MODEL                             *****

      CALL CSPACE(0.0,XSP,0.0,1.0)
      CALL PSPACE(0.0,XSP,0.0,1.0)
      CALL MAP(0.0,1.0,0.0,1.0)
      CALL BORDER
      CALL PSPACE(0.0,XSP,0.0,YSP)
      CALL MAP(XMAP1,XMAP2,YMAP1,YMAP2)
      CALL BOX(0.0,XMAX,0.0,YMAX)
C**** DRAW ELEMENTS                                                       *****

      DO 750 IGRID=1,NEL
      IF (IGRID.EQ.1) GO TO 752
      IF (NODEL(1,IGRID).EQ.NODEL(1,(IGRID-1))) GO TO 751
  752 CALL POSITN(X(NODEL(1,IGRID)),Y(NODEL(1,IGRID)))
  751 CALL JOIN(X(NODEL(2,IGRID)),Y(NODEL(2,IGRID)))
      CALL JOIN(X(NODEL(3,IGRID)),Y(NODEL(3,IGRID)))
      CALL JOIN(X(NODEL(1,IGRID)),Y(NODEL(1,IGRID)))
  750 CONTINUE
C**** WRITE MATERIAL NUMBERS                                              *****

      CALL CTRMAG(10)
      DO 760 INUM=1,NEL
      XCEN=((X(NODEL(1,INUM))+X(NODEL(2,INUM))+X(NODEL(3,INUM)))
     1      /3.0)+(XSC/100.0)
      YCEN=(Y(NODEL(1,INUM))+Y(NODEL(2,INUM))+Y(NODEL(3,INUM)))/3.0
      CALL PLOTNI(XCEN,YCEN,ITYP(INUM))
  760 CONTINUE
C**** ANNOTATE PLOT                                                       *****

      CALL CTRMAG(15)
      IPLACE=(XSP*77.0)-20
      CALL PLACE(IPLACE,4)
      CALL TYPECS('ELEMENT MESH',12)
      CALL LINEFD(2)
      CALL SPACE(-17)
      CALL TYPECS('(WITH MATERIAL NUMBERS)',23)
C**** WRITE TITLE AND LABEL AXES                                          *****

      CALL LABEL

      WRITE(7,795)
  795 FORMAT(1H0,10X,'DIAGRAM OF PROPERTIES PRODUCED')
      WRITE(6,794)
  794 FORMAT('0DIAGRAM OF PROPERTIES PRODUCED')
      CALL TIME(1,1)
```

```
      RETURN
      END


***************************************************************************

      SUBROUTINE MESH(IMESH,NNODB,NELB,WIDB,NSID,NNODA,NELA)
      =======================================================          *****
***** TO GENERATE MESH FROM A BASIC BLOCK OF WIDTH WIDB                 *****

      IMPLICIT REAL*8 (A-H,O-W)
      COMMON /NOD/ X(300),Y(300),LEFT(6),LRIGHT(6),
     1             NODEND(8),COM1(1191),NNOD,NNOD2
      COMMON /EL/ ITYP(500),NODEL(3,500),NEL


***** NELA,NNODA ARE REPEAT VALUES FOR ELEMENT AND NODE NUMBERS         *****
***** WHILE NELB,NNODB ARE THE NUMBERS OF VALUES INPUT                  *****

      IF (NNODA.EQ.0) NNODA=NNODB
      IF (NELA.EQ.0) NELA=NELB
      WIDB=WIDB*1.003
      IF (NSID.EQ.0) GO TO 102

***** IF NSID IS NON-ZERO THE END MESH ELEMENTS ARE DIFFERENT           *****
***** FROM THOSE IN THE MAIN PART OF THE BODY                           *****
***** FIND LENGTH OF MODEL                                              *****

      NBLOCK=NNOD/NNODA
      BLOCKS=NBLOCK
      XEND=WIDB*BLOCKS
      IMNOD=NNODB+1

***** ASSIGN NODAL CO-ORDS TO MAIN PART OF BODY                         *****

      DO 110 IMNOD=IMNOD,NNOD
      X(IMNOD)=X(IMNOD-NNODA)+WIDB
      IF (X(IMNOD).NE.XEND) GO TO 111
      IEND=IMNOD
      GO TO 112
  111 Y(IMNOD)=Y(IMNOD-NNODA)
  110 CONTINUE
      WRITE(6,99)
   99 FORMAT('0** ERROR : X(NNOD).NE.XEND - RUN ABORTED')
      STOP

***** ASSIGN CO-ORDS OF END NODES, SETTING THE RIGHT END Y CO-ORDS *****
***** EQUAL TO THOSE OF THE LEFT END                              *****
***** STORE NUMBERS OF NODES IN THE LAST WIDB OF MODEL IN NODEND   *****

  112 DO 113 IENDN=IEND,NNOD
      X(IENDN)=XEND
      Y(IENDN)=Y(IENDN-IEND+1)
      NODECT=IENDN-IEND+1
      NODEND(NODECT)=IENDN
  113 CONTINUE
      KEND=IEND
      KDIF=1
  114 KEND=KEND-1
      IF (X(KEND).NE.X(KEND-1)) GO TO 115
      KDIF=KDIF+1
      GO TO 114
  115 KCT=KDIF
  116 NODECT=NODECT+1
      IF ((XEND-X(KEND)).GE.WIDB) GO TO 117
      NODEND(NODECT)=KEND
      KEND=KEND+1
      KCT=KCT-1
      IF (KCT.GT.0) GO TO 116
      KEND=KEND-KDIF
      KDIF=1
      GO TO 114
```

```
  117 KCOUNT=0
      KLEFT=NELA+2
```
```
      DO 118 ILEFT=1,KLEFT
      MARK=0
      DO 119 JLEFT=1,3
      IF(NODEL(JLEFT,ILEFT).LE.NSID) MARK=MARK+1
      IF(MARK.NE.2) GO TO 119
      KCOUNT=KCOUNT+1
      LEFT(KCOUNT)=ILEFT
  119 CONTINUE
  118 CONTINUE
      KCOUNT=KCOUNT+1
      DO 125 ILO=KCOUNT,6
  125 LEFT(ILO)=0
      IMELO=NELA+2
      KELA=NELA
      KCOUNT=0
      NEDGE=0
      KEDGE=0
```
***** FILL IN MAIN PART OF GRID WITH ELEMENTS   *****
```
      DO 124 IMEL=IMELO,NEL
      IF ((IMEL-KELA).GT.NELB) GO TO 121
      DO 120 KMEL=1,6
      IF ((IMEL-KELA).NE.LEFT(KMEL)) GO TO 120
      KELA=KELA-1
      GO TO 124
  120 CONTINUE
  121 MARK=0
      DO 122 JMEL=1,3
      N=NODEL(JMEL,(IMEL-KELA))
      IF (N.LT.NSID) GO TO 124
      NODEL(JMEL,IMEL)=N+NNODA
      IF (NODEL(JMEL,IMEL).GE.IEND) MARK=MARK+1
      IF (MARK.NE.2) GO TO 122
```
***** IF IMESH=1, ALL HORIZONTAL LINES CONTINUE TO EDGE   *****
```
      IF (IMESH.EQ.1) GO TO 128
      DO 127 KMEL=1,3
      IF (NODEL(KMEL,IMEL).LT.(IEND+KDIF)) GO TO 127
      KELA=KELA-1
      GO TO 129
  127 CONTINUE
  128 DO 130 LMEL=1,JMEL
      IF (NODEL(LMEL,IMEL).LT.(IEND+KDIF)) GO TO 130
      IF (NODEL(LMEL,IMEL).EQ.NEDGE) GO TO 130
      NEDGE=NODEL(LMEL,IMEL)
      KEDGE=KEDGE+1
  130 CONTINUE
```
***** PUT RIGHT END ELEMENTS INTO LRIGHT   *****
```
  129 KCOUNT=KCOUNT+1
      LRIGHT(KCOUNT)=IMEL
      GO TO 124
  122 CONTINUE
      ITYP(IMEL)=ITYP(IMEL-KELA)
      IF (MARK.NE.1) GO TO 124
      DO 131 MMEL=1,3
      IF (NODEL(MMEL,IMEL).LT.IEND) GO TO 131
      NODEL(MMEL,IMEL)=NODEL(MMEL,IMEL)+KEDGE
  131 CONTINUE
  124 CONTINUE
      IF (KCOUNT.EQ.0) GO TO 126
```
***** ASSIGN TOPOLOGIES AND PROPERTIES TO RIGHT END ELEMENTS   *****
```
      DO 123 IREND=1,KCOUNT
      DO 132 JREND=1,3
  132 NODEL(JREND,LRIGHT(IREND))=NODEND(NODEL(JREND,LEFT(IREND)))
```

```
      ITYP(LRIGHT(IREND))=ITYP(LEFT(IREND))
  123 CONTINUE

      RETURN
  126 WRITE(6,98)
   98 FORMAT('0** ERROR : NSID.NE.0 BUT LRIGHT IS EMPTY'/
     1        ' RUN ABORTED')
      STOP

C**** SEGMENT TO REPEAT A SIMPLE BLOCK TO A GIVEN SIZE, REPEATING   *****
C**** ELEMENTS EVERY NELA. USED IF NSID=0.                          *****

  103 IMELO=NELB+1
      DO 101 IMEL=IMELO,NEL
      ITYP(IMEL)=ITYP(IMEL-NELA)
      DO 100 JMEL=1,3
  100 NODEL(JMEL,IMEL)=NODEL(JMEL,(IMEL-NELA))+NNODA
  101 CONTINUE
      IMNODO=NNODB+1

C**** NODES REPEAT EVERY NNODA, THE X CO-ORD INCREASING BY WIDB     *****

      DO 102 IMNOD=IMNODO,NNOD
      X(IMNOD)=X(IMNOD-NNODA)+WIDB
      Y(IMNOD)=Y(IMNOD-NNODA)
  102 CONTINUE

      RETURN
      END
```

```
**** SETUP : TO FIND ITERATIVELY THE INITIAL                          *****
****          STRESS SYSTEM IN A MODEL                                 *****
****          TO BE INPUT TO FINITE ELEMENT PROGRAM FEVER             *****
****          (CALLING SUBROUTINES FROM FILE PRIMA).                   *****
****                                                                   *****
****               WRITTEN AT DURHAM UNIVERSITY BY JOHN PARK           *****
****                                              1979 - 1980          *****
****                                                                   *****
**** MAIN PROGRAM                                                      *****

      IMPLICIT REAL*8 (A-H,O-W)
      COMMON /NO / X(300),Y(300),DISP(600),FORCE(600),G,NNOD,NNOD2
      COMMON /EL/   NCOM2(2001)
      COMMON /MAT/ COM3(50),NCOM3(11)
      COMMON /FIX/ COM4(300),NCOM4(301)
      COMMON /SO/   COM5(2300),INST
      COMMON /K/    COM6(135000),NCOM6(3)
      COMMON /ST/   COM7(2001),NCOM7(1000)
      COMMON /CR/   COM8(2000),DTIME,TOTIME,KTIME,NTIME
      COMMON /WK/   FLOAD(600),LOAD(300),NLOAD,NCOM9,COM9(4539)
      COMMON /IN/   DISPO(600),XO(300),YO(300),ISET
      COMMON /MIS/ COMO(7),NCOMO(4)

      DIMENSION FO(600)

      CALL TIME(0,1)

**** READ IN NUMBER OF SOLUTION ITERATIONS                             *****

      WRITE (6,2099)
2099 FORMAT ('OENTER NSOL'/' ----')
      READ (5,2098) NSOL
2098 FORMAT(I4)

**** READ AND ECHO INPUT DATA                                          *****

      CALL READ
      CALL ECHO1
      CALL ECHO2

      NTIME=500
      DTIME=2.004

      DO 2020 KSOL=1,NSOL

**** WRITE HEADINGS (THE FIRST SOLUTION IS NUMBERED 0)                 *****

      KKSOL=KSOL-1
      WRITE (6,2097) KKSOL
2097 FORMAT ('OSOLUTION NUMBER',I3)
      WRITE (7,2096) KKSOL
      WRITE (8,2096) KKSOL
2096 FORMAT (1H1/1H0,10X,'SOLUTION NUMBER',I3/
     1               1H+,10X,'_____'/1H0)

**** FORM STIFFNESS MATRIX FOR CURRENT SOLUTION                        *****

      CALL KFORM

**** ON FIRST SOLUTION, INCLUDE BODY FORCES AND STORE FORCE VECTOR*****

      IF (KSOL.NE.1) GO TO 2022

      CALL FBODY
      CALL PORE
      DO 2021 JFO=1,NNOD2
      FO(JFO)=FORCE(JFO)
2021 CONTINUE
      NLOAD=NNOD

2022 CONTINUE

**** APPLY BOUNDARY CONDITIONS                                         *****

      CALL BOUNDS
      CALL ROTOR
```

```
****  SOLVE STIFFNESS EQUATION                                      *****
      CALL SOLVE
      CALL VISEL

****  CALCULATE AND WRITE OUT DIFFERENCES FROM REQUIRED MODEL        *****

      WRITE (7,2095) KSOL
2095  FORMAT (1H0,10X,'DIFFERENCES FROM REQUIRED MODEL AFTER',I3,
     1              ' SOLUTION(S) : X.DIF=X(N)+DISP(N)-X(0)'/
     2          1H0,30X,'NODE',12X,'XDIF : M',14X,'YDIF : M'/1H0)

      DO 2023 JDX=1,NNOD
      XDIF=X(JDX)+DISP(2*JDX-1) - X0(JDX)
      YDIF=Y(JDX)+DISP (2*JDX)  - Y0(JDX)
      WRITE(7,2094)JDX,XDIF,YDIF
2094  FORMAT (31X,I4,2(10X,E16.5))
2023  CONTINUE

****  ON ALL BUT THE FINAL SOLUTION, RESET ARRAYS FOR THE NEXT       *****

      IF (KSOL.EQ.NSOL) GO TO 2011

      DO 2024 IDX=1,NNOD
      JDX=2*IDX-1
      X(IDX)=X0(IDX)-DISP(JDX)
      FORCE(JDX)=F0(JDX)
      FLOAD(JDX)=F0(JDX)
      JDX=JDX+1
      Y(IDX)=Y0(IDX)-DISP(JDX)
      FORCE(JDX)=F0(JDX)
      FLOAD(JDX)=F0(JDX)
      LOAD(IDX)=IDX
2024  CONTINUE
      TOTIME=0.0

      CALL TIME(1.1)
2020  CONTINUE

2011  CONTINUE

****  ASSIGN DISPLACEMENTS TO DISP0, AND WRITE OUT RESULTING         *****
****     MODEL PARAMETERS FOR CONTINUATION                           *****

      ISET=NSOL
      DO 2012 IDISP=1,NNOD2
      DISP0(IDISP)=DISP(IDISP)
2012  CONTINUE
      CALL MORE

      CALL STRESS
      CALL PORE2
      CALL FAIL
      CALL OUTPUT
      CALL PSCALE
      CALL OUTLIN
      CALL VECPLT
      CALL FRAME
      CALL STRAIN
      CALL OUTLIN
      CALL VECPLT
      CALL GREND

      STOP
      END
```

BIBLIOGRAPHY

Anderson, E.M., 1942. The dynamics of faulting and dyke formation with
applications to Britain. Oliver and Boyd, Edinburgh. 191 pp.

Artyushkov, E.V., 1973. Stresses in the lithosphere caused by crustal
thickness inhomogeneities. J. geophys. Res., 78, 7675-7708.

Barazangi, M., Isacks, B., and Oliver, J., 1972. Propagation of seismic
waves through and beneath the lithosphere that descends under the
Tonga island arc. J. geophys. Res., 77, 952-958.

Beck, R.H., and Lehner, P., 1974. Oceans, new frontier in exploration.
Bull. Am. Assoc. Petrol. Geol., 58, 376-395.

Birch, F., 1966. Compressibility; elastic constants. In: Clark, S.P.,(ed.)
Handbook of physical constants, Mem. geol. Soc. Am., 97, 97-173.

Bischke, R.E., 1974. A model of convergent plate margins based on the recent
tectonics of Shikoku, Japan. J. geophys. Res., 79, 4845-4857.

Bott, M.H.P., 1971a. The interior of the Earth. Arnold, London, 316 pp.

Bott, M.H.P., 1971b. Evolution of young continental margins and formation
of shelf basins. Tectonophysics, 11, 319-327.

Bott, M.H.P., and Dean, D.S., 1972. Stress systems at young continental
margins. Nature phys. Sci., 235, 23-25.

Bouma, A.H., and Moore, J.C., 1975. Physical properties of deep-sea
sediments from the Phillipine Sea and Sea of Japan. In: Karig, D.E.,
Ingle, J.C., Jr., et al., Initial Rep. Deep Sea drill. Proj., 31,
535-568.

Boynton, C.H., Westbrook, G.K., Bott, M.H.P., and Long, R.E., 1979. A
seismic refraction investigation of crustal structure beneath the
Lesser Antilles island arc. Geophys. J.R. astron. Soc., 58, 371-393.

Brace, W.F., 1961. Dependence of fracture strength on grain size. Bull.
Miner. Inds. Stn. Penn. Univ., 76, 99-103.

Brace, W.F., 1964. Brittle fracture of rocks. In: Judd, W.R., (ed.),
State of stress in the Earth's crust, Elsevier, New York, 111-174.

Budd, W.F., 1970. The longitudinal stress and strain-rate gradients in ice
masses. J. Glaciol. London, 9, 19-27.

Budd, W.F., 1971. Stress variations with ice-flow over undulations.
J. Glaciol. London, 10, 177-195.

Byerlee, J.D., 1978. Friction of Rocks. Geofis. pura. appl., 116, 615-626.

Caldwell, J.G., Haxby, W.F., Karig, D.E., and Turcotte, D.L., 1976.
On the applicability of a universal elastic trench profile.
Earth planet. Sci. Lett., 31, 239-246.

Cathles, L.M., III, 1975. The viscosity of the Earth's mantle. Princeton
University Press, 386 pp.

Chapple, W.M., 1978. Mechanics of thin-skinned fold-and-thrust belts.
Bull. geol. Soc. Am., 89, 1189-1198.

Cowan, D.S., and Silling, R.M., 1978. A dynamic, scaled model of accretion
at trenches and its implications for the tectonic evolution of
subduction complexes. J. geophys. Res., 83, 5389-5396.

Creager, J.S., Scholl, D.W., et al., 1973. Initial reports of the Deep
Sea Drilling Project, 19, Washington (U.S. Government Printing
Office).

Curray, J.R., Shor, G.G., Jr., Raitt, R.W., and Henry, M., 1977. Seismic
refraction and reflection studies of crustal structure of the
eastern Sunda and western Banda arcs. J. geophys. Res., 82,
2479-2489.

Dean, D.S., 1973. Stress analysis of the lithosphere. Unpublished Ph.D.
thesis, University of Durham, 289 pp.

De Bremaecker, J-C., and Becker, E.B., 1977. Finite element models of
folding. Tectonophysics, 50, 349-367.

Dickinson, W.R., 1973. Widths of modern arc-trench gaps proportional to duration of igneous activity in associated magmatic arcs. J. geophys. Res., 78, 3376-3389.

Dickinson, W.R., and Seely, D.R., 1979. Structure and stratigraphy of fore-arc regions. Bull. Am. Assoc. Petrol. Geol., 63, 2-31.

Digby, P.G., and Murrell, S.A.F., 1976. The deformation of flat ellipsoidal cavities under large confining pressures. Bull. seismol. Soc. Am., 66, 425-432.

Drury, M.J., 1979. Electrical resistivity models of the oceanic crust based on laboratory measurements on basalts and gabbros. Geophys. J.R. astron. Soc., 56, 241-253.

Elliott, D., 1976. The motion of thrust sheets. J. geophys. Res., 81, 949-963.

Fischer, R.L., and Engel, C.G., 1969. Ultramafic and basaltic rocks dredged from the nearshore flank of the Tonga trench. Bull. geol. Soc. Am., 80, 1373-1378.

Gerrard, C.M., 1977. The roles of fabric and stress history. In: Gudehus, G., Finite elements in geomechanics, Wiley, London, 33-120.

Goldsmith, W., Sackman, J.L., and Ewert, C., 1976. Static and dynamic fracture strength of Barre granite. Int. J. rock Mech. Ming Sci., 13, 303-309.

Goodman, R.E., 1976. Methods of geological engineering in discontinuous rocks. West Publishing Co., St. Paul.

Goodman, R.E., Taylor, R.L., and Brekke, T.L., 1968. A model for the mechanics of jointed rock. J. soil Mech. Found. Div. Am. Soc. civil Eng., 94, 637-658.

Grow, J.A., 1973a. Crustal and upper mantle structure of the central Aleutian arc. Bull. geol. Soc. Am., 84, 2169-2192.

Grow, J.A., 1973b. Implications of deep sea drilling sites 186 and 187
on island arc structure. In: Creager, J.S., Scholl, D.W., et al.,
Initial Rep. Deep Sea drill. Proj., 19, 799-801.

Gutenberg, B., 1959. Physics of the Earth's interior. Academic Press,
New York, 240 pp.

Handin, J., 1966. Strength and ductility. In: Clark, S.P., Jr., Handbook
of physical constants, Mem. geol. Soc. Am., 97, 224-289.

Hasegawa, A., Umino, N., and Takagi, A., 1978. Double-planed deep seismic
zone and upper mantle structure in northeastern Japan arc.
Geophys. J.R. astron. Soc., 54, 281-296.

Hasegawa, A., Umino, N., Takagi, A., and Suzuki, Z., 1979. Double-planed deep
seismic zone and anomalous structure in the upper mantle beneath
northeastern Honshu (Japan). Tectonophysics, 57, 1-6.

Heard, H.C., and Raleigh, C.B., 1972. Steady state flow in marble at
500°C to 800°C. Bull. geol. Soc. Am., 83., 935-956.

Hilde, T.W.C., Wageman, J.M., and Hammond, W.T., 1969. The structure of
Tosa Terrace and Nankai Trough off southeastern Japan. Deep Sea
Res., 16, 67-75.

Hinton, E., and Owen, D.R.J., 1977. Finite element programming. Academic
Press, London, 305 pp.

Hopper, M.J., 1973. Harwell Subroutine Library. H.M.S.O.

Housner, G.W., and Vreeland, T., Jr., 1966. The analysis of stress and
deformation. Macmillan. New York, 434 pp.

Hubbert, M.K., and Rubey, W.W., 1959. Role of fluid pressure in mechanics
of overthrust faulting: I. Bull. geol. Soc. Am., 70, 115-166.

Hussong, D.M., Edwards, P.B., Johnson, S.H., Campbell, J.F., and Sutton, G.H.,
1976. Crustal structure of the Peru-Chile trench: 8°-12°S
latitude. In: The geophysics of the Pacific ocean basin and its
margin, Geophys. Monogr. Washington, 19, 71-85.

Hussong, D.M., Uyeda, S., et al., 1978. D.S.D.P. Leg 60 ends in Guam. Geotimes, 23(10), 19-22.

Ingle, J.C., Jr., Karig, D.E., et al., 1973. D.S.D.P. Leg 31 - western Pacific floor. Geotimes, 18(10), 22-25.

Ingle, J.C., Jr., Karig, D.E., et al., 1975. Initial reports of the Deep Sea Drilling Project, 31. Washington (U.S. Government Printing Office).

Isacks, B., and Molnar, P., 1971. Distribution of stresses in the descending lithosphere from a global survey of focal-mechanism solutions of mantle earthquakes. Rev. Geophys., 9, 103-174.

Jaeger, J.C., and Cook, N.G.W., 1976. Fundamentals of rock mechanics. Second edition, Chapman and Hall Science Paperbacks, 585 pp.

Jeffreys, H., 1939. The times of P, S and SKS, and the velocities of P and S. Mon. Not. R. astron. Soc. geophys. Suppl., 4, 498-533.

Julian, B.R., and Anderson, D.L., 1968. Travel times, apparent velocities and amplitude of body waves. Bull. seismol. Soc. Am., 58, 339-366.

Kaplan, W., 1962. Advanced calculus. Addison-Wesley, London. 679 pp.

Karig, D.E., 1974. Evolution of arc systems in the western Pacific. Ann. Rev. Earth planet. Sci., 2, 51-75.

Karig, D.E., 1977. Growth patterns on the upper trench slope. In: Talwani, M., and Pitman, W.C., III,(eds.) Island arcs, deep sea trenches and back arc basins, A.G.U. Washington, 175-185.

Karig, D.E., Caldwell, J.G., and Parmentier, E.M., 1976. Effects of accretion on the geometry of the descending lithosphere. J. geophys. Res., 81, 6281-6291.

Karig, D.E., Cardwell, R.K., Moore, G.F., and Moore, D.G., 1978. Late Cenozoic subduction and continental margin truncation along the northern Middle America trench. Bull. geol. Soc. Am., 89, 265-276.

Karig, D.E., Lawrance, M.B., Moore, G.F., and Curray, J.R., 1980. Structural framework of the fore-arc basin, N.W. Sumatra. <u>J. geol. Soc. London</u>, <u>137</u>, 77-91.

Karig, D.E., and Sharman, G.F., III, 1975. Subduction and accretion in trenches. <u>Bull. geol. Soc. Am.</u>, <u>86</u>, 377-389.

Kieckhefer, R.M., Shor, G.G., Jr., Curray, J.R., Sugiart, W., and Hehuwat, F., 1980. Seismic refraction studies of the Sunda trench and forearc basin. <u>J. geophys. Res.</u>, <u>85</u>, 863-889.

Kulm, L.D., von Heune, R., et al., 1973. <u>Initial reports of the Deep Sea Drilling Project</u>, <u>18</u>. Washington (U.S. Government Printing Office).

Kusznir, N.J., 1976. <u>Theoretical studies of the geodynamics of accretion boundaries in plate tectonics</u>. Unpublished Ph. D. thesis, University of Durham, 145 pp.

Kusznir, N.J., and Bott, M.H.P., 1977. Stress concentration in the upper lithosphere caused by underlying visco-elastic creep. <u>Tectonophysics</u>, <u>43</u>, 247-256.

Lee, H.J., 1973. Measurements and estimates of engineering and other physical properties, Leg 19. In: Creager, J.S., Scholl, D.W., et al., <u>Initial Rep. Deep Sea drill. Proj.</u>, <u>19</u>, 701-720.

Lee, E.H., Radok, T.R.M., and Woodward, W.B., 1959. Stress analysis for linear visco-elastic materials. <u>Trans. Soc. Rheol.</u>, <u>3</u>, 41-59.

Leggett, J.K., McKerrow, W.S., and Eales, M.H., 1979. The Southern Uplands of Scotland: a lower Palaeozoic accretionary prism. <u>J. geol. Soc. London</u>, <u>136</u>, 755-770.

Ludwig, W.J., Nafe, J.E., and Drake, C.L., 1970. Seismic refraction. In: Maxwell, A.E., (ed.) <u>The sea</u>, <u>4</u>, Wiley, New York, 53-84.

Malvern, L.E., 1969. <u>Introduction to the mechanics of a continuous medium</u>. Prentice-Hall, New Jersey. 713 pp.

Matsuda, T., and Uyeda, S., 1971. On the Pacific-type orogeny and its model - extension of the paired belts concept and possible origin of marginal seas. Tectonophysics, 11, 5-27.

McClintock, F.A., and Walsh, J.B., 1962. Friction on Griffith cracks under pressure. Proc. U.S. natl. Congr. appl. Mech., 4, 1015-1021.

McKenzie, D.M., 1977. The initiation of trenches. In: Talwani, M., and Pitman, W.C., III,(eds.) Island arcs, deep sea trenches and back arc basins. A.G.U. Washington, 57-61.

Melosh, H.J., 1978. Dynamic support of the outer rise. Geophys. Res. Lett., 5, 321-324.

Melosh, H.J., and Raefsky, A., 1980. The dynamical origin of subduction zone topography. Geophys. J.R. astron. Soc., 60, 333-354.

Meyer, R.P., Mooney, W.D., Hales, A.L., Helsley, L.E., Woollard, G.P., Hussong, D.M., Kroenke, L.W., and Ramirez, J.E., 1976. Project Nariño III: refraction observation across a leading edge, Malpelo Island to the Colombian Cordillera Occidental. In: The geophysics of the Pacific ocean basin and its margin, Geophys. Monogr. Washington, 19, 105-132.

Minster, J.B., and Jordan, T.H., 1978. Present-day plate motions. J. geophys. Res., 83, 5331-5350.

Moore, G.F., and Karig, D.E., 1976. Development of sedimentary basins on the lower trench slope. Geology, 4, 693-697.

Moore, J.C., and Karig, D.E., 1976. Sedimentology, structural geology and tectonics of the Shikoku subduction zone, southwestern Japan. Bull. geol. Soc. Am., 87, 1259-1268.

Moore, J.C., and Watkins, J.S., 1979. D.S.D.P. Leg 66, JOIDES J., 5(3), 11-21.

Moore, J.C., Watkins, J.S.. et al., 1979a. Middle America trench. Geotimes, 24(9), 20-22.

Moore, J.C., Watkins, J.S., et al., 1979b. Progressive accretion in the Middle America trench, southern Mexico. Nature, 281, 638-642.

Murdock, J.N., 1969a. Short-term seismic activity in the central Aleutian region. Bull. seismol. Soc. Am., 59, 789-797.

Murdock, J.N., 1969b. Crust-mantle system in the central Aleutian region - a hypothesis. Bull. seismol. Soc. Am., 59, 1543-1558.

Murrell, S.A.F., 1965. The effect of triaxial stress systems on the strength of rocks at atmospheric temperatures. Geophys. J.R. astron. Soc., 10, 231-281.

Nagumo, S., Kasahara, J., and Koresawa, S., 1980. Large Poisson's ratio and low S-wave velocity within the Japan trench inner wall toe. Mar. Geol., 35, 129-133.

Oliver, J., and Isacks, B., 1967. Deep earthquake zones, anomalous structures in the upper mantle and the lithosphere. J. geophys. Res., 72, 4259-4275.

Parrish, D.K., Krivz, A., and Carter, N.L., 1976. Finite element folds of similar geometry. Tectonophysics, 32, 183-207.

Petelin, V.P., 1964. Hard rocks in the deep-water trenches of the southwestern part of the Pacific Ocean. Int. geol. Congr. 22, Reports of Soviet Geologists, 16, 78-86.

Price, N.J., 1977. Aspects of gravity tectonics and the development of listric faults. J. geol. Soc. London, 133, 311-327.

Richter, F.M., and McKenzie, D.P., 1978. Simple plate models of mantle convection. J. Geophys., 44, 441-471.

Rutherford, D.E., Fluid dynamics. Oliver and Boyd, Edinburgh, 226 pp.

Rubey, W.W., and Hubbert, M.K., 1959. Role of fluid pressure in mechanics of overthrust faulting: II. Bull. geol. Soc. Am., 70, 167-205.

Seely, D.R., 1977. The significance of landward vergence and oblique structural trends on trench inner slopes. In: Talwani, M., and Pitman, W.C., III,(eds.) Island arcs, deep sea trenches and back arc basins. A.G.U. Washington, 187-198.

Seely, D.R., Vail, P.R., and Walton, G.G., 1974. Trench slope model. In: Burke, C.A., and Drake, C.L., The geology of continental margins, Springer-Verlag, New York, 249-260.

Service, K.G., and Douglas, A., 1973. Boundaries and fractures in finite element models of geological structures. Geophys. J.R. astron. Soc., 32, 1-14.

Shipley, T.H., McMillen, K.J., Watkins, J.S., Moore, J.C., Sandoval-Ochoa, J.H., and Worzel, J.L., 1980. Continental margin and lower slope structures of the Middle America trench near Acapulco (Mexico). Mar. Geol., 35, 65-82.

Shor, G.G., Jr., and von Heune, R., 1972. Marine seismic refraction studies near Kodiak, Alaska. Geophysics, 4, 697-700.

Stein, R., and Wickham, J., 1980. Viscosity-based numerical model for fault-zone development in drape folding. Tectonophysics, 66, 225-251.

Sykes, L.R., 1971. Aftershock zones of great earthquakes, seismicity gaps, and earthquake prediction for Alaska and the Aleutians. J. geophys. Res., 76, 8021-8041.

Toksöz, M.N., Chinnery, M.A., and Anderson, D.L., 1967. Inhomogeneities in the Earth's mantle. Geophys. J.R. astron. Soc., 13, 31-59.

Tullis, J.A., 1979. High temperature deformation of rocks and minerals. Rev. Geophys., 17, 1137-1154.

Turcotte, D.L., McAdoo, D.C., and Caldwell, J.G., 1978. An elastic-perfectly plastic bending of the lithosphere at a trench. Tectonophysics, 47, 193-205.

von Huene, R., 1972. Structure of the continental margin and tectonism at the eastern Aleutian trench. Bull. geol. Soc. Am., 83, 3613-3626.

von Huene, R., Auboin, J., et al., 1980. Leg 67: The Deep Sea Drilling Project mid-America trench transect off Guatemala. Bull. geol. Soc. Am., I, 91, 421-432.

von Huene, R., Lathram, E.H., and Reimnitz, E., 1971. Possible petroleum resources of offshore Pacific margin Tertiary basin, Alaska. Mem. Am. Assoc. Petrol. Geol., 15, 136-151.

Walcott, R.I., 1970. Flexural rigidity, thickness and viscosity of the lithosphere. J. geophys. Res., 75, 3941-3954.

Wang, C-Y., 1980. Sediment subduction and frictional sliding in a subduction zone. Geology, 8, 530-533.

Wang, C-Y., and Mao, N-H., 1979. Shearing of saturated clays in rock joints at high confining pressures. Geophys. Res. Lett., 6, 825-828.

Watkins, J.S., Moore, J.C., et al., in press. Accretion, underplating, subduction and tectonic evolution, Middle America trench, southern Mexico: results from Leg 66, D.S.D.P. Int. geol. Congr. 26.

Watts, A.B., and Cochran, J.R., 1974. Gravity anomalies and flexure of the lithosphere along the Hawaiian-Emperor seamount chain. Geophys. J.R. astron. Soc., 38, 119-141.

Watts, A.B., and Talwani, M., 1974. Gravity anomalies seaward of deep-sea trenches and their tectonic implications. Geophys. J.R. astron. Soc., 36, 57-90.

Weertman, J., and Weertman, J.R., 1975. High temperature creep of rock and mantle viscosity. Ann. Rev. Earth planet. Sci., 3, 293-315.

Westbrook, G.K., 1975. The structure of the crust and upper mantle in the region of Barbados and the Lesser Antilles. Geophys. J.R. astron. Soc., 43, 201-242.

Woodward, D.J., 1976. Visco-elastic finite element analysis of subduction zones. Unpublished Ph.D. thesis. University of Durham, 215 pp.

Yoshii, T., 1979. A detailed cross-section of the deep seismic zone beneath north-eastern Honshu, Japan. Tectonophysics, 55, 349-360.

Yoshii, T., and Asano, S., 1972. Time term analyses of explosion seismic data. J. Phys. Earth, 20, 47-57.

Yu, G-K., and Mitchell, B.J., 1979. Regionalized shear velocity models of the Pacific upper mantle from observed Love and Rayleigh wave dispersion. Geophys. J.R. astron. Soc., 57, 311-341.

Zienkiewicz, O.C., 1971. The finite element method in engineering science. Second edition, McGraw-Hill, London, 521 pp.

Zienkiewicz, O.C., Watson, M., and King, I.P., 1968. A numerical method of visco-elastic stress analysis. Int. J. mech. Sci., 10, 807-827.